



Computing Radiation Dosimetry – CRD 2002

Workshop Proceedings
Sacavém, Portugal
22-23 June 2002



Nuclear Science

Computing Radiation Dosimetry CRD 2002

**Workshop Proceedings
Sacavém, Portugal
22-23 June 2002**

Hosted by



Instituto Tecnológico Nuclear

© OECD 2004
NEA No. 4311

NUCLEAR ENERGY AGENCY
ORGANISATION FOR ECONOMIC CO-OPERATION AND DEVELOPMENT

ORGANISATION FOR ECONOMIC CO-OPERATION AND DEVELOPMENT

Pursuant to Article 1 of the Convention signed in Paris on 14th December 1960, and which came into force on 30th September 1961, the Organisation for Economic Co-operation and Development (OECD) shall promote policies designed:

- to achieve the highest sustainable economic growth and employment and a rising standard of living in member countries, while maintaining financial stability, and thus to contribute to the development of the world economy;
- to contribute to sound economic expansion in member as well as non-member countries in the process of economic development; and
- to contribute to the expansion of world trade on a multilateral, non-discriminatory basis in accordance with international obligations.

The original member countries of the OECD are Austria, Belgium, Canada, Denmark, France, Germany, Greece, Iceland, Ireland, Italy, Luxembourg, the Netherlands, Norway, Portugal, Spain, Sweden, Switzerland, Turkey, the United Kingdom and the United States. The following countries became members subsequently through accession at the dates indicated hereafter: Japan (28th April 1964), Finland (28th January 1969), Australia (7th June 1971), New Zealand (29th May 1973), Mexico (18th May 1994), the Czech Republic (21st December 1995), Hungary (7th May 1996), Poland (22nd November 1996), Korea (12th December 1996) and the Slovak Republic (14th December 2000). The Commission of the European Communities takes part in the work of the OECD (Article 13 of the OECD Convention).

NUCLEAR ENERGY AGENCY

The OECD Nuclear Energy Agency (NEA) was established on 1st February 1958 under the name of the OEEC European Nuclear Energy Agency. It received its present designation on 20th April 1972, when Japan became its first non-European full member. NEA membership today consists of 28 OECD member countries: Australia, Austria, Belgium, Canada, the Czech Republic, Denmark, Finland, France, Germany, Greece, Hungary, Iceland, Ireland, Italy, Japan, Luxembourg, Mexico, the Netherlands, Norway, Portugal, Republic of Korea, the Slovak Republic, Spain, Sweden, Switzerland, Turkey, the United Kingdom and the United States. The Commission of the European Communities also takes part in the work of the Agency.

The mission of the NEA is:

- to assist its member countries in maintaining and further developing, through international co-operation, the scientific, technological and legal bases required for a safe, environmentally friendly and economical use of nuclear energy for peaceful purposes, as well as
- to provide authoritative assessments and to forge common understandings on key issues, as input to government decisions on nuclear energy policy and to broader OECD policy analyses in areas such as energy and sustainable development.

Specific areas of competence of the NEA include safety and regulation of nuclear activities, radioactive waste management, radiological protection, nuclear science, economic and technical analyses of the nuclear fuel cycle, nuclear law and liability, and public information. The NEA Data Bank provides nuclear data and computer program services for participating countries.

In these and related tasks, the NEA works in close collaboration with the International Atomic Energy Agency in Vienna, with which it has a Co-operation Agreement, as well as with other international organisations in the nuclear field.

© OECD 2004

Permission to reproduce a portion of this work for non-commercial purposes or classroom use should be obtained through the Centre français d'exploitation du droit de copie (CCF), 20, rue des Grands-Augustins, 75006 Paris, France, Tel. (33-1) 44 07 47 70, Fax (33-1) 46 34 67 19, for every country except the United States. In the United States permission should be obtained through the Copyright Clearance Center, Customer Service, (508)750-8400, 222 Rosewood Drive, Danvers, MA 01923, USA, or CCC Online: <http://www.copyright.com/>. All other applications for permission to reproduce or translate all or part of this book should be made to OECD Publications, 2, rue André-Pascal, 75775 Paris Cedex 16, France.

FOREWORD

Establishing reliable computational methods and tools for radiation dosimetry is of great importance today due to the increased use of radiation in a number of areas of science, technology and medical applications. Fields concerned include radiation protection, radiation shielding, radiation therapy, radiobiology, biophysics and radiation detection.

A first workshop with tutorials and lectures on this subject was sponsored by the OECD/NEA Nuclear Science Committee and hosted by the Instituto Tecnológico Nuclear (ITN), Sacavém, Lisbon, Portugal, with the objective of providing the best information available and state-of-the-art methods to the younger generation of scientists and researchers. Existing knowledge and acquired competencies in this field need to be transmitted further if a high standard of radiation safety and protection is to be maintained. This is an important aspect of knowledge management.

Radiation dosimetry is the calculation of the energy imparted by radiation per unit mass and the relation of this parameter to biological effects, such as the risk of cancer induction or cell death, or damage to materials in intensive radiation fields. It is necessary for radiation protection purposes in practically all uses of ionising radiation. Examples where radiation dosimetry is needed in particular include:

- Ensuring that the right amount of radiation is emitted in industrial radiography for the purpose of producing clear images of objects and monitoring the radiation levels in the surrounding environment.
- Determining the radiation dose to patients or staff that may be administered or received, so as to determine the radiation shielding required in diagnostic radiology and nuclear medicine.
- Ensuring, during radiation therapy, that the right level of radiation is delivered to tumours without damaging healthy tissues located nearby.

The course was designed to give an overview of the evolving dosimetry field and to examine different technologies such as Monte Carlo or deterministic methods. The current proceedings provide a summary of the workshop, together with the text of the presentations made. These proceedings are a valuable reference for those wishing to better understand and to learn about the most advanced computational methods in radiation dosimetry.

This text is published on the responsibility of the OECD Secretary-General. The views expressed are those of the authors and do not necessarily correspond to those of the national authorities concerned.

Acknowledgements

Acknowledgements are due to the staff of ITN, Sacavém, Portugal, in particular Pedro Vaz and Isabel Gonçalves, for the outstanding workshop organisation and hospitality. Many thanks are also expressed to the lecturers for their particular efforts to make the subject matter attractive to the young generation. Special thanks go to Amanda Costa for her dedication in preparing these proceedings for publication.

TABLE OF CONTENTS

Foreword.....	3
Executive Summary	7
OPENING SESSION	11
<i>P. Pihet</i>	
Importance of Computing Methods in Radiation Protection Dosimetry and Related R&D Activities – EURADOS Contribution.....	
	13
SESSION I	21
Chair: F. Salvat	
<i>A.E. Nahum</i>	
Dosimetric Fundamentals.....	
	23
<i>B. Grosswendt</i>	
Physics of Electron and Photon Transport for Dosimetry Calculations.....	
	37
<i>G. Gualdrini</i>	
Monte Carlo Studies in the Field of Area Monitoring and Personal Dosimetry for Photons Between 10 keV and 10 MeV and Neutrons Below 20 MeV	
	57
<i>M. Pelliccioni</i>	
Monte Carlo Calculation of Conversion Coefficients for High-energy Radiation.....	
	83
SESSION II	97
Chair: B. Grosswendt	
<i>A.E. Nahum</i>	
Monte Carlo Approaches to Important Problems in Radiotherapy Dosimetry	
	99
<i>M. Krämer, B. Bathelt, C. Brusasco, O. Geiss, T. Haberer, E. Rietzel, D. Schardt, M. Scholz, U. Weber, O. Jäkel</i>	
From Ion Tracks to Ion Radiotherapy	
	115
<i>G. Gualdrini</i>	
Monte Carlo Studies in the Field of Internal Dosimetry of Incorporated Radionuclides	
	125
<i>F. Salvat, J.M. Fernández-Varea, J. Sempau, J. Asenjo, A. Sánchez-Reyes, X. Llovet, C. Campos</i>	
PENELope: Specific Features and Applications	
	147

SESSION III	159
<i>Chair: A.E. Nahum</i>	
<i>B. Grosswendt</i>	
Track Structure Simulation: A Basic Tool for Molecular Radiation Biology and Nanodosimetry	161
<i>A. Ferrari, P.R. Sala</i>	
Intermediate- and High-energy Nuclear Reactions in Dosimetry Calculations	179
<i>H.G. Hughes, R.E. Prael</i>	
Modelling Charged-particle Energy-loss Straggling	207
<i>C.R.E. de Oliveira, C.C. Pain, M.D. Eaton, A.K. Ziver, A.J.H. Goddard</i>	
Neutron and Gamma-ray Dosimetry of the Tokai-mura and Sarov Criticality Accidents Using a Deterministic Transport Methodology	217
<i>G.W. McKinney, J.S. Hendricks, L.S. Waters, T.H. Prettyman</i>	
Using MCNPX for Space Applications.....	235
List of Participants	247
List of Organisers, Sponsors, Teachers.....	253

EXECUTIVE SUMMARY

Introduction

The workshop and training course has focused on computational issues and state-of-the-art techniques in dosimetry, radiation protection, radiation shielding, biophysics, medical physics, etc. Students and young scientists have participated in this education and training initiative organised by ITN (Nuclear and Technological Institute, Lisbon) with the following international sponsors:

- The Nuclear Science Committee of the Nuclear Energy Agency (NEA).
- The Radiation Safety Information Computational Center (RSICC) of the USA.
- The European Radiation Dosimetry Group (EURADOS).

Workshop tutorials/lectures

The workshop was opened by Professor J. Carvalho Soares (President of ITN, Portugal), who welcomed participants. This was followed by introductory remarks on the scope and objectives of this training initiatives made by P. Vaz and a presentation by E. Sartori, introducing the international activities of the OECD/NEA in this domain.

The following lectures were delivered:

- P. Pihet (IRSN, France), “Importance of Computing Methods in Radiation Protection Dosimetry and Related Research and Development Activities”.
- A. Nahum (ICR, UK), “Dosimetric Fundamentals”.
- G. Gualdrini (ENEA, Italy), “Monte Carlo Studies in the Field of Area Monitoring and Personal Dosimetry for Photons Between 10 keV and 10 MeV and Neutrons Below 20 MeV”.
- M. Pelliccioni (INFN, Italy), “Monte Carlo Calculation of Conversion Coefficients for High-energy Radiation”.
- A. Nahum (ICR, UK), “Monte Carlo Solutions to Important Problems in Radiotherapy Dosimetry”.
- M. Kraemer (GSI, Germany), “From Ion Tracks to Ion Radiotherapy”.
- G. Gualdrini (ENEA, Italy), “Monte Carlo Studies in the Field of Internal Dosimetry of Incorporated Radionuclides”.
- F. Salvat (U. Barcelona, Spain), “PENELOPE: Special Features and Applications”.

- N. Hertel (Georgia Tech, USA), “Numerical Simulation of Radiation Instrument and Dosimeter Responses” (oral presentation, overhead handouts).
- B. Grosswendt (PTB, Germany), “Track Structure Simulation: A Basic Tool for Molecular Radiation Biology and Nanodosimetry”.
- A. Ferrari (CERN), “Intermediate- and High-energy Nuclear Reactions in Dosimetry Calculations”.
- G. Hughes (LANL, USA), “Modelling Charged-particles Energy-loss Straggling”.
- C. Oliveira (Imperial College, UK), “Computing Radiation Dosimetry: Deterministic Calculations”.
- E. Sartori (OECD/NEA), “Use of Dosimetry Data in Atmospheric Dispersion, Waste Management and Transport of Radioactive Materials” (oral presentation, overhead handouts).

Objectives of the Workshop on Computing Radiation Dosimetry

The main objectives were to discuss and review the state-of-the-art *computational* methods and techniques used in different fields and applications, such as:

- Dosimetry.
- Radiation protection.
- Radiation shielding.
- Radiation therapy.
- Radiobiology.
- Biophysics.
- Biology-related (emerging) “applications”.
- Radiation detection.

The workshop has pin-pointed the importance of R&D activities in radiation physics, radiation dosimetry, radiation protection, biophysics, biomedical engineering, biology and of computational methods used today for these research areas.

The workshop aimed essentially at education and training, and the initiative responded to concerns outlined in:

- *Nuclear Education and Training: Cause for Concern?*, Summary report from the OECD/NEA (2000).
- *How to Maintain Nuclear Competence in Europe: A Reflection Paper Prepared by the CCE Fission Working Group on Nuclear Education Training and Competence*, EURATOM document EUR 19787.

as well as to studies on the topic of “Radiation Serving Society” published in:

- *Better Integration of Radiation Protection in Modern Society*, OECD/NEA Workshop Proceedings (2002).
- *Policy Issues in Radiological Protection Decision Making*, OECD/NEA Workshop Proceedings (2001).

One reason for holding this workshop in Portugal in conjunction with a hands-on training course using the MCNPX code was to strengthen international co-operation in:

- Projects/working groups/task forces co-ordinated by international organisations.
- Consortia of organisations from different countries.
- “Networks of excellence”.

and within Portugal to foster co-operation between:

- ITN.
- Academia.
- Research institutes.
- Industry.
- Hospitals.
- Other “actors”.

OECD/NEA activities in this area

Radiation dosimetry is of great importance today, both to countries generating electricity from nuclear power, and to those using radiation in many other technological applications, medicine and biology. The OECD/NEA, the international sponsor of the workshop, and other international organisations co-ordinate activities in this field that are of common interest and benefit to the different countries.

OECD/NEA committees involved with radiation dosimetry include:

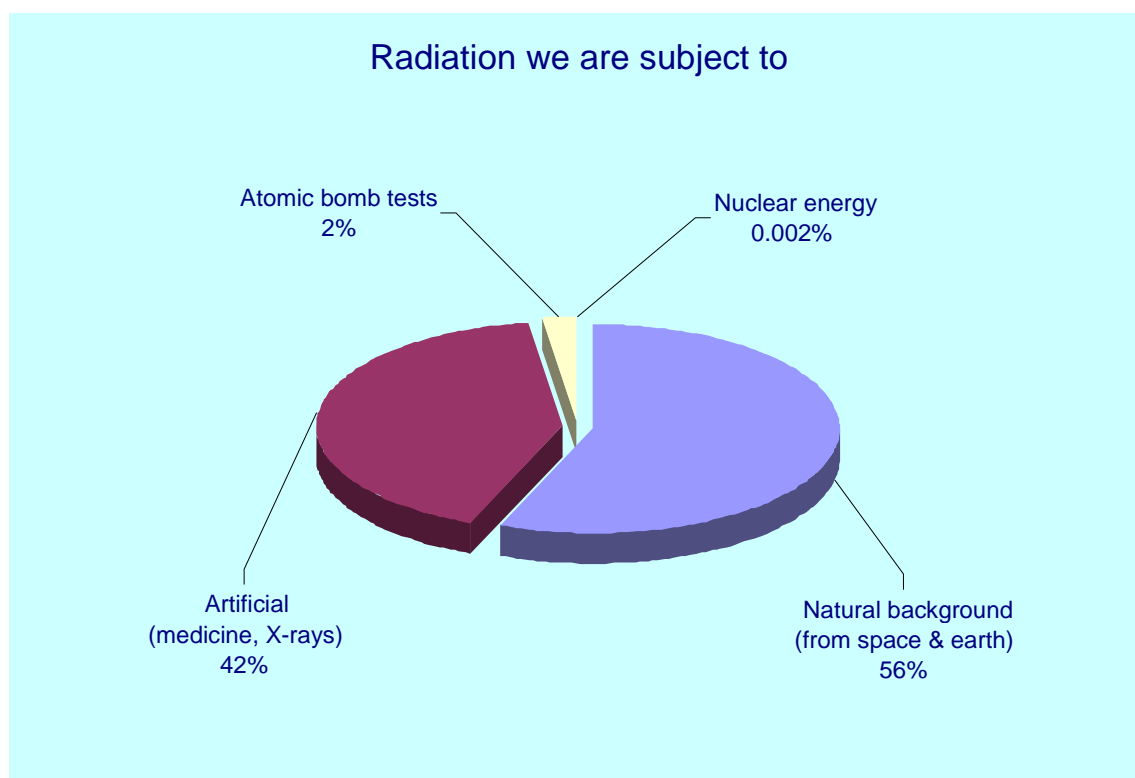
- Radiation Protection.
- Safety of Nuclear Installations.
- Nuclear Science.

The Nuclear Science Committee (NSC) covers the aspect of radiation shielding and radiation dosimetry including in particular basic data for shielding and dosimetry, computer codes for radiation transport, and integral experiments relative to shields and dosimetry.

Radiation safety is of concern to all countries, and smaller countries or countries not having embarked in nuclear power are starting to play an important role in providing increasing contributions to this field. Non-nuclear power applications of radiation involve an increasing workforce as applications expand.

Educational aspects of radiation physics are important for an efficient and safe use of radiation in technology, medical and biological sciences.

The following figure shows the average proportion of different radiation sources to which the world population is subjected (source ANS).



Conclusions

The Workshop on Computing Radiation Dosimetry, followed by an MCNP-X training course was held at ITN, Lisbon, Portugal. The course was attended by 58 participants from 13 countries and 3 international organisations, all of whom were provided with a CD-ROM containing all presentations as well as some other background reports. Fourteen lectures were given by international experts. During the discussion it was concluded that computation methods and codes developed recently can help users to design devices measuring as close as possible what happens in the human body or biology in radiation fields. An important aspect is the extension to lower energies (100 eV – this is the range of cell nuclei and chromosomes), providing greater insight into what happens in radiation biology. There is a need to obtain better data specific to this field. The new knowledge acquired needs to be included into today's codes: recent studies show that we should cast some doubt onto results of the past and revisit the problems in a critical way using new insight.

OPENING SESSION

**IMPORTANCE OF COMPUTING METHODS IN RADIATION PROTECTION
DOSIMETRY AND RELATED R&D ACTIVITIES – EURADOS CONTRIBUTION**

P. Pihet

Institut de Radioprotection et de Sûreté Nucléaire (IRSN)
Fontenay-aux-Roses

Abstract

The European Radiation Dosimetry Group (EURADOS) has, over the years, had a continuous interest in the implications of evolving computing methods in radiation protection dosimetry. The use and actual capabilities of computing methods has indeed drastically increased in the last twenty years and concern all areas of dosimetry, including research and applications. Depending on the needs expressed, EURADOS contributions have taken various forms including working groups and collaborations in the framework of concerted actions. These activities are described in this paper.

The first working group set up within the EURADOS programme (and with the support of the European Commission) concerned numerical dosimetry. It dates from the 80s and was first chaired by Georges Burger (National Research Centre for Environment and Health, GSF, Neuherberg, Germany) followed by Bernd Siebert (Physikalisch technische bundesanstalt, PTB, Braunschweig, Germany). As of 1996, work was carried on in dedicated concerted actions within the EC's Framework Programme (4th FP and 5th FP). The project currently underway in this framework is known as Quality Assurance of Computational Tools for Dosimetry (QUADOS). The secretariat of these groups has been handled, successively, by David Thomas (NPL, Teddington, UK), Chris Perks (AEA, Harwell, UK) and at present Robert Price (Clatterbridge Centre for Oncology, UK). In addition to their own contributions, these groups have won considerable experience in the fields of development, use and qualification of computing methods in dosimetry. They could provide useful assistance to different thematic working groups and contributions in various training courses. The review of these contributions shows the importance and diversity of computing radiation dosimetry. A few examples briefly illustrate this diversity. More details can be found in related reports and publications:

- *Response functions of multi-sphere neutron spectrometry systems [1]*. Multi-sphere systems are a widely used technique to assess neutron spectra *in situ*. The system uses the moderation of neutrons vs. neutron energy by coupling polyethylene spheres of variable size and ³He proportional counters. The interest of this method therefore rests on the reliability of the response functions necessary to unfold the neutron spectra from the set of multi-sphere measurements. The detailed intercomparison work performed demonstrated the conditions under which the agreement between the methods used in different laboratories is obtained and provided information on the influence of the detector design. It contributed directly to the quality assurance of the method and its application for workplace monitoring.

Figure 1 illustrates part of the results obtained in this investigation. It compares the calculations of the response functions corresponding to two spheres as obtained by different methods. We can distinguish calculations using the ANISN code giving the response in pre-selected ranges of energy ("adjoint mode") and those using Monte Carlo (MCNP and BOKU) codes giving the function as discrete point corresponding to the incident neutron energy ("pointwise cross-section mode"). In addition, calculations in the adjoint mode are shown with and without taking into account the binding effects of the carbon and the hydrogen in the polyethylene. The ANISN approach was actually used by many groups for calculating multi-sphere response functions. It was therefore important to know how accurate they are, especially at low energies. As can be seen, a good agreement is observed between Monte Carlo and ANISN data (IKE code) providing that binding effects are taken into account. Ref. [1] can be consulted for a more detailed discussion.

- *Compilation and analysis of W data in tissue-equivalent gas [2]*. In this work, a close collaboration was established between a thematic working group of EURADOS dealing with the application of gas ionisation devices in dosimetry and microdosimetry and experts of the numerical dosimetry group to consider the difficult problem of providing reliable and up-to-date basic physical data, the mean energy required to produce an ion pair W in this case, for determining the response of gas ionisation devices. The work indeed implies the analysis of experimental data of different origins and their reduction in the form of analytical expressions. It provides an excellent example of a situation in which, over the period of a couple of years, experts joined their efforts to produce new analytical expressions traceable to old algorithms, to discriminate unphysical results derived from calculations, to resolve the comparison of experimental and predicted data and to identify remaining uncertainties and the need for further investigations (Figure 2). Moreover, the results could provide practical data (i.e. W vs. neutron energy curves, Figure 3) and assess the impact of the new curve on actual measurements (i.e. microdosimetric spectra, Figure 4).

Figure 1 Response functions calculated for two spheres with different diameters (polyethylene density = 0.92 g. cm⁻³)

Reproduced from [1] by courtesy of Radiation Protection Dosimetry

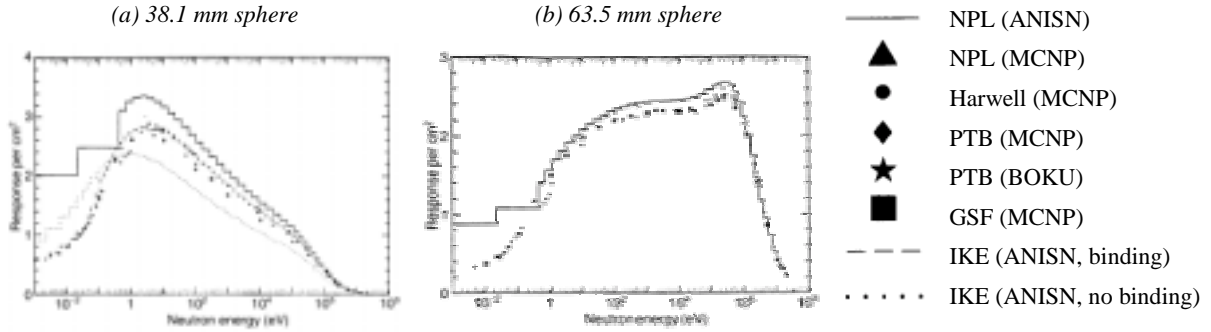


Figure 2. Analysis of W values for protons in CH₄ tissue-equivalent gas as a function of proton energy

Upper part – integral W values, lower part – differential w values

The symbols correspond to different set of experimental values analysed from published data

The lines correspond to different methods for fitting the data (see Ref. [2] for more detailed description)

Reproduced from [2] by courtesy of Radiation Protection Dosimetry

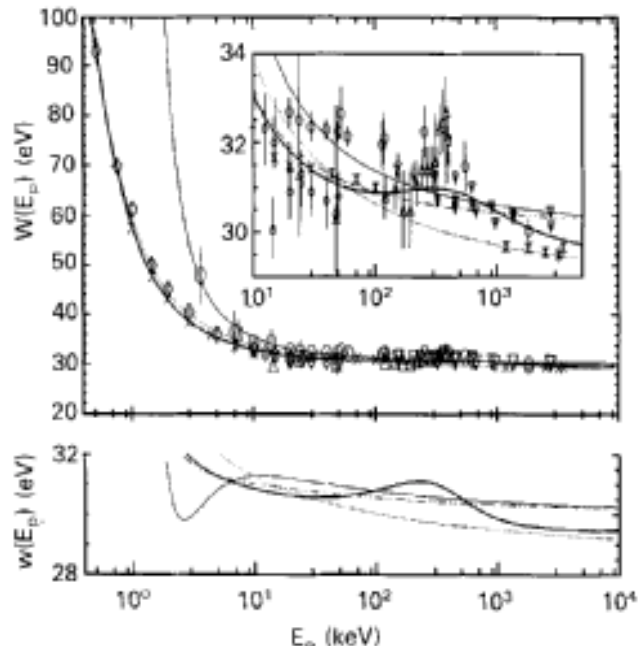


Figure 3. Computation of W_n values as function of neutron energy (E_n) for an infinite cavity of tissue-equivalent gas and using different models for W_p (see Figure 2)

Reproduced from [2] by courtesy of Radiation Protection Dosimetry

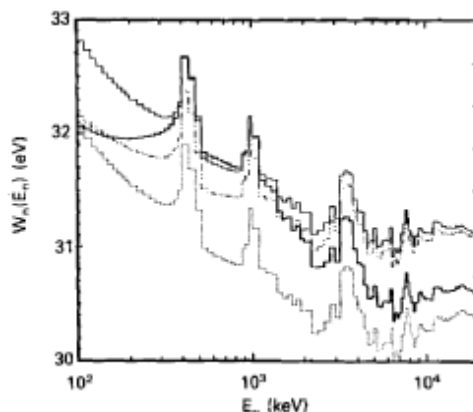
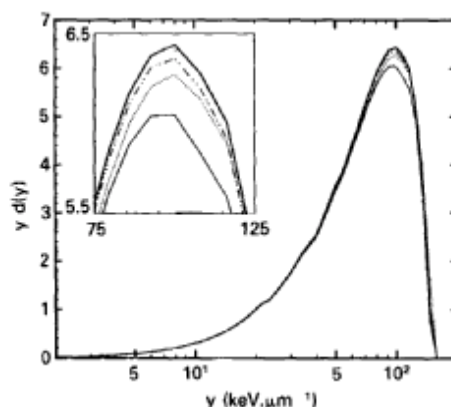


Figure 3. Microdosimetric spectra computed using different W_p models (see Figure 2) for a TEPC with A-150 tissue-equivalent plastic wall, filed CH_4 gas to simulate a $1 \mu m$ cavity at 145 keV neutron energy

Reproduced from [2] by courtesy of Radiation Protection Dosimetry



- *Conversion factors for use in radiological protection against external radiation [3].* In 1990, the International Commission on Radiological Protection (ICRP) published recommendations implying changes to the specification of radiation protection quantities. The International Commission on Radiation Units and Measurements (ICRU) developed a set of measurable operational quantities following earlier ICRP recommendations. It was therefore necessary to investigate to what extent these operational quantities still adequately represented the protection quantities, which implied carrying out a considerable amount of expert calculations. Experts of the above-mentioned numerical dosimetry groups (including J.L. Chartier, B. Grosswendt, N. Petoussi-Henss, M. Zankl, B.R.L. Siebert) have made substantial contributions as members of the joint ICRP-ICRU task group specially set up to perform these investigations, the results of which can be found and examined in more detail in Ref. [4].
- *Use of Monte Carlo methods in radiation protection and dosimetry [4].* Prior to the present training course, several sessions sponsored by the Organisation for Economic Co-operation and Development (OECD) were organised in collaboration with EURADOS, namely in

Bologna (1996) and London (1998), on the reliable use of stochastic methods in computational dosimetry. These courses have been regularly attended by increasing groups of participants, Monte Carlo methods being more and more widely used to achieve reliable radiation transport calculations for various investigations. A good knowledge of the methods, principles and capabilities of their features, underlying assumptions and limitations is a definite prerequisite to ensure the correct use of these codes. The collaboration of EURADOS and OECD allowed a comprehensive treatment of this field, including theoretical background, physics aspects, numerical methods as well as practical training. Moreover, the work plan of the concerted actions included the provision of a compendium of Monte Carlo codes used in dosimetry, in particular those used for high-energy applications [5].

- *Quality assurance of computational tools for dosimetry [6].* Within the framework of the concerted action currently carried out (5th FP), the QUADOS group has promoted an international intercomparison on the usage of computational codes (Monte Carlo, analytic and semi-analytic codes or deterministic methods) for dosimetry in radiation protection and medical physics based on eight problems selected for their relevance to the radiation dosimetry community. The results currently collected and assessed will be presented at a workshop planned in Bologna in July 2003 [7]. The aims of this action include:
 - “providing a snapshot of the methods and codes currently in use;
 - furnishing information on the methods used to assess the reliability of computational results;
 - disseminating “good practice” throughout the radiation dosimetry community;
 - providing the users of computational codes with an opportunity to quality-assure their own procedures;
 - informing the community about the benefits to be obtained from sensitivity and uncertainty analysis;
 - informing the community about more sophisticated approaches that may be available to them.”

Different applications and areas of dosimetry in which computing methods play a key role could be added to these examples. Some of them have been addressed within the EURADOS framework, for example numerical modelling of tissue-equivalent proportional counters [8] or, in collaboration with the European Late Effects Project (EULEP) group, the methods used for assessing internal dose due to the intake of radionuclides [9,10]. Other fields of application have emerged more recently, such as the use of Monte Carlo methods for the modelling and calibration of *in vivo* spectrometry measurements.

Each of these applications presents particular difficulties and specific requirements, in particular regarding acceptable uncertainties. However, they all involve the same process consisting of the “connecting and ordering of known data, by means of relations based on theory or established models, in order to create new data and to reveal new insights” [11]. Furthermore, as pointed out by the authors of this publication, they all require an expert knowledge of the methods and reliability of the results which relies at some levels on an indispensable comparison between calculated and experimental data which is nothing more than “dosimetry” – the word itself being composed of “dose” (i.e. implying numbers) and “metry” (i.e. the art of measuring).

In 2002, QUADOS expressed its views on the actions which should be carried on in the field of numerical dosimetry. Indeed, the fundamental basis of reliable radiation protection is quality-assured measurements, and the quality of measurements in radiation protection relies increasingly on the use of computational methods and on the extent to which a reliable uncertainty can be stated. Furthermore, there should be a link between the need for practice and mechanisms to assure the transfer from pure to applied research and to practical application. In the Expression of Interest published on Internet [12], the subjects of further work assessed by the group as most relevant future projects include research on advanced tools such as:

- *“VOXEL phantoms.* “VOXEL” phantoms are anatomical models, composed by about a million cells, which allow a very high level of detail in the object description. Due to the rather large variety of models already developed, they should be intercompared and checked, both from the point of view of the image segmentation and from the point of view of the Monte Carlo techniques employed to speed up the particle tracking.
- *Unfolding codes.* Unfolding of measured spectra, for instance at work places is essential for a more accurate dosimetry. Members of the group work on including the uncertainty of the response matrices into the uncertainty analysis.
- *Combination of Monte Carlo and deterministic codes.* This technique can considerably reduce computing times and supports the uncertainty analysis of complex transport problems.
- *Simulation of complex measurements (virtual experiments and response functions).* Virtual experiments are the ideal tool for understanding, optimising and evaluating complex experiments.
- *High-level sensitivity and uncertainty analysis and propagation.* Sensitivity analysis and uncertainty analysis and propagation are the backbone of quality assurance and are required by ISO 17025.”

EURADOS intends to carry on with computational dosimetry as a priority axis of its future programme and is currently investigating with the group QUADOS suitable conditions for continuing this work.

REFERENCES

- [1] Perks, CA., D.J. Thomas, B.R.L. Siebert, S. Jetzke, G. Hehn and H. Schraube, “Comparison of Response Function Calculation for Multi-spheres, *Rad. Prot. Dosim.*, 44, 85-88 (1992).
- [2] Siebert, B.R.L., J.E. Grindborg, B. Grosswendt and H. Schuhmacher, “New Analytical Representation of W Values for Protons in Methane-based Tissue-equivalent Gas”, *Rad. Prot. Dosim.*, 52, 123-127 (1994).
- [3] International Commission on Radiation Units and Measurements, *Conversion Factors for Use in Radiological Protection Against External Radiation*, ICRU Report 57, Bethesda, USA (1998).

- [4] Gualdrini, G and L. Casalini, eds., *Use of MCNP in Radiation Protection and Dosimetry*, Proceedings of a training course held at ENEA (Italian National Agency for New Technology, Energy and the Environment), Bologna, May 1996, ISBN 88-8286-000-1.
- [5] Chartier, J.L., A. Ferrarri, B. Grosswendt, G. Gualdrini, P. Leuthold, H.G. Menzel, R. Price, B.R.L. Siebert, H. Tagziria, R. Tanner, M. Terrisol, *Review of Monte Carlo and Deterministic Codes in Radiation Protection and Dosimetry*, Hamid Tagziria, ed., National Physical Laboratory, NPL Report ISBN 0 946754 32 2 (1999).
- [6] Concerted action *Quality Assurance of Computational Tools for Dosimetry (QUADOS)*, Ref. FIGD-CT2000-20062 (<http://www.cordis.lu/fp5-euratom/src/projects.htm>).
- [7] *Intercomparison on the Usage of Computational Codes in Radiation Dosimetry*, International Workshop, Bologna, 14-16 July 2003 (see <http://www.nea.fr/download.quados/quados.html> or <http://www.eurados.org>).
- [8] Schmitz, Th., A.J. Waker, P. Kliauga and J. Zoetelief, "Design, Construction and Use of Tissue Equivalent Proportional Counters", EURADOS report, *Radiat. Prot. Dosim.*, 61(4) (1995).
- [9] Gibson, J.A.B., A. Birchall, R.K. Bull, K. Henrichs, E. Iranzo, D.J. Lord, J. Piechowski, E. Sollett, N.P. Tancock and C. Wernli, "European Intercomparisons of Methods Used for the Assessment of Intakes of Internally Deposited Radionuclides", *Rad. Prot. Dosim.* 40, 245-257 (1992), EC Report EUR 1419 (1992) and EC Report EUR 14195 (1994).
- [10] Doerfel, H., A. Andrasi, M. Bailey, A. Birchall, C. Castellani, C. Hurtgen, N. Jarvis, L. Johansson, B. Le Guen, G. Tarroni, "Third European Intercomparison Exercise on Internal Dose Assessment. Results of a Research Programme in the Framework of the EULEP/EURADOS Action Group *Derivation of Parameter Values for Application to the Model of the Human Respiratory Tract for Occupational Exposure 1997-1999*", FZKA 6457 (2000).
- [11] Siebert, B.R.L. and R.H. Thomas, "Computational Dosimetry", *Proc. of the 8th Symposium on Neutron Dosimetry*, H.G. Menzel, J.L. Chartier, R. Jahr and A. Rannou, eds., *Rad. Prot. Dosim.*, 70 (1-4), 371-378 (1997).
- [12] Siebert, B.R.L., *Quality Assurance for Dosimetry*, Expression of Interest, EOI.FP6.2002 (www.cordis.lu/fp6/eoi-analysis.htm).

SESSION I

Chair: F. Salvat

DOSIMETRIC FUNDAMENTALS

Alan E. Nahum

Radiation Oncology Dept., Fox-Chase Cancer Center
Philadelphia PA 19111, USA
alan_e_nahum@yahoo.co.uk

Abstract

This text covers some important concepts in radiation dosimetry with an emphasis on cavity theory, i.e. the theoretical evaluation of D_{med}/D_{det} , for two important classes of detector, “large” and Bragg-Gray. Monte Carlo simulation continues to play a major role in evaluating this expression through its ability to compute the fluence spectra of electrons and photons as a function of their position in a medium. The key results in the paper can be summarised thus:

- Fluence $\Phi = dN/da = \sum ds/dV$ and is a scalar quantity.
- Kerma $K = dE_{tr}/dm$, i.e. kinetic energy (k.e.) transferred per unit mass; collision kerma K_c excludes charged-particle k.e. converted to bremsstrahlung.
- Kerma and fluence are related by $K_{med} = \Phi E (\mu_{tr}/\rho)_{med}$ for photons of energy E ; for collision kerma, K_c , the mass energy-absorption coefficient μ_{en} replaces μ_{tr} .
- $D_{med} = (K_c)_{med}$ under conditions of charged particle equilibrium (CPE), for a medium med irradiated by photons.
- For a fluence Φ of charged particles, e.g. electrons, in medium med , the absorbed dose $D_{med} = \Phi (S_{col}/\rho)_{med}$ provided there is δ -ray equilibrium.
- For large detectors under photon irradiation (i.e. in which there is CPE as e^- ranges \ll detector size), D_{med}/D_{det} is given by $(\mu_{en}/\rho)_{med}/(\mu_{en}/\rho)_{det}$ which is evaluated over the photon spectrum at the detector position: e.g. TLD (e.g. LiF) in kV X-ray beams are large.
- For “small” or Bragg-Gray detectors under photon or electron irradiation (e^- ranges \gg detector dimensions), D_{med}/D_{det} is given by $(S_{col}/\rho)_{med}/(S_{col}/\rho)_{det}$, the (mass) stopping-power ratio, usually written $s_{med,det}$: e.g. (air-filled) ionisation chambers behave as Bragg-Gray detectors in megavoltage photon and electron beams, but not in kV X-ray beams.
- Bragg-Gray theory was extended by Spencer and Attix to take into account the finite range of δ -rays.
- General cavity theory provides an approximate treatment of detectors which are neither “large” nor “small”.

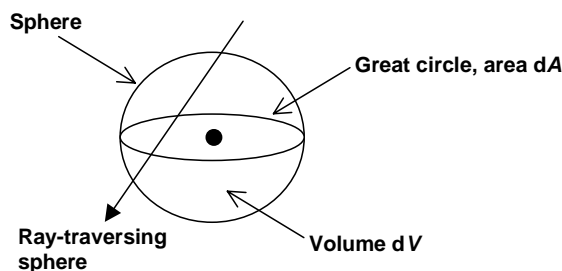
Introduction

The accurate determination of absorbed dose is crucial factor in the success of radiotherapy. The interpretation of the reading of a detector, when used as a dosimeter, generally requires some appreciation of the theoretical aspects of radiation dosimetry, as does the calculation of the dose distribution inside the complicated inhomogeneous geometry of the patient. In this brief text the main ideas and principles involved in the subject, sometimes known as “cavity theory”, are covered. The basic expressions that will be derived and discussed are those relating the dose in the uniform, i.e. undisturbed, medium at the point of interest to that in the detector or dosimeter, thus D_{med}/D_{det} . In principle it is not necessary to know the numerical value of this ratio in cases where the detector is calibrated to read absorbed dose (usually for *medium* = water) in the particular radiation quality of interest. However, frequently this is not the case, and it becomes necessary to convert the detector response at the calibration quantity, which would typically be ^{60}Co γ -rays, to that at the quality of interest, e.g. 10 MeV electrons. A further introductory point is that the process of converting the raw detector response, e.g. charge for an ionisation chamber, chemical yield for the ferrous sulphate detector, light output for a thermoluminescent dosimeter (TLD), to absorbed dose to the sensitive material of the detector (via W/e for an ion chamber, G-value for the FeSO_4 dosimeter) is not generally dealt with under the heading of cavity theory and consequently is not covered in what follows. The reader is referred to several excellent general texts in the medical physics literature [1-7].

Particle fluence

In order to be able to calculate absorbed dose we require quantities which describe the radiation field. Particle fluence is a very important basic quantity, concerning the number of particles per unit area. The concept is illustrated in Figure 1.

Figure 1. Characterisation of the radiation field at a point P in terms of the radiation traversing the spherical surface S (redrawn from [2])



Let N be the expectation value of the number of rays striking a finite sphere surrounding point P (during a finite time interval). If the sphere is reduced to an infinitesimal one at P with a diameter of da , then the fluence Φ is given by:

$$\Phi = \frac{dN}{dA} \quad (1)$$

which is usually expressed in units of m^{-2} or cm^{-2} . Note that fluence is a scalar quantity – the direction of the radiation is not taken into account. Additionally it is useful to define the energy fluence ψ :

$$\psi = E\Phi \quad (2)$$

The convention in radiation dosimetry is to write the fluence, differential in energy, as Φ_E :

$$\Phi_E = \frac{d\Phi}{dE} \quad (3)$$

and thus the (total) fluence is given by:

$$\Phi = \int_0^{E_{max}} \Phi_E dE \quad (4)$$

It is important to realise that fluence can also be expressed as the quotient of the sum of the track lengths of the particles crossing the elementary sphere divided by the volume of the sphere [8]:

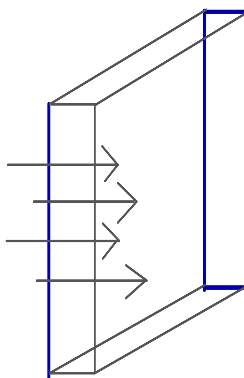
$$\Phi = \frac{\sum ds}{dV} \quad (5)$$

This expression is extremely useful when considering so-called cavity integrals (see later) which generally involve evaluating the fluence averaged over a volume and subsequently the absorbed dose in that volume; this is generally the technique used in Monte Carlo simulations.

Relation between fluence and kerma

We are now in a position to relate quantities concerning energy transferred to or deposited in a medium to the fluence, which is a basic description of the radiation field. Consider the following schematic of N radiation tracks, of indirectly ionising radiation, each of energy E , crossing a thin layer dl of area dA :

Figure 2. A thin slab of material, thickness dl , area dA , mass dm , density ρ , traversed (perpendicularly) by radiation; here N photons of energy E



Recalling now the definition of the mass energy transfer coefficient μ_{tr}/ρ (e.g. ICRU 1998) and rearranging this:

$$dE_{tr} = (\mu_{tr})_{med} d\Phi E \quad (6)$$

then dividing by the mass of the layer dm :

$$\frac{dE_{tr}}{dm} = (\mu_{tr}) E \left[\frac{Ndl}{dm} \right] \quad (7)$$

and replacing dm by $\rho \times dV$ we can write:

$$\frac{dE_{tr}}{dm} = \left(\frac{\mu_{tr}}{\rho} \right)_{med} E \left[\frac{Ndl}{dV} \right] \quad (8)$$

in which we recognise the expression in the square brackets as the sum of the track lengths divided by the volume, i.e. fluence, and in place of dE_{tr}/dm we can write kerma (in medium med):

$$K_{med} = \left(\frac{\mu_{tr}}{\rho} \right)_{med} E\Phi \quad (9)$$

or, in terms of energy fluence ψ :

$$K_{med} = \left(\frac{\mu_{tr}}{\rho} \right)_{med} \psi \quad (10)$$

Thus far we have confined ourselves to particles crossing the thin layer all with a single energy. In the case of spectrum of energies, described by the fluence differential in energy, Φ_E , we evaluate the K_{med} from:

$$K_{med} = \int_0^{E_{max}} E \Phi_E \left(\frac{\mu_{tr}(E)}{\rho} \right)_{med} dE \quad (11)$$

where the energy dependence of μ_{tr} has been shown explicitly.

We will also want to calculate collision kerma, K_c . The mass energy transfer coefficient μ_{tr}/ρ is replaced by the mass energy absorption coefficient μ_{en}/ρ , where energy “absorbed” is defined to exclude that part of the initial kinetic energy of charged particles converted to bremsstrahlung photons. The two coefficients are related by:

$$\mu_{en} = \mu_{tr} (1 - g) \quad (12)$$

which is naturally also the factor that relates K_c to K . It therefore follows that:

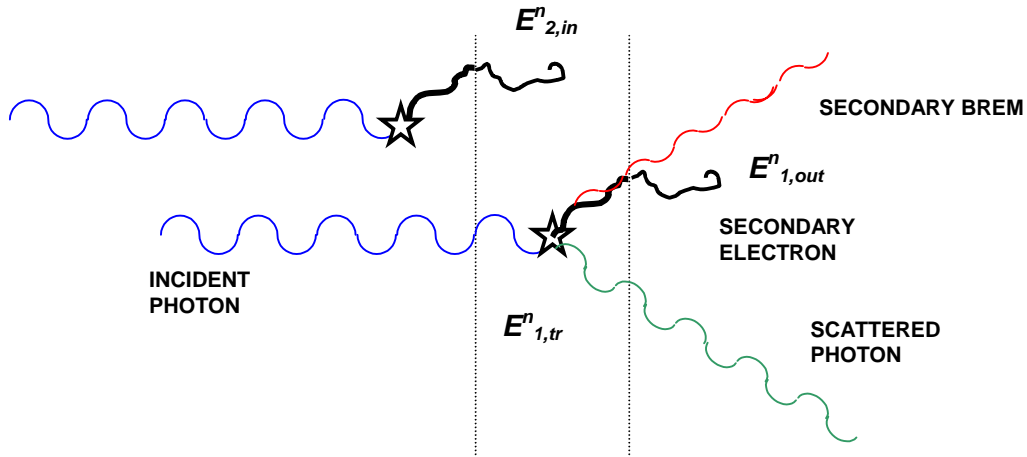
$$(K_c)_m = \left(\frac{\mu_{en}}{\rho} \right) E\Phi \quad (13)$$

and similarly for the integral over Φ_E in the case of a spectrum of incident photons.

Relation between kerma and absorbed dose

The absorbed dose D_{med} in medium med concerns the (mean) value of energy imparted to an elementary volume, whereas kerma concerns energy transferred, which is not the same thing at all, as the charged particles can leave the elementary volume (or thin layer), taking a fraction of the initial kinetic energy with them. This is illustrated in Figure 3. Note that the quantity denoted in the figure by E_{tr}^n is the net energy transferred, which excludes that part of the initial kinetic energy converted into bremsstrahlung photons; it is equal to $E_{tr}(1 - g)$ as we have seen above.

Figure 3. Schematic illustration of charged particle equilibrium in a thin layer in a medium irradiated by photons



Let the energy imparted to the layer be denoted by ε , the (net) kinetic energy entering the layer on charged particles by E_{in}^n and the (net) kinetic energy leaving the layer by E_{out}^n . Then we have:

$$\varepsilon = E_{tr}^n - E_{out}^n + E_{in}^n \quad (14)$$

If now the electron track that leaves the layer happens to be replaced by an identical track that enters the layer such that:

$$E_{in,2}^n = E_{out}^n \quad (15)$$

it follows that:

$$\varepsilon = E_{tr}^n \quad (16)$$

The equality between energy leaving and energy entering on charged particles is known as charged particle equilibrium (CPE); this condition can be realised to a very good approximation under certain circumstances (see next section).

Dividing both sides by the mass of the layer or volume element, we can write:

$$D_m = (K_c)_{m}^{CPE}$$

and therefore:

$$(K_c)_m = \left(\frac{\mu_{en}}{\rho} \right) E\Phi \quad (17)$$

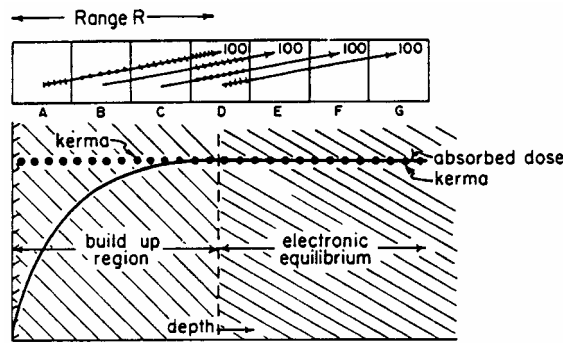
which are very important results.

Charged particle equilibrium (CPE)

Charge particle equilibrium (CPE) is said to exist in a volume V in an irradiated medium if each charged particle of a given type and energy leaving V is replaced by an identical particle of the same energy. Figure 4, for the case of a photon beam, taken from [4], illustrates how CPE can actually be achieved in a photon beam, provided that there is no/negligible attenuation of the beam. Note that square D, where CPE is first attained, contains all the sections of an electron track.

Figure 4. The development of charged particle equilibrium in a medium irradiated by photons

Reproduced from [4] with permission



In practice, in the megavoltage beams encountered in modern radiotherapy, there is only partial CPE as the attenuation of the photons is not negligible in a distance equal to the range, $r_{max,e-}$, of the maximum energy secondary electron. However, in kilovoltage X-ray beams (e.g. used for diagnostic purposes and some superficial radiotherapy) there is negligible attenuation in a distance $r_{max,e-}$ (due to the rapidly increasing collision stopping power at sub-relativistic electron energies); thus there is an excellent approximation to full CPE.

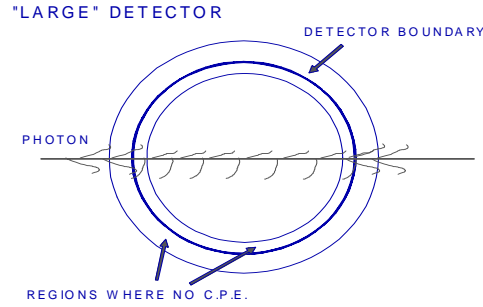
Photon detectors

The relation between absorbed dose and collision kerma can be exploited in predicting the relation between the reading of a dosimeter and the dose in the uniform medium in the absence of the dosimeter, for the case of indirectly ionising radiation. Let a beam of monoenergetic radiation be incident on a phantom of material med with energy fluence ψ at the depth of interest z . Provided that this depth is sufficient for CPE to be established then we can equate D_{med} with K_c and thus write:

$$D_{med}^{CPE} = \psi_{med,z} \left(\frac{\mu_{en}}{\rho} \right)_{med} \quad (18)$$

Suppose now that the detector is placed with its centre at the depth z and that the sensitive material of the detector, denoted by det , is large enough for there to be CPE in this material, i.e. that its extent is very much greater than the maximum range of the secondary electrons generated in this material. Figure 5 illustrates what is intended.

Figure 5. A schematic illustration of the concept of a “large” or photon detector, where the electron tracks are much shorter than the cavity dimensions



The photon track goes through a spherical detector and produces secondary electrons tracks (changes in the photon direction/energy have been ignored for simplicity). Within the dotted regions on either side of the boundary there is no CPE but elsewhere there is. The detector can be said to be “large” when the volume of the dotted region is small compared to the total detector volume. Then we can write:

$$D_{det}^{CPE} = \Psi_{det,z} \left(\frac{\mu_{en}}{\rho} \right)_{det} \quad (19)$$

where now the energy fluence is that in the detector material. If we further assume that the detector does not disturb the fluence existing in the medium, i.e.:

$$\Psi_{det,z} = \Psi_{med,z} \quad (20)$$

then it follows that:

$$\frac{D_{med}}{D_{det}} = \frac{\Psi_{med,z} (\mu_{en}/\rho)_{med}}{\Psi_{med,z} (\mu_{en}/\rho)_{det}} = \frac{(\mu_{en}/\rho)_{med}}{(\mu_{en}/\rho)_{det}} \quad (21)$$

which is a standard result for a “large” detector. Naturally the detector must not have a dimension in the direction of the beam, which is large with respect to the attenuation of photons within it, i.e. detector thickness $t \ll 1/\mu_{att}$, the (average) photon mean free path, otherwise it would be impossible to fulfil the requirement that the (energy) fluence in the detector be negligibly different from that in the medium. In the more realistic case of a polyenergetic photon beam, the dose ratio is evaluated as:

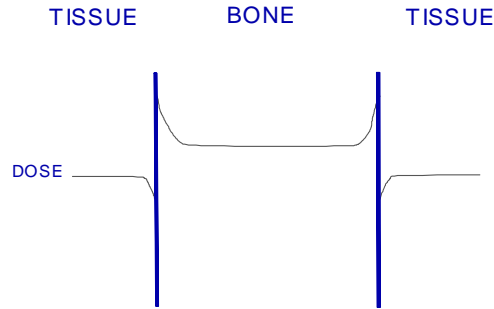
$$\frac{D_{med}}{D_{det}} = \frac{\int_0^{E_{max}} \frac{d\Psi_{med,z}}{dE} \left(\frac{\mu_{en}(E)}{\rho} \right)_{med} dE}{\int_0^{E_{max}} \frac{d\Psi_{med,z}}{dE} \left(\frac{\mu_{en}(E)}{\rho} \right)_{det} dE} \quad (22)$$

which is often written in shorthand form as:

$$\frac{D_{med}}{D_{det}} = (\bar{\mu}_{en}/\rho)_{med,det} \quad (23)$$

An example of the application of the “large” detector is the use of small TL dosimeters in low-energy photon fields. Another application is the calculation of the change in the absorbed dose when the material changes from tissue to bone in a patient irradiated by a low-energy X-ray beam. Figure 6 illustrates schematically what would happen to the dose levels when the medium changes, for the case where there is CPE in both media (except extremely close to the boundary where differential secondary-electron backscattering effects are evident). The equilibrium dose levels in the tissue and the bone are proportional to $(\bar{\mu}_{en}/\rho)_{tissue}$ and $(\bar{\mu}_{en}/\rho)_{bone}$, respectively.

Figure 6. A schematic illustration of the variation of absorbed dose at a tissue-bone-tissue interface, where the bone is acting as a photon detector; interface effects due to electron build-up and scattering will occur very close to the medium boundaries



Electron or Bragg-Gray detectors

Relation between fluence and dose for electrons

A relation between charged particle fluence, in particular for electrons, and absorbed dose will now be developed. Consider that there are N electron tracks t perpendicularly incident on a thin layer of thickness dl (refer to Figure 2). Recall that stopping power is energy lost per unit track length [9] and denote this energy by dE_l to distinguish it from dE_{tr} used for indirectly ionising radiation. We are interested in energy locally deposited in the thin layer, so it is clearly appropriate to employ the collision stopping power, S_{col} , rather than the total stopping power as the latter would include the energy lost in the form of bremsstrahlung which would escape. Thus we can write:

$$dE_l = S_{col} dl N \quad (24)$$

Note that unlike the analogous Eq. (6) for photons we do not need the energy of the particles. Dividing both sides by the mass of the layer dm and expressing this as $\rho \times dV$ on the right hand side we obtain:

$$\frac{dE_l}{dm} = \frac{S_{col} N dl}{\rho dV} \quad (25)$$

which can be regrouped to give:

$$\frac{dE_l}{dm} = \frac{S_{col}}{\rho} \left[\frac{NdI}{dV} \right] \quad (26)$$

where, as in the case of indirectly ionising radiation, the quantity in the square brackets is the fluence Φ :

$$\frac{dE_l}{dm} = \Phi \frac{S_{col}}{\rho} \quad (27)$$

Until recently there has not been an equivalent of kerma for the case of charged particles, i.e. a quantity to express the energy transferred as opposed to imparted or absorbed. However, the quantity CEMA (converted energy per unit mass) has been proposed [9,10]. In the above case CEMA is simply equal to our dE_l/dm and thus to the product of electron fluence and mass collision stopping power.

In order to bring absorbed dose into the picture we must be able to say that any charged particle kinetic energy that leaves the thin layer or elementary volume is replaced by an exactly equal amount entering the layer and being deposited in it/imparted to it. The particles that leave, in the present case, are energetic delta rays. Thus we have to assume that there is delta-ray equilibrium in order to be able to equate CEMA and absorbed dose and thus to write, for a medium *med*:

$$D_{med}^{\delta\text{-eqm}} = \Phi \left(\frac{S_{col}}{\rho} \right)_{med} \quad (28)$$

or, in the case of polyenergetic electron radiation:

$$D_{med}^{\delta\text{-eqm}} = \int_0^{E_{max}} \Phi_E \left(\frac{S_{col}(E)}{\rho} \right)_{med} dE \quad (29)$$

where Φ_E is the fluence, differential in energy (see earlier).

Bragg-Gray cavity theory

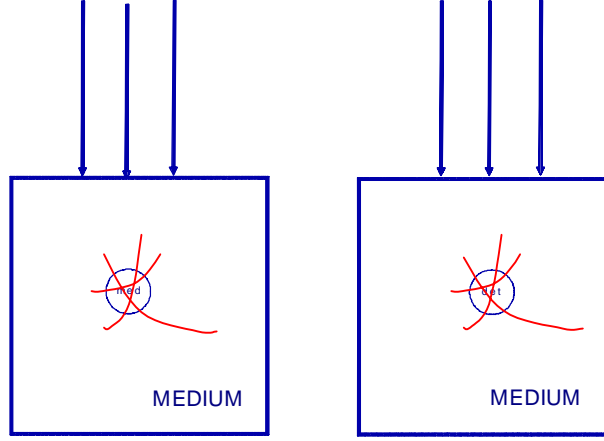
We have seen that in the case of detectors with sensitive volumes large enough for the establishment of CPE, the ratio D_{med}/D_{det} is given by $(\overline{\mu_{en}/\rho})_{med,det}$ for the case of indirectly ionising radiation. In the case of charged particles one requires an analogous relation in terms of stopping powers. If we assume that the electron fluences in the detector and at the same depth in the medium are given by Φ_{det} and Φ_{med} respectively, then according to Eq. (28) we must be able to write:

$$\frac{D_{med}}{D_{det}} = \frac{\Phi_{med} (S_{col}/\rho)_{med}}{\Phi_{det} (S_{col}/\rho)_{det}} \quad (30)$$

where we recall that \overline{D}_{det} is the mean dose over detector volume, i.e. that which is proportional to the detector signal. Consider the situation shown Figure 7.

Figure 7. Schematic illustration of the electron detector or Bragg-Gray principle; a beam of photons irradiates the uniform medium

*Left – a fictitious detector volume in the medium, right – an identical volume made of detector material
Both volumes are traversed by identical electron fluences*



If we assume that the detector does not disturb the electron fluence existing in the undisturbed medium, i.e. if:

$$\Phi_{det} = \Phi_{med} \quad (31)$$

then the fluences in Eq. (30) cancel out, yielding:

$$\frac{D_{med}}{D_{det}} = \frac{(S_{col}/\rho)_{med}}{(S_{col}/\rho)_{det}} \quad (32)$$

The above expression is known as the (mass) stopping-power ratio, often written as $s_{med,det}$ (or as $s_{med/det}$). For the practical case of a spectrum of electron energies, the stopping-power ratio must be evaluated from:

$$\frac{D_{med}}{D_{det}} = \frac{\int_0^{E_{max}} \Phi_E (S_{col}(E)/\rho)_{med} dE}{\int_0^{E_{max}} \Phi_E (S_{col}(E)/\rho)_{det} dE} \quad (33)$$

where the energy dependence of the stopping powers has been made explicit and it is understood that Φ_E refers to the undisturbed medium in both the numerator and the denominator. It should be stressed that this is the fluence of primary electrons only; no delta rays are involved (see following section). For reasons that will become apparent in the next paragraph, it is convenient to denote the stopping-power ratio evaluated according to Eq. (33) by $s_{med,det}^{BG}$ [11].

The stopping-power ratio result was originally derived for the case of ionisation chambers irradiated by photons, not electrons. A small gas-filled cavity will never fulfil the CPE condition discussed above for so-called photon detectors, as the ranges of the most energetic electrons in a gas easily exceed the

dimensions of the cavity. However, if the gas cavity is sufficiently small then it can be assumed that the cavity does not disturb the electron fluence set up by the photons in the surrounding medium. This is equivalent to saying that the dose to the gas in the cavity results entirely from electrons generated in the surrounding medium and not from the few electrons generated by photon interactions in the cavity gas itself. These principles were first enunciated separately by Bragg and Gray more than 50 years ago, and detectors fulfilling these assumptions are known as Bragg-Gray cavities [e.g. 2-4]

The commonly used air-filled ionisation chamber irradiated by a megavoltage photon beam is the clearest case of a Bragg-Gray cavity. However for typical ion chamber dimensions for kilovoltage X-ray beams, the percentage of the dose to the air in the cavity due to photon interactions in the air is far from negligible, as has been shown explicitly in [12].

In the case of electron beams there are no photon-generated electrons to consider and the stopping-power ratio will always be the relevant quantity. However, the assumption that the fluence must not be appreciably disturbed by the ‘‘cavity’’ limits the applicability of the above theory to detectors that are small compared to the range of the primary electrons. The response of TLD chips and semiconductor diodes in megavoltage electron beams, for example, should be predicted by the stopping-power ratio. Departures from Bragg-Gray assumptions are generally treated as perturbations; see [13].

The Spencer-Attix modification of Bragg-Gray theory

In the previous section we neglected the question of delta-ray equilibrium, which is a prerequisite for the strict validity of the stopping-power ratio as evaluated in Eq. (33). The original Bragg-Gray theory effectively assumed that all collision losses resulted in energy deposition within the cavity. Spencer and Attix [14] proposed an extension of the Bragg-Gray idea that took account, in an approximate manner, of the effect of the finite ranges of the delta rays. All the electrons above a cut-off energy Δ , whether primary or delta rays, were now considered to be part of the fluence spectrum incident on the cavity. All energy losses below Δ in energy were assumed to be local to the cavity and all losses above Δ were assumed to escape entirely. The local energy loss was calculated by using the collision stopping power restricted to losses less than Δ , L_Δ . This two-component model leads to a stopping-power ratio given by [10,14,15]:

$$\frac{D_{med}}{D_{det}} = \frac{\int_{\Delta}^{E_{max}} \Phi_E^\delta (L_\Delta(E)/\rho)_{med} dE + [\Phi_E(\Delta)(S_{col}(\Delta)/\rho)_{med} \Delta]}{\int_{\Delta}^{E_{max}} \Phi_E^\delta (L_\Delta(E)/\rho)_{det} dE + [\Phi_E(\Delta)(S_{col}(\Delta)/\rho)_{det} \Delta]} \quad (34)$$

The electron fluence has been denoted by Φ^δ to emphasise that (all generations of) delta rays must be included. The term in square brackets accounts for the energy deposition by those electrons falling below Δ in energy, the so-called track-end term [15]. The shorthand form recommended by ICRU report 35 [11] for the Spencer-Attix stopping-power ratio is $s_{med,det}^{SA}$. The use of $s_{med,det}^{SA}$ instead of the conventional Bragg-Gray ratio based on the unrestricted stopping power $s_{med,det}^{BG}$ has been shown to result in improved agreement with experiment [2]. However, for cases where the atomic composition, and hence the mean atomic number, Z , of the cavity and the medium are closely matched, there is little difference between $s_{med,det}^{SA}$ and the simpler $s_{med,det}^{BG}$. All modern codes of practice for the absolute dose

determination in megavoltage photon and electron radiotherapy beams use values of $s_{water,air}^{SA}$ evaluated according to Eq. (34) (see Andreo [16]) as part of the conversion of the reading of an ion chamber to absorbed dose in water.

General cavity theory

Two extreme cases have been covered:

- 1) Detectors which are large compared to the electron ranges (indirectly ionising radiation only).
- 2) Detectors which are small compared to the electron ranges and which do not disturb the electron (strictly, charged particle) fluence – so-called Bragg-Gray cavities (directly or indirectly ionising radiation).

Many situations involve measuring the dose from photon (or neutron) radiation using detectors which fall into neither of the above categories. In such cases there is no exact theory. However, so-called “general cavity theory” was developed by Burlin [17] as a simple approximation. A detailed discussion is beyond the scope of the present lecture (see [18]), but in essence these theories yield a factor which is a weighted mean of the stopping-power ratio and the mass-energy absorption coefficient ratio, as the Burlin expression shows:

$$\frac{\bar{D}_{det}}{D_{med}} = ds_{det,med} + (1-d) \left[\frac{\mu_{en}}{\rho} \right]_{med}^{det} \quad (35)$$

where d is the fraction of the dose in the cavity originating from electrons generated in the surrounding medium and $(1-d)$ is the dose from photon interactions in the cavity. Various “recipes” for estimating the magnitude of d have been proposed (e.g. Horowitz [18]). Much work remains to be done in improving the accuracy of this approach (e.g. Mobit, *et al.* [19]).

REFERENCES

- [1] Alm Carlsson, G., “Theoretical Basis for Dosimetry” in *The Dosimetry of Ionizing Radiation* Vol. 1, 1-75, K.R. Kase, B.E. Bjärngard and F.H. Attix, eds., London, Academic Press (1985).
- [2] Attix, F.H., *Introduction to Radiological Physics and Radiation Dosimetry*, New York, Wiley (1986).
- [3] Greening, J.R., *Fundamentals of Radiation Dosimetry*, Bristol, IoP (1981).
- [4] Johns, H.E. and J.R. Cunningham, *The Physics of Radiology*, 4th edition, Springfield, Illinois, Charles C. Thomas (1983).

- [5] Kase, K.R. and W.R. Nelson, *Concepts of Radiation Dosimetry*, New York, Pergamon, ISBN 0-08-023162-4 (1978)
- [6] Mayles, W.P.M., A.E. Nahum and J-C. Rosenwald, *Handbook of Radiotherapy Physics: Theory and Practice*, Bristol and Philadelphia, Institute of Physics Publishing, UK (2003).
- [7] Metcalfe, P., T. Kron and P. Hoban, *The Physics of Radiotherapy X-rays from Linear Accelerators*, Madison, WI, Medical Physics Publishing (1997).
- [8] Chilton, A.B., "Further Comments on an Alternative Definition of Fluence", *Health Phys.*, 36, 637 (1979).
- [9] ICRU (International Commission on Radiation Units and Measurements), *Fundamental Quantities and Units for Ionizing Radiation*, Report 60, Bethesda, Maryland (1998).
- [10] ICRU, *Radiation Dosimetry: Electron Beams with Energies Between 1 and 50 MeV*, Report 35, Bethesda, Maryland (1984).
- [11] Kellerer, A.M., K. Hahn and H.H. Rossi, "Intermediate Dosimetric Quantities", *Radiation Research*, 130, 15-25 (1992).
- [12] Ma, C-M. and A.E. Nahum, "Bragg-Gray Theory and Ion Chamber Dosimetry for Photon Beams", *Phys. Med. Biol.*, 36, 413-428 (1991).
- [13] Nahum, A.E., "Perturbation Effects in Dosimetry: Part I. Kilovoltage X-rays and Electrons", *Phys. Med. Biol.*, 41, 1531-1580 (1996).
- [14] Spencer, L.V. and F.H. Attix, "A Theory of Cavity Ionization", *Radiation. Research*, 3, 239-254 (1995).
- [15] Nahum, A.E., "Water/Air Mass Stopping-power Ratios for Megavoltage Photon and Electron Beams", *Physics in Medicine and Biology*, 23, 24-38 (1978).
- [16] Andreo, P., "Stopping-power Ratios for Dosimetry", in *Monte Carlo Transport of Electrons and Photons*, T.M. Jenkins, W.R. Nelson, A. Rindi, A.E. Nahum and D.W.O. Rogers, eds., New York, Plenum, pp. 485-501 (1988).
- [17] Burlin, T.E., "A General Theory of Cavity Ionization", *British Journal of Radiology*, 39, 727-734 (1966).
- [18] Horowitz, Y.P., "Photon General Cavity Theory", *Radiat. Prot. Dosim.*, 9, 5-16 (1984).
- [19] Mobit, P.N., A.E. Nahum and P. Mayles, "An EGS4 Monte Carlo Examination of General Cavity Theory", *Physics in Medicine and Biology*, 42, 1319-1334 (1997).

PHYSICS OF ELECTRON AND PHOTON TRANSPORT FOR DOSIMETRY CALCULATIONS

Bernd Grosswendt

Physikalisch-Technische Bundesanstalt, Germany

Abstract

The main objective of the physics of particle transport in the fields of radiation protection and of radiation dosimetry for therapy purposes is the determination of the spatial distribution of energy deposition in the human body while exposing it to external ionising radiation. The central physical quantity to be used for this purpose is the absorbed dose to soft tissue or water. Since the direct measurement of absorbed dose distributions within a patient's body is neither directly possible nor reasonable, it must be replaced by measuring procedures in phantoms and by recipes which are well suited to deduce the desired dose distributions. To justify such measuring procedures and recipes, sophisticated Monte Carlo simulations based on interaction cross-sections and particle transport theories are commonly used. The first part of the talk analyses the effort needed to simulate the penetration of photons and high-energy electrons through matter, and summarises the basic physical principles of electron or photon transport models. In a second part, these principles are applied to study a few general aspects of electron or photon histories in water. Here, special emphasis is laid on the depth dependence of spectral electron distributions in primary photon or electron fields and on the range of high-energy electrons as a function of their initial energy. In a final section, the role of low-energy electrons is briefly discussed from the point of view of radiation damage and compared with that of photons and light ions.

Introduction

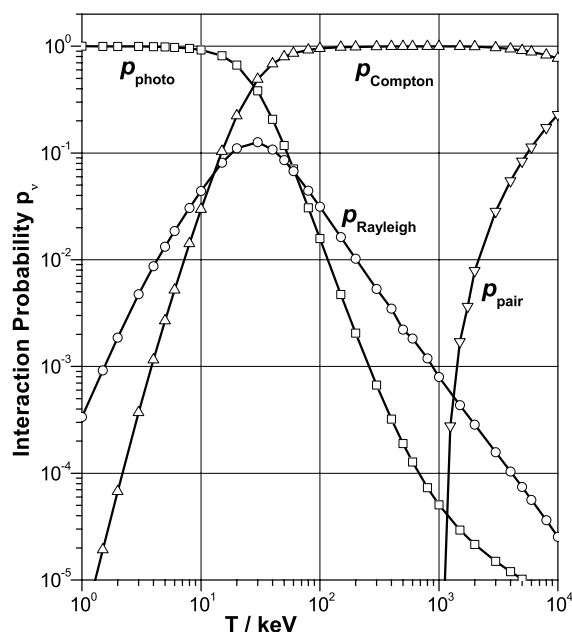
The main objective of radiation physics in the fields of protection against ionising radiation and of dosimetry for therapy purposes is, in the end, the determination of the spatial distribution of energy deposition in the human body while exposing it to external radiation. According to the recommendations of the ICRU [1], the central quantity to be used for these purposes is the absorbed dose $D(P)$ at a specified point P in soft tissue or water. It is defined as the quotient $d\mathcal{E}/dm$, where $d\mathcal{E}$ is the mean energy imparted by ionising radiation to a small piece of matter of mass dm localised at point P and applies to all kinds of ionising radiation. The value of the absorbed dose caused by ionising radiation at the specified point depends strongly on the kind of primary radiation and also on the degradation properties of all secondary particles set in motion by primary interaction processes. Due to the fact that in many practical situations the direct measurement of absorbed dose distributions is either not directly possible or not possible with the necessary accuracy, or that it is too costly in terms of time and labour, sophisticated calculation methods based on particle transport theories are commonly used. These must be well suited with respect to the irradiation conditions encountered in practice and to the shape and structure of the irradiated system. The most direct and at the same time most versatile method for this purpose is the Monte Carlo simulation of the histories of a great number of primary particles for the particular irradiation geometry one has in mind or for geometries which are assumed to be reasonably well suited from the practical point of view. The aim of the present paper is to summarise briefly the physical background of primary electron and photon interactions with matter.

The most important photon interaction process at lower energies is the photoelectric effect, in which the photon is absorbed by an atom and a photoelectron is emitted, leaving a vacancy in the atom, usually in the K-shell. The second interaction process, predominant at photon energies of the order of 1 MeV, is the Compton interaction, in which the photon is inelastically scattered, thus liberating secondary electrons and possibly causing again a vacancy in a target atom. A third major interaction process at lower energies is the Rayleigh scattering effect, in which the photon is elastically scattered, transferring an only negligible energy fraction to a recoil atom. At high photon energies, the pair creation may be the predominant photon interaction process. In this case the photon interacts with the field of an atomic nucleus or an atomic electron and is absorbed while creating an electron-positron pair. Other interaction effects such as nuclear-resonance scattering, Delbrück scattering or photonuclear reactions are, in general, of no importance as far as radiation protection or radiation dosimetry is concerned.

The fraction of photons interacting with matter by one of these processes is given by the probability $p_v(T) = \sigma_v(T)/\sigma_{\text{tot}}(T)$, where $\sigma_v(T)$ is the partial cross-section of photon interaction of type v and $\sigma_{\text{tot}}(T)$ is the total interaction cross-section at photon energy T . For values of these cross-sections or of the corresponding partial or total mass attenuation coefficients see, for instance, the tabulations by Hubbell [2], Plechaty, *et al.* [3], Berger and Hubbell [4], and Higgins, *et al.* [5]. To give an impression of such data, Figure 1 shows the interaction probabilities of photons in water as a function of photon energy T . At a glance, the predominance of the photoelectric effect at energies smaller than about 10 keV and of the Compton scattering at energies greater than about 20 keV becomes obvious. In high- Z materials, the energy region in which Compton scattering predominates is strongly reduced because of an increased importance of the photoelectric effect and of electron-positron pair creation.

Filling up the inner-shell vacancy after photoelectron ejection takes place through a complex cascade of radiative and radiationless events and ends in a multiply ionised state of the target atom, unless electrons are captured from the outside. To simplify matters, it is commonly assumed that the filling up of vacancies occurs by emission of either fluorescence photons or Auger electrons whose energies and emission probabilities depend strongly on the target species. The need for taking into account Auger electrons and fluorescence radiation when performing Monte Carlo simulations thus

Figure 1. Interaction probability p_v of photons at energy T in liquid water, based on the tables of Higgins, *et al.* [5]



depends strongly on the problem to be solved. For many applications in radiation protection dosimetry and radiation therapy, at least in low- Z materials such as water or soft tissue, the production of Auger electrons or of fluorescence radiation can be ignored because the probability of creating fluorescence radiation is negligible and the potential energy of Auger electrons is smaller than the cut-off energy commonly assumed in the simulation. In high- Z materials, however, the creation of fluorescence radiation might be of importance because of the high values of the fluorescence yield and the possibly high energies of fluorescence photons.

To see what happens to photons when they penetrate through matter, let us assume a narrow beam of monoenergetic 100 keV photons penetrating the front face of a water cylinder 20 cm in diameter and height in a direction parallel to the cylinder's main axis. If we were able to follow by eye the path each photon takes within the phantom after having penetrated its front face, we would see a picture like that shown in Figure 2. The photons are scattered elastically by Rayleigh scattering or inelastically by Compton scattering, transferring part of their initial energy to secondary electrons, or they are absorbed by the photoelectric effect and leave the greater part of their energy also to electrons. The main information that could be extracted from the figure is that, during photon slow-down in matter, a great number of secondary electrons is set in motion whose starting points are distributed over the whole volume of the water cylinder, due to a large mean free interaction length of photons and to their strong angular scattering.

If we were able to track also the path of secondary electrons through the phantom, we would see a picture like that shown in Figure 3. The electron tracks appear as only more or less extended small spots, showing that the spatial energy transfer of electrons takes place in dimensions very small as compared with that of photons. The reason for this is the electron range which is generally much smaller than the mean free path length of photons. To demonstrate this fact quantitatively, Figure 4 shows the mean free interaction length $\lambda(T)$ of photons and the continuous-slowing-down range $R_{\text{csda}}(T)$ of electrons in liquid water as a function of the primary particle energy T . The great difference between $R_{\text{csda}}(T)$ and $\lambda(T)$ is obvious from the figure. At the same initial energy the mean free photon interaction length is

Figure 2. Movement of 100 keV photons in a water cylinder in the case of perpendicular incidence along the phantom's main axis

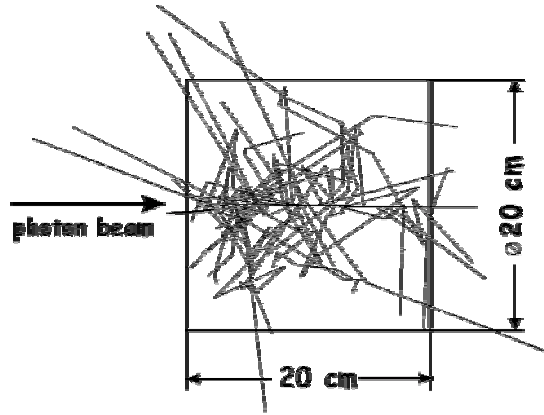


Figure 3. Tracks of secondary electrons liberated in water by the 100 keV photons of Figure 2

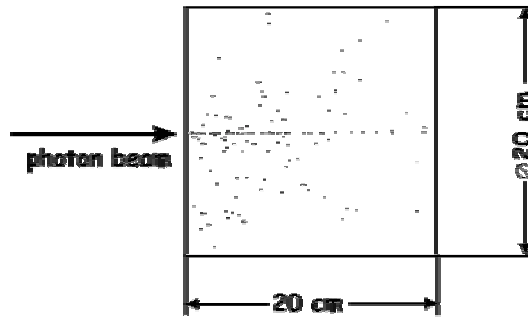
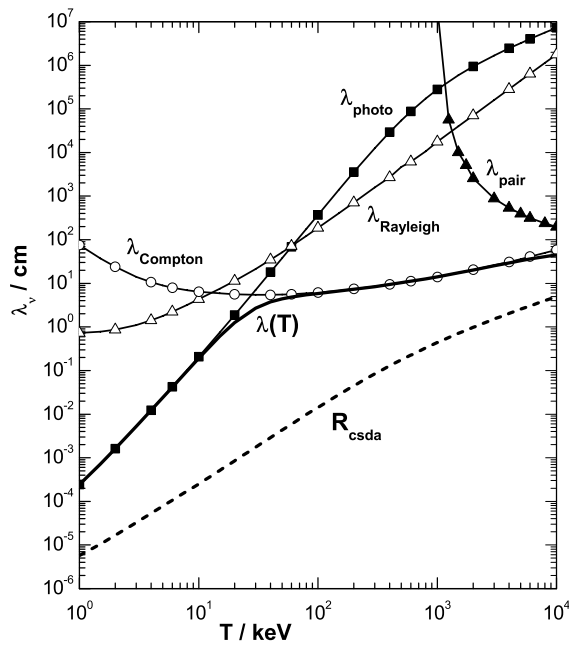


Figure 4. Mean free interaction lengths λ_v of photons at energy T in water, in comparison with the continuous-slowing-down range R_{csda} of electrons at the same energy

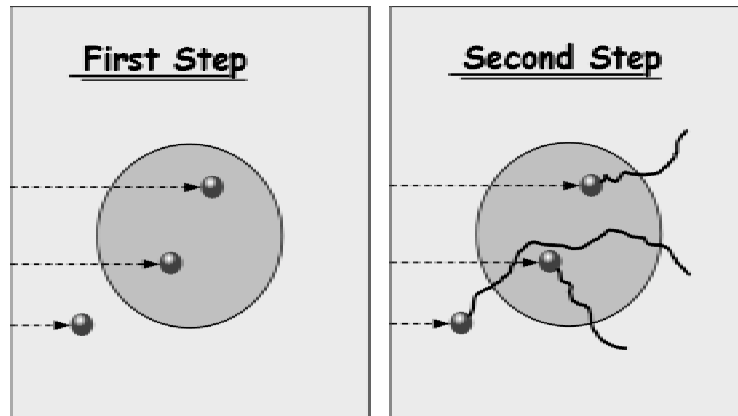


greater than the electron range by a factor of up to 10^3 . In view of this fact, a photon track can be assumed as a collection of single electron tracks the starting points of which are distributed over distances that are large as compared with the mean photon interaction length.

The two-step model of photon transport through matter

Because of the large mean free interaction length of a photon as compared with the range of a secondary electron, the spatial distribution of the absorbed dose caused by photon radiation in matter can be assumed to be produced in two steps (see Figure 5). In the first step, a fraction of the photon energy is transferred to secondary electrons at interaction points separated by rather large distances. In the second step, this energy is distributed by electron transport processes, in the neighbourhood of the photon interaction points. The simulation of the spatial distribution of energy deposition to matter by primary photons can, therefore, be subdivided into two parts. The first is the determination of the spatial distribution of energy transfer interactions of photons and the second one is the transport of energy by secondary electrons. In homogeneous media, the simulation of electron transport can be ignored, in general, because the electron ranges are small as compared with the mean free path lengths of photon interactions (see Figure 4). Nevertheless, the creation of bremsstrahlung due to electron slow down and the annihilation of positrons may be of importance to solve special problems also in homogeneous media. In heterogeneous media, a coupled photon-electron simulation is generally necessary to obtain realistic dose distributions, in particular near surfaces.

Figure 5. The two-step model of energy deposition by photons; in a first step, energy is transferred to electrons by photon interactions, and in the second step this energy is transported by electron interactions



The photon transport through matter

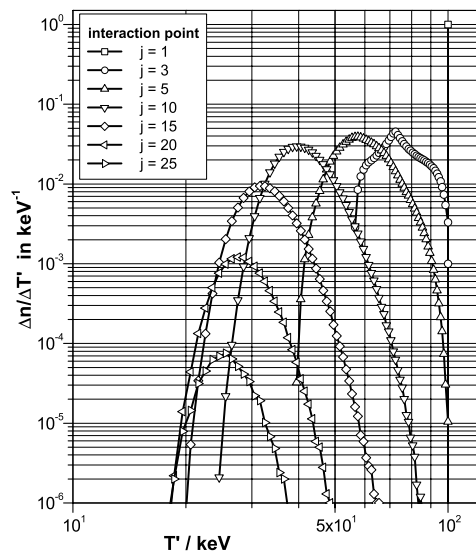
The main steps for simulating the penetration of photons through matter are:

- The determination of the travelling distance of photons between two successive interaction events.
- The selection of the type of interaction a photon suffers after having covered the travelling distance.
- The sampling of energy loss and deflection angle caused by the selected interaction process.

As is obvious from photon attenuation measurements in homogeneous media, the distance between successive interaction points of a photon at energy T is governed by an exponential probability density. This probability density is completely described by the total linear photon attenuation coefficient which is equal to the reciprocal of the mean free interaction length of the photons (Figure 4). The type of photon interaction at each single interaction point is given by the probability $p_\nu(T)$ of photon interactions of type ν which are taken into account in the calculation (commonly: photoelectric absorption, Rayleigh scattering, Compton scattering, and electron-positron pair creation if $T > 1.022$ MeV). After determination of the point of interaction and of the type of interaction process, the energy loss and the new photon direction after interaction have to be determined on the basis of the physical properties of all major photon interaction processes which might be of importance to the solution of a particular problem. For details on photon interaction processes see, for instance, the comprehensive publication by Davisson and Evans [6]. The history of each primary photon is tracked from collision to collision until the photon either leaves the target volume, is absorbed in it, or until its energy has been degraded to a value small enough to be sure that a further continuation of photon transport simulation no longer influences the final results. For details on the Monte Carlo simulation of photon transport see, for instance, the publications by Zerby [7], Nahum [8], Baró, *et al.* [9] and Grosswendt [10,11].

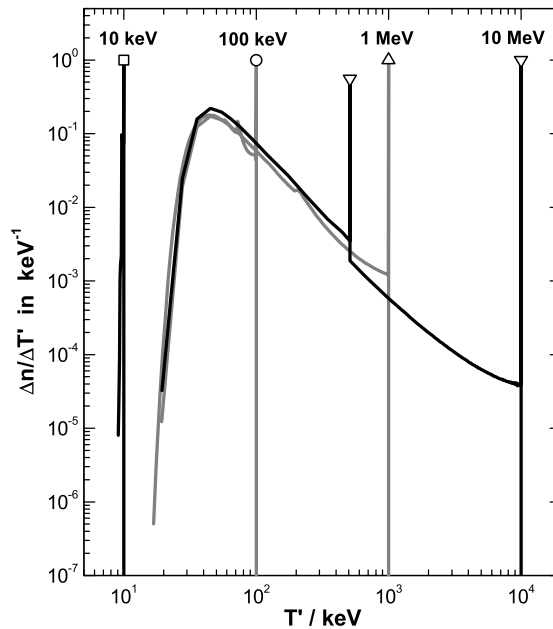
To give an impression of what happens to the photons during their penetration through matter, Figure 6 shows the mean spectral photon distribution $\Delta n/\Delta T'$ per primary photon at interaction number j in the case of monoenergetic primary photons emitted by a point source in water at an energy of 100 keV [11]. The transmutation of the needle-shaped spectral photon distribution at $j = 1$ into a rather broad energy distribution at $j > 1$, and the shift of the energy distribution to smaller energies with increasing interaction number j are obvious. A very interesting feature of the distributions is that they are restricted to energies greater than about 20 keV. This behaviour is due to the competition between Compton scattering and photoelectric absorption. With increasing interaction number, the photon energy decreases (as does the energy transfer to Compton electrons) and the probability of photoelectric absorption rises (see Figure 1). In consequence, the probability of Compton scattering decreases with increasing interaction number whereas the probability of photoelectric absorption strongly goes up, in particular, at the low-energy side of the photon distribution.

Figure 6. Mean spectral photon distribution $\Delta n/\Delta T'$ of initially 100 keV photons at interaction number j in water as a function of photon energy T'



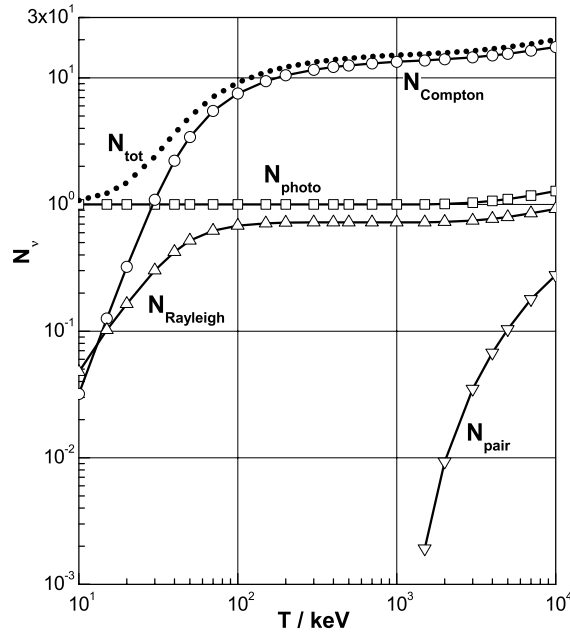
Let us now assume that a photon source works continuously, emitting monoenergetic photons of energy T . Then, after having waited for a time long enough to be sure that there are enough photons of any state of degradation within the water medium, one can ask for the spectral energy distribution $\Delta n/\Delta T'$ of photons responsible for the production of secondary electrons during a subsequent interaction. Figure 7 presents the results for $\Delta n/\Delta T'$ (per primary photon of initial energy T) as a function of photon energy T' for the four selected primary energies of $T = 10$ keV, 100 keV, 1 MeV and 10 MeV [11]. Apart from the occurrence of annihilation quanta of 511 keV in the case of $T = 10$ MeV, it can be seen at a glance that the spectral photon distributions related to the three higher primary energies nearly coincide in their overlapping energy regions, thus demonstrating a rather similar photon degradation process. This is due to the fact that in this energy region Compton scattering is the most important type of interaction (see again Figure 1). Hence, in the case of heavy energy losses or, and that is the same, of large scattering angles, the photon energy after scattering is in the same energy region independent of the photon's primary energy. For instance, the large-angle scattering of a 10 MeV photon leads to an energy after scattering of between about $250 \text{ keV} \leq T' \leq 485 \text{ keV}$ while that of 1 MeV photons leads to an energy of between $204 \text{ keV} \leq T' < 388 \text{ keV}$. If the photon energy decreases, the maximum energy loss decreases as well, leading to a rather continuous photon degradation in the case of Compton scattering which in turn enters more and more into competition with photoelectric absorption. This competition and the almost continuous photon degradation are the reasons for the bump of the spectral photon distribution around 40 keV and also for the very slim distribution in the case of 10 keV primary photons.

Figure 7. Mean spectral photon distribution $\Delta n/\Delta T'$ of initially 10 keV, 100 keV, 1 MeV and 10 MeV photons as a function of energy T' , after complete photon slow-down in water, as a function of photon energy T'



Due to the fact that a photon track can be interpreted as a series of electron tracks separated by more or less large distances, the mean number N_{tot} of electron tracks is one of the basic features of a photon track. This mean number is equal to the mean number of inelastic photon interactions in a specified piece of matter. Figure 8 shows the mean number N_{tot} of photon interactions upon the total degradation of primary photons in water, as a function of its energy T (upper curve) [11]. Interesting

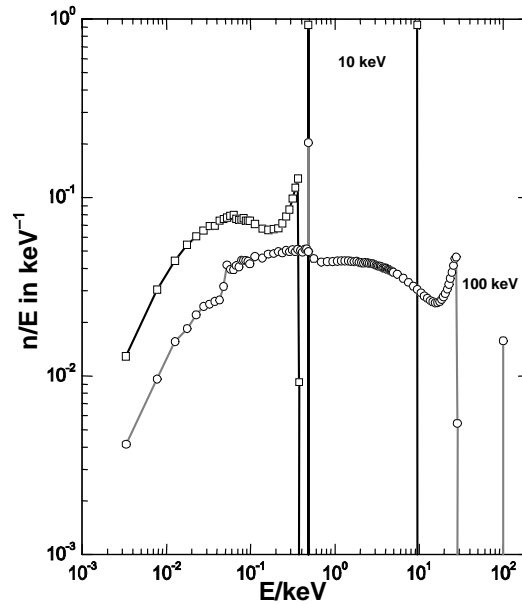
Figure 8. Mean number N_{tot} of photon interactions upon complete photon slow down in water and the mean numbers N_v of a specified interaction type, as a function of photon energy T



aspects of the mean number of interactions are (i) its strong energy dependence between 10 and 100 keV followed by an only slight increase in the energy range between 100 keV and 10 MeV, and (ii) its small value even at high photon energies. To give an impression of the different types of interaction contributing to N_{tot} , the figure also shows the number N_v of photoelectric absorptions, Rayleigh or Compton scatterings, and electron-positron pair creations. The overwhelming contribution of Compton scattering to N_{tot} for energies greater than 50 keV is apparent from the figure. Its strong increase in the low-energy region is due to the increasing probability of Compton scattering with increasing photon energy (see Figure 1). The increasing number of photoelectric absorptions and Rayleigh scatterings at the high-energy end can be ascribed to the electron-positron pair creation followed by the production of annihilation quanta which were interpreted as primary photons because of their high energy of 0.511 MeV [11].

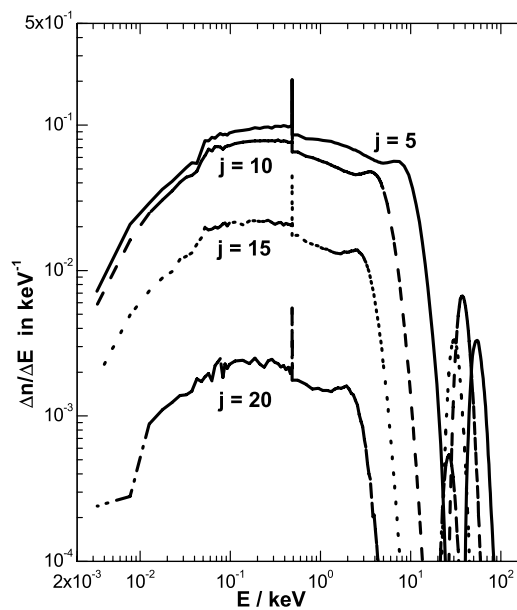
During the simulation of primary photons, the directions and energies of secondary particles (electrons, positrons and fluorescent X-rays) and also the spatial co-ordinates of their starting points are stored and used as initial parameters if the transport of the secondaries is to be taken into account. In consequence, it is worthwhile to consider the energy transfer to secondary electrons in more detail. For this purpose, Figure 9 shows the mean spectral distribution $\Delta n/\Delta E$ of secondary electrons produced in water by photons at 10 keV or 100 keV in the first interaction [11]. Despite the rather complex structure of these distributions they can easily be interpreted on the basis of primary photon interactions. In the case of 100 keV photons the needle-shaped line at about 100 keV, for instance, is produced by photoelectric absorption (about 1.6% at 100 keV), and the edge at 28.1 keV by Compton scattering at $\theta = 180^\circ$. The more or less continuous energy distribution at lower energies is due to the Compton effect at smaller scattering angles, with the exception of the second line at 486 eV which is shaped like a δ -function and represents the Auger electrons created during photoelectric absorption or Compton scattering at an electron of the K-shell of oxygen. If one looks at the secondary electron distribution produced by 10 keV photons in their first interaction, the same features can be found as for the secondary electrons initiated by 100 keV photons, apart from the fact that the Compton edge is at 377 eV and has, therefore, an energy smaller than that of the Auger electron line.

Figure 9. Mean spectral distribution $\Delta n/\Delta E$ of secondary electrons produced by 10 keV or 100 keV photons in water in the first photon interaction as a function of electron energy E



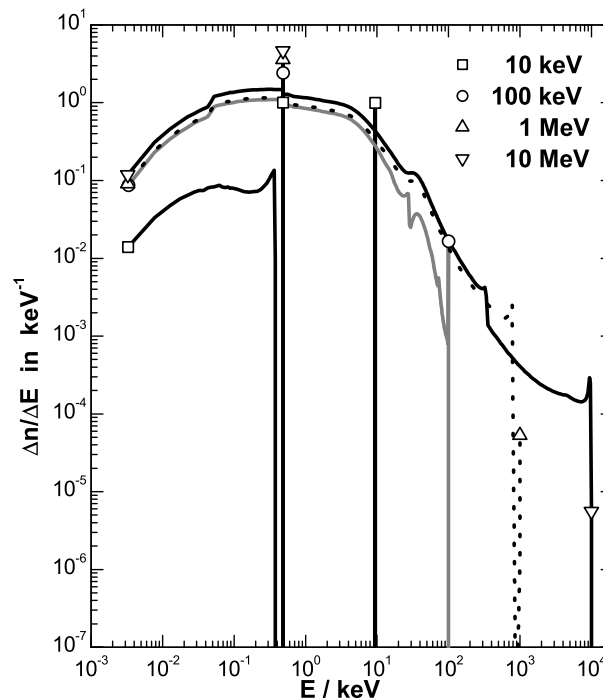
To give an impression of the development of the secondary electron distribution with increasing value of the interaction number j of photons, Figure 10 shows $\Delta n/\Delta E$ produced by 100 keV photons at different values of j [11]. The very complex structure of electron production is obvious. But all interaction points have in common that the spectral electron distribution at any interaction point is composed of two components, a first one at lower energies, which is mainly caused by energy transfer to Compton electrons (in part after multiple photon scattering), and a second one which is caused by photoelectric absorption of multiply scattered Compton photons.

Figure 10. Mean spectral distribution $\Delta n/\Delta E$ of secondary electrons produced by 100 keV photons at interaction j in water as a function of electron energy E



The spectral secondary electron distributions after complete photon slow-down at the primary energies of Figure 7 are presented in Figure 11. The complex structure and the very extended energy range of the secondary electrons from almost the initial energy of the primary photons down to a few eV are striking and can be easily interpreted from the properties of photoelectric absorption, Compton scattering and Auger electron production [11]. At first glance, the similarity of the spectral secondary electron distributions at energies $E \leq 10$ keV (including Auger electrons) caused by primary photon energies $T \geq 100$ keV is noticeable, as is that caused by 1 MeV and 10 MeV photons at $10 \text{ keV} \leq E \leq 200$ keV. In addition, the structure of the distribution related to 100 keV photons can easily be recognised in the distribution for the higher energies. In detail, however, some differences in $\Delta n/\Delta E$ can be seen. These are, for instance, the structure near the Compton edges and the increasing gap (in the logarithmic energy scale) between the photoelectric absorption peak and the Compton edge with decreasing primary photon energy. All these features of the electron energy distribution can be understood if one remembers the spectral photon distributions of Figure 7 and the consequences of the competition between Compton scattering and photoelectric absorption.

Figure 11. Mean spectral distribution $\Delta n/\Delta E$ of secondary electrons produced upon the complete slow-down by primary photons at energy T (see the inset) in water as a function of electron energy E



Summarising the properties of photon tracks it can be stated that:

- The number of interaction points of a typical photon track is restricted to rather small values of about 15 at 1 MeV, depending only slightly on the primary photon energy.
- The interaction points are distributed over large volumes due to the large mean free path lengths of photon interactions and of Compton scattering, in particular (this fact leads to statistical problems when quantities must be determined which are defined at a point in matter like absorbed dose).

- The spectral photon distribution in matter shows a shape which is almost independent of primary photon energy, at least if this energy is large as compared with the energy of absorption edges of photoelectric absorption.
- The spectral distribution of liberated secondary electrons is extended over a large energy range and also depends only slightly on the primary photon energy.

The most important of these features of photon degradation is the large mean free interaction length of photons as compared with the ranges of secondary particles, as it enables the calculation of the spatial distribution of energy deposition to matter to be subdivided into two parts, the first being the determination of the spatial distribution of primary energy transfer interactions (the kerma approximation) and the second, if necessary at all, that of the energy transport by secondary electrons. Because of the comparably short ranges of the secondaries, the simulation of their histories can, in general, be ignored in homogeneous media or in heterogeneous media far away from surfaces. Problems arise near surfaces, however, because of a possible lack of a secondary electron equilibrium. The question is, therefore, how the liberated secondary electrons behave in matter and how they contribute to the energy transfer in photon fields.

Electron transport through matter

When penetrating through matter, electrons are scattered elastically, transferring a negligible fraction of their kinetic energy to atoms or molecules of the target medium, or they are scattered inelastically by impact ionisation or excitation of the target constituents. In addition, at higher initial energies, they can lose part of their energy by the production of bremsstrahlung photons.

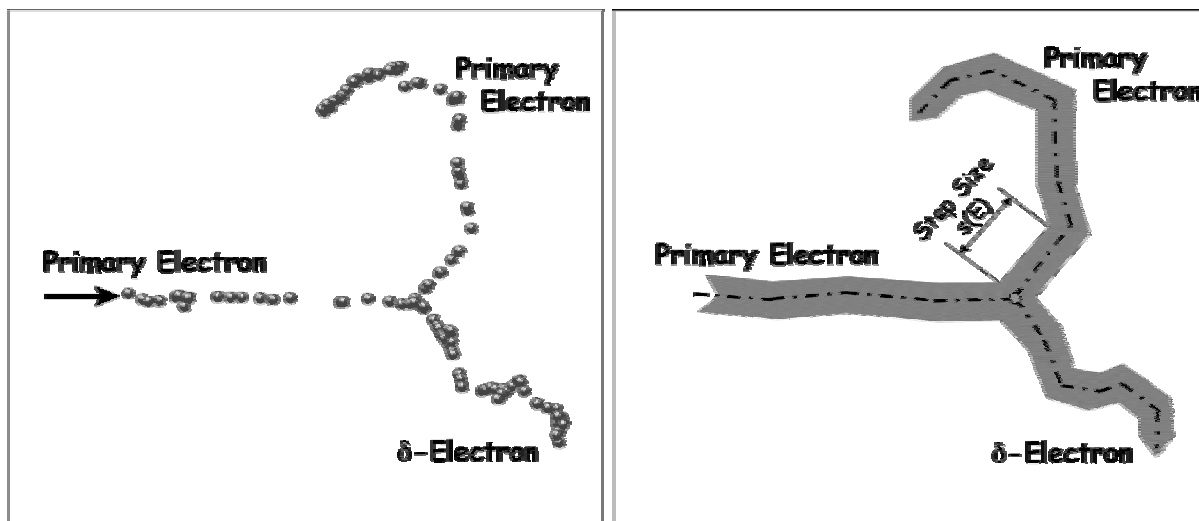
To estimate the mean number of interactions which an electron of kinetic energy E suffers during its complete slow-down in matter, the mean energy W required to produce an ion pair can be used. It is defined by $W = E/N$, where N is the mean number of ion pairs caused during the complete electron slowing-down process. If we assume an initial electron energy of 3 MeV and a W value of 30 eV, which is typical of many media of interest in practice, the mean number N of ion pairs is equal to 10^5 . To determine the total number of electron interactions, the number N must be multiplied by a factor of the order of 2 to 3 (depending on electron energy and stopping medium) to include elastic scattering and excitation. In consequence, the number of interactions belonging to one single electron track is about 3×10^5 and is, thus, by a factor of the order of 10^4 greater than the number of primary interactions of a photon at the same energy. The simulation of a great number of electron histories, collision after collision as is typical of photon Monte Carlo models, is therefore hardly feasible for electrons at higher energies, though basically possible, and other methods must be applied.

The methods used today for this purpose are more or less completely based on the fundamental publication by Berger [12], realising that the greater part of electron interactions, as shown in the left part of Figure 12, is accompanied by only small energy losses and minor changes of the electron flight direction, now and then interrupted by interactions with heavier energy loss and scattering angle, visible by a branching of the main track due to the ejection of electrons with noticeable ranges, the so-called δ -electrons. Such interactions, completed by the creation of bremsstrahlung photons, are summarised as catastrophic interactions. Following this concept, the electron tracks are simulated as shown schematically in the right part of the figure:

- All interactions with an energy loss smaller than a predefined threshold energy are bundled together and treated as continuous energy loss governed by the electron stopping power and by the path segments covered by the electron; this bundling-together is schematically indicated by the shaded region around the main track, characterising secondary electrons of short ranges.

- Energy loss straggling and angular electron scattering, which are caused by the stochastic nature of energy deposition and the bundling-together of single interactions along the path segments, are handled within the framework of multiple scattering theories.
- The occurrence of catastrophic events is taken into account separately by treating the ejected δ -electrons and bremsstrahlung photons like primary particles.

Figure 12. Schematic view of a realistic electron track (left) and of a track simulated within the framework of a condensed-history model (right)



The central procedure of simulating electron tracks on the basis of such a condensed-history model is, therefore, the determination of the distance to the next catastrophic interaction and of the step size necessary to calculate the continuous energy loss, including energy loss straggling and the change of particle direction caused by multiple scattering.

The distance $l(E)$ which an electron of kinetic energy E travels before suffering a catastrophic event can be determined in the same way that used for photons when treating the distance between two successive interaction points. This means that an exponential probability density is assumed which is completely described by the probabilities per unit length with respect to a setting-in-motion of δ -electrons and to a creation of bremsstrahlung photons.

Whereas the determination of $l(E)$ is straightforward, the choice of the step size $s(E)$ for the continuous energy loss causes some problems in view of various conflicting requirements which have to be taken into account for its determination, even in homogeneous media. On the one hand, $s(E)$ should be large enough to restrict the number of step sizes per electron track, and to justify the use of multiple scattering theories. On the other hand, $s(E)$ should be small enough to justify the assumption that the electron path can be approximated by a straight line covering $s(E)$, and to justify the use of multiple scattering theories that do not really take into account the energy loss of electrons while penetrating a material layer of thickness $s(E)$. In addition, the path segments must be short to avoid serious complications near the surfaces of heterogeneous media. One way out of this problem is to define only those secondary electrons as δ -electrons, whose energies are greater than a lower limit, and to use a step size $s(E)$ based on the restricted linear stopping power and a fixed value of the fraction of energy which an electron loses continuously when travelling along $s(E)$.

The transport of electrons is now simulated in such a way that the travelling distance $l(E)$ for catastrophic interactions is calculated first and $s(E)$ afterwards. If $l(E)$ is smaller than $s(E)$, the step is terminated with a travelling distance $l(E)$ by a catastrophic event, otherwise the new electron energy is calculated according to the continuous energy loss along the distance $s(E)$ (including energy loss straggling), and its new direction is determined within the framework of a multiple scattering theory; afterwards a new value of the step size is calculated at the new electron energy as long as the electron reaches the travelling distance for catastrophic events.

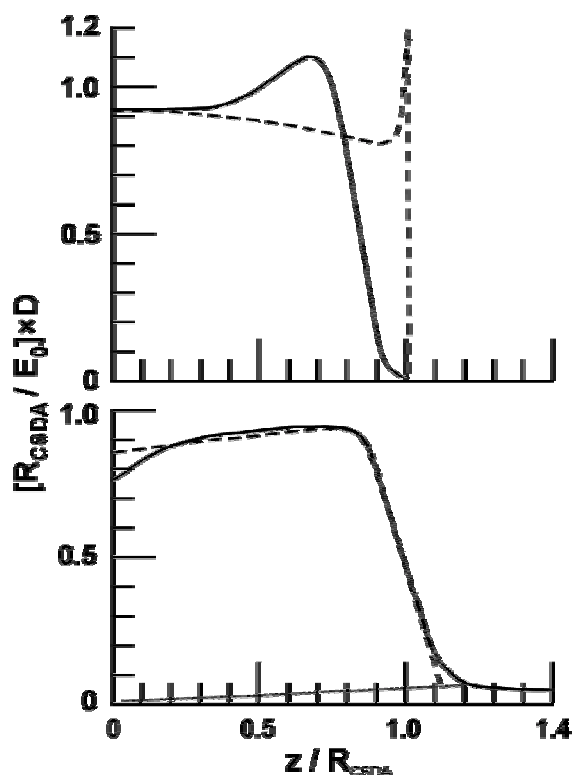
The type of a catastrophic event is determined, in analogy to the procedure of sampling the type of photon interactions, using the appropriate relative probabilities for δ -electron production or the creation of bremsstrahlung photons. After the determination of the type and position of a catastrophic interaction, the appropriate energy loss and the new electron direction are calculated, based on the physics of bremsstrahlung creation or δ -electron production. The energy, the direction and the spatial co-ordinates of the secondaries caused by catastrophic events are stored if the energy is greater than a pre-selected cut-off energy; they are used as initial parameters if tracing of their histories has to be taken into account.

The history of each electron (including the contributions by all secondary particles) is followed up as long as the particle leaves the target volume or its energy has been degraded to the cut-off energy which must be chosen low enough to be sure that a further continuation of the simulation process would not markedly influence the final results. For details of the simulation of the energy transport by electrons, in particular, also of taking into account energy loss straggling and angular scattering based on multiple scattering theories, see, for instance, the publications by Nahum [8], Grosswendt [10], Berger [12], Andreo and Brahme [13], Seltzer [14,15], Berger [16], Berger and Wang [17], Rogers and Bielajew [18], and by Andreo, *et al.* [19].

In contrast to photon tracks which can be interpreted as a sequence of single interaction points, a single electron track within the framework of a condensed-history model can be interpreted as a sequence of straight line segments representing continuous energy losses, now and then interrupted by the ejection of δ -electrons or the creation of bremsstrahlung photons. The change of the primary electron direction, the energy losses and, in the case of catastrophic interactions, also the energy and direction of the secondary radiation are governed by statistical rules related to the physics of primary electron interaction processes or multiple scattering theories. To give an impression of the influence which these effects have on the energy transport by electrons, Figure 13 shows the scaled depth-dose distribution per initial electron at the depth z of a half-infinitely extended water medium for a narrow beam of monoenergetic 30 MeV electrons of perpendicular incidence on the surface of the water medium ($z/R_{\text{csda}} = 0$); $D(z)$ is the absorbed dose to water at depth z , E_0 is the initial kinetic electron energy and $R_{\text{csda}} = 13.1$ cm the corresponding continuous-slowing-down range [20]. The depth-dose distributions were calculated using different approximations. The upper part of the figure shows the results which do not take into account energy loss straggling and catastrophic interactions. The dashed curve presents the calculated energy deposition without angular deflection of the electrons due to multiple scattering. At a glance it can be seen from the curve that the energy deposition decreases with increasing depth z as long as z is smaller than the electron range R_{csda} because of the decreasing electron energy. It increases, however, more or less sharply (depending on the increment Δz) at $z = R_{\text{csda}}$, since all particles reach the same depth where the remaining kinetic energy is completely absorbed. If multiple angular scattering is taken into account (see the unbroken curve), the depth dependence of energy deposition changes drastically. With increasing depth the energy deposition increases first until it reaches a maximum, and decreases afterwards if the depth is further increased. This behaviour of depth deposition is caused by the fact that the greater part of the initial electrons, due to the angular deflections caused by multiple scattering, do not reach the depth $z = R_{\text{csda}}$ but lose their total kinetic energy at smaller depths.

Figure 13. Scaled absorbed-dose distribution for electrons at initial energy E_0 as a function of depth z in water

Upper: (---) pure continuous-slowing-down approximation, (—) multiple angular scattering is taken into account
 Lower: (---) energy-loss straggling and multiple angular scattering taken into account, (—) catastrophic events included

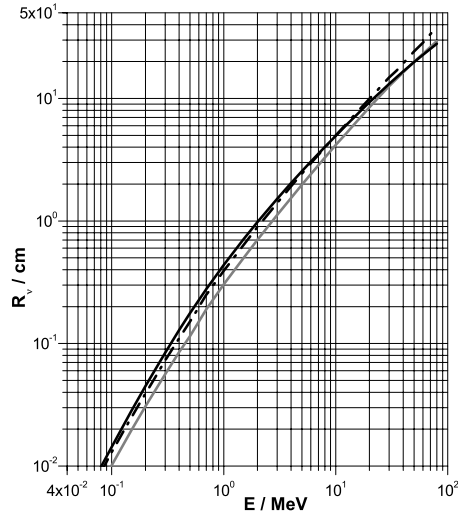


If energy loss straggling and catastrophic interactions are also taken into account, the depth dependence of energy deposition changes again, as shown in the lower part of Figure 13. The broken curve presents the energy deposition calculated while taking multiple scattering and energy loss straggling into account but neglecting the energy transport by δ -electrons; the unbroken curve shows the results without the latter approximation. As compared with the data calculated within the framework of the pure continuous-slowing-down approximation (see the upper part of Figure 13), the energy deposition at small depths is decreased, in particular if the δ -electron transport is taken into account, and it is increased at great depths, partly as a result of δ -electrons or bremsstrahlung photons and partly as the result of an increase in the electron path length due to energy loss straggling.

In the field of dosimetry for radiation therapy purposes, electron depth-dose distributions are commonly used to derive parameters characterising the radiation quality. These parameters are commonly based on electron ranges in water (see, for instance, ICRU [21]). Figure 14 shows the extrapolated range R_p , the 50% range R_{50} , and the continuous-slowing-down range R_{csda} of electrons in water as a function of energy E in the region between 100 keV and 80 MeV [10]. An interesting aspect of the ranges is that R_{csda} is greater than R_p at lower energies, but smaller at high energies, clearly showing the effect of pronounced multiple scattering at lower energies and the importance of catastrophic interactions at high energies. In addition, the strong energy dependence of the ranges is striking. The extrapolated range, for instance, reaches from about 130 μm at 100 keV to about 40 cm at 80 MeV. As a rule of thumb, it can be assumed that for $1 \text{ MeV} < E < 100 \text{ MeV}$ the extrapolated range R_p is approximately equal to $0.5 \times (E/\text{MeV}) \text{ cm}$.

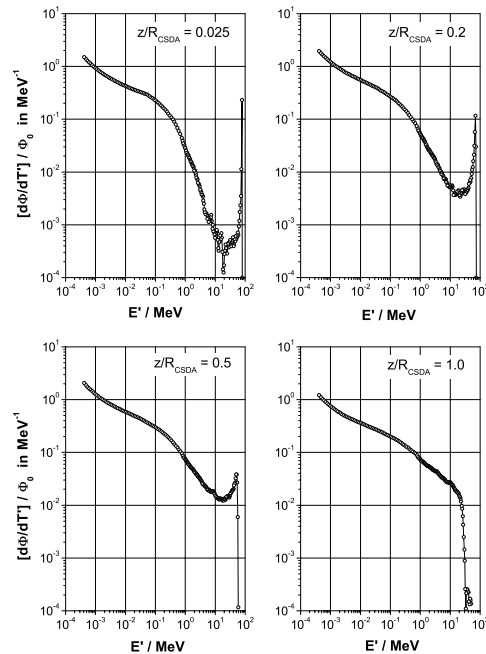
Figure 14. Ranges of electrons as a function of energy E in water

(—) continuous-slowed-down range R_{csdar} (—•—) projected range R_p (—) 50% range R_{50}



Another aspect of electron degradation is the spectral energy distribution of the primary particle and of all of its secondaries as a function of the electron penetration depth through matter. For its discussion, let us assume an electron source in a vacuum, which emits continuously with time monoenergetic electrons in a direction perpendicular to the front face of a water phantom. Then, after waiting a time long enough to be sure that a great number of electrons has reached any state of energy degradation, one can ask about the spectral energy distribution of electrons in a thin material layer at a fixed depth d of the phantom. Figure 15 shows the spectral fluence distribution $[d\Phi/dE']/\Phi_0$ of 80 MeV electrons slowed down in water, at four different depths. These distributions are normalised to the

Figure 15. Mean spectral electron fluence due to the degradation of primary electrons at 80 MeV in water, at four different depths ($R_{csda} = 27.95$ cm); Φ_0 is the primary electron fluence



primary electron fluence at the phantom surface and were calculated with a cut-off energy of 0.8 MeV for the electron transport, supplemented for lower energies by solving the Spencer-Fano equation using the method of McGuinnies [22]. Near the phantom surface ($z/R_{\text{csda}} = 0.025$; $R_{\text{csda}} = 27.95$ cm), the sharp peak of primary electrons at 80 MeV is the most prominent feature of the spectral energy distribution, followed by a deep minimum for decreasing electron energies and a strong increase if the electron energy is further decreased to low values. When looking at the primary electron peak it can be seen at a glance that its height decreases with increasing phantom depth and vanishes at depths almost equal to the electron range. At the same time, the minimum at lower energies is flattened. Both effects can be expected within the framework of a condensed-history model based to a great extent on the assumption of continuous energy loss mechanisms. It is, however, somewhat surprising that the spectral electron distribution in the low-energy region is almost independent of the penetration depth.

As far as electron degradation is concerned, the most important aspects are:

- The very great number of interactions during the complete slow-down of electrons of higher initial energies, preventing a fast simulation of electron degradation from one interaction point to the other.
- The more or less continuous energy loss of electrons caused by the fact that interactions with large energy transfers are rare events, enabling electron histories to be treated within the framework of condensed-history models.
- The short ranges as compared to the dimensions of macroscopic targets.
- The rather small angular deflections of electrons due to single interactions, which can be treated by multiple scattering theories and which, combined with the short particle ranges, lead to only limited statistical fluctuations of energy deposited in small volume elements even in the case of smaller numbers of simulated primary particles.
- The similarity of electron degradation spectra as a function of electron penetration depth.
- The strong influence of δ -electrons on the energy deposited near surfaces.

From the point of view of Monte Carlo simulation, the most important feature of electron degradation is the possibility of treating the histories of higher-energy electrons within the framework of condensed-history models. These, however, can be used without restrictions only in macroscopic target volumes of homogeneous media or of heterogeneous media far away from surfaces, because of the limited validity of available multiple scattering theories with respect to angular deflections and energy loss straggling. Handled with care, however, condensed-history models are very well suited for applications in the fields of dosimetry (for radiation therapy purposes) and radiation protection.

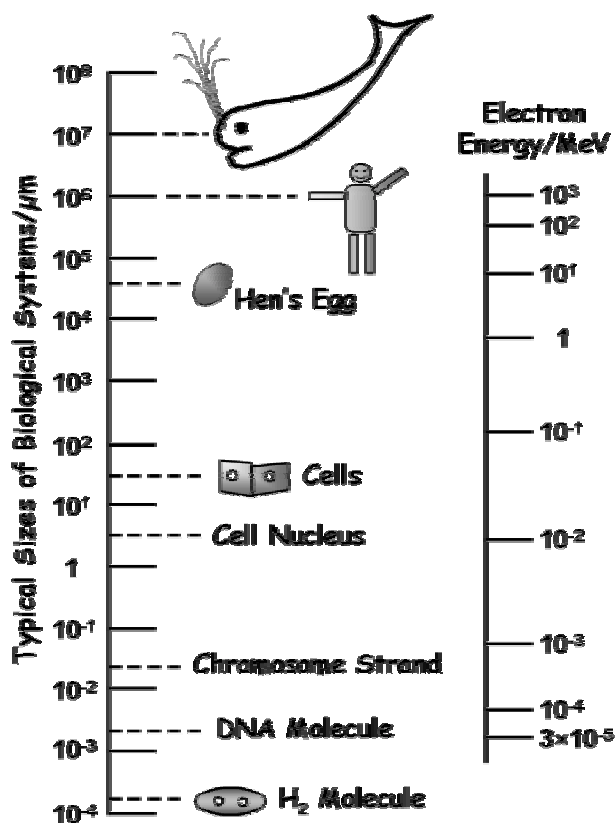
The role of track structure in biological targets

A serious disadvantage of condensed-history models is that they cannot be applied for studying the structure of electron tracks as they treat the whole set of low-energy transfer interactions within the framework of the continuous-slowing-down approximation which assumes continuous energy losses along straight path segments. Due to this fact, these models are not able to distinguish interaction points of low energy transfers. In addition, they are not able to treat the yields of different kinds of target species produced by electron interactions (ionised atoms or molecules, atoms or molecules at specified excitation states, dissociation products). In consequence, condensed-history models cannot be

used to solve problems which are sensitive, for instance, to the distance distribution of target species produced by a series of successive electron interactions representing the structure of an electron track. Examples of such problems are the dynamics of chemical reaction chains in radiation chemistry and the damage to sub-cellular structures in radiation biology. Here, it is commonly accepted that the knowledge of track structure of ionising particles is fundamental to a general understanding of the induction of radio-chemical or radio-biological effects.

Figure 16 shows the typical sizes of biological targets which we must bear in mind, at least in principle, when studying problems related to the irradiation of biological systems. On a micrometer scale, the characteristic sizes are extended from about $10^7 \mu\text{m}$ in the case of a whale to about $10^{-3} \mu\text{m}$ in the case of the DNA molecule, thus covering 10 orders of magnitude. The energy of electrons of comparable continuous-slowing-down range in water is indicated on the right scale of the figure. At first glance, it can be seen that the ranges of electrons at energies smaller than about 10 keV cover the whole area of characteristic sizes within a cell nucleus, and the ranges of electrons at energies smaller than about 1 keV the characteristic sizes of a chromosome fibre, which itself represents a highly structured target of DNA wound around so-called nucleosomes, about 9 nm in diameter. If we assume a W value of 25 eV for electrons in liquid water, a number of about 40 ion pairs is produced upon the complete slow-down of 1 keV electrons within a chromosome fibre. An appreciable fraction of these ion pairs would be produced within the DNA, which is commonly accepted as the most probable radiation sensitive sub-cellular structure of a biological target. In view of these facts, the distance distribution of single electron interactions within volumes a few nanometres in size is decisive for the understanding of initial radiation damage to cellular DNA, and must be taken into account in the definition of radiation quality. In microdosimetry, for instance, this is performed by defining

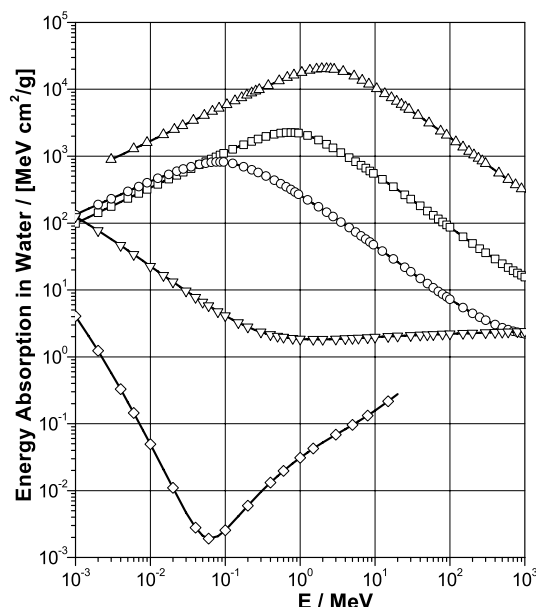
Figure 16. A selection of typical sizes of biological targets



radiation quality in terms of linear energy transfer, which represents the energy density in matter due to charged particle interactions and can be interpreted as a rough measure of the distance distribution of particle interactions. To give an impression of the energy density of charged particles, Figure 17 shows the collision stopping power of water for electrons as a function of energy E [20], in comparison with the collision stopping power for protons, α -particles and bare carbon ions [23]. These data are supplemented by the kerma factor $E \times [\mu/\rho]_{\text{en}}$ of photons at the same energy which is based on the so-called mass-energy-absorption coefficient $[\mu/\rho]_{\text{en}}$. The comparably small energy-deposition density of photons as compared with that of electrons is striking and demonstrates again that mean free interaction lengths of photons are generally much longer than the ranges of accompanying secondary electrons. The stopping power of electrons at energies smaller than about 1 keV is comparable, however, with that of protons and α -particles whereas the stopping power of high-energy electrons is much smaller and decreases with increasing particle energy, up to about 1 MeV. As regards radiation damage, it can be assumed, in consequence, that low-energy electrons are much more effective than high-energy electrons, and that their effectiveness should even be comparable with that of light ions.

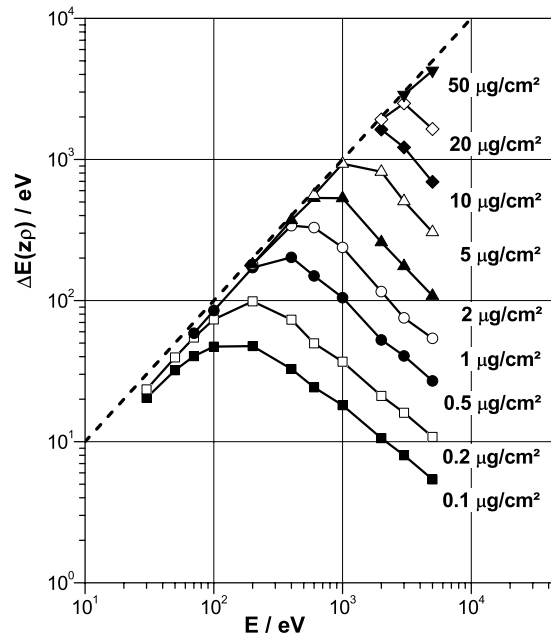
Figure 17. Density of energy absorption in water as a function of particle energy E

Δ – bare carbon ions, \square – α -particles, \circ – protons, ∇ – electrons, \diamond – photons



To further demonstrate the importance of low-energy electrons in sub-cellular structures, Figure 18 shows the energy $\Delta E(z\rho)$ deposited by electrons in material layers of density ρ and mass per area $z\rho$ of between $0.1 \mu\text{g}/\text{cm}^2$ and $50 \mu\text{g}/\text{cm}^2$ (corresponding to layer thicknesses of between 1 nm and 500 nm in liquid water) as a function of energy E , in the case of electrons normally penetrating the surface of the layers [24]. For layers of mass per area smaller than about $10 \mu\text{g}/\text{cm}^2$ (or 100 nm at unit density), the maximum energy is deposited by electrons at energies less than about 1 keV, and for layers of mass per area of $0.2 \mu\text{g}/\text{cm}^2$ (which corresponds to the diameter of DNA) by electrons at an energy of about 200 eV. Hence, in nanometric volumes, the energy absorption in matter due to the interactions of low-energy electrons is much greater than that due to the interactions of high-energy electrons, and is even comparable with that of light ions, as discussed above. The key problem of a detailed understanding of the initialisation of radiation damage to DNA is, therefore, the general understanding of the distance distribution of particle interactions (including the type of accompanying atomic or molecular target species) which is commonly summarised as the track structure of ionising particles.

Figure 18. Energy ΔE absorbed in layers of tissue-equivalent material of mass per area $z\rho$, as a function of electron energy E



REFERENCES

- [1] ICRU (International Commission on Radiation Units and Measurements), *Fundamental Quantities and Units for Ionizing Radiation*, Report 60, Bethesda, MD, USA (1998)
- [2] Hubbell, J.H., *Radiat. Res.*, 70, 58-81 (1977).
- [3] Plechaty, E.F., D.E. Cullen and R.J. Howerton, *Tables and Graphs of Photon Interaction Cross-sections from 0.1 keV to 100 MeV Derived from the LLL Evaluated Nuclear Data Library*, Publication UCRL-50400, Volume 6, Revision 3, Lawrence Livermore National Laboratory, Livermore, CA, USA (1981).
- [4] Berger, M.J. and J.H. Hubbell, *XCOM: Photon Cross-sections on a Personal Computer*, Publication NBSIR 87-3597, National Bureau of Standards, Gaithersburg, MD, USA (1987).
- [5] Higgins, P.D., F.H. Attix, J.H. Hubbell, M.J. Berger and C.H. Sibata, *Mass Energy Transfer and Mass Energy Absorption Coefficients, Including In-flight Positron Annihilation for Photon Energies 1 keV to 100 MeV*, Publication NISTIR 4812, National Institute of Standards and Technology, Gaithersburg, MD, USA (1992).
- [6] Davisson, C.M. and R.D. Evans, *Rev. Mod. Phys.* 24, 79-107 (1952).

- [7] Zerby, C.D., *Meth. Comp. Phys.*, 1, 89-134 (1963).
- [8] Nahum, A.E., *Calculation of Electron Flux Spectra in Water Irradiated with Megavoltage Electron and Photon Beams with Applications to Dosimetry*, Thesis, University of Edinburgh (1975).
- [9] Baró, J., M. Roteta, J.M. Fernández-Varea and F. Salvat, *Radiat. Phys. Chem.*, 44, 531-552 (1994).
- [10] Grosswendt, B., *Use of MCNP in Radiation Protection and Dosimetry*, G. Gualdrini and L. Casalini, eds., ISBN 88-8286-000-1, Ente per le Nuove Tecnologie, l'Energia e l'Ambiente (ENEA), Bologna, Italy, pp. 13-54 (1998).
- [11] Grosswendt, B., *Radiat. Environ. Biophys.*, 38, 147-161 (1999).
- [12] Berger, M.J., *Meth. Comp. Phys.*, 1, 135-215 (1963).
- [13] Andreo, P. and A. Brahme, *Radiat. Res.*, 100, 16-29 (1984).
- [14] Seltzer, S.M., *Appl. Radiat. Isot.*, 42, 917-941 (1991).
- [15] Seltzer, S.M., *Monte Carlo Transport of Electrons and Photons*, T.M. Jenkins, W.R. Nelson and A. Rindi, eds., Plenum Press, pp. 153-181 (1988).
- [16] Berger, M.J., *Monte Carlo Transport of Electrons and Photons*, T.M. Jenkins, W.R. Nelson and A. Rindi, eds., Plenum Press, pp. 57-80 (1988).
- [17] Berger, M.J. and R. Wang, *Monte Carlo Transport of Electrons and Photons*, T.M. Jenkins, W.R. Nelson and A. Rindi, eds., Plenum Press, pp. 21-56 (1988).
- [18] Rogers, D.W.O. and A.F. Bielajew, *The Dosimetry of Ionizing Radiation*, K.R. Kase, B.E. Bjärngård and F.H. Attix, eds., Academic Press, Vol. III, Chapter 5 (1990).
- [19] Andreo, P., J. Medin and A.F. Bielajew, *Med. Phys.*, 20, 1315-1325 (1993).
- [20] ICRU, *Stopping Powers for Electrons and Positrons*, Report 37, Bethesda, MD, USA (1984).
- [21] ICRU, *Radiation Dosimetry: Electron Beams with Energies Between 1 and 50 MeV*, Report 35, Bethesda, MD, USA (1984).
- [22] McGinnies, R.T., *Energy Spectrum Resulting from Electron Slowing Down*, NBS Circular 597, National Bureau of Standards, Washington DC, USA (1959).
- [23] ICRU, *Stopping Powers for Protons and Alpha Particles*, Report 49, Bethesda, MD, USA (1993).
- [24] Waibel, E. and B. Grosswendt, *Phys. Med. Biol.*, 37, 1127-1145 (1992).

**MONTE CARLO STUDIES IN THE FIELD OF AREA
MONITORING AND PERSONAL DOSIMETRY FOR PHOTONS
BETWEEN 10 keV AND 10 MeV AND NEUTRONS BELOW 20 MeV**

Gianfranco Gualdrini

ENEA – Istituto di Radioprotezione, Italy

Abstract

The system of dose limitation based on radiation protection quantities and defined on a complex mathematical model of anthropomorphic phantoms and operational simplified quantities relies on a wide set of conversion coefficients to be used both in area monitoring and personal dosimetry. These coefficients, reported in the open literature, have been calculated through Monte Carlo simulations. The present paper illustrates the role played by Monte Carlo modelling in the framework of conversion coefficients evaluation, in the numerical determination of reference radiation fields for the calibration and type test of personal dosimeters as well as in the characterisation of irradiation facilities in terms of operational quantities.

Introduction

Radiation transport calculations using the Monte Carlo [1,2] method have become a basic tool in radiation protection dosimetry. The reason for its growing importance, highlighted during the recent debate on new radiation protection quantities, is the fact that calculations based on the Monte Carlo method may often be the only means to link measurable quantities with radiation protection quantities. These new radiation protection quantities result from the ICRP recommendations; their implementation is necessary in order to guarantee that the system of dose limitations remains consistent with the biological and epidemiological evidence of the harm caused by radiation. Harmonisation and standardisation is therefore clearly required in view of the growing impact of such Monte Carlo calculations on radiation protection [3]. In recent years complex Monte Carlo code packages have been distributed among the users and are widely used for a variety of evaluations in the dosimetry and radiation protection fields. EGS4 [4,5], MCNP [6-8], MCNPX [9], FLUKA [10-12], McBEND [13], ETRAN [14-16] PENELOPE [17], TRIPOLI [18-20], etc., are some of the codes worth noting; all are based on different theoretical models and are able to treat different radiations and energy domains.

The present paper tries to offer some ideas of the role of Monte Carlo modelling in producing conversion coefficients from measurable physical quantities to radiation protection and operational quantities. Furthermore, some examples are presented concerning the Monte Carlo evaluation of field parameters for the type test and calibration of photon personal dosimeters and the characterisation of irradiation facilities in terms of operational quantities.

Monte Carlo evaluation of radiation protection and operational quantities for area monitoring and personal dosimetry

Radiation protection quantities

The radiation protection quantities are the organ equivalent dose (H_T) and effective dose (E) [21]. These quantities are not measurable and, for their calculation, it is necessary to build a mathematical model based on the standard man [22], containing all the organs taken into account in the ICRP-60 recommendation (wt tissue weighting factor table that includes gonads, red bone marrow, colon, lungs, stomach, bladder, breast, liver, oesophagus, thyroid, skin, bone surfaces and the remainder). For many years a large modelling activity has existed at the international level, aimed at developing progressively complex and realistic human mathematical phantoms. The Medical Internal Radiation Dose Committee (MIRD) [23] analytical model, originally hermaphrodite, was significantly improved over the years with the modelling of sex and age-dependent phantoms. Cristy and Eckerman [24,25] at ORNL (USA) developed a human model of different ages (0, 1, 5, 10, 15 years), whilst Kramer [26] derived the ADAM and EVA model, all based on the MIRD organ equations. Further developments, especially in recent years, were achieved by M. Zankl and co-workers [27] at GSF (Germany), through their adoption of a VOXEL representation of the model directly taken from CT scans of the body. A similar effort addressed to radiation protection purposes was carried out by Dimbylow and co-workers [28] at NRPB (UK) relying on data taken from magnetic resonance images. Various laboratories performed Monte Carlo calculations based on analytical human models to produce sets of conversion coefficients between measurable physical quantities (i.e. fluence for neutrons and electrons or “air kerma” for photons) and radiation protection quantities¹ [29,30]. The data are reported in documents ICRP-74 and ICRU-57. A complete set of air kerma to organ equivalent dose and effective dose conversion coefficients for photons from 10 keV to 10 MeV was calculated in the kerma approximation

¹ The average organ fluence is calculated through a track length estimator [volume tally that collects all the particle tracks within one organ, sums up all the contributions and divides by the volume (dimension cm^2)]. The volume of all the organs, which are defined by rather complex equations, can be calculated by Monte Carlo.

by Zankl and co-workers [31,32] using the ADAM and EVA mathematical models and Yamaguchi [33]. For neutrons (from thermal to 20 MeV) various sets of conversion coefficients were calculated by Morstin, *et al.*, Nabelssi and Hertel, Leuthold, *et al.*, Stewart and Holnagel [34-38].

An interesting contribution is represented by the calculations performed by Sato, *et al.* [39], who extended the studies to photons until 10 GeV also taking into account the effect of secondary electron transport on the results. The kerma approximation that does not take into account the photo-electron non-equilibrium conditions has a negligible effect on E for photon energies up to 10 MeV and generates more and more overestimations for higher energies (15% at 15 MeV, 50% at 50 MeV up to a factor of 20 at 1 GeV). Figure 1 shows a picture of the ADAM phantom developed in the MCNP format and Figure 2 reports a comparison of MCNP calculations performed at the ENEA Radiation Protection Institute (A/P photon irradiation of the lung) with reference data taken from ICRP-74 and ICRP-51.

Figure 1. ADAM skeleton and some internal organs (lungs, heart, thymus, gall bladder and sigma) (Sabrina [25], plots)

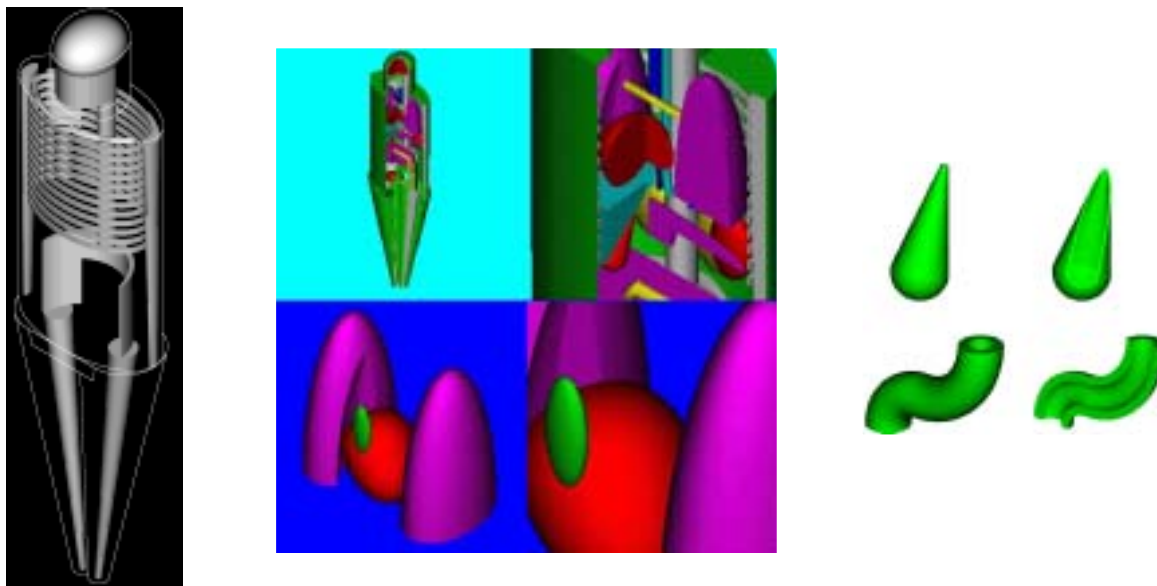


Figure 2. ADAM phantom (sectional view)

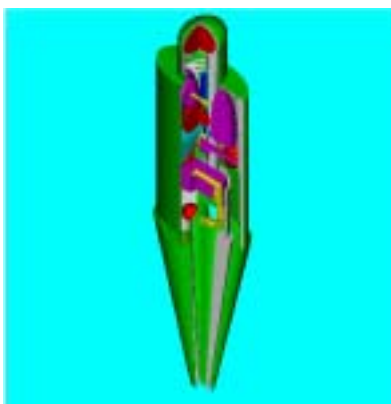
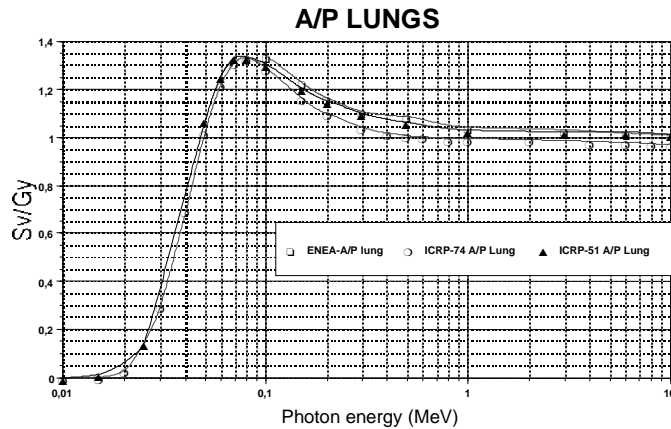


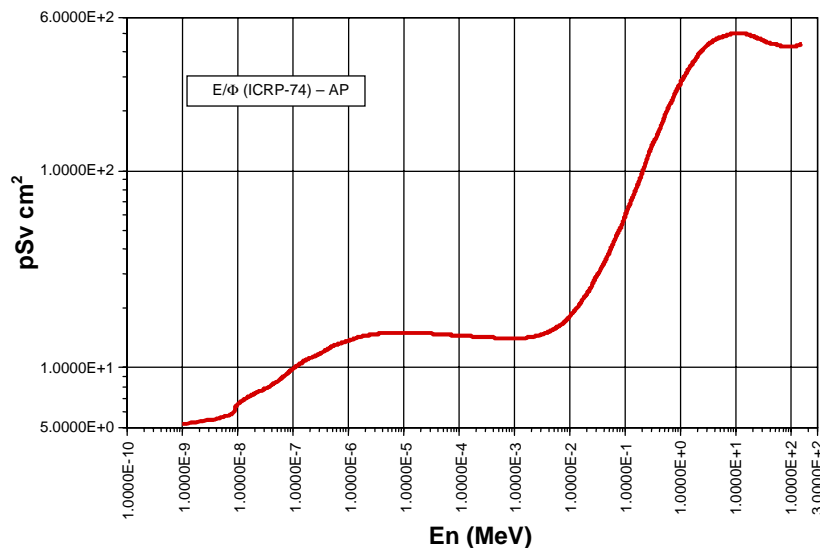
Figure 3. Lung equivalent dose per unit air kerma for photons (A/P)

The ENEA and ICRP-51 values refer to the standard male, whilst the ICRP-74 values are an average between male and female. The systematic underestimation of the ICRP-74 values is due to the presence of the breasts in the female phantom that implies a higher shielding on the lungs.



Translating the ADAM and EVA phantoms from MCNP to FLUKA, M. Pelliccioni, *et al.* [40] calculated a large set of fluence-to-effective dose conversion coefficients for high-energy radiations (up to 10 TeV for photons, electrons, protons, neutrons, muons, pions, etc.). In Figure 4 the fluence to effective dose conversion factor for neutrons for AP irradiation is shown (data taken from ICRP-74).

Figure 4. Fluence-to-effective dose conversion coefficient for neutron from 1.e-9 to 1.e+2 MeV (AP irradiation)



Operational quantities

Two simplified quantities are defined for area and personal dosimetry: the ambient dose equivalent $H^*(d)$ (Figure 5) and the personal dose equivalent $H_p(d, \alpha)$ (Figure 6) (with $d = 10$ mm for strongly penetrating radiation and $d = 0.07$ mm for weakly penetrating radiation). These quantities are defined on two simple receptors (a 30 cm diameter soft tissue sphere, the ICRU sphere or a $30 \times 30 \times 15$ cm

Figure 5. Introduction of the concept “ambient dose equivalent”

Courtesy of B. Grosswendt

Reference quantity: $H^*(d)$, ambient dose equivalent, and $H'(d,\alpha)$ directional dose equivalent, defined in a 30 cm diameter tissue equivalent sphere (ICRU sphere) under specified irradiation field conditions. The area monitors should be calibrated in terms of H^* without receptor.

$$H^*(d) = \int_{E_{min}}^{E_{max}} (d\phi/dE)_d E [\mu_{en}/\rho]_{ICRU} dE$$

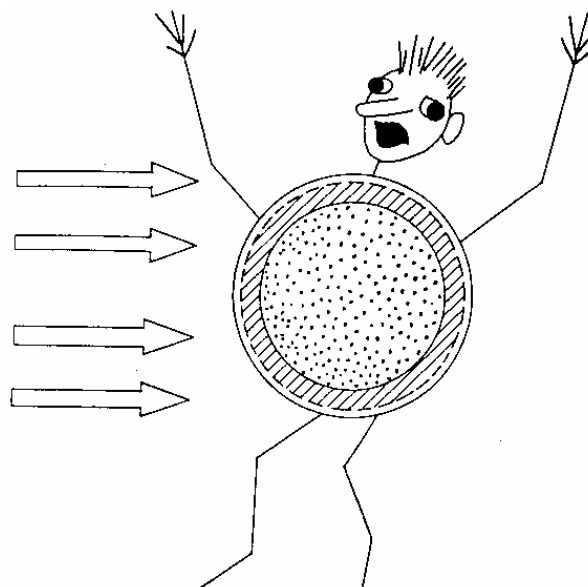
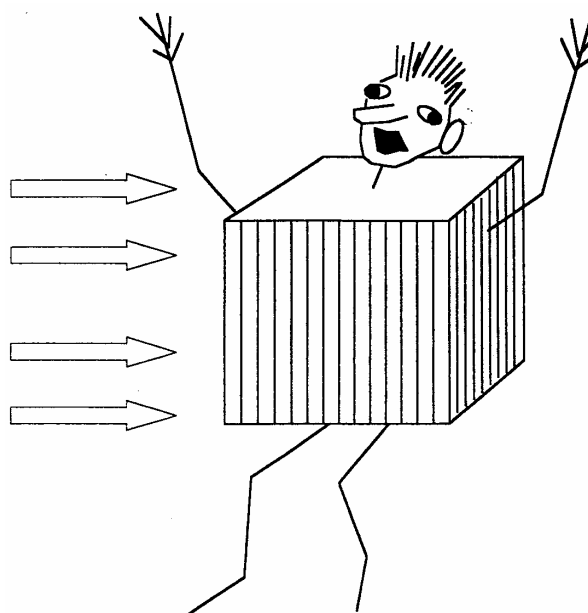


Figure 6. Introduction of the concept “personal dose equivalent”

Courtesy of B. Grosswendt

Reference quantity: $H_p(d,\alpha)$ personal dose equivalent, defined under a specified point of the human body (trunk). The conversion coefficients have been evaluated in simplified slab tissue equivalent phantoms. The calibrations in terms of H_p should be carried out on plastic phantoms, simulating the body (or part of it, e.g. extremities).

$$H^*(d) = \int_{E_{min}}^{E_{max}} (d\phi/dE)_d E [\mu_{en}/\rho]_{ICRU} dE$$

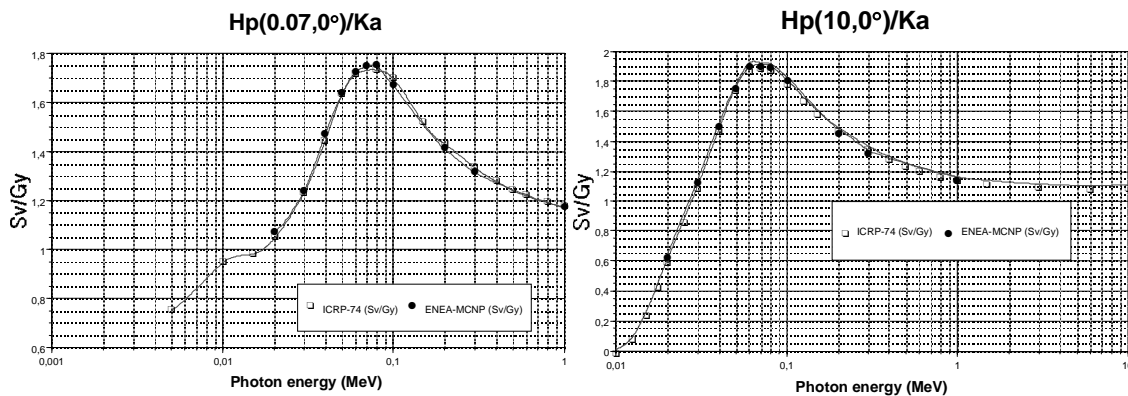


soft tissue slab respectively) and should provide (for every radiation and energy) a reasonable overestimation of the radiation protection quantities. Further, area monitors as well as personal dosimeters should be characterised by an energy (and angular for personal dosimeters) response as close as possible to the “quantity” conversion factor. On this concept a long discussion at the international level generated a series of criticisms on the operational quantities for neutrons and for photons with energy > 4-5 MeV. For photons in this energy domain the kerma approximation is no

longer valid at 10 mm depth in tissue, and the dose maximum takes place at progressively higher depths in the phantom, with the consequence of an underestimation of $H^*(10)$ and $H_p(10)$ versus E . Very significant contributions to the discussion in this field were produced by Ferrari and Pelliccioni with a rigorous work concerning the high-energy radiation field [41,42].

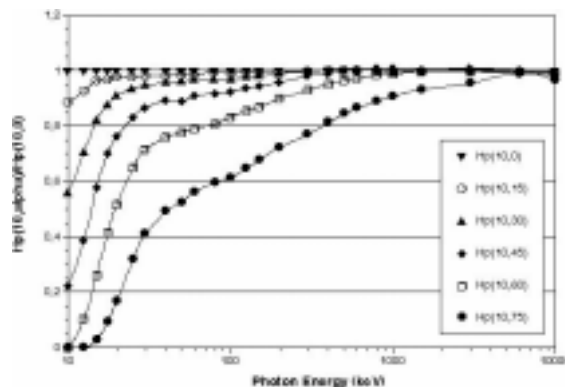
On the other hand, it should be pointed out that the choice of a fixed reference depth for the operational quantities guarantees the additivity of the dose values, in contrast with the formerly adopted quantity “dose index”, that is not additive due to its dependence on the depth within the phantom. In Figures 7 and 8 are reported the conversion coefficients $H_p(0.07,0^\circ)/Ka$ and $H_p(10,0^\circ)/Ka$ for photons from 10 keV to 10 MeV (kerma approximation) [43]. A good agreement between the data taken from ICRP-74 and MCNP results obtained at ENEA can be noted.

Figures 7-8. $H_p(0.07,0^\circ)/Ka$ and $H_p(10,0^\circ)/Ka$ conversion coefficients for photons between 10 keV to 10 MeV



It should be noted that the personal dose equivalent also has an angular dependence that should reproduce the behaviour of the effective dose under different angular irradiation conditions. A set of conversion coefficients depending on the angle of incidence is therefore provided (see Figure 9 for photons) and the angular response of a personal dosimeter should fit as close as possible to the conversion coefficient behaviour.

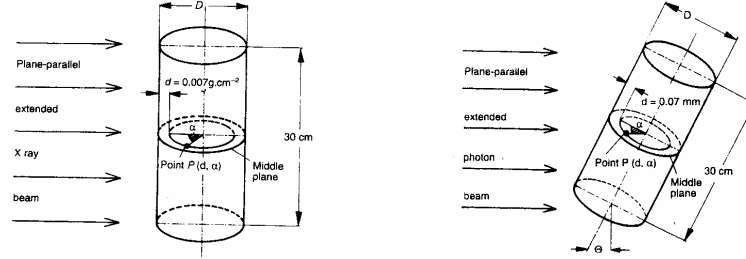
Figure 9. Ratio $H_p(10,\alpha)/H_p(10,0^\circ)$ for various angles of incidence



In the same manner as for the trunk, a series of conversion coefficients for photons has been produced by B. Grosswendt using the Monte Carlo method for the extremities [44,45], adopting mathematical cylindrical phantoms for the wrist and pillar (see Figure 10). It should be pointed out

Figure 10. Schematic view of the irradiation geometries and phantom shape for the Monte Carlo evaluation of extremity photon conversion coefficients

Courtesy B. Grosswendt



that the reference depth for the extremity dosimetry operational quantity is 0.07 mm. This depth corresponds to the extrapolated range of 70 keV electrons in tissue, which implies a very significant overestimation of the quantity at higher photon energies (due to the kerma approximation) especially if the coefficient is applied to source manipulation operative conditions. An improvement of the evaluations, taking into account secondary electron transport, was suggested by the author.

As far as the evaluation of operational quantities for neutrons is concerned, one must consult the reference work of Siebert and Schuhmacher [46], who produced a complete set of fluence to ambient dose equivalent and fluence to personal dose equivalent conversion coefficients from thermal to 200 MeV. The calculation of dose equivalents for neutrons is much more complex than for photons and electrons (quality factor = 1), it being necessary to evaluate the LET spectrum of neutron-induced secondaries and thereafter the LET spectrum of the dose to obtain the quality factor associated with each neutron energy according to the formula:

$$Q_n(E_n) = 1/D \int_{L_{min}}^{L_{max}} Q(L) D_L(L, E_n) dL$$

where $Q(L)$ and $D_L(L, E_n)$ are the LET quality factor and LET absorbed dose distributions respectively.

The H^*/Φ conversion coefficient is expressed as:

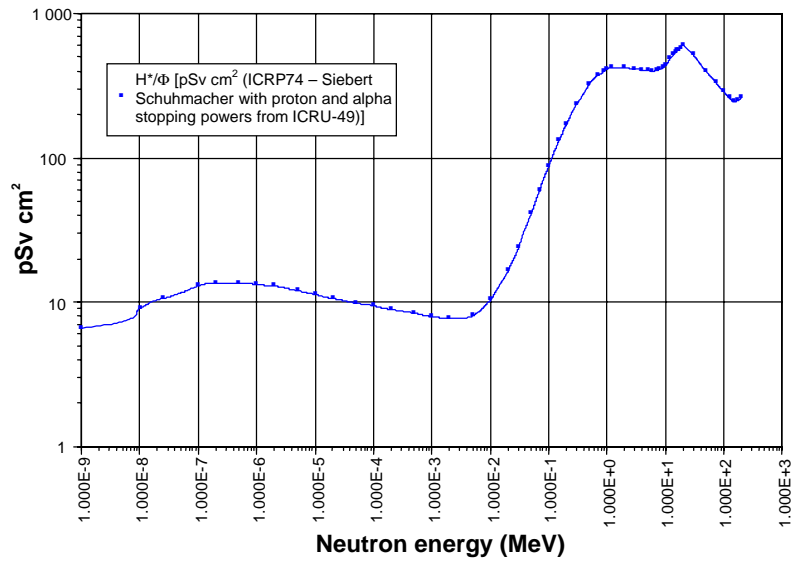
$$H^*(10)/\phi = (H_{1st}^*(10) + H_{mult}^*(10) + K_\gamma)/\phi$$

where:

- First collision contribution – $H_{1st}^*(10)/\phi = (Q_n(E_n)k_f(E_n)\exp(-d\Sigma_t(E_n)))/\phi$
- Multiple collision contribution – $H_{mult}^*(10)/\phi = \left(\int_{E_{min}}^{E_n} Q_n(E)k_E(E)\phi(E)dE \right) / \phi$
- Photon kerma contribution – K_γ

The behaviour of H^*/Φ is shown in Figure 11.

Figure 11. H^*/Φ conversion coefficient for neutrons from thermal to 200 MeV

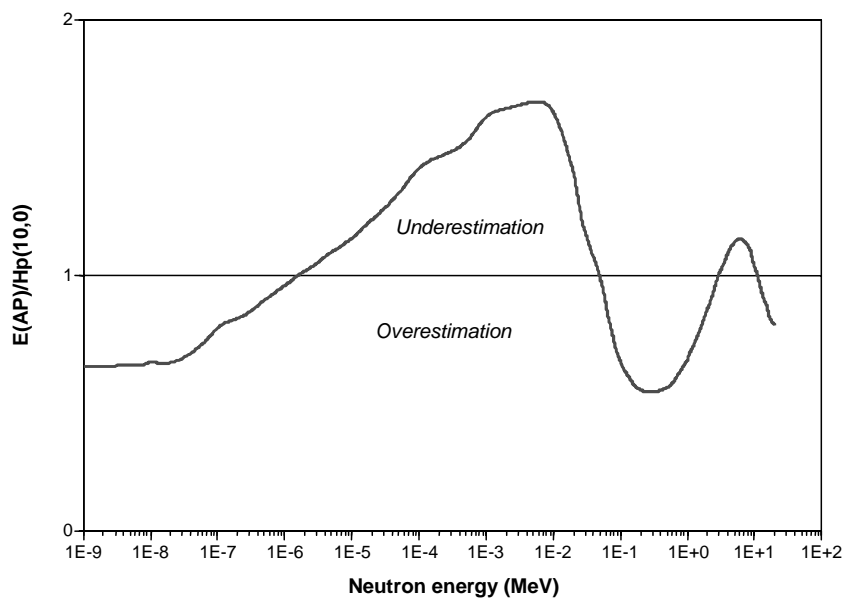


Operational quantities conservativity

As already explained, the operational quantities should be a conservative estimate of the radiation protection quantities. A long-standing debate engendered a series of criticisms regarding the suitability of these simplified quantities.

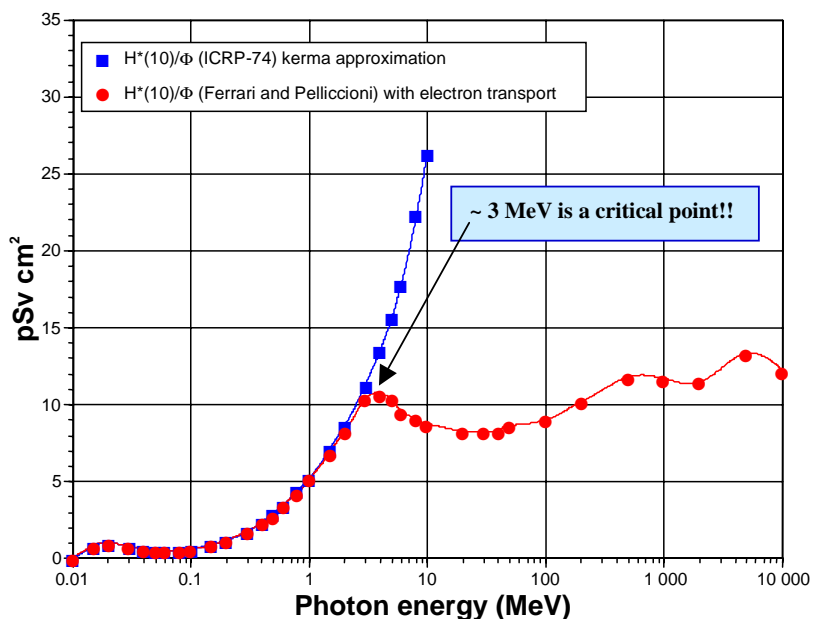
As far as neutrons are concerned, Figure 12 demonstrates the non-conservativity of the operational quantity $H_p(10,0^\circ)$ from ~2 eV to ~50 keV and from 3 MeV to 20 MeV.

Figure 12. Conservativity of personal dose equivalent $H_p(10)$ versus effective dose E for neutrons



As far as photons are concerned the ICRP-74 recommendation and ICRU-57 document supply conversion coefficients for photon energies between 10 keV and 10 MeV in the kerma approximation. If the conversion coefficients were calculated taking into account the secondary electron transport in the phantom (e.g. ICRU sphere in vacuum) at about 3 MeV an electron-photon non-equilibrium condition was put in evidence (Figure 13) [41].

Figure 13. Kerma approximation and secondary electron transport treatment effect on $H^*(10)$ evaluation for photons

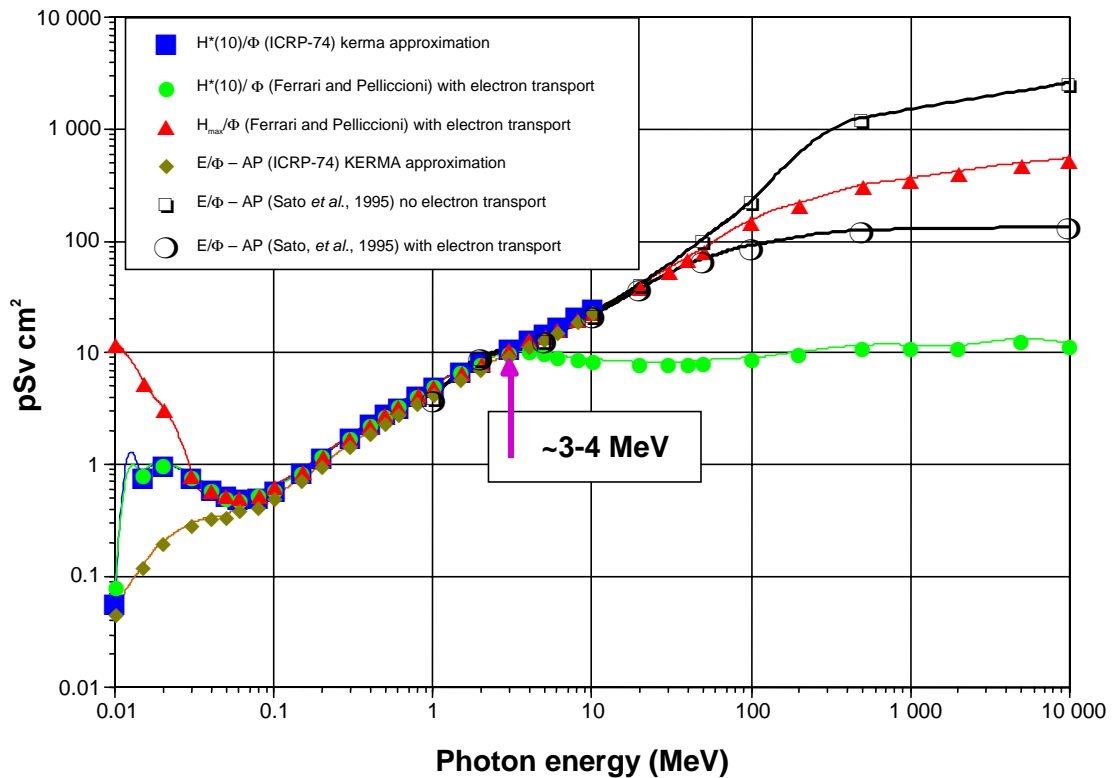


This consideration should be taken into account in the discussion on the conservativity of the operational quantities for photons. In this context it is therefore interesting to compare various quantities: 1) $H^*(10)$ in kerma approximation, 2) $H^*(10)$ with secondary electron transport, 3) the dose index with electron transport, 4) the effective dose (e.g. A/P irradiation) in kerma approximation (ICRP-74 and evaluations from Sato, *et al.*), 5) the effective dose with electron transport.

The radiation protection quantity, E , is the reference quantity for the discussion, the dose index is the maximum dose along the depth dose curve in a simplified phantom (e.g. ICRU sphere) and indicates the suitability of the selected depth “ d ” at which the operational quantity $H^*(d)$ is calculated. Figure 14 summarises the behaviour of the six quantities with data taken from Grosswendt, Pelliccioni and Ferrari, and Sato, *et al.* It can be noted that the $H^*(10)$ in the kerma approximation is a good estimate of the effective dose (AP irradiation) until 10 MeV. At the same time the comparison between $H^*(10)/\Phi$ and $H_{max}(10)/\Phi$ (both with electron transport) shows increasingly larger deviations for energies above 3 MeV² but above this energy the kerma approximation for H^* at 10 mm depth compensates the deviation and properly estimates the radiation protection quantity (on the other hand, it should be pointed out that the $H^*(10)/\Phi$ conversion coefficient referred to the ICRU sphere placed in vacuum to fulfil the definition of expanded and aligned field and, at the same time, based on secondary electron transport to take into account photon-electron non-equilibrium conditions, is not applicable in practical situations, where the air provides a partial equilibrium and perturbs the field alignment).

² The deviation means that the 10 mm depth is no more suitable for $H^*(d)$ (non-kerma approximation) to estimate H_{max} and E . Until 50 MeV a quite good agreement can be noted between E and H_{max} both in kerma and non-kerma approximation.

Figure 14. Comparison of radiation protection quantities and operational quantities for photons



In practice, since a suitable set of conversion factors for high-energy photon fields (>10 MeV) is not officially available, the use of the H_{max}/Φ set (even if not additive) should be recommended.

Evaluation of physical parameters for the design and type test of photon personal dosimeters

The type test and calibrations of photon personal dosimeters have to be carried out on suitable calibration phantoms (Figure 15). The dosimeter reading is, in this irradiation scenario, dependent on both the incident and backscattered radiation. In the past the calibration of personal dosimeters was carried out free in air, but this scenario was not in reality representative of the operative condition in which the human body contributes to the response.

Figure 15. The three ISO phantoms for the calibration of personal dosimeters

Left to right: trunk phantom, wrist phantom and finger phantom



In this new context Monte Carlo simulations can play a very significant role in the following topics:

- Evaluation of air kerma backscatter factors in calibration conditions (receptor present).
- Evaluation of the incident and backscattered spectra, i.e. the overall radiation field to which the dosimeter is exposed.
- Definition of an “homogeneity area” according to the ISO criteria for the contemporary calibration of personal dosimeters.

A set of air kerma backscattered factors for photons were produced by Grosswendt [47] for all the ISO X-ray series, various angles of incidence and for different kinds of tissue equivalent slab phantoms. At the same time an extensive study on the X-ray spectra modification due to the presence of the calibration phantom was carried out with MCNP at ENEA for all the ISO X-ray series [48]. The two examples reported in Figures 16 and 17 demonstrate the very significant spectral degradation due to Compton scattering in the point of measurement. When performing the type test of a personal dosimeter, various experimental and calculated parameters are available at the end [49]:

- Front and rear response of the bare dosimeter.
- Filtration.
- Air kerma backscatter factor.
- Backscattered fluence spectrum.

This information can be proficiently used to estimate the dosimeter response on a calibration phantom (see Figure 18) in terms of H_p , according to the equation:

$$\frac{R_{dos}(E, \alpha)}{H_p(d, \alpha)} = \frac{R_{E-in} e^{-\mu_m(Z) \cdot x(\alpha)} + (B(d', \alpha) - 1) \cdot R_{E-B} e^{-\mu_B(Z) \cdot x(\alpha)}}{K_{a,cal} \cdot \frac{H_p(d,0)}{K_a} \cdot \frac{H_p(d, \alpha)}{H_p(d,0)}}$$

A flow diagram illustrating the determination of H_p response of the personal dosimeter and the related involved parameters is presented in Figure 19.

Figures 16-17. Two evaluated X-ray spectra in presence of a calibration phantom

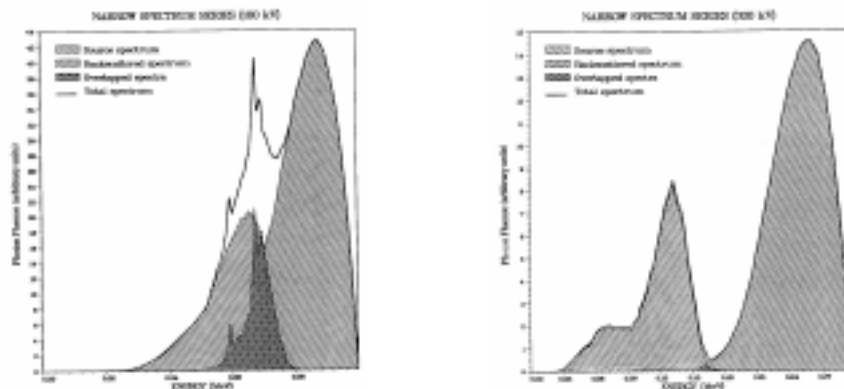


Figure 18. An ideal sketch of the irradiation geometry

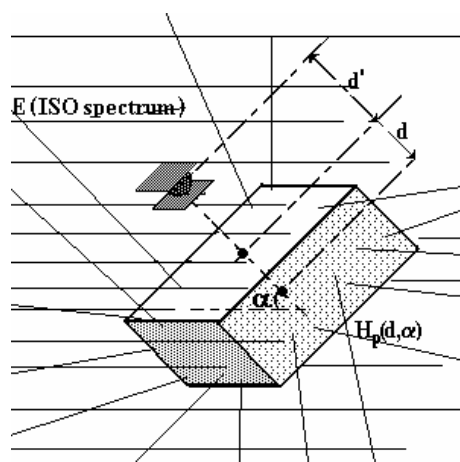
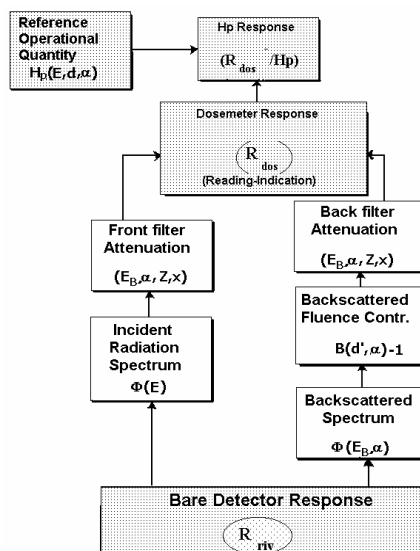


Figure 19. Personal dosimeter H_p response evaluation flow diagram



As suggested by the ISO international standards [50] the calibration of personal dosimeters to be worn on the human trunk should be carried out on a water $30 \times 30 \times 15$ slab phantom. This procedure allows the contemporary calibration of dosimeters mounted on a central area of the phantom front face, which should fulfil the ISO homogeneity criteria for the backscattered radiation. The extension of the area (for normal incidence) is a function of the X-ray beam quality. For angular irradiations on the other hand a higher degree of complexity is introduced to guarantee that all the dosimeters are irradiated in the same condition independently from their location on the phantom face central area.

The Monte Carlo method was extensively used at the ENEA [51] in this framework to evaluate homogeneity areas for the contemporary calibration of photon personal dosimeters. Figures 20-21 show a comparison between Monte Carlo calculations and ion chamber air kerma measurements along the face of a slab calibration phantom, as well as the homogeneity area dependence on the application of different criteria (i.e. percentage deviation from the maximum value at the face centre).

Figure 20. Ion chamber and Monte Carlo evaluation of air kerma backscatter factor along the face of a water slab calibration phantom

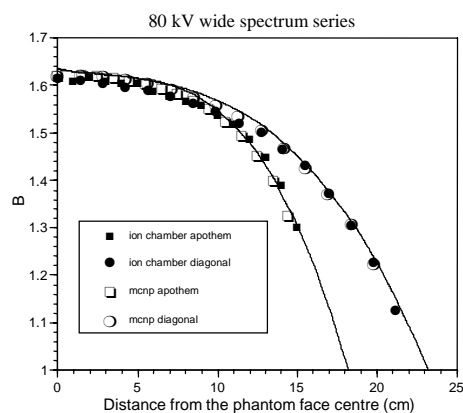
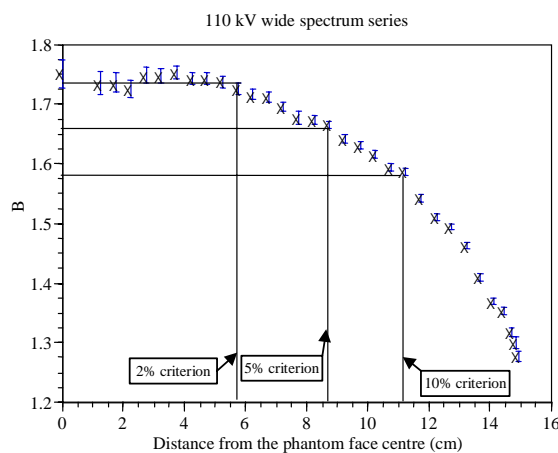


Figure 21. Example of the application of different homogeneity criteria to the evaluation of the area for contemporary calibration of photon personal dosimeters



Monte Carlo simulations for the design of radiation monitors and personal dosimeters

It is worthwhile to mention the large field of Monte Carlo investigations addressed to the design of monitors and dosimeters. The optimisation of the construction parameters can preliminarily be done numerically. Two examples from the neutron dosimetry field are briefly presented: the design of a rem counter carried out at the Physikalische Technische Bundesanstalt (PTB, Germany) [52] and the evaluation of the neutron response function for a superheated drop detector performed at the ENEA Radiation Protection Institute [53,54].

The Berthold rem counter (see Figure 22) is a proportional counter in which a central cavity filled with ^3He is surrounded by a polyethylene layer, contributing to the slowing down and thermalisation of neutrons and, thereafter, to the enhancement of the (n,p) reaction rate on ^3He ³.

³ The Monte Carlo calculation of the number of counts given by the rem counter per unit neutron fluence is obtained from the reaction rate of the (n,p)³He cross-section in the conditions of neutron spectrum present in the sensible volume multiplied by the number of ^3He atoms present in the same volume.

Figure 22. The LB6411 Berthold rem counter



The optimisation of the response function both in terms of fluence and $H^*(10)$ was carried out through a large number of MCNP simulations relying on neutron cross-sections from the European Fusion X-Section File (EFF) [55]. In order to evaluate the optimum response various parameters were varied, for example the moderator diameter and the positions of the embedded absorbing materials. The instrument, in its final configuration, was calibrated at PTB with monoenergetic neutrons and ISO standard sources from thermal energy up to 19 MeV. The neutron fluence response R_Φ and the ambient dose equivalent response $R_{H^*(10)}$ were evaluated. For the calibration factor (refer to ^{252}Cf) a satisfactory (<10%) agreement between measurements and calculations was obtained. A similar study, carried out with FLUKA, was addressed to the extension of a rem counter response until 400 MeV [56-59]. A lead converter was inserted for this purpose in the sensible volume.

Another example of Monte Carlo evaluation of response functions is the study of superheated drop detectors (Figure 23). A freon superheated emulsion is suspended within a gel matrix. The bubbles can be nucleated by neutron-induced charged particles with LET >35 keV/ μm where the minimum energy to produce an ionisation is 14 keV. Due to the lack of monoenergetic neutron sources, especially in the intermediate energy domain, Monte Carlo evaluation of the neutron spectra in the detector is necessary. A further, non-Monte Carlo analysis of the LET distribution of the secondaries is thereafter necessary together with a study both of the contributions to the response due to the secondaries generated in the drop and in the gel. The evaluation of the gel contribution to the response was based on a simplified analytical model of the drop (Figure 24). This coupled Monte Carlo/analytical approach allowed determining the useful number of collisions for the bubble nucleation per cm^3 and unit source particle (Figure 25). The peak at about 500 eV due to a resonance of the (n,p) cross-section on chlorine can be noted. The energy response was extended to energies >10 MeV by Agosteo, *et al.* [60].

Figure 23. A superheated drop detector

Left – before neutron irradiation, right – after neutron irradiation)



Figure 24. Analytical model for the evaluation of the contribution to the bubble nucleation from secondaries generated by the neutrons in the gel matrix

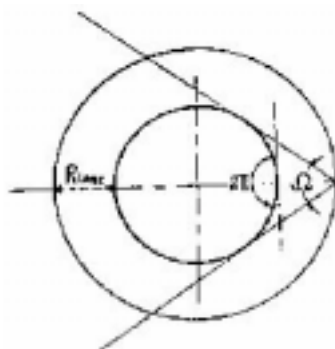
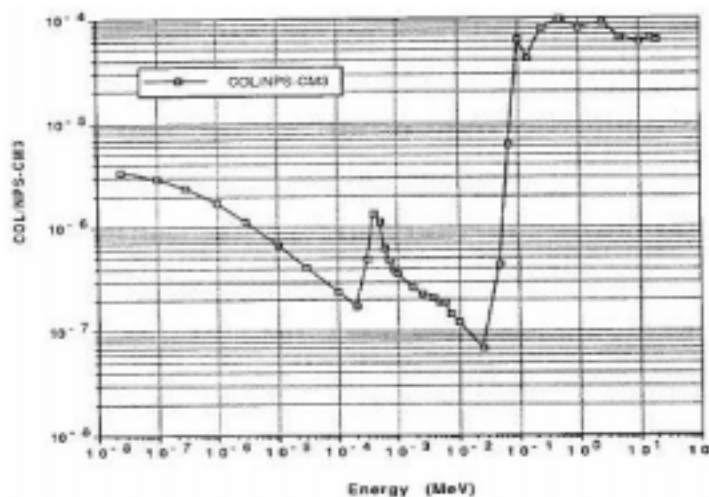


Figure 25. Superheated drop detector neutron response function for neutrons from thermal to 20 MeV



Monte Carlo characterisation of neutron irradiation facilities

In the radiation metrological field it is necessary to characterise the irradiation experiences with a high degree of accuracy. In this framework computational techniques, especially those based on Monte Carlo, allow a detailed study of the measurement experience, including accurate spectral analyses that cannot very often be carried out experimentally. The contemporary employment of measurements and Monte Carlo simulations is thus more and more frequent.

In the framework of the EURADOS activities a European intercomparison (“trial performance test”) was carried out on the measurement of $H_p(d)$ with personal dosimeter routinely used by the dosimetric services. For this purpose a series of irradiation facilities were employed at various leader European laboratories (IRSN, NRPB, PTB, ARCS) [61].

The neutron irradiations were performed at IRSN using a bare ^{252}Cf neutron source, the thermal neutron Sigma facility (see Figures 26 and 27) and the CANEL facility.

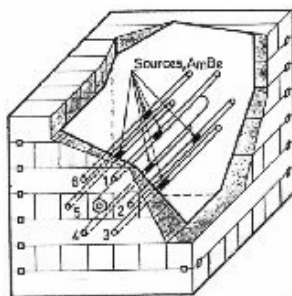
Figure 26. Sigma thermal neutron facility

Courtesy J.M. Bordy



Figure 27. Internal view of the Sigma facility for MCNP simulations

Courtesy J.M. Bordy



Thermal neutron irradiation facility characterisation

The Sigma facility supplies a nearly thermal neutron field and consists of a $150 \times 150 \times 150 \text{ cm}^3$ graphite cube containing six Am-Be sources (for a total of 3 552 GBq). The integral values and spectral distributions of the neutron fluence on the calibration phantom for personal dosimeters have been determined by J.M. Bordy through accurate MCNP simulations. An analogous study was carried out at the ENEA Radiation Protection Institute on a thermal neutron facility (see in Figures 28-29 the cube and the internal sources and irradiation cavities MCNP model).

The $100 \times 100 \times 100 \text{ cm}^3$ polyethylene cube contains three Am-Be sources (for a total of 555 GBq). Three coaxial measurement cavities are placed on the central horizontal axis of the facility. The thermal facility was fully characterised both in terms of ambient dose equivalent and spectral fluence by means of MCNP simulations [62] (in Figure 30 the Monte Carlo spectrum at a given measurement point inside one cavity is presented).

A dose equivalent mapping along the three measurement cavities was also performed using TL LiF detectors for thermal neutrons (relying on the ${}^6\text{Li}(n,\alpha){}^3\text{H}$ reaction, see Figure 31). The detectors were independently calibrated at the IRSN Sigma facility.

The Monte Carlo and experimental results were compared in an absolute way without any adjustment (apart from the $1/v$ behaviour of the ${}^6\text{Li}$ capture reaction); a very satisfactory agreement can be noted (error bars corresponding to two confidence intervals).

Figure 28. Picture of the ENEA thermal neutron facility



Figure 29. MCNP model of the facility internal cavities

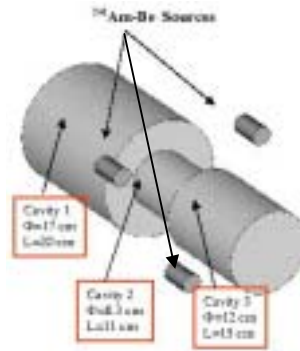


Figure 30. Monte Carlo evaluated neutron spectrum at one stated measurement point inside a measurement cavity

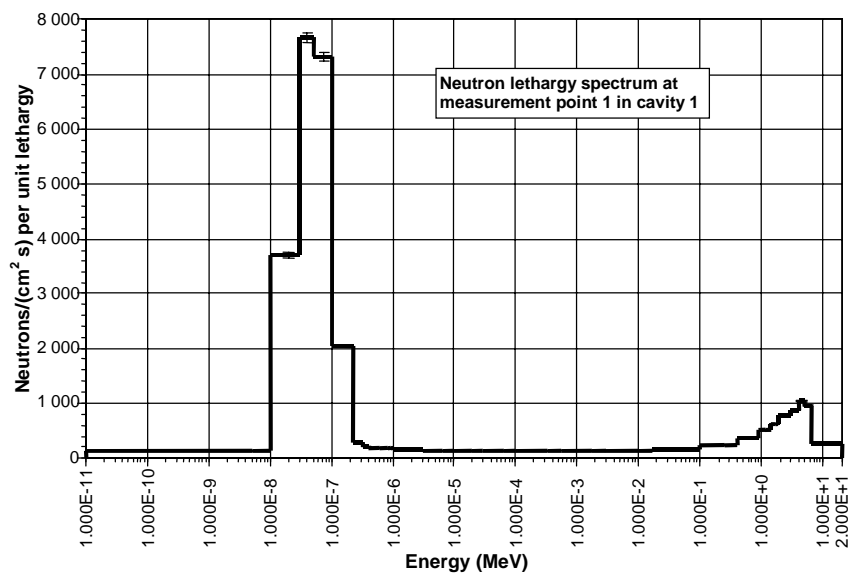
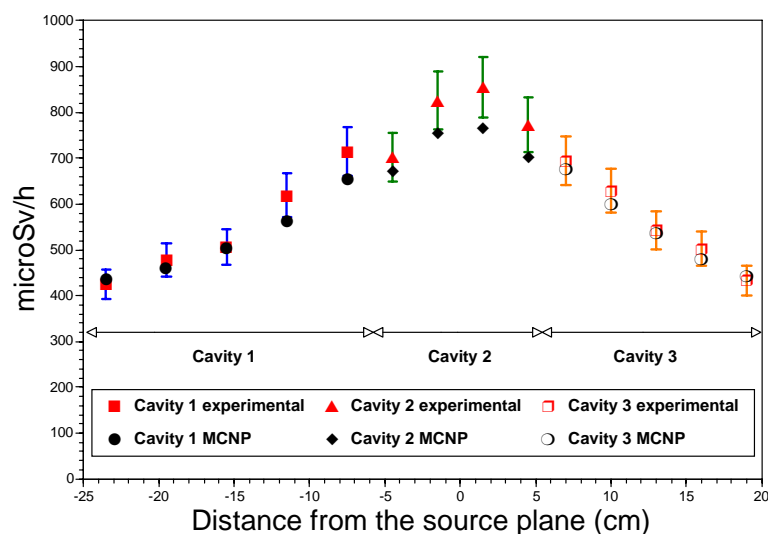


Figure 31. Monte Carlo and experimental mapping of the thermal $H^*(10)$ along the three irradiation cavities



Neutron irradiation room characterisation

Neutron irradiation rooms (see Figures 32 and 33) should be characterised, according to the ISO procedures [63], both in terms of fluence and dose equivalent, separating the direct and scattered components of the radiation field. Experimental procedures, like the shadow cone, can be applied to evaluate the scattered contribution coming from walls, floor, ceiling, source banks, etc. In this framework Monte Carlo simulation of all the room geometry, with an accurate representation of all the materials (that sometimes could imply some complication) is a good support to the experimental evaluations, at the same time allowing calculating the spectra in the various measurement points in the room.

The study herewith presented is an example of this application for a neutron irradiation room operative at the ENEA Radiation Protection Institute [64] (Figures 32-33). The black dot in the figure represents the measurement point to which the source can be moved using an automatic mechanism. The shadow cone is also modelled along with all the source banks, etc., that can significantly contribute to the scattering process.

Due to the very small dimensions of the measurement point a volume Monte Carlo estimator (track length estimator) could not provide a satisfactory precision of the results in reasonable CPU time. Point detectors (next event estimators) have therefore been applied. This guarantees at every source and scattering event the calculation of the contribution to the response in an analytical way.

The Monte Carlo modelling allowed determining the neutron spectra at the measurement points. In Figures 34-36 the spectra for bare Am-Be, bare Cf and moderated Cf sources are presented; the spectrum modification due to the scattered component can be noted.

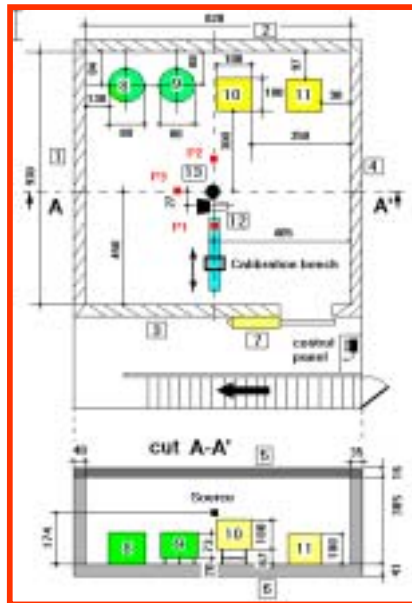
Conclusions

Monte Carlo simulation plays a fundamental role, integrated with experimental measurements, in the field of area monitoring and personal dosimetry for radiation protection purposes.

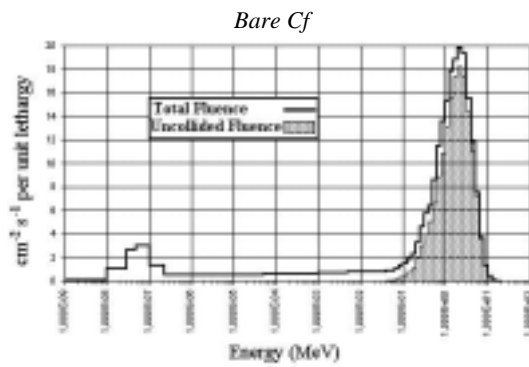
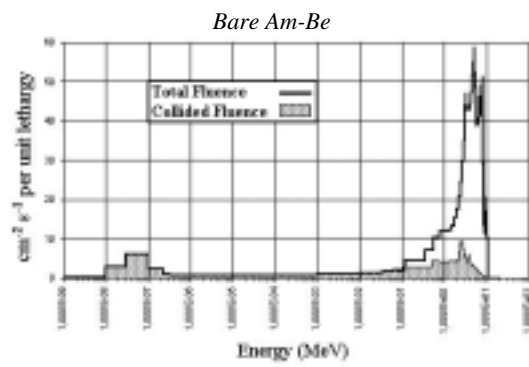
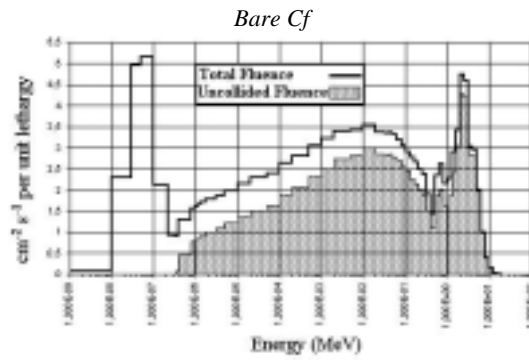
Figures 32. The ENEA neutron irradiation room



Figure 33. Horizontal and vertical sections of the ENEA neutron irradiation room



Figures 34-36. Three Monte Carlo evaluated neutron spectra in the measurement point inside the irradiation room: moderated californium, bare Am-Be and bare californium



REFERENCES

- [1] Lux and L. Koblinger, *Monte Carlo Particle Transport Methods: Neutron and Photon Calculations*, CRC Press, Boca Raton (1991).
- [2] *Monte Carlo Simulation in the Radiological Sciences*, R.L. Morin, ed., CRC Press, Boca Raton, (1988).
- [3] Siebert, B.R.L. and R.H. Thomas, "Computational Dosimetry", *Proceedings of the 8th Symposium on Neutron Dosimetry*, Paris, 13-17 November 1995; *Rad. Prot. Dosim.* Vol. 70, Nos. 1-4 (1997).
- [4] Nelson, W.R., H. Hirayama, D.W.O. Rogers, *The EGS4 Code System*, Stanford Linear Accelerator Centre, Report SLAC-265 (1985).
- [5] Bielajew, A.F., H. Hirayama, W.R. Nelson, D.W.O. Rogers, *History, Overview and Recent Improvements of EGS4*, NRCC, Ottawa, Canada, Report NRC-PIRS-0436 (1994).
- [6] *MCNP – A General Monte Carlo N-Particle Transport Code, Version 4B*, RSICC, Oak Ridge National Laboratory, Judith F. Briesmeister, ed., LANL Manual LA-12625-M Version 4B, Los Alamos (1997).
- [7] Hendricks, J.S., S.C. Frankle, J.D. Court, *ENDF/B-VI Data for MCNP*, LANL Report LA-12891 Los Alamos (1994).
- [8] Hendricks, J.S., J.D. Court, *MCNP4B Verification and Validation*, LANL Report LA-13181, Los Alamos (1996).
- [9] *MCNPXTM User's Manual*, L. Waters, ed., TPO-E83-G-UG-X-00001 Rev 0 (November 1999).
- [10] Ferrari, A., P.R. Sala, "The Physics of High-energy Reactions", *Proceedings of the Workshop on Nuclear Reaction Data and Nuclear Reactors Physics, Design and Safety*, International Centre for Theoretical Physics, Miramare-Trieste, Italy, 15-17 April, World Scientific (Maggio 1996).
- [11] Ferrari, A., P.R. Sala, "A New Model for Hadronic Interactions at Intermediate Energies for the FLUKA Code", *Proceedings of the MC93 International Conference on Monte Carlo Simulation in High-energy and Nuclear Physics*, Tallahassee, Florida, 22-26 February 1993, P. Dragovitsch, S.L. Linn, M. Burbank, eds., World Scientific, Singapore, 277-288 (1994).
- [12] Ferrari, A., P.R. Sala, R. Guaraldi, F. Padoani, "An Improved Multiple Scattering Model for Charged Particle Transport", International Conference on Radiation Physics, Dubrovnik, 1991, *Nucl. Instr. Meth. in Phys. Res.*, B71, 412-426 (1992).
- [13] *User Guide to MCBEND*, ANSWERS/MCBEND 5, AEA Technology, Winfrith, UK (1994).

- [14] Seltzer, S.M., “An Overview of ETRAN Monte Carlo Method”, *Monte Carlo Transport of Electron and Photons*, T.M. Jenkins, Walter R. Nelson and Alessandro Rindi, eds., Plenum Press, New York, 153-181 (1988).
- [15] Seltzer, S.M., “Electron-photon Monte Carlo Calculations: The ETRAN Code”, *Appl. Radiat. Isot.*, 42, 917-941 (1991).
- [16] Nelson, W.R., “Application of EGS and ETRAN to Problems in Medical Physics and Dosimetry”, *Computer Techniques in Radiation Transport and Dosimetry*, W.R. Nelson and T.M. Jenkins, eds., Plenum Press, New York, 256-266 (1980).
- [17] Baro, J., J. Sempau, J.M. Fernandez-Varea and F. Salvat, “PENELOPE, An Algorithm for Monte Carlo Simulation of Penetration and Energy Loss of Electrons and Positrons in Matter”, *Nucl. Instr. & Meth.*, B100, p. 31 (1995).
- [18] Nimal, J.C., T. Vergnaud, F. Marcel, *TRIPOLI-3: Code de Monte Carlo Tridimensionnel Polycinétique – Manuel d’utilisation (Version 3.3)*, CEA Report DMT 96/026/SERMA/LEPP/96/1863.
- [19] Both, J.P., H. Derriennic, B. Morillon and J.C. Nimal, “A Survey of TRIPOLI-4”, *Proceedings of the 8th International Conference on Radiation Shielding*, 24-28 April, Arlington, Texas, USA (1994).
- [20] Vergnaud, T., *Qualification du Code de Monte Carlo TRIPOLI-3 (Version 3.4)*, CEA Report DMT SERMA/LEPP/RT/98/2184/A.
- [21] ICRP (International Commission on Radiological Protection), *Recommendations of the International Commission on Radiological Protection*, Publication 60, *Annals of ICRP 21 (1-3)*, Pergamon Press, Oxford (1991).
- [22] ICRP, *Report of the Task Group on the Reference Man*, Publication 23, Pergamon Press, Oxford (1975).
- [23] Snyder, W.S., M.R. Ford, G.G. Warner, *Estimates of Specific Absorbed Fractions for Photon Sources Uniformly Distributed in Various Organs of a Heterogeneous Phantom*, nm/mird Pamphlet No. 5, Health Physics Division, ORNL, Oak Ridge, TN 37830 (1978).
- [24] Cristy, M., K.F. Eckerman, *Specific Absorbed Fractions of Energy at Various Ages from Internal Photon Sources. Part I: Methods*, ORNL/TM-8381 VI, Oak Ridge National Laboratory, Oak Ridge, TN (1987).
- [25] Cristy, M., *Mathematical Phantoms Representing Children of Various Ages for Use in Estimates of Internal Dose*, ORNL/NUREG/TM-367, Oak Ridge National Laboratory, Oak Ridge, TN (1980).
- [26] Kramer, R., M. Zankl, G. Williams G. Drexler, *The Calculation of Dose from External Photon Exposures Using Reference Human Phantoms and Monte Carlo Methods. Part I: The Male (ADAM) and Female (EVA) Adult Mathematical Phantoms*, GSF-Bericht S-885 GSF – Forschungszentrum für Umwelt und Gesundheit, Neuherberg, Germania (1982).

- [27] Zankl, M., U. Fill, N. Petoussi-Henss and D. Regulla, "Organ Dose Conversion Coefficients for External Photon Irradiation of Male and Female Voxel Models", *Phys. Med. Biol.*, 47, pp. 2367-2385 (2002).
- [28] Dimbylow, P.J. "The Development of Realistic Voxel Phantoms for Electromagnetic Field Dosimetry", *Proceedings of the Workshop on Voxel Phantom Development*, P.J. Dimbylow, ed., NRPB, Chilton, UK (1995).
- [29] ICRP, *Conversion Coefficients for Use in Radiological Protection Against External Radiation*, Publication 74, Pergamon Press, Oxford (1995).
- [30] ICRU (International Commission on Radiation Units and Measurements), *Conversion Coefficients for Use in Radiological Protection Against External Radiation*, Report 57, Bethesda, MD, USA (1998).
- [31] Zankl, M., N. Petoussi, G. Drexler, "Effective Dose and Effective Dose Equivalent – The Impact of the New ICRP Definition for External Photon Irradiation", *Health Phys.*, 62(51), 395-399 (1992).
- [32] Zankl, M., G. Drexler, N. Petoussi-Henb, K. Saito, *The Calculation of Dose from External Photon Exposures Using Reference Human Phantoms and Monte Carlo Methods Part VII: Organ Doses Due to Parallel and Environmental Exposure*, Geometries GSF-Bericht Neuherberg (1997).
- [33] Yamaguchi, Y., "JUENESSE: A Computer Code to Calculate Photon External Doses Using Age-specific Phantoms", *Hoken Butsuri (J. Japan Health Phys. Soc.)*, 27, 305-312 (1992).
- [34] Morstin, K., M. Kopec, Th. Schmitz, "The Equivalent Dose Versus Dose Equivalent for Neutrons Based on New ICRP Recommendations", *Radiat. Prot. Dosim.*, 44 159-164 (1992).
- [35] Nabelssi, B.K., N.E. Hertel, "Effective Dose Equivalent and Effective Dose for Neutrons from 30 to 180 MeV", *Radiat. Prot. Dosim.*, 48, 227-243 (1993).
- [36] Leuthold, G., V. Mares, H. Schraube, *Monte Carlo Calculation of Dose Equivalents for Neutrons in Anthropomorphic Phantoms Using ICRP-60 Recommendations*, GSF-Bericht, private communication.
- [37] Stewart, R.D., J.E. Tanner, J.A. Leonowich, "An Extended Tabulation of Effective Dose Equivalent for Neutrons Incident on a Male Anthropomorphic Phantom", *Health Phys.*, 65(4), 405-413 (1993).
- [38] Hollnagel, R.A., "Conversion Functions of Effective Dose, E and Effective Dose Equivalent, H_E for Neutrons with Energies from Thermal to 20 MeV", *Radiat. Prot. Dosim.*, 54, 227-230 (1994).
- [39] Sato, O., S. Iai, S. Tanaka, T. Uehara, Y. Sakamoto, N. Yosiza, S. Furihata, "Calculations of Equivalent Dose and Effective Dose for Photons from 1 MeV to 10 GeV", *Radiat. Prot. Dosim.*, 62, 119-130 (1995).
- [40] Pelliccioni, M., "Overview of Fluence-to-effective Dose and Fluence-to-ambient Dose Equivalent Conversion Coefficients for High-energy Radiation Calculated Using the FLUKA Code", *Radiat. Prot. Dosim.*, 88(4) (2000).

- [41] Ferrari, A., M. Pelliccioni, "Fluence-to-dose Equivalent Conversion Coefficients for Electrons and Photons of Energy Up to 10 GeV", *Proceedings 8th Conf. on Radiation Shielding*, Arlington, Texas, 24-28 April 1994, American Nuclear Society, ed., 2, 893-899 (1994).
- [42] Ferrari, A., M. Pelliccioni, "The Effect of Air on the Dose Equivalent at 10 mm Depth in the ICRU Sphere", *Radiat. Prot. Dosim.*, 60(3), 243-247 (1995).
- [43] Grosswendt, B., "The Angular Dependence and Irradiation Geometry Factor for Dose Equivalent for Photons in Slab Phantoms of Tissue-equivalent Material and PMMA", *Rad. Prot. Dosim.*, 31, 219-231 (1993).
- [44] Grosswendt, B., "Angular Dependence Factors and Air Kerma to Dose Equivalent Conversion Coefficients for Cylindrical Phantoms Irradiated by Extended Plane-parallel Photon Beams of Oblique Incidence Relative to the Cylinder Main Axis", *Rad. Prot. Dosim.*, Vol. 59, No. 3, pp. 195-203 (1995).
- [45] Grosswendt, B., "Air Kerma to Dose Equivalent Conversion Coefficients for 1.9 cm Rod and 7.3 cm Pillar Phantoms Irradiated by Extended Monodirectional X-ray Beams", *Rad. Prot. Dosim.*, Vol. 59, No. 3, pp. 181-193 (1995).
- [46] Siebert, B.R.L., H. Schumaker, "Quality Factors, Ambient and Personal Dose Equivalent for Neutrons, Based on the New ICRU Stopping Power Data for Protons and Alpha Particles", *Rad. Prot. Dosim.*, 58, 177-183 (1995).
- [47] Grosswendt, B., "Backscatter Factors for X-rays Generated at Voltages Between 10 and 100 kV", *Phys. Med. Biol.*, Vol. 29, No. 5, 579-591 (1984).
- [48] Gualdrini, G., L. Lembo, F. Monteventi, F. Padoani, "Monte Carlo Calculations of Field Parameters for the ICRU Sphere with Reference Photon Beams", *Radiat. Prot. Dosim.*, 46(1) (1993).
- [49] Fantuzzi, E., G. Gualdrini, B. Morelli, F. Monteventi, "Monte Carlo Computed Field Parameters for the Design of Photon Personal Dosimeters", *Proceedings of the Austrian-Italian-Hungarian Radiation Protection Symposium*, Obergurgl, Austria, 28-30 April (1993).
- [50] *ISO/DIS 4037-3 X and Gamma Reference Radiation for Calibrating Dosemeter and Dose Rate Meters and for Determining Their Response as a Function of Photon Energy. Part 3: Area and Personal Dosimeters*, ISO/TC 85/SC 2 (1997).
- [51] Gualdrini, G. and B. Morelli, *Studies on the Homogeneity of Photon Fields for Contemporary Calibration of Personal Dosimeters on Slab Phantoms*, ENEA, RT/AMB/96/22 (1996).
- [52] Burkhardt, B., G. Flieg, A. Klett, A. Plewnia, B.R.L. Siebert, "The Neutron Fluence and H^{*}(10) Response of the New LB6411 Rem Counter", 8th Symposium on Neutron Dosimetry, Paris, France, 13-17 November 1995, *Radiat. Prot. Dosim.*, 70(1-4) (1997).
- [53] D'Errico, F., R.E. Apfel, G. Curzio, E. Dietz, E. Egger, G. Gualdrini, S. Guldbakke, R. Nath, B.R.L. Siebert, "Superheated Emulsions: Neutronics and Thermodynamics", 8th Symposium on Neutron Dosimetry, Paris, France, 13-17 November 1995, *Radiat. Prot. Dosim.*, 70(1-4) (1997).

- [54] G. Gualdrini, F. D'Errico, P. Noccioni, *Monte Carlo Evaluation of the Neutron Detection Efficiency of a Superheated Drop Detector*, ENEA, RT/AMB/97/1 (1997).
- [55] Vontobel, P., *EFFILIB: A Enjoy Generated Neutron Data Library Based on EFF-1 for the Continuous Energy Monte Carlo MCNP*, PSI Report No. 107 (1991).
- [56] Birattari, C., A. Ferrari, C. Nuccetelli, M. Pelliccioni and M. Silari, "An Extended Range Neutron Remcounter", *Nucl. Instr. Meth.*, A297 250-257 (1990).
- [57] Birattari, C., A. Esposito, A. Ferrari, M. Pelliccioni and M. Silari, "A Neutron Survey-meter with Sensitivity Extended Up to 400 MeV", *Radiat. Prot. Dosim.*, 44 193-197 (1992).
- [58] Birattari, C., A. Esposito, A. Ferrari, M. Pelliccioni and M. Silari, "Calibration of the Neutron Remcounter LINUS in the Energy Range from Thermal to 19 MeV", *Nucl. Instr. Meth.*, A324 232-238 (1993).
- [59] Birattari, C., A. Esposito, A. Ferrari, M. Pelliccioni, T. Rancati and M. Silari, "The Extended Range Neutron rem Counter LINUS: Overview and Latest Developments", *Radiat. Prot. Dosim.*, 76, 135-148 (1997).
- [60] Agosteo, S., M. Silari, L. Ulrici, "Improved Response of Bubble Detectors to High-energy Neutrons", *Radiat. Prot. Dosim.*, 88(2), 149-156 (2000).
- [61] Bordy, J.M., H. Stadmann, P. Ambrosi, D.T. Bartlett, P. Christensen, T. Colgan, H. Hyvonen, "EURADOS Report Part Three: Performance Test of Dosimetric Services in EU Members States and Switzerland for the Routine Assessment of Individual Doses (Photon, Beta and Neutron)", *Rad. Prot. Dosim.*, Vol. 89(1-2), 107-154 (2000).
- [62] Vilela, E., B. Morelli, G. Gualdrini, K.W. Burn, F. Monteventi, "Experimental and Monte Carlo Evaluations of the Dosimetric Characteristics of a Thermal Neutron Calibration Assembly", 12th Conference on Solid State Dosimetry, Burgos, Spain, June 1998, *Rad. Prot. Dosim.*, Vol. 80(1-4) (1999).
- [63] *Reference Neutron Radiations – Part 2: Calibration Fundamentals Related to the Basic Quantities Characterizing the Radiation Field*, ISO 8529-2, draft (1998).
- [64] Bedogni, R., G. Gualdrini and F. Monteventi, "Field Parameters and Dosimetric Characteristics of a Fast Neutron Calibration Facility: Experimental and Monte Carlo Evaluations", *Int. Workshop on Neutron Fields Spectrometry in Science, Technology and Radiation Protection*, Pisa, Italy, 4-8 June (2000).

MONTE CARLO CALCULATION OF CONVERSION COEFFICIENTS FOR HIGH-ENERGY RADIATION

Maurizio Pelliccioni

Istituto Nazionale di Fisica Nucleare, Italy

Abstract

Two types of quantities are specifically defined for use in radiological protection: protection quantities, which are defined by the ICRP, and operational quantities, which are defined by the ICRU. Conversion coefficients, which relate protection and operational quantities to physical quantities, are calculated using radiation transport codes and the appropriate mathematical models. ICRP and ICRU recommended conversion coefficients for photons and electrons of energies up to 10 MeV and for neutrons with energies up to 180 MeV. However, conversion coefficients for higher energies are needed for various purposes. Sets of fluence-to-effective dose and fluence-to-ambient dose equivalent conversion coefficients for monoenergetic photons, electrons, positrons, protons, neutrons, muons, pions and kaons, with incident energies up to 10 TeV, have been calculated by the Monte Carlo transport code FLUKA. Details on the calculations and a graphical presentation of the calculated results are given in the present paper.

Introduction

There are two types of quantities specifically defined for use in radiological protection: protection quantities, defined by the ICRP, and operational quantities, defined by the ICRU. Dose limits are expressed in terms of protection quantities and compliance with these limits is demonstrated by a determination of the appropriate operational quantity. Both the protection quantities and operational quantities can be related to the basic physical quantities by means of conversion coefficients.

Protection quantities

The most recent set of protection quantities was recommended in ICRP Publication 60 [1]. It includes the tissue or organ equivalent doses, H_T , and the effective dose, E .

The equivalent dose, H_T , in a tissue or organ, T , is given by:

$$H_T = \sum_R w_R D_{T,R} \quad (1)$$

where $D_{T,R}$ is the average absorbed dose from radiation R , in tissue T , and w_R the radiation weighting factor of radiation R (see Table 1).

Table 1. Values for radiation weighting factors recommended in ICRP Publication 60

Radiation	w_R
Photons	1
Electrons and muons	1
Neutrons, energy	
< 10 keV	5
10 keV-100 keV	10
> 100 keV-2 MeV	20
> 2 MeV-20 MeV	10
> 20 MeV	5
Protons, other than recoils protons, energy >2 MeV	5
Alpha particles, fission fragments, heavy nuclei	20

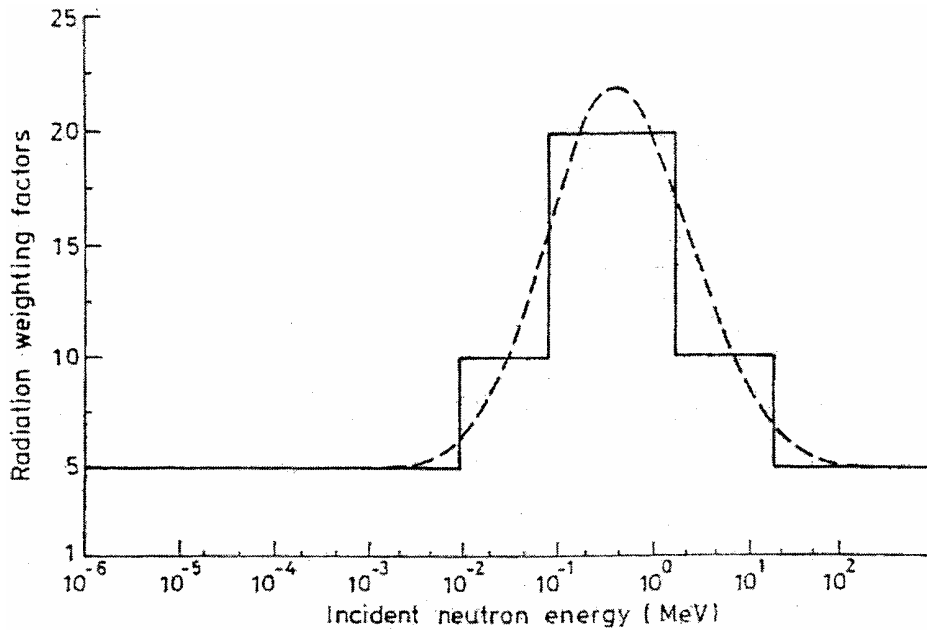
It is noticeable that, in the case of neutrons, as an approximation, a continuous function was also recommended in Paragraph (A12) of ICRP Publication 60:

$$w_R = 5 + 17e^{-(\ln(2E_n))^2/6} \quad (2)$$

where E_n is the neutron energy.

Sometimes this fact is a reason of confusion because, practically, two sets of w_R values are recommended in the energy region 100 keV-100 MeV, diverging up to several tens per cent at some neutron energies (see Figure 1).

Figure 1. Radiation weighting factors for neutrons [1]



The effective dose, E, is the sum of the weighted equivalent doses in all the tissues and organs of the body. It is given by the expression:

$$E = \sum_T w_T H_T \quad (3)$$

where H_T is the equivalent dose in tissue or organ T and w_T is the weighting factor for tissue T (see Table 2).

Table 2. Tissue weighting factors recommended in ICRP Publication 60

Tissue or organ	w_T
Gonads	0.20
Red bone marrow, colon, lung, stomach	0.12
Bladder, breast, liver, oesophagus, thyroid, remainder	0.05
Bone surface, skin	0.01

The remainder includes the following 10 organs and tissues: adrenals, brain, kidney, muscle, pancreas, small intestine, extra-thoracic airways, spleen, thymus, uterus.

The protection quantities (H_T and E) are not directly measurable but may be related by calculation to the radiation field if the conditions of irradiation are known. The only way to estimate H_T and E is to measure the radiation field outside the body and convert it using previously calculated conversion coefficients.

Operational quantities

The mean absorbed dose $D_{T,R}$ was soon recognised as a quantity that cannot be evaluated experimentally [2,3]. Therefore, according to the ICRU [3], Eqs. (1) and (3) cannot be used as a basis for measurements. For these purposes, the operational quantities defined in terms of quality factor (Q),

namely ambient dose equivalent, directional dose equivalent and personal dose equivalent, should be used. The operational quantities were first defined in ICRU Report 39 [4]. Changes to the definitions of the quantities recommended for individual monitoring were subsequently made. A complete compilation of all operational quantities currently recommended by the ICRU is available in ICRU Report 51 [3]. For strongly penetrating radiation, the appropriate operational quantity for area monitoring is the ambient dose equivalent. The ambient dose equivalent, $H^*(d)$, at a point in a radiation field is the dose equivalent that would be produced by the corresponding expanded and aligned field in the ICRU sphere at a depth, d , on the radius opposing the direction of the aligned field. The currently recommended value of d for penetrating radiation is 10 mm.

For some types of radiation and their energies or directions of incidence, the dose equivalent at a single depth may provide an unacceptable underestimate of the effective dose. In such instances, the dose equivalent at other depths may be considered [4].

According to paragraphs 70 and 319 of both ICRP Publication 74 [5] and ICRU Report 57 [6], the operational quantities are intended to provide a reasonable estimate of the protection quantities in assessing compliance with the limits. This may be simply expressed by the goal that the value of the appropriate protection quantity is less than that of the operational quantity:

$$\frac{H_{prot}}{H_{oper}} \leq 1 \quad (4)$$

Since neither the protection quantities nor the operational quantities can be measured directly, it is extremely important to relate them to basic physical quantities (such as particle fluence), which is done with conversion coefficients.

The international bodies provided conversion coefficients for protection and operational quantities in the case of photons and electrons up to 10 MeV and for neutrons up to 180 MeV [5,6].

However, fluence-to-dose conversion coefficients at higher energies are needed. They are the basic data for various purposes like radiation protection around high-energy particle accelerators, cosmic ray dosimetry, air crew dose assessment, space dosimetry.

Conversion coefficients for high-energy radiation

Over the past few years, conversion coefficients relating protection and operational quantities to the particle fluence for high-energy radiation have been calculated using the Monte Carlo radiation transport code FLUKA [7,8]. Sets of conversion coefficients for all kinds of radiation (photons, electrons, positrons, protons, neutrons, muons, charged pions, kaons) and incident energies (up to 10 TeV) of practical interest have been provided. The energy ranges investigated were extended to low energies for comparison with the recommended values. Details about the physical models adopted by the FLUKA code are given elsewhere [7,8,9].

In computing effective dose a hermaphrodite mathematical model has been used [10]. It was derived from ADAM, the male phantom developed for the MCNP code at GSF (Germany). The MCNP phantom was translated in terms of bodies and regions appropriate for the combinatorial geometry of FLUKA. A list of the bodies used in order to realise the mathematical model includes: sphere (SPH), right circular cylinder (RCC), right elliptical cylinder (REC), truncated right angle cone (TRC), ellipsoid of revolution (ELL), infinite half-space (XYP, XZP, YZP, PLA), infinite elliptical cylinder (ZEC). The geometry of some organs was changed due to the minor number of surfaces available. Female

organs (breast, ovaries, uterus) were added. Additional changes with respect to the original model concern the representation of bone surfaces and red bone marrow. The various organs and tissues of the human body have been represented by 68 regions. Tissue considered: lungs ($0.296 \text{ g}\cdot\text{cm}^{-3}$); bone ($1.486 \text{ g}\cdot\text{cm}^{-3}$); red bone marrow ($1.028 \text{ g}\cdot\text{cm}^{-3}$); soft tissues ($0.987 \text{ g}\cdot\text{cm}^{-3}$); skin ($1.105 \text{ g}\cdot\text{cm}^{-3}$). The composition of these five tissues was limited to 14 elements: H, C, N, O, Na, Mg, P, S, Cl, K, Ca, Fe, Zr, Pb.

The ICRP frequently revised the specification about the organs to be included and the rules to be applied for the calculation of the effective dose. In the FLUKA calculations, the higher value of doses to ovaries and testes was applied to the gonad-weighting factor. The breast dose was assumed to be the dose to female breast. The lung dose was assumed to be the higher value of doses to the single lungs. For the organs or tissues represented by more than one region the dose has been determined as the arithmetic mean of the doses to the single regions. Concerning the so-called remainder the dose has been evaluated as the arithmetic mean of doses to nine organs and tissues (according to ICRP Publication 67 [11]). Footnote 3 of Table 2 of ICRP Publication 60 has been ignored.

Four geometries of irradiation that have been considered include: anterior-to-posterior (AP); posterior-to-anterior (PA); lateral from the right side to the left side (RLAT); isotropic incidence from all directions (ISO).

The results of the calculations [12-20] have been summarised in Ref. [21]. As an example, Figures 2 and 3 provide a graphical presentation of the calculated effective dose per unit of fluence as a function of the incident particle energy for various kinds of particles, in the case of AP and ISO irradiation, respectively. Usually AP irradiation gives the maximum effective dose per unit of fluence in the case of low incident energies (up to 50-100 MeV). Conversely ISO irradiation gives the highest values at high incident energies (in excess of about 100 MeV).

In order to obtain the fluence-to-ambient dose equivalent conversion coefficients, the depth-dose distribution along the principal axis of an ICRU sphere exposed in the vacuum to an expanded and aligned particle beam was determined. The energy deposited has been scored as a function of the depth and radius in one r-z binning cylindrical structure. The Q-L relationship according to ICRP Publication 60 has been considered. The values of the ambient dose equivalent have been averaged over the depth 0.95-1.05 or 0.9-1.1 cm, according to the incident energy. The calculated results have been discussed through several papers [16,17,20,22-27]. Figure 4 gives a graphical presentation of the calculated ambient dose equivalent per unit of fluence as a function of the incident energy for the various particles considered. A summary of the calculated data can be found in the summarising paper mentioned above [21].

Some remarks on the calculated conversion coefficients

Ambient dose equivalent for photons of energy lower than 10 MeV: A comparison with the recommended conversion coefficients

Figure 5 shows a comparison between calculated and recommended fluence-to-ambient dose equivalent conversion coefficients for photons. The significant discrepancies between the two sets of data, in the energy range 3-10 MeV, are due to the differences in the way in which the value of the ambient dose equivalent is calculated. While in the FLUKA calculations the medium between the source and the ICRU sphere was assumed to be a vacuum, the recommended conversion coefficients assume that the sphere is located in air and that secondary charged-particle equilibrium exists at the point in the radiation field where a measurement is made.

Figure 2. Calculated effective dose (AP) per unit fluence as a function of particle energy for various kinds of radiation

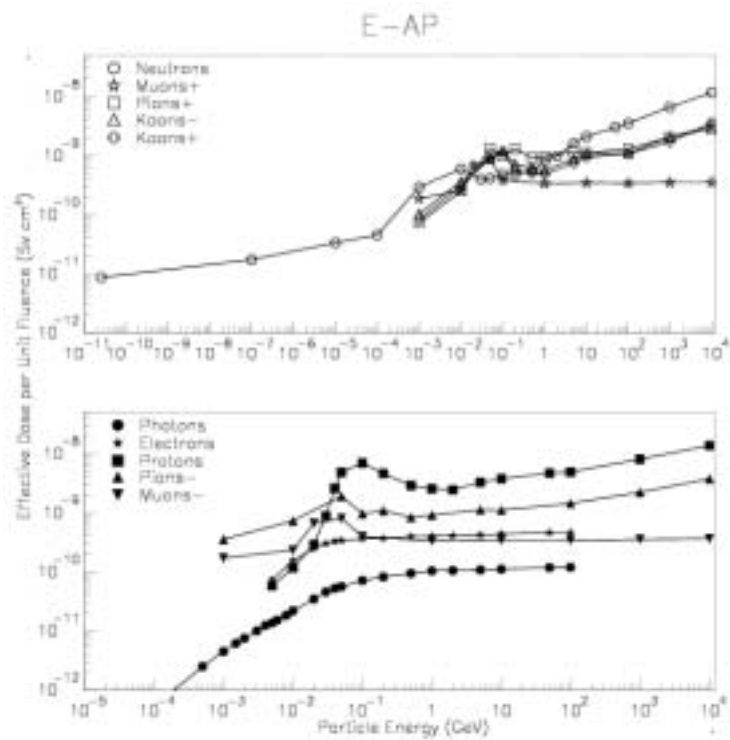


Figure 3. Calculated effective dose (ISO) per unit fluence as a function of particle energy for various kinds of radiation

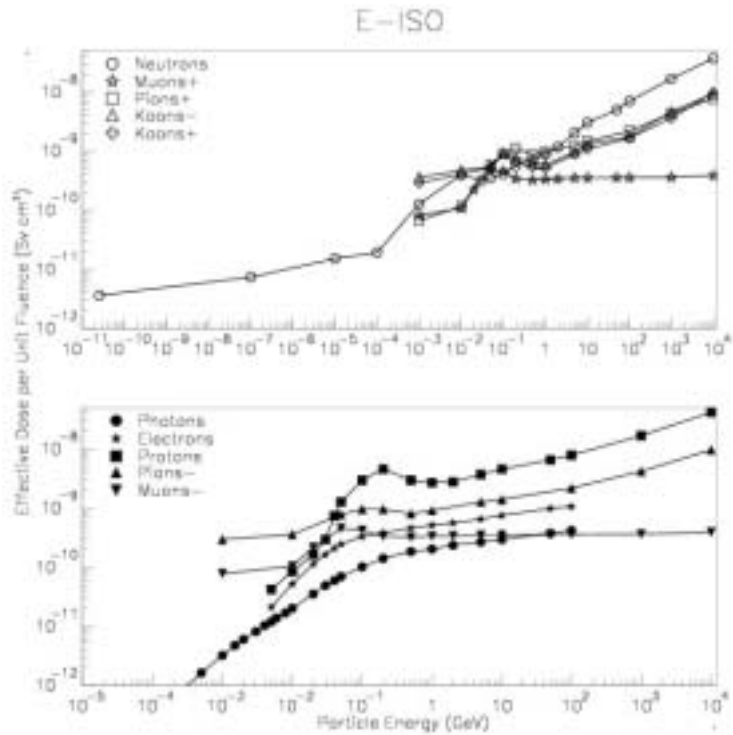


Figure 4. Calculated ambient dose equivalent per unit fluence as a function of particle energy for various kinds of radiation

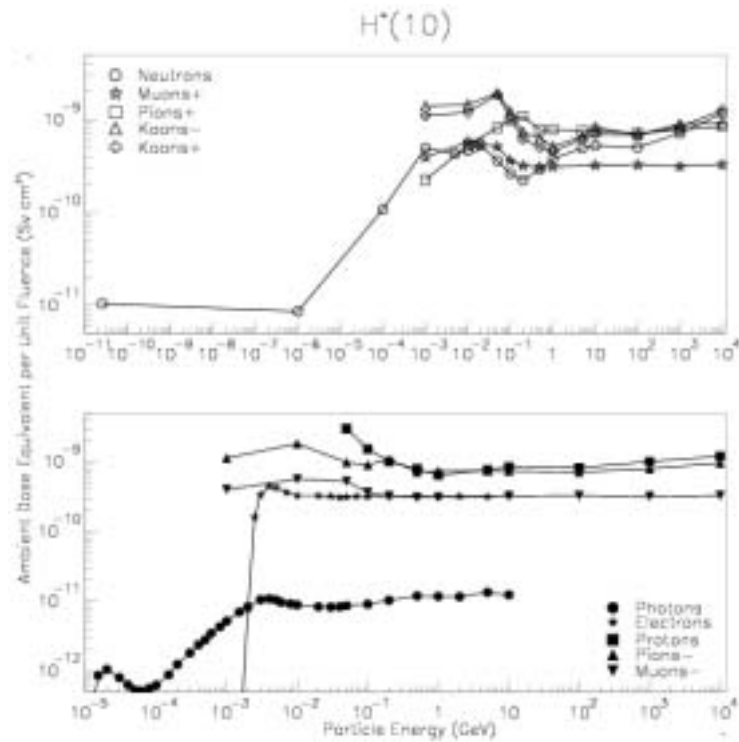
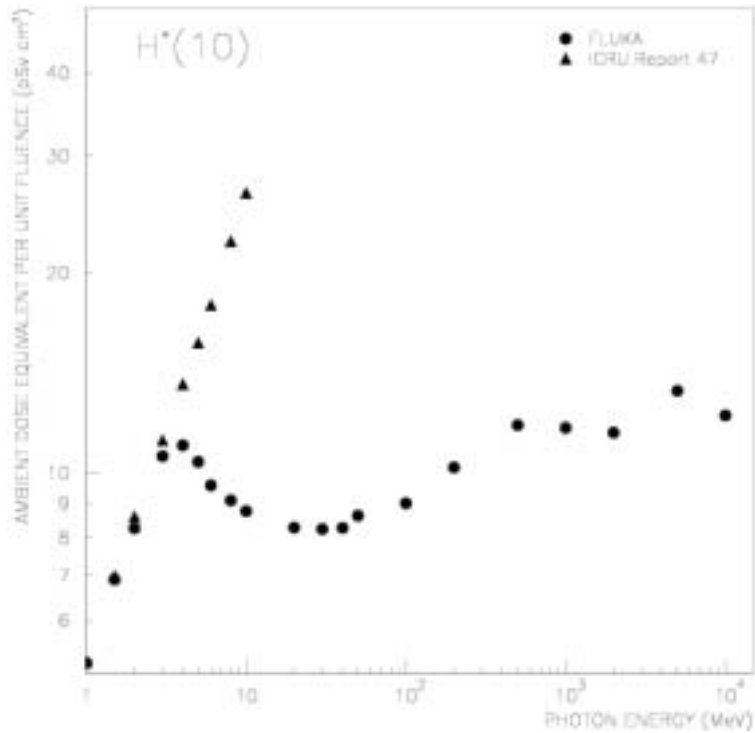


Figure 5. Calculated and recommended fluence-to-ambient dose equivalent conversion coefficients for photons



In the opinion of the present author the calculation of the conversion coefficients for photons in air under charged particle equilibrium is arbitrary. By contrast with the definition of ambient dose equivalent, the air prevents the beam to impinge aligned and expanded on the sphere [22,28].

Relationship between effective dose and ambient dose equivalent for high-energy radiation

Inspection of Figures 2, 3 and 4 permits a qualitative understanding of the relationship between effective dose and ambient dose equivalent in the case of high-energy radiation.

In particular, Figures 2 and 3 show that the effective dose increases practically over the entire energy interval investigated. On the contrary, the shape of the curves showing the dependence of the ambient dose equivalent to the energy appears to become flat at high energies.

As a consequence it is expected that the ambient dose equivalent can not be a conservative estimate of effective dose for high-energy radiation.

Figures 6 and 7 show a comparison between $H^*(10)$ and effective dose, in various conditions of irradiation, for photons and neutrons, respectively. The data shown in these figures confirm that $H^*(10)$ systematically underestimates the effective dose at high energies.

Figure 6. Calculated effective dose, maximum dose equivalent and ambient dose equivalent per unit of fluence as a function of photon energy

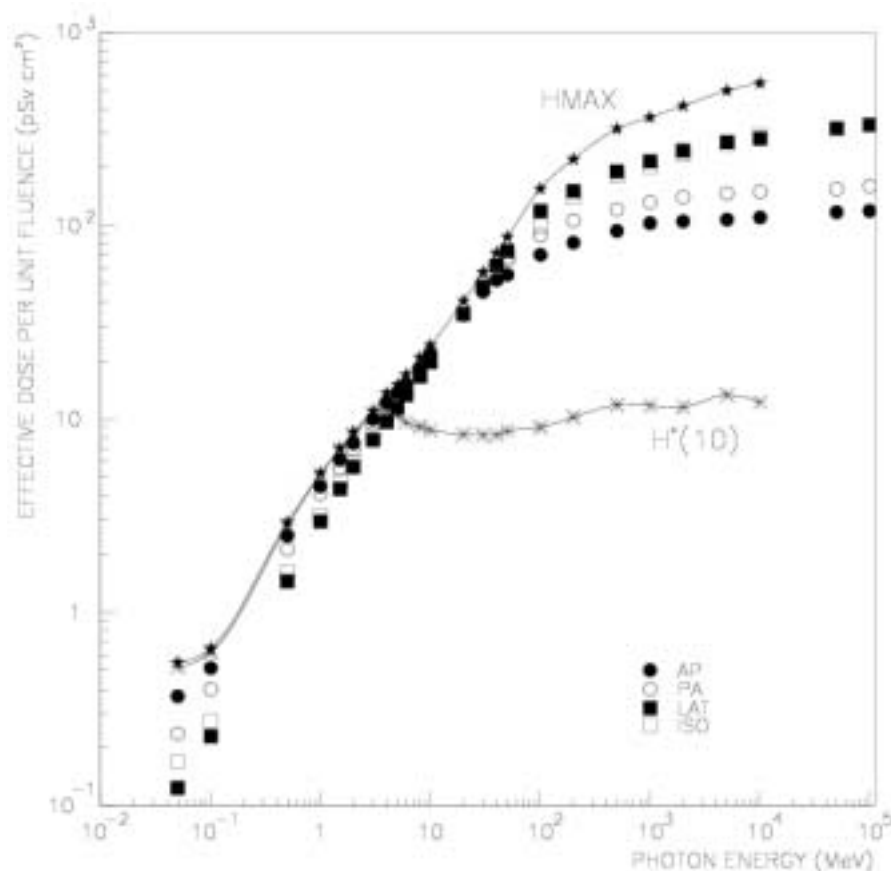
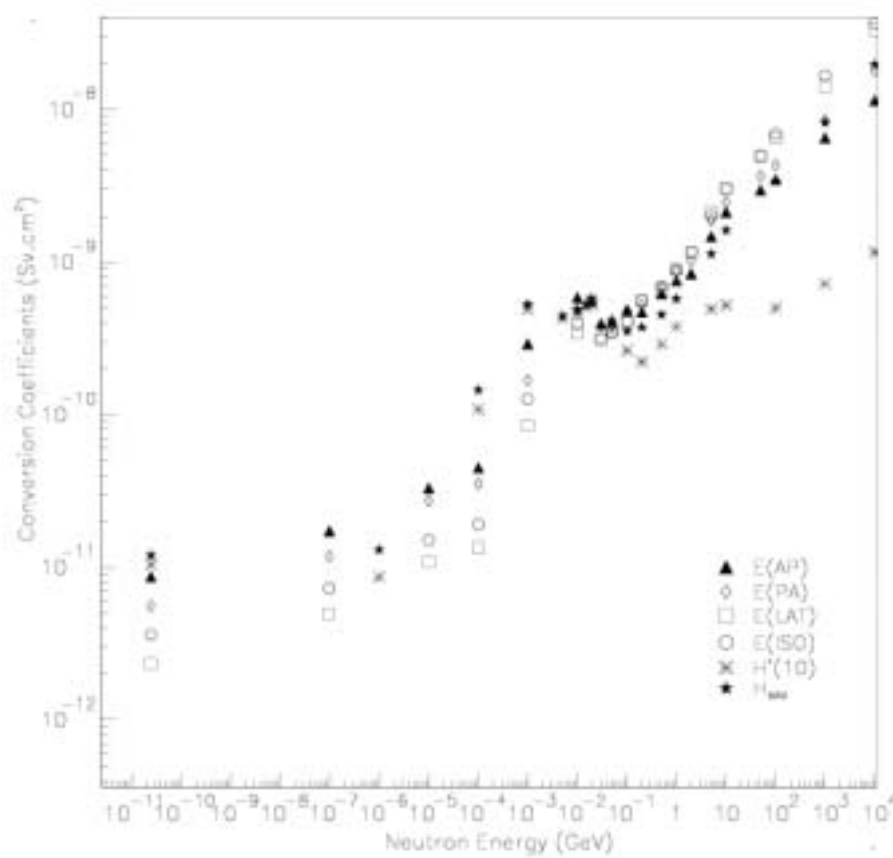


Figure 7. Calculated effective dose, maximum dose equivalent and ambient dose equivalent per unit of fluence as a function of neutron energy



Unfortunately the maximum dose equivalent along the principal diameter of the ICRU sphere also does not give a conservative approximation of the effective dose for neutrons (see Figure 7). This means that a simple value of depth, d , which would make $H^*(d)$ an appropriate operational quantity irrespective of incident neutron energy can not be specified. The ICRU sphere seems to be a simplified phantom inadequate for high-energy neutron dosimetry, probably because of its insufficient mass compared with that of an anthropomorphic model.

Comparison with the results of other authors

Other groups of authors [29-47] have performed calculations of effective dose and ambient dose equivalent for radiation of energy in excess of those considered by the international bodies. The agreement with the results of the FLUKA calculations is generally satisfactory. Nevertheless, significant discrepancies have been found for neutrons in the GeV region, probably due to the different physical models adopted by the different codes at intermediate energies.

In order to make clear the reasons for these discrepancies, at the SATIF-4 meeting a simple benchmark was planned with the Monte Carlo codes FLUKA, MCNPX and HETC-3STEP. The scope of the benchmark was the calculation of the energy deposition in four single elements (H, C, N, O) and in ICRU tissue cylindrical phantoms for incident neutron energies from 100 MeV to 10 GeV. The depth absorbed dose distributions in the central region ($R = 1$ cm) and in the whole region

(R = 10 cm) of the phantoms were calculated. The results were very surprising. There were large differences especially for the single-element phantoms [48]. In addition the results showed significant discrepancies not only between FLUKA and the other two codes, but also between MCNPX and HETC-3STEP. The benchmark confirmed that the predictions of the various codes in the GeV region are quite different, without explaining the reason why.

A systematic calculation of the conversion coefficients in terms of effective dose, although only for isotropic irradiation and for incident energies up to 10 GeV, was recently carried out by another group of authors using the MCNPX code [49]. The results were presented at the SATIF-6 meeting (SLAC, April 2002) and compared to the data obtained using FLUKA. The agreement was found to be generally satisfactory for photons, electrons, muons and protons. In the case of neutrons, MCNPX data are systematically higher than those calculated with FLUKA for energies higher than 200 MeV.

Incidentally, it is interesting to recall that the prediction power of FLUKA has been proven to be very reliable in numerous applications at high-energy accelerators, where detailed comparisons with experimental data are possible. In any case, the problem of discrepancies between the various codes for the calculation of the neutron conversion coefficients in the GeV region remains an open question.

REFERENCES

- [1] ICRP (International Commission on Radiological Protection), *1990 Recommendations of the International Commission on Radiological Protection*, Publication 60, Annals of ICRP, 21(1-3) (1991).
- [2] Kellerer, A.M., *Rigour within Uncertainty*, ICRU News, December 1990.
- [3] ICRU (International Commission on Radiation Units and Measurements), *Quantities and Units in Radiation Protection Dosimetry*, Report 51, Bethesda, MD (1993).
- [4] ICRU, *Determination of Dose Equivalents Resulting from External Radiation Source*, Report 39, Bethesda, MD (1985).
- [5] ICRP, *Conversion Coefficients for use in Radiological Protection Against External Radiation*, Publication 74, Annals of ICRP, 26, No. 3/4 (1996).
- [6] ICRU, *Conversion Coefficients for use in Radiological Protection Against External Radiation*, Report 57, Bethesda, MD (1998).
- [7] Fassò, A., A. Ferrari and P.R. Sala, "Electron-photon Transport in FLUKA: Status", *Proceedings of the Monte Carlo 2000 Conference*, Lisbon, 23-26 October 2000, A. Kling, F. Barao, M. Nakagawa, L. Tavora, P. Vaz, eds., Springer-Verlag, Berlin, pp. 159-164 (2001).

- [8] Fassò, A., A. Ferrari, J. Ranft and P.R. Sala, "FLUKA: Status and Prospective for Hadronic Applications", *Proceedings of the Monte Carlo 2000 Conference*, Lisbon, 23-26 October 2000, A. Kling, F. Barao, M. Nakagawa, L. Tavora, P. Vaz, eds., Springer-Verlag, Berlin, pp. 955-960 (2001).
- [9] Ferrari, A., *Intermediate and High Energy Nuclear Reactions in Dosimetry Calculations*, these proceedings.
- [10] Pelliccioni, M. and M. Pillon, "Comparison Between Anthropomorphic Mathematical Phantoms Using MCNP and FLUKA Codes", *Rad. Prot. Dos.*, 67 (4), 253-256 (1996).
- [11] ICRP, *Age-dependent Doses to Members of the Public from Intakes of Radionuclides: Part 2 Ingestion Dose Coefficients*, Publication 67, Annals of ICRP, 23, No. 3/4 (1993).
- [12] Ferrari, A., M. Pelliccioni and M. Pillon, "Fluence to Effective Dose and Effective Dose Equivalent Conversion Coefficients for Photons from 50 keV to 10 GeV", *Radiat. Prot. Dosim.*, 67 (4), 245-251 (1996).
- [13] Ferrari, A., M. Pelliccioni and M. Pillon, "Fluence to Effective Dose and Effective Dose Equivalent Conversion Coefficients for Electrons from 5 MeV to 10 GeV", *Radiat. Prot. Dosim.*, 62 (9), 97-104 (1997).
- [14] Ferrari, A., M. Pelliccioni and M. Pillon, "Fluence to Effective Dose Conversion Coefficients for Protons from 5 MeV to 10 TeV", *Radiat. Prot. Dosim.*, 71 (2) 85-91 (1997).
- [15] Ferrari, A., M. Pelliccioni and M. Pillon, "Fluence to Effective Dose Equivalent Conversion Coefficients for Neutrons up to 10 TeV", *Radiat. Prot. Dosim.*, 71 (3), 165-173 (1997).
- [16] Ferrari, A., M. Pelliccioni and M. Pillon, "High-energy Electron and Photon Dosimetry", *Proceedings of the 30th Midyear Topical Meeting of the Health Physics Society*, 5-8 Jan. 1997, San José, California (USA), 151-161 (1997).
- [17] Pelliccioni, M., "Conversion Coefficients for High-energy Radiation", *Proceedings of SATIF-3*, Tohoku University, Sendai, Japan, 12-13 May 1997, 289-298, OECD Proceedings (1998).
- [18] Ferrari, A., M. Pelliccioni and M. Pillon, "Fluence to Effective Dose Conversion Coefficients for Muons", *Radiat. Prot. Dos.*, 74 (4), 227-233 (1997).
- [19] Ferrari, A., M. Pelliccioni and M. Pillon, "Fluence to Effective Dose Conversion Coefficients for Negatively and Positively Charged Pions", *Radiat. Prot. Dosim.*, 80 (4), 361-370 (1998).
- [20] Pelliccioni, M., "Radiation Weighting Factors and Conversion Coefficients for High-energy Radiation", *Proceedings of SATIF-4*, Knoxville, TN, 17-18 September 1998, 179-192, OECD Proceedings (1999).
- [21] Pelliccioni, M., "Overview of Fluence to Effective Dose and Fluence to Ambient Dose Equivalent Conversion Coefficients for High-energy Radiation Calculated Using the FLUKA Code", *Radiat. Prot. Dos.*, 88, 279-298 (2000).
- [22] Ferrari, A. and M. Pelliccioni, "On the Conversion Coefficients from Fluence to Ambient Dose Equivalent", *Radiat. Prot. Dosim.*, 51 (4), 251-255 (1994).

- [23] Ferrari A. and M. Pelliccioni, "Dose Equivalents for Monoenergetic Electrons Incident on the ICRU Sphere", *Radiat. Prot. Dos.*, 55, 207-210 (1994).
- [24] Ferrari A. and M. Pelliccioni, "Dose Equivalents for Monoenergetic Positrons Incident on the ICRU Sphere", *Radiat. Prot. Dos.*, 55, 309-312 (1994).
- [25] Ferrari, A. and M. Pelliccioni, "Fluence to Dose Equivalent Conversion Coefficients for Electrons and Photons of Energy up to 10 GeV", *Proceedings 8th International Conference on Radiation Shielding*, Arlington, TX, 24-28 April 1994, 2, 893-899 (1994).
- [26] Ferrari, A. and M. Pelliccioni, "Fluence to Dose Equivalent Conversion Data and Effective Quality Factors for High-energy Neutrons", *Radiat. Prot. Dosim.*, 76 (4), 215-224 (1998).
- [27] Pelliccioni, M. "Fluence to Dose Equivalent Conversion Data and Radiation Weighting Factors for High-energy Radiation", *Radiat. Prot. Dosim.*, 77(4), 159-170 (1998).
- [28] Ferrari A. and M. Pelliccioni, "On the Ambient Dose Equivalent", *J. Radiol. Prot.*, 14 (4), 331-335 (1994).
- [29] Sato, O., S. Iwai, S. Tanaka, T. Uehara, Y. Sakamoto, N. Yoshizawa and S. Furihata, "Calculations of Equivalent Dose and Effective Dose Conversion Coefficients for Photons from 1 MeV to 10 GeV", *Radiat. Prot. Dos.*, 62 (3), 119-130 (1995).
- [30] Iwai, S., T. Uehara, O. Sato, N. Yoshizawa, S. Furihata, S. Tanaka and Y. Sakamoto, "Evaluation of Effective Dose Irradiated by High-energy Radiation", *Proceedings of SATIF-1*, Arlington, TX, 28-29 April 1994, 305-322, OECD Proceedings (1995).
- [31] Mares, V., G. Leuthold and H. Schraube, *Organ Doses and Dose Equivalents for Neutrons above 20 MeV*, *Proceedings of the 8th Symposium on Neutron Dosimetry*, Paris, 13-17 Nov. 1995, *Radiat. Prot. Dosim.*, 70 (1-4), 391-394 (1997).
- [32] Sannikov, A.V. and E.N. Savitskaya, *Ambient Dose Equivalent Conversion Factors for High Energy Neutrons Based on the New ICRP Recommendations*, IHEP 95-98 (1995).
- [33] Iwai, S., T. Uehara, O. Sato, N. Yoshizawa, S. Furihata, S. Takagi, S. Tanaka and Y. Sakamoto, *Evaluation of Fluence to Dose Equivalent Conversion Coefficients for High Energy Neutrons – Calculation of Effective Dose Equivalent and Effective Dose*, *Proceedings of SATIF-2*, CERN, Switzerland, 12-13 October 1995, 193-220, OECD Proceedings (1996).
- [34] Sannikov, A.V. and E.N. Savitskaya, "Ambient Dose Equivalent Conversion Factors for High Energy Neutrons Based on the ICRP 60 Recommendations", *Radiat. Prot. Dos.*, 70 (1-4), 383-386 (1997).
- [35] Iwai, S., T. Uehara, O. Sato, N. Yoshizawa, S. Furihata, S. Takagy, S. Tanaka and Y. Sakamoto, "Overview of Fluence to Dose Equivalent Conversion Coefficients for High Energy Radiations – Computational Methods and Results of Effective Dose Equivalent and Effective Dose per Unit Particle Fluence", *Proceedings of SATIF-3*, Tohoku University, Sendai, Japan, 12-13 May 1997, OECD Proceedings, 299-332, 1998.

- [36] Uehara, T., S. Iwai, O. Sato, N. Yoshizawa, S. Furihata, S. Tanaka and Y. Sakamoto, "Evaluation of Fluence to Dose Equivalent Conversion Coefficients for High-energy Photons (II) – Evaluation of the Conversion Coefficients for Effective Dose by Use of the Mathematical Phantom of the Human Body", *Proceedings 8th International Conference on Radiation Shielding*, Arlington, TX, 24-28 April 1994, 2, 1188-1204 (1994).
- [37] Nielsen, A.D., N.E. Hertel and L.S. Waters, "Calculations of Ambient Dose Equivalent to 2 GeV", *Proceedings of AccApp'98, 2nd International Topical Meeting on Nuclear Applications of Accelerator Technology*, 20-23 September 1998, Gatlinburg, Tennessee, 269-275 (1998).
- [38] Yoshizawa, N., O. Sato, S. Takagi, S. Furihata, S. Iwai, T. Uehara, S. Tanaka and Y. Sakamoto, "External Radiation Conversion Coefficients using Radiation Weighting Factor and Quality Factor for Neutron and Proton from 20 MeV to 10 GeV", *Journal of Nuclear Science and Technology*, 35 (12), 928-942 (1998).
- [39] Sutton, M.R., N.E. Hertel, L.S. Waters and L.S. Walker, "High-energy Neutron Conversion Coefficients", Health Physics Society Annual Meeting, 27 June-1 July 1999, Philadelphia, PA, *Health Physics*, 76, No. 6, S111 (1999).
- [40] Iwai, S., T. Uehara, O. Sato, N. Yoshizawa, S. Furihata, S. Takagi, S. Tanaka and Y. Sakamoto, "Overview of Fluence to Dose Equivalent Conversion Coefficients for High Energy Radiations – Calculational Methods and Results of Effective Dose Equivalent and Effective Dose per Unit Particle Fluence", *Proceedings of SATIF-4*, Knoxville, TN, 17-18 September 1998, 193-220, OECD Proceedings (1999).
- [41] Yoshizawa, N., N. Nakao, Y. Sakamoto and S. Iwai, "Comparison of Computer Code Calculations for the ICRU Slab Phantom", *Proceedings of SATIF-4*, Knoxville, TN, 17-18 September 1998, 231-238, OECD Proceedings (1999).
- [42] Bozkurt, A. and X.G. Xu, "Organ Dose Calculations for High-energy Protons Using Anthropomorphic Phantoms", Health Physics Society Annual Meeting, 27 June-1 July 1999, Philadelphia, PA, *Health Physics*, 76, No. 6, S111 (1999).
- [43] Hertel, N.E., M.R. Sutton and J.E. Sweezy, *Preliminary Set of Fluence-to-effective-dose Conversion Coefficients*, Technical Memorandum to Accelerator Production of Tritium, Technical Program Office, LNAL (1999).
- [44] Yoshizawa, N., O. Sato, S. Takagi, S. Furihata, J. Funabiki, S. Iwai, T. Uehara, S. Tanaka and Y. Sakamoto, *Fluence to Dose Conversion Coefficients for High-energy Neutrons, Protons and Alpha Particles*, paper presented at the 9th International Conference on Radiation Shielding (ICRS-9), Tsukuba, Japan, 17-22 October 1999.
- [45] Iwai, S., T. Uehara, O. Sato, N. Yoshizawa, S. Furihata, S. Takagi, S. Tanaka and Y. Sakamoto, *Calculational Method and Results of Two Kinds of Effective Dose per Unit Particle Fluence*, paper presented at 9th International Conference on Radiation Shielding (ICRS-9), Tsukuba, Japan, 17-22 October 1999.
- [46] Sutton, M.R., N.E. Hertel and L.S. Waters, *High-energy Neutron Dosimetry*, presented at the 9th International Conference on Radiation Shielding (ICRS-9), Tsukuba, Japan, 17-22 October 1999.

- [47] Bozkurt, A., T.C. Chao and X.G. Xu, "Fluence-to-dose Conversion Coefficients Based on the VIP-man Anatomical Model and MCNPX Code for Monoenergetic Neutrons above 20 MeV", *Health Physics*, 81, 184-202 (2001).
- [48] N. Yoshizawa, Y. Sakamoto, S. Iwai and H. Hirayama, "Benchmark Calculation with Simple Phantom for Neutron Dosimetry", *Proceedings of SATIF-5*, Paris, France, 18-21 July 2000, 253-264, OECD Proceedings (2001).
- [49] Mares V. and H. Schraube, "The Effect of the Fluence to Dose Conversion Coefficients upon the Dose Estimation to Cosmic Radiation", these proceedings, SLAC, April 2002.

SESSION II

Chair: B. Grosswendt

MONTE CARLO APPROACHES TO IMPORTANT PROBLEMS IN RADIOTHERAPY DOSIMETRY

Alan E. Nahum

Radiation Oncology Dept., Fox-Chase Cancer Center
Philadelphia PA 19111, USA
alan_e_nahum@yahoo.co.uk

Abstract

Monte Carlo codes such as EGS4 and MCNP are essential for simulating electron and photon transport in radiotherapy, e.g. Monte Carlo (MC) derived values of the water-to-air stopping-power ratio, $S_{w/air}$, are used in all *Codes of Practice* for absolute dose determination in radiotherapy clinics. Further, MC simulation can compute directly D_{med}/D_{det} for a dosimeter. Low gas density in ionisation chambers poses problems for most codes based on condensed history (CH) electron transport. However, combining single- with multiple-scattering, as recently implemented in EGSnrc, enables arbitrarily accurate chamber-response simulations. Monte Carlo can now compute doses in radiotherapy patients with uncertainties of $\approx 1\%$ (1 SD) in mm-sized voxels in a few minutes for an electron beam and in < 60 min. for photon beams using sub \$20 000 hardware, thus avoiding approximations previously made for the effect of heterogeneities. In the microdosimetry/track structure field, CH based codes demonstrate depth- and (incident) energy-independent electron ($d\Phi/dE$) per unit dose at low energies, thus explaining the negligible RBE variation over a wide range of low-LET radiations.

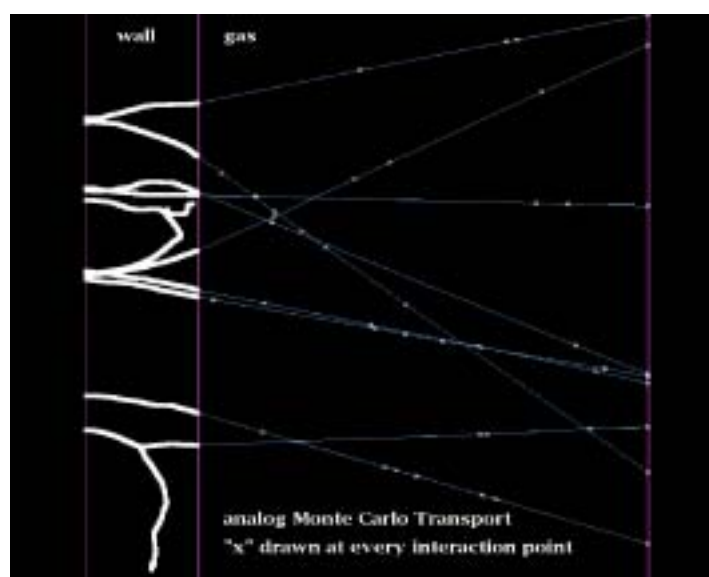
Introduction

Monte Carlo simulation of radiation transport is a very powerful technique. There are basically no exact analytical solutions to the Boltzmann Transport equation. Even the “straightforward” situation (in radiotherapy) of an electron beam depth-dose distribution in water proves to be too difficult for analytical methods without making gross approximations such as ignoring energy-loss straggling, large-angle single scattering and bremsstrahlung production. But the true power of Monte Carlo is utilised when radiation is transported from one medium into another. As the particle (be it a neutron, photon, electron, proton) crosses the boundary then a new set of interaction cross-sections is simply read in and the simulation continues as though the new medium were infinite until the next boundary is encountered.

However, at the extreme (in terms of density differences) gas/condensed medium interface in an ionisation chamber, Condensed history charged-particle MC simulation has difficulties [1-4]. This is due to the fact that CH simulation always has an analytical component. As will be discussed below, the only way to completely eliminate such problems is to revert back to analogue MC [5].

Figure 1. Electron tracks at the wall/gas interface of an ionisation chamber

Alex Bielajew, private communication



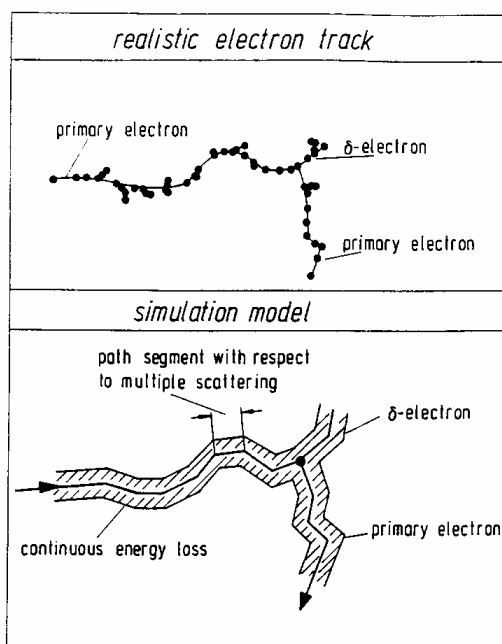
Schemes for electron transport

The analytical description of the penetration of electron beams in matter is complex due to the very large cross-section for interactions and hence the extremely large number of interactions, be they inelastic with the atomic electrons, bremsstrahlung involving the nucleus or elastic scattering with the positively charged nucleus. Analogue, i.e. interaction-by-interaction or event-by-event Monte Carlo, is in principle possible [6] but the processing time required to execute a sufficient number of histories to yield results such as the energy deposited in a small volume with an acceptable uncertainty is prohibitive with the computer hardware small-to-medium-sized research groups can afford. However, when the quantity of interest is the structure of the charged particle tracks, in order to understand, for example, the details of the interaction of radiation with the structures in the cells of living matter, then event-by-event MC codes are an essential tool [6-9].

Macroscopic schemes for MC electron transport group together the individual interactions using multiple-scattering theory for elastic angular changes and stopping power for energy losses [10,11]. An up-to-date, detailed treatment of condensed-history charged-particle simulation can be found in Salvat, *et al.* [12]; only certain aspects will be treated here. Condensed history (CH) codes have successfully simulated the transport of the electrons, for example, in radiotherapy dosimetry. Public domain MC codes such as EGS4 [13] and MCNP [14] have made this powerful tool available to medical physicists and stimulated research [15-17].

Figure 2. An “event-by-event” electron track (labelled “realistic”) is contrasted with the condensed history (CH) approach (labelled “simulation”)

Reproduced from [16] with permission



There are alternative ways of condensing the charged-particle histories. The MCNP code [14] and the ITS [18] and ETRAN [19,20] codes upon which it is based, use a so-called Class I algorithm which groups all energy losses into distributions to be sampled from, and thus can also include energy-loss straggling. In contrast, EGS4 [13], and certain other one-off codes, e.g. Nahum [21] and Andreo [22], contain a Class II algorithm: events above a certain threshold or cut-off are simulated explicitly (δ -rays and bremsstrahlung photons), i.e. in an analogue manner, and only those events below this cut-off are grouped together, using the restricted stopping power [13]. A disadvantage with the Class II approach is that energy-loss straggling is difficult to simulate correctly [23,24]; straggling due to those events above the cut-off is simulated completely naturally but straggling due to fluctuations in events below the cut-offs is ignored. In practice the absence of the latter has little effect on most results of interest in medical radiation physics, because it is precisely those relatively large energy losses, which are explicitly simulated, that give rise to virtually all of the straggling.

There is also considerable current interest in simulating the transport of protons [25]; beams of protons with incident energies of the order of 200 MeV or more are increasingly being used in radiation therapy [26]. MC transport schemes for protons are similar to those for electrons; a recent informative review on this subject can be found in [27]. There is negligible bremsstrahlung and the energies of the secondary electrons are very much lower in the case of protons compared to electrons.

Applications in dosimetry

Instruments for measuring radiation dose fall into two categories: 1) absolute, such as calorimeters and certain types of ionisation chambers and 2) relative, such as thermoluminescent dosimeters (TLDs), photographic film and semiconductors. In both cases one wishes to relate the mean absorbed dose in the sensitive region of the dosimeter, e.g. the air in an ion chamber, the heat absorbing element in a calorimeter, to the absorbed dose at some specified or reference position in the undisturbed medium into which the detector is placed, i.e. evaluate the ratio D_{med}/D_{det} . This can only be done by theory in two ideal cases:

- A large detector in a beam of indirectly ionising radiation such as photons, through the $(\mu_{en}/\rho)_{med,det}$ ratio.
- A small or Bragg-Gray detector in either photon or electron radiation, through the mass stopping-power ratio, $s_{med,det}$. Generally there will be deviations from perfect fulfilment of the required conditions, necessitating the addition of a perturbation factor [28].

Monte Carlo simulation has been an invaluable tool in the computation of the quantity $s_{med,det}$ [29-31], and to a lesser extent the $(\mu_{en}/\rho)_{med,det}$ ratio, and also other detector-response related parameters such as the backscatter factor, B for kilovoltage X-ray qualities [32,33]. Such computations involve numerical integration over the spectrum of photons or electrons at a given depth in an irradiated uniform medium; this requires the power of Monte Carlo simulation due to the complex changes in the radiation spectrum with depth. All Codes of Practice for absolute dose determination in radiotherapy beams now use MC generated $s_{water,air}$ for both megavoltage photons and electrons [34-37]; hence everyday radiotherapy practice all over the world has benefited directly from Monte Carlo. Stopping-power ratios for proton beams [38] have also been computed by Monte Carlo simulation.

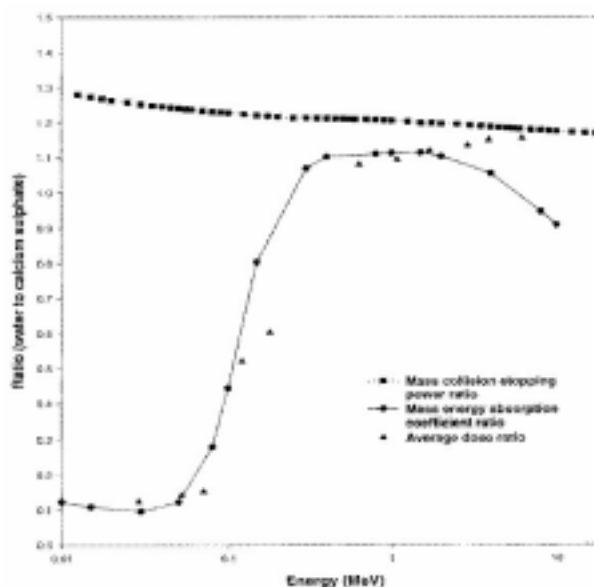
MC can also compute directly the dose ratio D_{med}/D_{det} for the exact geometry of the detector at a certain position in a medium. This is just one specific application of the general case of determining the dose in a heterogeneous medium. Such simulations can then be interpreted to yield the perturbation factor for a particular detector, assumed to fulfil approximately Bragg-Gray conditions [39], by comparing D_{med}/D_{det} with $s_{med,det}$. Such simulations are computationally inefficient as only a small fraction of the particles incident on the phantom surface traverse the small dosimeter. Correlated sampling (CS) can be exploited to reducing the variance; one single set of histories is split at the depth where the geometry of the medium and detector first differ [40]. The computation of the ratio D_{det1}/D_{det2} can then be highly efficient; one example is the effect of a change in central-electrode material in an ion chamber [41]. The behaviour of small LiF TLDs in the form of 1 cm rods and chips in radiotherapy beam qualities has also been investigated [42] by exploiting CS to yield D_{water}/D_{LiF} ; this has settled the “arguments” in the literature concerning the magnitude of the perturbation factor in electron beams. Figure 3, taken from EGS4 simulations by Mobit, *et al.* [43], shows very clearly how the dose ratio, here for calcium fluoride TLD discs of 0.9 mm thickness, is equal to the (μ_{en}/ρ) ratio, i.e. the large detector result, at low photon energies (very short electron ranges) but approaches the stopping-power ratio at high energies where the greater electron ranges result in Bragg-Gray detector behaviour.

Ion chamber simulation

The air-filled ionisation chamber is the most important instrument for the determination of absorbed dose in radiotherapy. Its often-complicated construction makes it an ideal candidate for MC simulation. However, the low density of the gaseous sensitive medium poses problems for MC codes

Figure 3. The ratio $D_{water}/D_{Calcium Fluoride}$ for TLD discs 0.9 mm thick, over a broad range of photon-beam qualities computed directly using the EGS4 code and compared to the two extreme idealised cavity-theory results

Reproduced from Mobit, et al. [43] with permission



that utilise the condensed-history approach for electron transport [1,4,44,45]. In CH codes the (artificial) electron step-lengths have to be made extremely short in the chamber wall and in the gas cavity itself. The PRESTA scheme (Bielajew and Rogers [46]) was specifically developed so that ion-chamber response could be correctly simulated by the EGS4 code system; PRESTA automatically adjusts step-lengths in the vicinity of interfaces. However, the Molière multiple-scattering formalism is no longer valid for such ultra-short step-lengths because they consist of too few single-scattering events. This problem effectively put a limit on ion-chamber simulation accuracy of the order of 1% for low atomic number materials [47]. Nevertheless, some impressive simulations have been carried out, e.g. Rogers [48] on parallel-plate chambers in a ^{60}Co beam; large changes in chamber response due to the inhomogeneous wall materials were demonstrated.

Recent advances in electron-transport theory [49] have enabled multiple scattering to be combined with single scattering. This will enable D_{med}/D_{air} for ion chambers to be precisely computed and hence important effects such as the finite size of the air cavity and the effect of different material(s) in the chamber walls can now be simulated with a high degree of confidence.

Monte Carlo based radiotherapy treatment planning

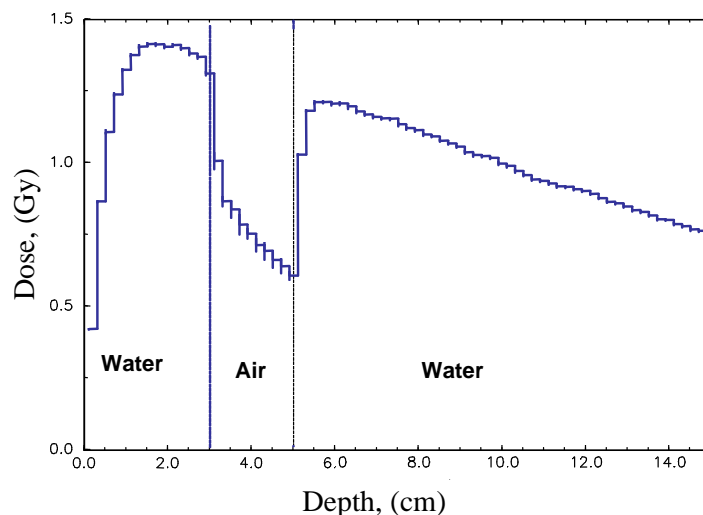
The computation of the dose distribution in the inhomogeneous “geometry” of a patient undergoing radiotherapy is an obvious candidate for MC simulation [50]. Up to the present time, most radiotherapy treatment planning systems (TPS), i.e. the software, involve algorithms of varying degrees of sophistication; these “correct” the measured distribution in a water phantom for the irregular patient skin surface, and inhomogeneities, most notably bone, air passages and cavities, and lung tissue. In high-energy (or megavoltage) X-ray beams, electron transport close to interfaces of different density is an intractable problem for any analytical method [51,52].

In the case of electron beams the failure of analytical methods (including 3-D pencil-beam convolution) to model the effect of density differences on electron scatter is even more serious than for photon beams [53]. Conformal therapy, by which is meant the modification of beam directions, apertures and possibly other properties to cause the region, in 3-D, of high-dose to conform to the shape of the target (see below) [54] causes special difficulties for analytical, i.e. non-MC, algorithms due to irregular field shapes, Multileaf Collimators, small-field stereotactic techniques and most notably due to the recent emphasis on so-called Intensity-Modulated radiotherapy (IMRT), very small beam elements, each of a different intensity, i.e. fluence rate. Such very small photon-beam fields do not exhibit charged-particle equilibrium (CPE) on the central axis [55] due to the range of secondary electrons exceeding the dimensions of the beam cross-section. Figure 4 shows what happens when a narrow photon beam crosses a broad low-density inhomogeneity: due to electron transport away from the central axis, which is uncompensated by transport towards the axis, the dose in the air region falls and there is then a re-build-up in the water beyond. The discontinuity in dose at the first water/air interface is a consequence of the water/air stopping-power ratio (this is not unity); MC always yields the absorbed dose in whatever the medium is, whereas all the current analytical methods [56] effectively yield equivalent water dose.

Figure 4. Loss of equilibrium on the central axis due to a low-density region in a narrow photon beam clearly predicted in a Monte Carlo simulation involving electron transport

Cephas Mubata, private communication

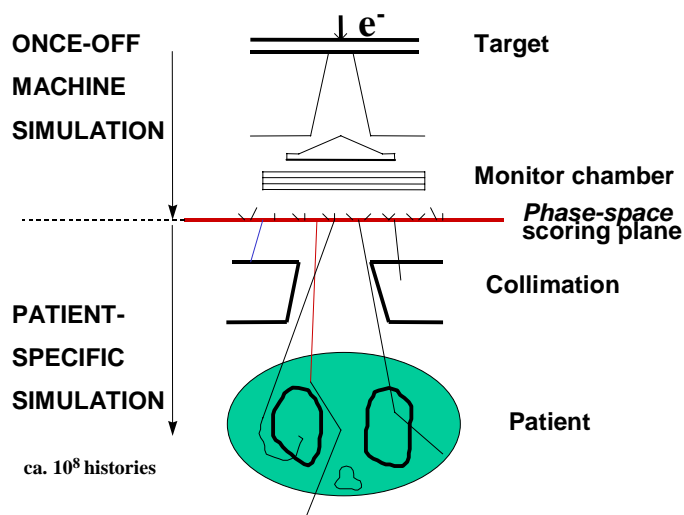
PDD curve for 6MV beam(PSD), 4x4 cm² field, Voxel size 5x5x2 mm³, for 30x30x20 cm³ phantom, accuracy: 0.6% 10⁸ histories ECUT=700MeV; using BEAM/EGS4



The only factor that has delayed the application of MC methods to the computation of dose distributions in radiotherapy is the amount of computer-processing power necessary; some 15 years ago this was estimated to be of the order of 100s of hours for a photon-beam radiotherapy treatment plan [50]. In the last five years or so, the picture has changed radically; very fast processors (which cost thousands of dollars rather than 10-100 times this) are now available – principally so-called PCs. Furthermore, there have been extensive efforts to simulate the full geometrical detail of the passage of radiation through the so-called treatment head (target, flattening filter, monitor chamber, collimating jaws, etc.) in modern linear accelerators for radiotherapy [56]. It has been demonstrated, originally by Mohan [57] for photon beams, and by Udale [58] for electron beams, that when all the detail is modelled, that one can obtain excellent agreement with measurement (in water phantoms). There is an

impressively comprehensive detailed EGS4 usercode called BEAM for the purpose of detailed treatment head modelling [56]. BEAM can produce a so-called phase-space file of co-ordinates (particle type, energy, direction, position), e.g. above the level of the devices which define the beam collimation for the particular patient undergoing treatment. The final patient-specific simulation is then (re-)started from this phase-space file [57,58]. This approach is illustrated schematically in Figure 5.

Figure 5. Schematic illustration of the two-step approach to Monte Carlo simulation in radiotherapy patient dose computation



For electron beams, run times of the order of a few minutes for 1-2% uncertainty (1σ) with a small voxel size (1-2 mm) were first demonstrated by Neuenschwander, *et al.* [60] using the macro-MC (MMC) approach [61]. In the case of megavoltage photon beams (the “bread and butter” of radiotherapy all over the world) of the order of $2-10 \times 10^8$ histories are required to fulfil the above specifications on voxel size and statistical uncertainty, essentially independent of the number of beams, (cf. $\approx 10^7$ for electrons). Through a combination of ingenious variance reduction techniques, mostly concerned with speeding up (secondary) electron transport simulation, and generally using between 10 and 30 state-of-the-art PCs in parallel, i.e. each CPU executes a certain number of histories independently of all the others, several radiotherapy physics research groups [62-68] have demonstrated that photon beam treatment plans can be calculated in acceptable runtimes of the order of an hour or less. Articles documenting essentially perfect agreement between measurements and MC simulation in both homogeneous (i.e. water) and heterogeneous phantoms (e.g. Rando standard man) irradiated by radiotherapy beams are now appearing at a rapid rate in the medical physics research journals [69,70]. This excellent agreement includes not only relative dose distributions but also absolute dose determination; the latter is often referred to, using radiotherapy jargon, in terms of monitor units (MUs) and output factors (OFs) [71,72].

Two clinical examples of Monte Carlo calculated dose distributions, shown in terms of so-called isodose lines connecting points of equal dose, and superimposed on CT sections through the patient under study, are now given in the next two figures. Figure 6 shows an electron-beam treatment plan; the effect of the inevitable statistical noise is seen as a slight unevenness in the isodoses. The extension of the irradiated volume into the low-density lung is clearly shown. Figure 7 is a dramatic illustration of the difference between calculated dose distributions for a narrow photon beam, incident here on the extremely heterogeneous anatomy of the head and neck region; in the figure on the left we see the smooth dose isodoses produced by the so-called pencil-beam algorithm, widely employed in

Figure 6. Electron beam treatment plan in the lung with the dose distribution shown as isodose lines

16 MeV beam; $10 \times 10 \text{ cm}^2$ field, calculated with EGS4/BEAM using full phase-space data from Varian 2100C linear accelerator; $5 \times 5 \times 5 \text{ mm}$ scoring voxels, 2×10^6 histories, CPU time 16 min. on DEC 500 MHz, uncertainty (1σ) 1.5%

Cephas Mubata, private communication

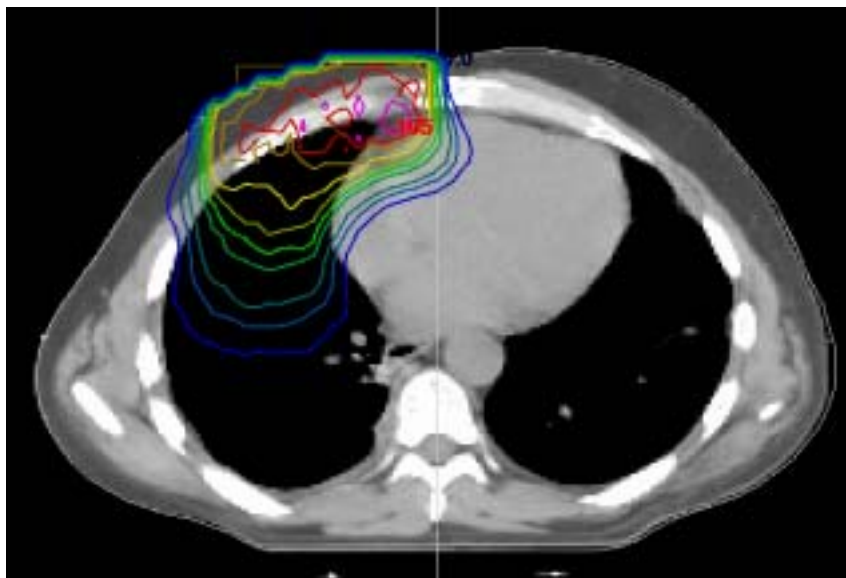
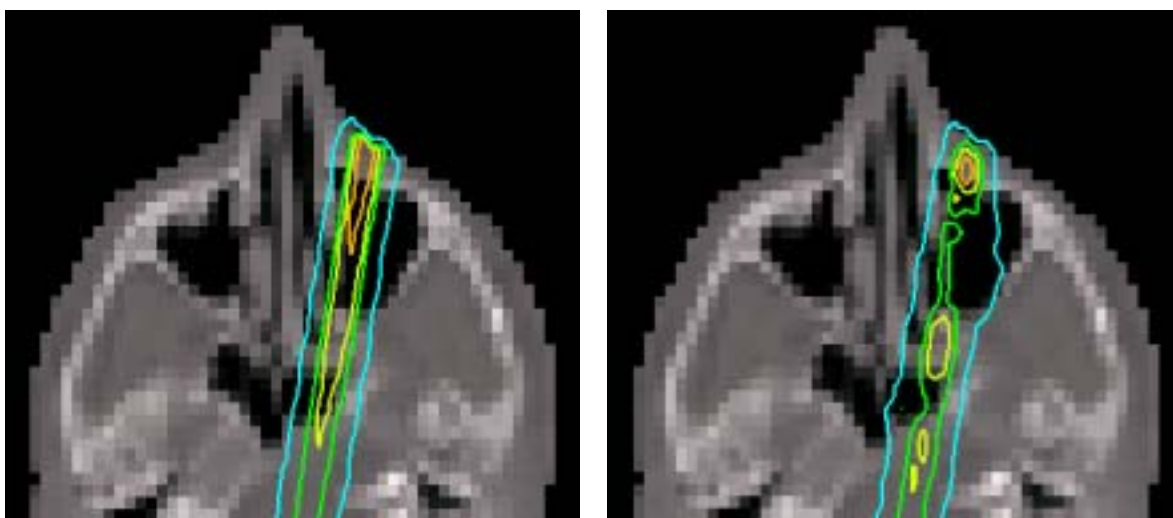


Figure 7. A narrow (megavoltage) photon beam incident on the anatomy in the head (represented by a computer tomograph image)

Left: doses computed using a pencil-beam algorithm, right: Monte Carlo simulation

Charlie Ma, private communication



commercial radiotherapy treatment planning systems (TPS), whereas on the right the true behaviour of such a narrow photon beam in heterogeneous terrain is displayed. In fact, it is precisely such grossly distorted dose distributions that comprise the input of so-called inverse planning algorithms which are used to deduce the fluence-profile modulation patterns subsequently delivered in the IM radiotherapy technique. Fortunately this extremely unsatisfactory situation is about to change as a result of the fact

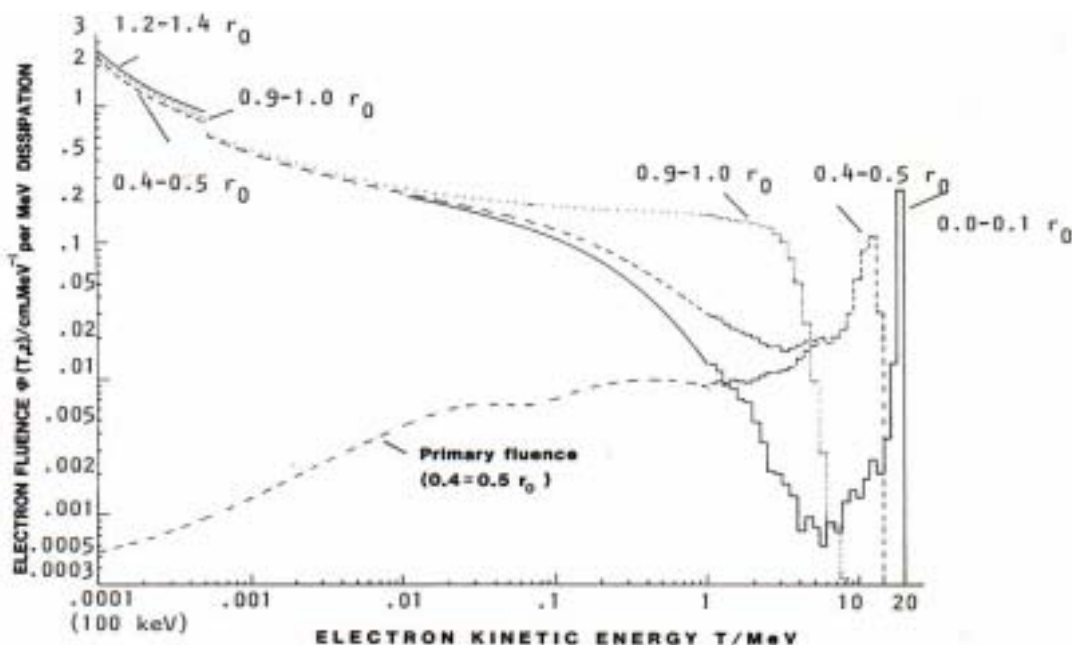
that several companies are implementing Monte Carlo simulation into their patient dose calculation systems and, very significantly, also adapting MC to model today's increasingly complex treatment delivery techniques, e.g. using MLCs to shape fields to the tumour shape and to modulate the fluence across the beam to reduce the irradiation of so-called organs at risk.

Will it be possible to prove that the increased accuracy of patient dose computation via Monte Carlo influences the clinical outcome of radiotherapy? The rapidly developing subject of so-called Biological Modelling, i.e. the estimation of the probability of tumour (local) control (TCP) and of the probability of complications (unwanted side effects) to normal tissue (NTCP) using the detailed dose distribution in the tumour and the organs-at-risk [73-75] is furnishing us with this possibility.

Track-structure aspects

Have (condensed history) MC codes also led to contributions to the microdosimetry/track structure field? Before specialised microdosimetric detectors (e.g. [76]) were developed, biological differences between different radiation qualities were analysed in terms of so-called LET distributions, which could subsequently be computed directly from the electron fluence spectra calculated by MC codes [21,77]. A clear contribution to the understanding of biological effects is the demonstration that the electron fluence spectrum, $(d\Phi/dE)$, at low electron energies, normalised to unit absorbed dose, is virtually independent of incident particle energy or depth. Figure 8 shows this depth-independence for a 20-MeV electron beam in water at various depths.

Figure 8. Electron fluence per unit dose, differential in energy, at different depths in a 20-MeV electron beam in water computed by a Monte Carlo CH code [21]



In the 1960s before the use of megavoltage electron beams for radiotherapy was established, there was considerable uncertainty about the relative clinical, i.e. biological or cell-killing, effectiveness of this new therapy modality. Cell irradiation experiments indicated that high-energy electrons had a relative biological effectiveness (RBE) close to unity, i.e. the same as Cobalt-60 or high-energy

X-rays; furthermore, there was no indication either of any significant variation of RBE with depth. The number of low-energy electrons (per unit absorbed dose in water) for all of these radiation qualities, as computed by C-H MC codes, was virtually identical. For so-called conventional (i.e. kilovoltage) X-ray beams, however, this number was slightly greater, which is consistent with their slightly higher RBE. All the above findings are consistent with assuming that the biological effectiveness (of so-called low-LET radiation) is basically due to the number of low-energy electrons (per unit dose); it is these electrons which have relatively high values of stopping power, i.e. high density of ionisations (and excitations) along their tracks and it is energy transferred in this way which is believed to cause almost all the cell killing, through DNA double-strand breaks in the cell nucleus [78]. However, for information on the detailed electron track structure at very small length scales, such as that of the DNA in cell nuclei, event-by-event charged-particle codes [6-8] take over from ones based on the condensed history approach.

Monte Carlo simulation of radiation transport has also played an essential role not only in radiotherapy with external beams but also in several other branches of bio-medical physics, e.g. in imaging and therapy in so-called nuclear medicine (i.e. unsealed sources of radioisotopes administered to the patient) [79-81], and imaging generally with ionising radiation, principally kilovoltage X-ray beams [82]. It is to be hoped, however, that the ever-decreasing cost of the ever-increasing processing speed of computer hardware will not discourage scientists from applying their brains and creativity to making MC radiation transport simulation more efficient [83]; otherwise the brilliant, pioneering work of Martin Berger [10] in developing the condensed history approach to charged-particle Monte Carlo may never be rivalled. Perhaps, ironically, the very fact that processing speed per Euro increases by a factor of 2 to 3 per year, instead of, say, by 10 or more, will still give Professor Berger a chance of the Nobel prize for what will come to be seen as his essential contribution to the improvement of the well-being of our species through increased rates of cancer cure by radiation therapy.

Acknowledgements

I wish to acknowledge the financial support of professors Alan Pollack and Charlie Ma, Radiation Oncology Department, Fox-Chase Cancer Center, during the writing of this review.

REFERENCES

- [1] Bielajew, A.F., D.W.O. Rogers and A.E. Nahum, "Monte Carlo Simulation of Ion Chamber Response to ^{60}Co – Resolution of Anomalies Associated with Interfaces", *Phys. Med. Biol.*, 30, 419-28 (1985).
- [2] Nahum, A.E., "Simulation of Dosimeter Response and Interface Effects", in T.M. Jenkins, W.R. Nelson, A. Rindi, A.E. Nahum, D.W.O. Rogers (eds.), *Monte Carlo Transport of Electrons and Photons*, New York, Plenum, pp. 523-43 (1988).
- [3] Rogers, D.W.O., "How Accurately can EGS4/PRESTA Calculate Ion-chamber Response?", *Med. Phys.*, 20, 319-23 (1993).

- [4] Foote, B.J. and V.G. Smyth, “The Modeling of Electron Multiple-scattering in EGS4/PRESTA and its Effect on Ionization-chamber Response”, *Nucl. Instr. Meth.*, B100, 22-30 (1995).
- [5] Kawrakow, I. and A.F. Bielajew, “On the Condensed History Technique for Electron Transport”, *Nucl. Instr. Meth.*, 142B, 253-280 (1998).
- [6] Ito, A., “Electron Track Simulation for Microdosimetry”, in T.M. Jenkins, W.R. Nelson, A. Rindi, A.E. Nahum, D.W.O. Rogers (eds.), *Monte Carlo Transport of Electrons and Photons*, New York, Plenum, pp. 485-501 (1988).
- [7] Nikjoo, H., D.T. Goodhead, D.E. Charlton, H.G. Paretzke, “Energy Deposition in Small Cylindrical Targets by Ultrasoft X-rays”, *Phys. Med. Biol.*, 34, 691-705 (1989).
- [8] Nikjoo, H., D.T. Goodhead, D.E. Charlton, H.G. Paretzke, “Energy Deposition in Small Cylindrical Targets by Monoenergetic Electrons”, *Int. J. Radiat. Biol.*, 60, 739-56 (1991).
- [9] Stewart, R.D., W.E. Wilson, J.C. McDonald and D.J. Strom, “Microdosimetric Properties of Ionizing Electrons in Water: A Test of the PENELOPE Code System”, *Phys. Med. Biol.*, 47, 79-88 (2002).
- [10] Berger, M.J., “Monte Carlo Calculation of the Penetration and Diffusion of Fast Charged Particles”, in *Methods in Computational Physics*, Vol. I, New York, Academic Press, pp. 135-215 (1963).
- [11] Andreo, P., “Monte Carlo Simulation of Electron Transport. I. Principles and Some General Results”, in A.E. Nahum (ed.), *The Computation of Dose Distributions in Electron Beam Radiotherapy*, University of Umeå, Sweden, pp. 80-97 (1985).
- [12] Salvat, F., J.M. Fernández-Varea, J. Sempau and J. Mazurier, “Practical Aspects of Monte Carlo Simulation of Charged Particle Transport: Mixed Algorithms and Variance Reduction Techniques”, *Radiat. Environ. Biophys.*, 38, 15-22 (1999).
- [13] Nelson, W.R., H. Hirayama and D.W.O. Rogers, “The EGS4 Code System”, Stanford Linear Accelerator Center, Report SLAC-265, Stanford, CA (1985).
- [14] Briesmeister, J.F., “MCNP – A General Monte Carlo N-particle Transport Code”, Los Alamos National Laboratory, Report LA-12625-M, Los Alamos, NM (1993).
- [15] Mackie, T.R., “Applications of the Monte Carlo Method in Radiotherapy”, in K.R. Kase, B.E. Bjärngard and F.H. Attix (eds.), *The Dosimetry of Ionizing Radiation*, Vol III, San Diego, Academic Press, pp. 541-620 (1990).
- [16] Rogers, D.W.O., A.F. Bielajew, “Monte Carlo Techniques of Electron and Photon Transport for Radiation Dosimetry”, in K.R. Kase, B.E. Bjärngard and F.H. Attix (eds.), *The Dosimetry of Ionizing Radiation*, Vol. III, San Diego, Academic Press, pp. 427-539 (1990).
- [17] Andreo, P., “Monte Carlo Techniques in Medical Radiation Physics”, *Phys. Med. Biol.*, 36 861-920 (1991).
- [18] Halblieb, J., “Structure and Operation of the ITS Code System”, in T.M. Jenkins, W.R. Nelson, A. Rindi, A.E. Nahum and D.W.O. Rogers (eds.), *Monte Carlo Transport of Electrons and Photons Below 50 MeV*, New York, Plenum, pp. 249-262 (1988).

- [19] Seltzer, S.M., “An Overview of ETRAN Monte Carlo Methods”, in T.M. Jenkins, W.R. Nelson, A. Rindi, A.E. Nahum and D.W.O. Rogers (eds.), *Monte Carlo Transport of Electrons and Photons Below 50 MeV*, New York, Plenum, pp. 153-182 (1988).
- [20] Seltzer, S.M., “Electron-photon Monte Carlo Calculations: The ETRAN Code”, *Appl. Radiat. Isot.*, 42, 917-35 (1991).
- [21] Nahum, A.E., “Calculations of Electron Flux Spectra in Water Irradiated with Megavoltage Electron and Photon Beams with Applications to Dosimetry”, PhD thesis, University of Edinburgh, UK, University Microfilms International, Ann Arbor, MI, order no. 77-70006 (1976).
- [22] Andreo, P., “Aplicacion del metodo de monte carlo a la penetracion y dosimetria de haces de electrones”, PhD thesis, University of Zaragoza (1981).
- [23] Andreo, P. and A. Brahme, “Restricted Energy-loss Straggling and Multiple Scattering of Electrons in Mixed Monte-Carlo Procedures”, *Radiat. Res.*, 100, 16ff (1984).
- [24] Chibani, O., “Energy-loss Straggling Algorithms for Monte Carlo Electron Transport”, *Med. Phys.*, 29, 2374-83 (2002).
- [25] Berger, M.J., *Proton Monte Carlo Transport Program PTRAN*, National Institute for Standards and Technology (NIST), Report NISTIR 5113, Gaithersburg (1993).
- [26] A.E. Nahum, D.P. Dearnaley and G.G. Steel, “Prospects for Proton-beam Radiotherapy”, *European Journal of Cancer*, 30A, 1577-1583 (1994).
- [27] Medin, J., “Studies of Clinical Proton Dosimetry Using Monte Carlo Simulation and Experimental Techniques”, PhD thesis, University of Stockholm, ISBN 91-7153-572-1 (1997).
- [28] Nahum, A.E., “Perturbation Effects in Dosimetry, Part I. Kilovoltage X-rays and Electrons”, *Phys. Med. Biol.*, 41, 1531-80 (1996).
- [29] Nahum, A.E., “Water/Air Mass Stopping-power Ratios for Megavoltage Photon and Electron Beams”, *Phys. Med. Biol.*, 23, 24-38 (1978).
- [30] Andreo, P., “Stopping-power Ratios for Dosimetry”, in T.M. Jenkins, W.R. Nelson, A. Rindi, A.E. Nahum, D.W.O. Rogers (eds.), *Monte Carlo Transport of Electrons and Photons*, Plenum, New York, pp. 485-501 (1988).
- [31] Andreo, P., “Depth-dose and Stopping-power Data for Mono-energetic Electron Beams”, *Nucl. Instr. Meth.*, B51, 107-21 (1990).
- [32] Knight, R.T., *Absorbed Dose Conversion Factors Therapeutic Kilovoltage and Megavoltage X-ray Beams Calculated by the Monte Carlo Method*, PhD thesis, University of London, Report ICR-PHYS-1/96, available from Joint Dept. of Physics, Royal Marsden NHS Trust, Sutton SM2 5PT, UK (1996).
- [33] Klevenhagen, S.C., R.J. Aukett, R.M. Harrison, C. Moretti, A.E. Nahum, K.E. Rosser, “The IPEMB Code of Practice for the Determination of Absorbed Dose for X-rays Below 300 kV Generating Potential (0.035 mm Al-4 mm Cu HVL; 10-300 kV Generating Potential)”, *Phys. Med. Biol.*, 41, 2605-25 (1996).

- [34] Thwaites, D.I., D.T. Burns, S.C. Klevenhagen, A.E. Nahum, W.G. Pitchford, “The IPEMB Code of Practice for Electron Dosimetry for Radiotherapy Beams of Initial Energy from 2 to 50 MeV Based on an Air Kerma Calibration”, *Phys. Med. Biol.*, 41, 2557-603 (1996).
- [35] International Atomic Energy Agency (IAEA), *Absorbed Dose Determination in Photon and Electron Beams: An International Code of Practice*, H. Svensson, P. Andreo, J.R. Cunningham, K. Hohlfeld (eds.), TRS No. 277, Vienna (1987).
- [36] IAEA, *The Use of Plane-parallel Ionization Chambers in High-energy Electron and Photon Beams: An International Code of Practice*, P. Andreo, P.R. Almond, O. Mattsson, A.E. Nahum, M. Roos (eds.), TRS No. 381, Vienna (1997).
- [37] IAEA, *Absorbed Dose Determination in External Beam Radiotherapy: An International Code of Practice Based on Standards of Absorbed Dose to Water*, P. Andreo, P.R. Almond, O. Mattsson, A.E. Nahum, M. Roos (eds.), TRS No. 398, Vienna (2000).
- [38] Medin, J. and P. Andreo, “Monte Carlo Calculated Stopping-power Ratios, Water/Air, for Clinical Proton Dosimetry (50-250 MeV)”, *Phys. Med. Biol.*, 42, 89-105 (1997).
- [39] Ma, C-M. and A.E. Nahum, “Bragg-Gray Theory and Ion Chamber Dosimetry for Photon Beams”, *Phys. Med. Biol.*, 36, 413-28 (1991).
- [40] Ma C-M., *Monte Carlo Simulation of Dosimeter Response Using Transputers*, PhD thesis, University of London, Report ICR-PHYS-1/92, available from Joint Dept. of Physics, Royal Marsden NHS Trust, Sutton SM2 5PT, UK (1992).
- [41] Ma, C-M. and A.E. Nahum, “Effect of the Size and Composition of the Central Electrode on the Response of Cylindrical Ionisation Chambers in High-energy Photon and Electron Beams”, *Phys. Med. Biol.*, 38, 267-90 (1993).
- [42] Mobit, P.N., *Monte Carlo and Experimental Studies of Dose Measurements in Radiotherapy Beams with LiF-TLDs and Other Solid State Dosimeters*, PhD thesis, University of London Report ICR-PHYS-2/96, available from Joint Dept. of Physics, Royal Marsden NHS Trust, Sutton SM2 5PT, UK (1996).
- [43] Mobit, P.N., A.E. Nahum and P. Mayles, “A Monte Carlo Study of the Quality Dependence of Common TLD Materials in Photon and Electron Beams”, *Phys. Med. Biol.*, 43, 2015-32 (1998).
- [44] Rogers, D.W.O., A.F. Bielajew, A.E. Nahum, “Ion Chamber Response and A_{wall} Correction Factors in a ^{60}Co Beam by Monte Carlo Simulation”, *Phys. Med. Biol.*, 30, 429-43 (1985).
- [45] Nahum, A.E., “Simulation of Dosimeter Response and Interface Effects”, in T.M. Jenkins, W.R. Nelson, A. Rindi, A.E. Nahum and D.W.O. Rogers (eds.), *Monte Carlo Transport of Electrons and Photons Below 50 MeV*, New York, Plenum, pp. 523-547 (1988).
- [46] Bielajew, A.F. and D.W.O. Rogers, “PRESTA – The Parameter Reduced Electron-step Algorithm for Electron Monte Carlo Transport”, *Nucl. Instr. Meth.*, B18, 165-81 (1987).
- [47] Rogers, D.W.O., “How Accurately can EGS4/PRESTA Calculate Ion-chamber Response?”, *Med. Phys.*, 20, 319-23 (1993).

- [48] Rogers, D.W.O., “Calibration of Parallel-plate Chambers: Resolution of Several Problems by Using Monte Carlo Calculations”, *Med. Phys.*, 19, 889ff (1992).
- [49] Kawrakow, I. and A.F. Bielajew, “On the Condensed History Technique for Electron Transport”, *Nucl. Instr. Meth.*, 142B, 253-280 (1998).
- [50] Nahum, A.E., “Overview of Photon and Electron Monte Carlo”, in T.M. Jenkins, W.R. Nelson, A. Rindi, A.E. Nahum, D.W.O. Rogers (eds.), *Monte Carlo Transport of Electrons and Photons Below 50 MeV*, New York, Plenum, pp. 3-20 (1988).
- [51] Mohan, R., “Why Monte Carlo?” *Proceedings of the XIIth International Conference on the Use of Computers in Radiation Therapy*, Salt Lake City, Utah, 27-30 May 1997, pp. 16-18 (1997).
- [52] Bielajew, A.F., “Monte Carlo Modelling in External Electron Beam Radiotherapy – Why Leave it to Chance?”, *Proceedings of the XIth International Conference on the Use of Computers in Radiation Therapy*, Manchester, 20-24 March 1994, A.R. Hounsell, J.M. Wilkinson and P.C. Williams (eds.), pp. 2-5 (1994).
- [53] Mackie, T.R., P.J. Reckwerdt, C.M. Wells, *et al.*, “The OMEGA Project: Comparison among EGS4 Electron Beam Simulations, 3-D Fermi-Eyges Calculations, and Dose Measurements”, *Proceedings of the XIth International Conference on the Use of Computers in Radiation Therapy*, Manchester, 20-24 March 1994, A.R. Hounsell, J.M. Wilkinson, P.C. Williams (eds.), pp. 152-153 (1994).
- [54] Tait, D.M., A.E. Nahum, “Conformal Therapy and its Applications in Clinical Radiotherapy”, in J.S. Tobias, P.R.M. Thomas (eds.), *Current Radiation Oncology*, Vol. 1, Sevenoaks, UK, Edward Arnold, pp. 51-68 (1994).
- [55] Solberg, T.D., F.E. Holly, A.A.F. De Salles, *et al.*, “Implications of Tissue Heterogeneity for Radiosurgery in Head and Neck Tumors”, *Int. J. Radiat. Oncol. Biol. Phys.*, 32, 235-239 (1995).
- [56] Siebers, J.V., P.J. Keall, A.E. Nahum and R. Mohan, “Converting Absorbed Dose to Medium to Absorbed Dose to Water for Monte Carlo Based Photon Beam Dose Calculations”, *Physics in Medicine and Biology*, 45, 983-995 (2000).
- [57] Rogers, D.W.O., B.A. Faddegon, G.X. Ding, *et al.*, “BEAM: A Monte Carlo Code to Simulate Radiotherapy Treatment Units”, *Med. Phys.*, 22, 503-24 (1995).
- [58] Mohan, R., “Monte Carlo Simulation of Radiation Treatment Machine Heads”, in T.M. Jenkins, W.R. Nelson, A. Rindi, A.E. Nahum, D.W.O. Rogers (eds.), *Monte Carlo Transport of Electrons and Photons below 50 MeV*, New York, Plenum, pp. 453-468 (1988).
- [59] Udale, M., “A Monte Carlo Investigation of Surface Doses for Broad Electron Beams”, *Phys. Med. Biol.*, 33, 939-54 (1988).
- [60] Hartmann Siantar, C.L., P.M. Bergström, W.P. Chandler, “Validation and Clinical Implementation of the PEREGRINE Monte Carlo Dose Calculation System for Photon Beam Therapy”, *Proc. of World Congress on Medical Physics and Biomedical Engineering*, Part 2, Nice, p. 1102 (1997).

- [61] DeMarco, J.J., T.D. Solberg and J.B. Smathers, "A CT-based Monte Carlo Simulation Tool for Dosimetry Planning and Analysis", *Med. Phys.*, 25, 1-11 (1998).
- [62] Neuenschwander, H., W. Volken, C. Cris, *et al.*, "Fast Monte Carlo Algorithms for Electron Beam Treatment Planning", *Proceedings of the XIIth International Conference on the Use of Computers in Radiation Therapy*, Salt Lake City, Utah, 27-30 May 1997, pp. 23-26 (1997).
- [63] Neuenschwander, H. and E.J. Born, "A Macro Monte Carlo Method for Electron Beam Dose Calculations", *Phys. Med. Biol.*, 37, 107-25 (1992).
- [64] Mubata, C.D., A.E. Nahum, I. Rosenberg and A.F. Bielajew, "Parameter Study for Optimizing Monte-Carlo Simulation in External-beam Treatment Planning", Abstract PO-87, *Med. Phys.*, 25, A185 (1998).
- [65] Wang, L., C-S. Chui and M. Lovelock, "A Patient-specific Monte Carlo Dose-calculation Method for Photon Beams", *Med. Phys.*, 25, 867-78 (1998).
- [66] Sempau, J., S.J. Wilderman and A.F. Bielajew, "DPM, a Fast, Accurate Monte Carlo Code Optimised for Photon and Electron Radiotherapy Treatment Planning Dose Calculations", *Phys. Med. Biol.*, 45, 2263-91 (2000).
- [67] Li, J.S., T. Pawlicki, J. Deng, S.B. Jiang, E. Mok and C-M. Ma, "Validation of a Monte Carlo Dose Calculation Tool for Radiotherapy Treatment Planning", *Phys. Med. Biol.*, 45, 2969-85 (2000).
- [68] Kawrakow, I., M. Fippel, K. Friedrich, "3-D Electron Dose Calculation using a Voxel-based Monte Carlo Algorithm", *Phys. Med. Biol.*, 23, 445-57 (1996).
- [69] Wang, L., E. Yorke and C-S. Chui, "Monte Carlo Evaluation of Tissue Inhomogeneity Effects in the Treatment of the Head and Neck", *Int. J. Radiat. Oncol. Biol. Phys.*, 50, 1339-49 (2001).
- [70] Wang, L., M. Lovelock and C-S. Chui, "Experimental Verification of a CT-based Monte Carlo Dose-calculation Method in Heterogeneous Phantoms", *Med. Phys.*, 26, 2626-34 (1999).
- [71] Kapur, A., C-M. Ma, E.C. Mok, *et al.*, "Monte Carlo Calculations of Electron Beam Output Factors for a Medical Linear Accelerator", *Phys. Med. Biol.*, 43, 3479-94 (1998).
- [72] Verhaegen, F., C. Mubata, J. Pettingell, A.M. Bidmead, I. Rosenberg, D. Mockridge and A.E. Nahum, "Monte Carlo Calculation of Output Factors for Circular, Rectangular, and Square Fields of Electron Accelerators (6-20 MeV)", *Medical Physics*, 28, 938-949 (2001).
- [73] Cattaneo, G.M., G. Gagliardi and A.E. Nahum (eds.), "The Practical Use of TCP and NTCP Models for the Evaluation of Treatment Plans in Radiotherapy", *Physica Medica*, Vol. XVII, Supplement 2 (2001).
- [74] Nahum, A.E. and B. Sanchez-Nieto, "Tumour Control Probability Modelling: Basic Principles and Applications in Treatment Planning", *Physica Medica*, 17, Suppl. 2, 13-23 (2001).
- [75] Buffa, F.M. and A.E. Nahum, "Monte-Carlo Dose Calculations and Radiobiological Modelling: Analysis of the Effect of the Statistical Noise of the Dose Distribution on the Probability of Tumour Control", *Physics in Medicine and Biology*, 45, 3009-23 (2000).

- [76] Paretzke, H.G., “Radiation Track Structure Theory”, in G.R. Freedman (ed.), *Kinetics of Nonhomogeneous Processes*, New York, Wiley, pp. 89-170 (1987).
- [77] Nahum, A.E., H. Svensson and A. Brahme, “The Ferrous Sulphate G-value for Electron and Photon Beams: A Semi-empirical Analysis and its Experimental Support”, *Proceedings of the 7th Symposium on Microdosimetry*, Booz, Ebert and Hartfield (eds.), Oxford, 8-12 Sept. 1980, Harwood Academic Publishers, pp. 841-852 (1981)
- [78] J.D. Chapman, “The Single-hit Mechanism of Tumor Cell Killing by Radiation”, *Int. J. Radiat. Biol.*, in press 2002.
- [79] Zaidi, H. and G. Sgouros (eds.) *Therapeutic Applications of Monte Carlo Calculations in Nuclear Medicine*, Bristol and Philadelphia, Institute of Physics Publishing (2003).
- [80] Zaidi, H. and P. Andreo, “Monte Carlo Techniques in Nuclear Medicine Dosimetry”, in H. Zaidi and G. Sgouros (eds.), *Therapeutic Applications of Monte Carlo Calculations in Nuclear Medicine*, Bristol and Philadelphia, Institute of Physics Publishing, pp. 28-54 (2003).
- [81] Del Guerra, A., G. Di Domenico and D. Mukhopadhyay, “PET Dosimetry in Proton Radiotherapy: A Monte Carlo Study”, *Appl. Radiat. Isot.*, 18, 1617-24 (1997).
- [82] Flampouri, S., P.M. Evans, F. Verhaegen, A.E. Nahum, E. Spezi and M. Partridge, “Optimization of Accelerator Target and Detector for Portal Imaging Using Monte Carlo Simulation and Experiment”, *Physics in Medicine and Biology*, 47, 3331-3349 (2002).
- [83] Deasy, J.O., M.V. Wickerhauser and M. Picard, “Accelerating Monte Carlo Simulations of Radiation Therapy Dose Distributions Using Wavelet Threshold De-noising”, *Med. Phys.*, 29, 2366-73 (2002).

FROM ION TRACKS TO ION RADIOTHERAPY

**M. Krämer, B. Bathelt, C. Brusasco, O. Geiss, T. Haberer,
E. Rietzel, D. Schardt, M. Scholz, U. Weber**
Gesellschaft für Schwerionenforschung, Germany

O. Jäkel
Deutsches Krebsforschungszentrum, Germany

Abstract

This contribution describes the application of swift ion beams in cancer radiotherapy. We start with a discussion of the rationale for choosing light ions over protons or photons. We shortly describe the microscopic simulation of ion interaction with matter with the TRAX Monte Carlo code. The GSI radiotherapy pilot project uses a magnetic raster scanner and active energy variation to achieve dose conformation in 3-D. We describe the necessary steps for treatment planning such as beam modelling, absorbed dose and biological effectiveness calculation, dose optimisation and verification, as implemented in our TRiP98 treatment planning code.

Introduction

One of the main objectives in radiotherapy is the conformal delivery of the prescribed dose to the target volume, whereas the surrounding healthy tissue and critical structures should be spared as much as possible. In comparison with conventional photon beams, therapeutic ion beams in general offer the advantage of a depth dose distribution with a pronounced maximum (Bragg maximum) and a sharp dose fall-off at large penetration depth, in contrast to the exponential dose deposition of photons or neutrons, or the broad maximum generated by electrons. This is also known as inverted dose profile and it allows a higher degree of dose conformation to the target volume. Heavier ions like ^{12}C offer further advantages over protons or other lighter charged particles. First, the lateral scattering in tissue is reduced roughly by a factor of 3. Second, carbon ions possess an increased relative biological effectiveness (RBE), especially in the stopping region at the Bragg peak. These particular properties make carbon ion beams an ideal candidate to be combined with the evolving techniques of intensity modulated radiotherapy (IMRT).

Microdosimetric calculations

In order to gain some insight on the ion interaction at the microscopic scale, i.e. cell nucleus or DNA level, *ab initio* Monte Carlo computations are needed, for example with our TRAX code [1,2]. It simulates ionisation, excitation and elastic scattering events for both the primary ions as well as the subsequently emitted (δ -) electrons and their secondaries. Due to the small scale (micro- or nanometers) and the low electron energies involved (mostly of the order of 100 eV or below) the calculations must be performed on a single interaction basis, rather than condensed random walk. As an example Figure 1 shows a comparison of proton and carbon ion tracks for various initial energies. The comparison with the inserted DNA gives an idea about the effectiveness of carbon ions versus protons.

An important quantity in microdosimetry is the radial dose distribution around an ion path. Figure 2 shows a comparison of experimental data (obtained with tissue-equivalent gas but scaled to the density of liquid water) for oxygen ions with various calculations.

One may now be tempted to use this *ab initio* Monte Carlo method to calculate both absorbed as well as biologically equivalent dose on a macroscopic scale, i.e. a patient plan based on computer tomography. Unfortunately, this does not appear to be feasible at present [3]. For the absorbed dose there are two obstacles. The first one is the immense amount of CPU time which would be required for each patient plan. The second, more serious one is the lack of accurate basic interaction cross-sections. For biological effects the knowledge of the ionisation or energy deposition pattern alone is not enough. Chemical conditions and repair capacity play an important role for the biological effect. A pragmatic approach to solve the task of RBE calculation is the Local Effect Model shortly described in a later section. It uses the microscopic spatial energy distribution as obtained from codes like TRAX, but relies on empirical dose-effect curves for photon radiation to determine the biological endpoint.

Radiotherapy at GSI

In December 1997 an experimental heavy-ion radiotherapy facility became operational at the German heavy-ion research centre *Gesellschaft für Schwerionenforschung* (GSI), Darmstadt. The aim is to investigate the clinical impact of the unique properties of heavy ions and to show which patients can benefit from such a therapy.

Figure 1. Paths of electron created by various ions, as simulated by the TRAX code

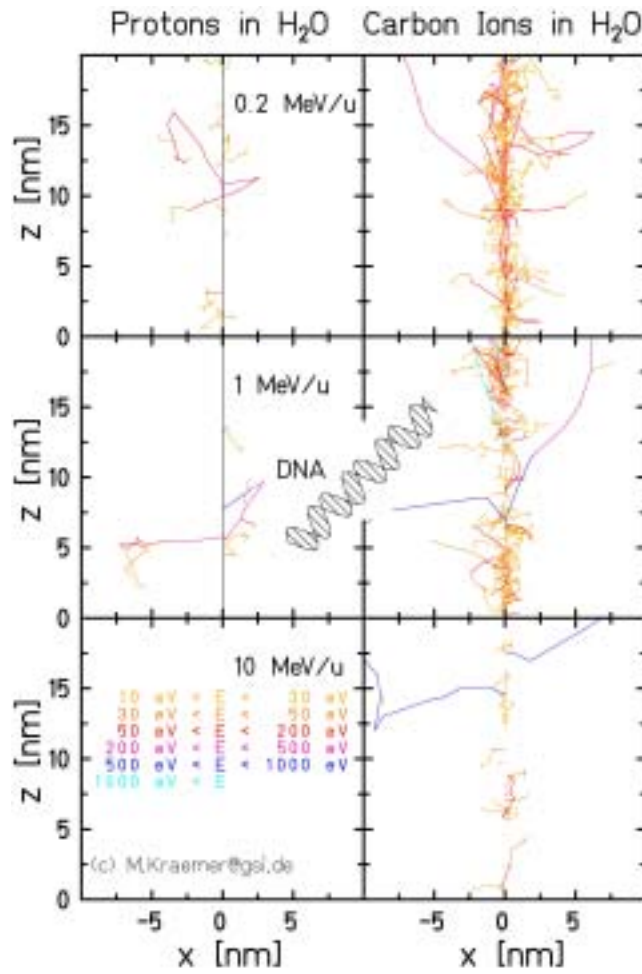
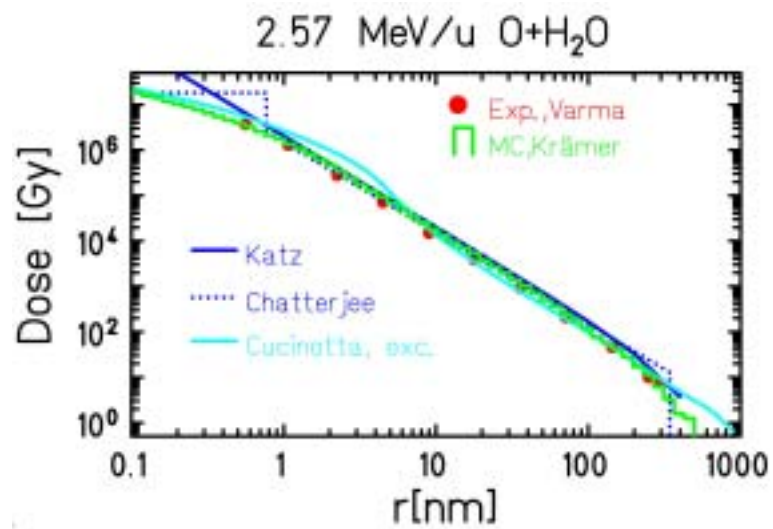


Figure 2. Radial dose distribution around an oxygen ion

Symbols are gas measurements, the MC histogram is obtained with TRAX

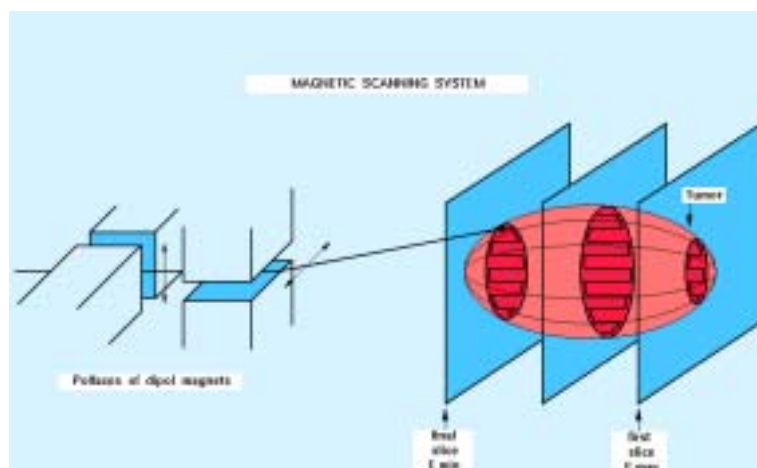


The GSI facility realises for the first time a combination of an active field shaping, using a scanned beam [4], with an active energy variation of the beam, thus making full use of the advantages of heavy charged particles for therapy. This novel irradiation technique requires a method for dose calculation and optimisation which is radically different from conventional approaches used for example in photon and even proton therapy, due to the strong dependence of the RBE on particle charge, energy and absorbed dose. A prerequisite is the development of a physical beam model as well as a radiobiological model to describe the interactions of ion beams with biological material.

Beam delivery system

The general design idea is to use completely active volume scanning in three dimensions. This can be achieved by magnetic deflection of the ^{12}C beam in lateral direction (intensity-controlled raster scan [4]) and by energy variation of the GSI synchrotron to cover different depths in order to spread out the dose across the target volume. Figure 3 shows a schematic overview. In order to match the needs of radiotherapy the accelerator control system was modified to allow selection of the energy, beam spot size and intensity level of the ^{12}C beam from one synchrotron cycle to the next [5]. A list of 253 energies has been set up in order to achieve a constant spacing of the corresponding ranges in water. This is important to obtain a homogenous depth dose distribution. The energy range is between 80 MeV/u and 430 MeV/u corresponding to a range in tissue between 20 mm and 330 mm, respectively. The ion energy can be switched within ≈ 5 seconds and thus different depths can be reached without the need of additional absorbers. This way the target region is divided into subsequent slices corresponding to beams of different energies. A large tumour may require up to 50 000 different beam positions.

Figure 3. Schematic view of the magnetic scanning system



Requirements for treatment planning

For photon beams numerous commercial and research prototype software packages exist. For heavy ions commercial treatment planning systems do not exist. We thus decided to couple an existing conventional radiotherapy planning system (Voxelplan, developed at the German Cancer Research Centre, DKFZ [6]) with a newly developed code from GSI (TRiP, Treatment planning for Particles [7]). Voxelplan covers the conventional tasks of graphics rendering and user interface, whereas TRiP handles all physical and radiobiological aspects of heavy ions, including dose optimisation.

Treatment planning for scanned heavy-ion beams starts just like conventional planning, that is, imaging devices such as magnetic resonance (MR) and computer tomography (CT) are used to generate a digital model of the irradiation region. While MR images deliver high-resolution information on tumour location and critical structures, the CT data are mandatory for dose computation and optimisation.

The main task of treatment planning for scanned ion beams is to determine the different particle fluence values for all beam energy slices and beam positions. This is best achieved by applying a pencil model (rather than Monte Carlo) for the individual beams and by using inverse planning methods to obtain the desired values automatically from the prescribed dose distribution.

Physical beam model

The beam model we use so far is based on the fact that for ion beams as heavy as ^{12}C the multiple elastic scattering plays only a minor role. The light fragments, which are generated while a heavy ion traverses matter, will experience larger deflections. However, since they contribute only a small amount to the overall dose, their multiple scattering is neglected as well in first order.

Under these assumptions the (partial) dose generated by a single heavy-ion beam with energy E_{beam} can be described as:

$$D(E_{\text{beam}}, \vec{x})[\text{Gy}] = 1.6 \times 10^{-8} \times d(E_{\text{beam}}, z) \left[\frac{\text{MeV}}{\text{gcm}^{-2}} \right] \times \frac{N}{2\pi\sigma^2 [\text{mm}^2]} \exp\left(-\frac{1}{2} \frac{r^2}{\sigma^2}\right) \quad (1)$$

where r is the distance from the beam centre, σ is the actual width (variance) of the Gaussian beam profile and N is the total number of particles. The most important quantity, however, is the energy loss distribution $d(E_{\text{beam}}, z)$, for a given initial beam energy, E_{beam} , as a function of penetration depth, z , which has to be described by an appropriate model. Such a model has to include not only the single particle energy loss, but also the energy loss straggling and the process of projectile fragmentation in order to reproduce experimentally determined dose profiles with sufficient accuracy [8]. For the sake of brevity we will not describe the model in detail, we refer to [7] instead.

For practical use in therapy planning it is sufficient to calculate the depth dose profiles in steps of 10 MeV/u initial beam energy from 50 to 500 MeV/u. The profiles are calculated only once and then stored as tables. The fragment spectra $dN(E_{\text{beam}}, z, T, E) = dE$ for each depth are stored as well, to be used in algorithms where the fragment and energy distribution is required, such as calculation of RBE or response of solid-state detectors. When beam energies are required which are not represented in the pre-calculated database, linear interpolation between the next neighbours is performed.

Radiobiological beam model

A main advantage of heavy charged particles in radiotherapy is their increased RBE, which is due to increased local ionisation density on the level of the cell nucleus. Many attempts have been made in the past to describe charged particle radiation action on biological systems [9]. For the GSI radiotherapy we chose the local effect model (LEM) of Scholz [10,11] which is based on the X-ray sensitivity of cells, the structure of a heavy ion track (radial dose distribution) and the size of the cell nucleus. This model is the best choice for a number of reasons:

- It clearly separates the physical properties of the radiation from the biological properties of the irradiated object.
- The relevant biological properties can be measured or estimated, like the radiation sensitivity represented by the α/β ratios of X-ray dose-effect curves for single cells and by the known response of tumours and normal tissue to X-rays.
- The physical properties of the radiation, that is the radial dose distribution around a heavy-ion track can be described with reasonable accuracy by various models, either analytical [12] or by Monte Carlo simulations [1].

LEM essentially allows to predict the response of biological systems irradiated with particles of a particular type and energy from the knowledge of the X-ray response. This is an important advantage because few experimental data for tissue response to ion radiation are available.

In the context of treatment planning we apply this model to replace the physically absorbed dose by the biologically effective dose [13]:

$$D_{biol} = D_{abs} \times RBE(\vec{x}, D_{abs}) \quad (2)$$

where the RBE depends on the location within the irradiated volume as well as on the absorbed dose level.

Dose optimisation

For the dose optimisation it is sufficient in first order to use one-dimensional dose distributions $d(E_{beam}, z)$ because the lateral beam scattering is negligible compared to the initial beam width as delivered by the beam optics. In this case the dose computation [Eq. (1)] can be simplified to:

$$D(E_{beam}, \vec{x})[\text{Gy}] = 1.6 \times 10^{-8} \times d(E_{beam}, z) \left[\frac{\text{MeV}}{\text{gcm}^{-2}} \right] \times F(E_{beam}, x, y) [\text{mm}^{-2}] \quad (3)$$

with the fluence:

$$F(E_{beam}, x, y) = \frac{N(E_{beam}, x, y)}{\Delta x \Delta y} \quad (4)$$

where the Δx and Δy are the scanner step sizes in x and y , respectively. Within the target volume the lateral overlapping of neighbouring beam positions compensates for this crude approximation of a Gaussian profile by a delta function.

The task of particle fluence optimisation with respect to dose represents a least squares minimisation with respect to the fluence values $F(E_{beam}, x, y)$:

$$\begin{aligned} \chi^2 &= \sum_z w(\vec{x}) (D_{prescribed} - D(\vec{x}))^2 \\ \partial \chi^2 / \partial F &= 0 \end{aligned} \quad (5)$$

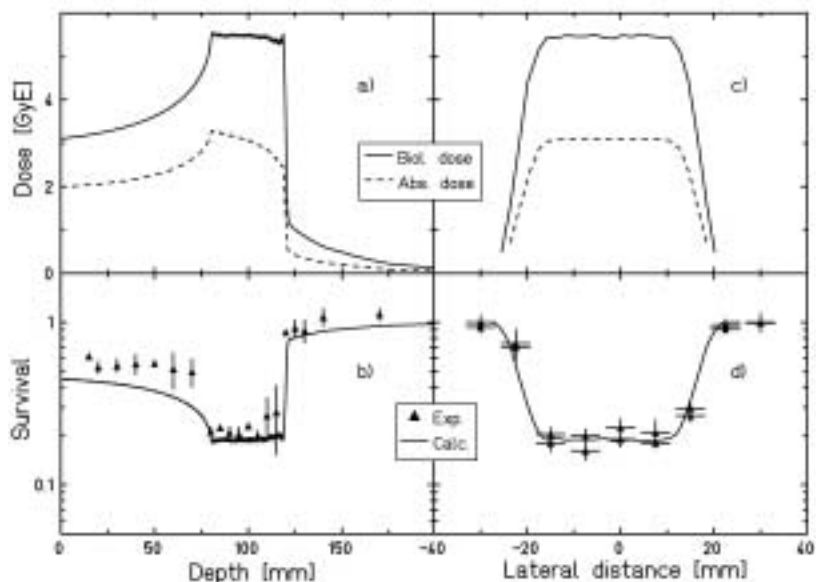
with appropriately chosen weight factors $w(\vec{x})$ and the dose $D(\vec{x})$ as given by Eq. (3).

The task is solved by iteration in two major steps, as described in [7]. First a simple dose matching procedure is applied, proceeding from the distal to the proximal slices of the target volume. With the resulting fluences as start values, text book minimisation algorithms like Conjugate Gradients or Marquardt's algorithm are used in a second step to yield satisfactory dose conformation. The method works for absorbed as well as for biologically effective dose provided the RBE is correctly calculated as a function of the absorbed dose level and the location within the irradiated volume.

Figure 4 illustrates a biologically effective dose optimisation including experimental verification performed for CHO cells. The target region was a cuboid with a volume $40 \times 100 \times 40 \text{ mm}^3$. For a description of the experimental procedure we refer to [14]. As expected the absorbed dose decreases in the distal part of the target volume due to the increasing RBE of stopping particles. The lower left part of the figure compares measured and calculated survival profiles as a function of depth. While there is good agreement in the target region and beyond, the calculated cell response in the entrance channel is larger than the measured one due to experimental dose rate effects. In any case we are on the safe side, since the biologically effective dose is overestimated rather than underestimated. The lower right part finally shows the lateral survival profile on a line through the centre of the target volume. Here good agreement could be achieved between measurement and calculation, which includes the finite beam width.

Figure 4. Biologically effective dose equivalent optimisation for CHO cells. The prescribed dose was 5.5 GyE in a single fraction, corresponding to a 20% survival level. The target region was between 80 and 120 mm depth, field size $40 \times 100 \text{ mm}^2$. Experimental data from [14].

- a) Calculated absorbed and biologically effective dose profile as a function of depth
- b) Measured (symbols) and calculated survival as a function of depth
- c) Calculated absorbed and biologically effective lateral dose profile
- d) Measured (symbols) and calculated survival in lateral direction



Summary and conclusion

We have developed and described the first ion therapy planning system based on the concept of biologically effective dose which is able to generate a strictly tumour-conformal irradiation using intensity-modulated fields of scanned heavy ions. These features make it a unique tool for cancer

treatment with heavy ions. The algorithms and procedures presented in this contribution have been in regular use since 1995 for the planning of numerous irradiation experiments including cell and animal experiments such as mini-pig lungs and skin, and the central nervous system of rats, where they have proven to be correct. Finally, the methods have been transferred unchanged to patient treatment planning. More than 140 patients have been planned with this software. Good tumour response and almost no acute side effects have been observed.

Future developments will be directed towards further exploitation of the high RBE, for example simultaneous multi-port optimisation in order to take full advantage of the high RBE of stopping ^{12}C in a larger part of the target volume.

Monte Carlo simulations may improve dose calculation in cases of sharp density gradients because here the effects of multiple scattering might be significant. We plan, however, to implement MC directly into our code rather than relying on external packages.

REFERENCES

- [1] Krämer, M., G. Kraft, *Rad. Environ. Biophysics*, 33, 91-109 (1994).
- [2] <http://www.gsi.de/bio/DOCS/TRAX/DOCS/trax.html>.
- [3] Krämer, M., in: *GSI Scientific Report 2000*, p. 157; <http://www.gsi.de/annrep2000>.
- [4] Haberer, Th., *et al.*, *Nucl. Inst. Meth.*, A330, 296-305 (1993).
- [5] Eickhoff, T., B. Franczak, U. Krause, C. Riedel, W. Rösch, R. Steiner, *Accelerator Development for the GSI Therapy Project*, GSI-report 96-01.
- [6] Gademann, G., W. Schlegel, J. Bürkelbach, C. Laier, S. Behrens, S. Brieger, M. Wannemacher, *Strahlentherapie und Onkologie*, 169, 159-167 (1993).
- [7] Krämer, M., O. Jäkel, T. Haberer, G. Kraft, D. Schardt, U. Weber, *Phys. Med. Biol.*, 45/11, 3299-3317 (2000).
- [8] Haberer, Th., *Entwicklung eines magnetischen Strahlführungssystems zur tumorkonformen Strahlentherapie mit schweren geladenen Teilchen*, GSI-report 94-09.
- [9] Chadwick, K.H., G. Moschini, M.N. Varma, *Biophysical Modelling of Radiation Effects*, Adam Hilger, Bristol (1992).
- [10] Scholz, M., G. Kraft, *Adv. Space Res.*, 18 1/2, 5-14 (1996).
- [11] Scholz, M., A.M. Kellerer, W. Kraft-Weyrather, G. Kraft, *Rad. Environ. Biophysics*, 36, 59-66 (1997).

- [12] Zhang, C.X., D.K. Dunn and R. Katz, *Radiat. Prot. Dosim.* 13/1-4, 215-218 (1985).
- [13] Krämer, M., M. Scholz, *Phys. Med. Biol.*, 45/11, 3319-3330 (2000).
- [14] Mitaroff, A., W. Kraft-Weyrather, O. B.Geiß G. Kraft, *Rad. Environ. Biophysics*, 37, 47-51 (1998).

MONTE CARLO STUDIES IN THE FIELD OF INTERNAL DOSIMETRY OF INCORPORATED RADIONUCLIDES

Gianfranco Gualdrini

ENEA-Istituto di Radioprotezione, Italy

Abstract

The radiation doses received by individuals from radionuclides which enter the human body cannot be measured directly but must be inferred. In these calculations several measurable quantities (such as the internal whole body burden or urine daily excretion) and quantities derived from models are employed.

The radiation protection quantities for internal dosimetry are in principle the same as for external dosimetry with the addition of quantities taking into account that the doses in the body are protracted. Other parameters are also necessary for dose assessment, like the specific absorbed fractions (SAFs). All these quantities are calculated using Monte Carlo codes and complex anthropomorphic phantoms. The present paper summarises, with some examples, the role played by Monte Carlo modelling in this field.

Introduction

The radiation doses received by individuals from radionuclides which enter the human body cannot be measured directly but must be inferred. In these calculations several measurable quantities (such as the internal whole body burden or urine daily excretion) and quantities derived from models are compared.

The first step in estimating the effective dose to an individual is to estimate the total amount (Bq) of radioactive material that has entered in the body (intake) and the second step is to estimate the effective dose from the intake.

The characteristics of internal dosimetry are:

- In internal dosimetry doses cannot be measured directly.
- The distribution of activity in the body is extremely inhomogeneous.
- The doses from internal dosimetry are protracted and radionuclides can continue to deliver dose throughout life.
- Each element can behave differently.

A series of quantities and parameters are necessary for a dose estimate and Monte Carlo techniques play a crucial role in the evaluation of such quantities. Furthermore, due to the great importance of a rigorous design of suitable calibration phantoms for *in vivo* measurements, the Monte Carlo method can also be proficiently employed as a valuable tool to optimise calibration systems design.

Definition of quantities for internal dosimetry

The basic dosimetric quantities are common to both external and internal dosimetry. We therefore refer to ICRP-ICRU documents [1-4] for the definition of the quantities: absorbed dose in an organ, equivalent dose to tissue and effective dose.

Other quantities are peculiar to internal dosimetry [5].

Committed equivalent dose

Since radionuclides continue to irradiate organs of the body after intake the term committed equivalent dose $H_T(\tau)$ is defined as the time integral over the time τ of the equivalent dose rate in a particular tissue. It is defined as the total equivalent dose to which that organ or tissue would be committed during the τ years after intake:

$$H_T(\tau) = \int_{t_0}^{t_0+\tau} H_T(t) dt$$

When the period of integration is not given, a period of 50 years is assumed for adults or a period of up to the age of 70 years for children.

Committed effective dose

If the committed equivalent doses from an intake are multiplied for the appropriate tissue weighting factors then the result is the committed effective dose $E(\tau)$:

$$E(\tau) = \sum_{\tau} H_{\tau}(\tau)w_{\tau}$$

Reference man

Many of the quantities calculated in internal dosimetry rely on the anatomical and physiological parameters of a person, and since it is not possible to measure all of these parameters in each individual, reference values are assumed. This set of parameters constitutes the reference man, a person with the anatomical and physiological characteristics defined in ICRP Publication 23 [6]. Monte Carlo codes have been employed for the evaluation of the quantities relying on complex mathematical models of the standard man. The same models have also been used to calculate dosimetric quantities for external irradiation.

Source and target organs

Radionuclides may decay in the lungs, in the gastrointestinal (GI) tract or in specific organs. These are known as source organs. The tissue in which energy is deposited following a nuclear decay is known as target organs. There are as many as 23 target organs listed in ICRP publications to be considered.

Absorbed fraction

The absorbed fraction is defined as the fraction of energy emitted within source region S that is absorbed in the target region T :

$$AF(T \leftarrow S) = \frac{\text{Energy absorbed in } T}{\text{Energy emitted in } S}$$

This fraction depends on the anatomical model, the type and the energy of radiation. For some source-target pairs AF may be largely independent of energy while for other pairs the values are highly dependent on the energy.

Absorbed fraction data are required for each radiation type:

Photon	Data are found in reference man (MIRD pamphlet)
Electron	Assume $AF(T \leftarrow T) = 1$, elsewhere=0
Alpha	Assume $AF(T \leftarrow T) = 1$, elsewhere=0

Additional considerations are required for wall organs and bone.

For walled organs $AF(T \leftarrow S)$ for particulate radiations where S is the content of a walled organ and T is the wall are derived assuming the dose at the interface is the equilibrium dose. The absorbed fraction is:

$$AF(T \leftarrow S) = \frac{1}{2} \frac{M_T}{M_S} \nu$$

where M_T and M_S are the mass of the walls and contents and ν is a factor representing the degree to which the radiation penetrate the mucosal layer. ν is taken as 1 for electrons, zero (0) for recoil atoms and 0.01 for alpha particles.

For bone the following Table 1 is applicable on AF values (see later for the meaning of trabecular and cortical bone).

Table 1. Absorbed fraction in bone for particulate radiations

AF	Alpha emissions		Beta emissions		
	Volume	Surface	Volume	Surface	
				E < 0.2 MeV	E > 0.2 MeV
$AF(BS \leftarrow TB)$	0.025	0.25	0.025	0.25	0.025
$AF(BS \leftarrow CB)$	0.01	0.25	0.015	0.25	0.015
$AF(RM \leftarrow TB)$	0.05	0.5	0.35	0.5	0.5
$AF(RM \leftarrow CB)$	0.0	0.0	0.0	0.0	0.0

RM – red marrow, TB – trabecular bone, BS – bone surface, CB – cortical bone

The computation of the values of $AF(T \leftarrow S)$ for each combination source to target organ is performed by means of Monte Carlo radiation transport calculations on anthropomorphic numerical phantoms.

The value of AF divided by M_T , the mass of the target organ, is known as specific absorbed fraction (SAF). The values of SAFs have been calculated and revised on the basis of the Oak Ridge series of analytical anthropomorphic phantoms.

Calculation of committed effective dose E(50)

The first step is to calculate the number of decays in each source organ S in 50 years (U_S). This implies solving the biokinetic models which represents the internal behaviour of the radionuclide. This can be done using mathematical tools to solve the system of linear differential equations describing the model.

Thus if $q_S(t)$ is the amount of radioactivity for radiation R in organ S at time t and U_S is the number of nuclear transformations in organ source S during 50 y post intake, then:

$$U_S = \int_0^{50y} q_S(t) dt$$

The second stage is to calculate the specific effective energy, $SEE(T \leftarrow S)$, which is defined as the dose to the target organ T per decay in the source organ S . SEE is given by:

$$SEE(T \leftarrow S) = \frac{\sum_R E_R Y_R w_R AF(T \leftarrow S)_R}{M_T}$$

where SEE is the specific effective energy absorbed in target organ T due to the emission of radiation R in source organ S , E_R is the energy of the emitted radiation R , Y_R is the yield of radiation R per nuclear transformation, w_R is the radiation weighting factor for radiation R , $AF(T \leftarrow S)_R$ is the absorbed fraction of energy in organ T for emission of radiation R in organ S and M_T is the mass of the target organ T .

For the calculation of committed equivalent dose the following equation can be used:

$$H_T(50) = \sum_S U_S SEE(T \leftarrow S)$$

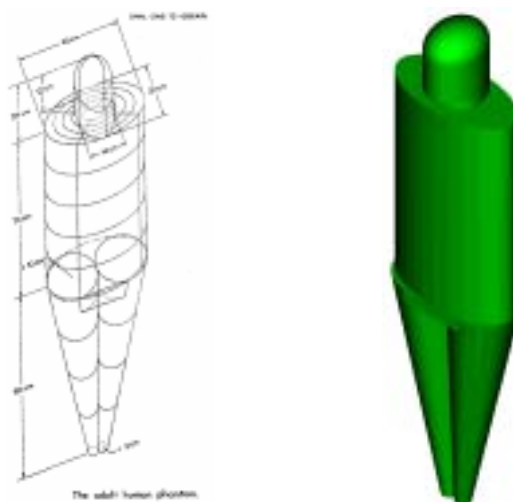
Finally, the committed effective dose is obtained multiplying the equivalent dose to each tissue by the appropriate tissue weighting factor and summing over all tissues.

Dosimetric models

Anthropomorphic numerical phantoms are used for the calculation of SEE (and SAF) values. A mathematical description of the reference man is used to compute the energy deposition in organs/tissues of the body from photon radiation. Phantoms consist of three types of tissues: lung, skeletal tissue and soft tissue. Such phantoms are used in Monte Carlo radiation transport simulations where the source is usually located within each source organ. Models have been extended to take age groups other than adults into account.

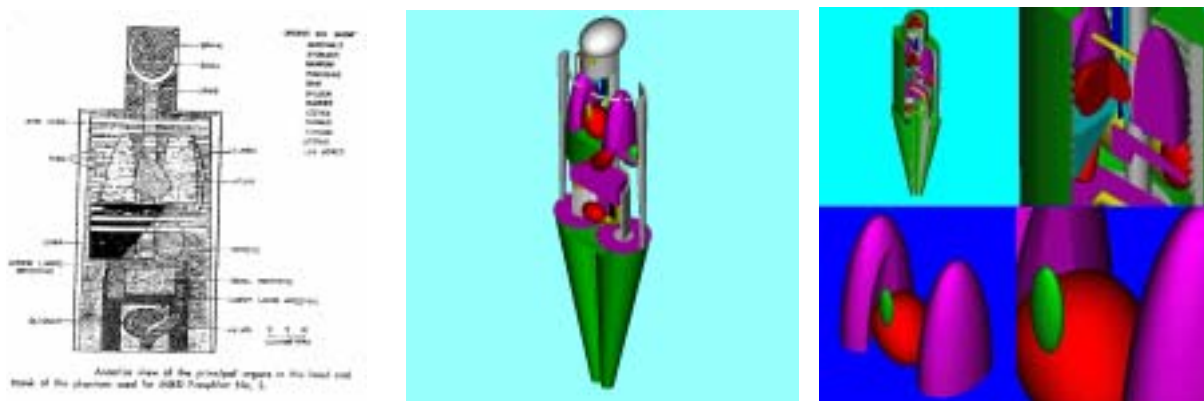
In Figure 1 the external dimensions of the adult human phantom are reported.

Figure 1. The adult human phantom, external view (on the right an MCNP™ model of ADAM)



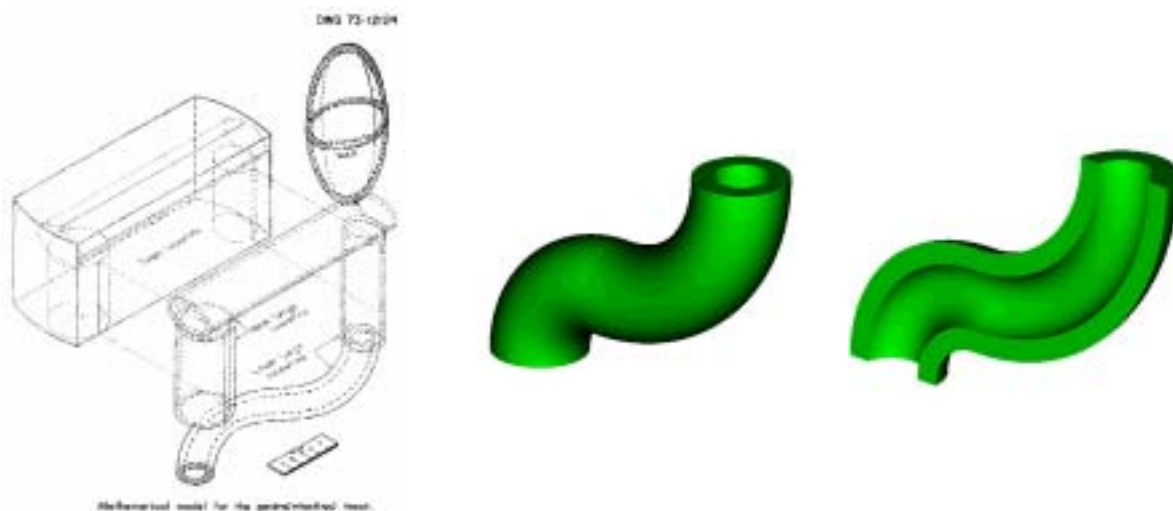
In Figure 2 the internal disposition of organs is shown. Each organ is described by means of equations in the space considering a common system of co-ordinates.

Figure 2. The adult human phantom, internal disposition of organs in the trunk (on the right an MCNPTM model of ADAM internal organs)



In the model the skeleton consists of six parts: the leg bones, arm bones, pelvis, spine, skull and the ribs. In Figure 3 the description of the gastrointestinal tract is reported.

Figure 3. The adult human phantom, GI tract (on the right an MCNPTM model of the sigma)



Summarising

To summarise the committed dose assessment procedure some simplified schemes can be useful.

In Figure 4 the concept of E(50) is briefly presented. To determine E(50) we need to carefully estimate the total number of nuclear transformation in source organ *S* during 50 years post intake (see Figure 4). This quantity can be determined through compartment modelling (see Figure 5) and excreta analysis or *in vivo* measurements.

Figure 4. Conceptual scheme of E(50) evaluation

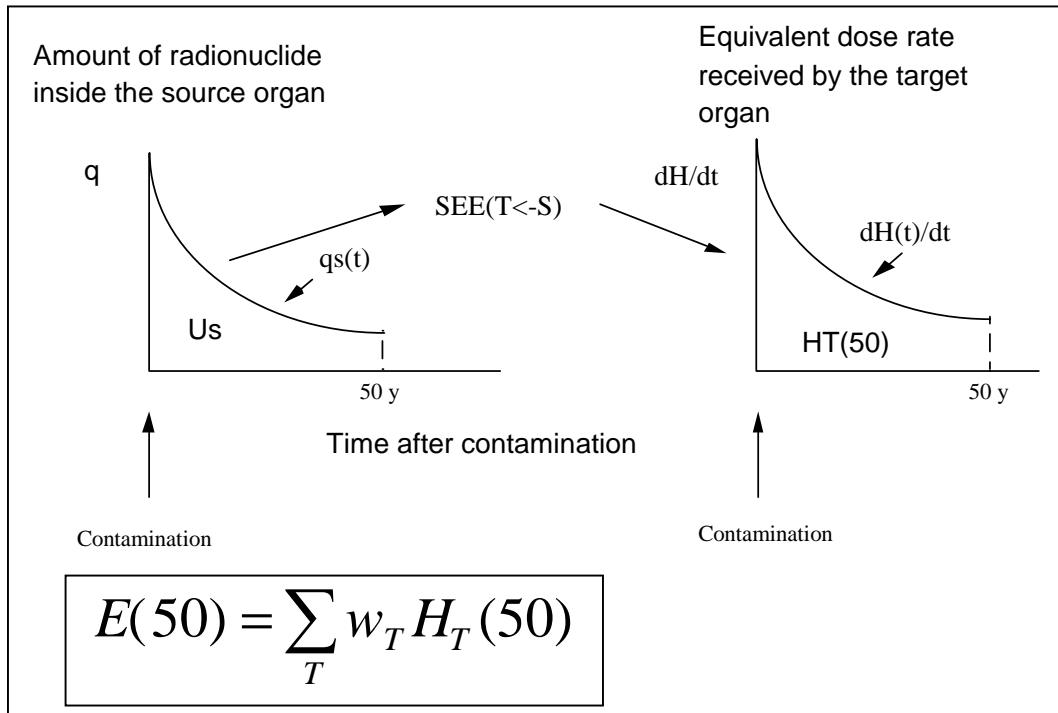
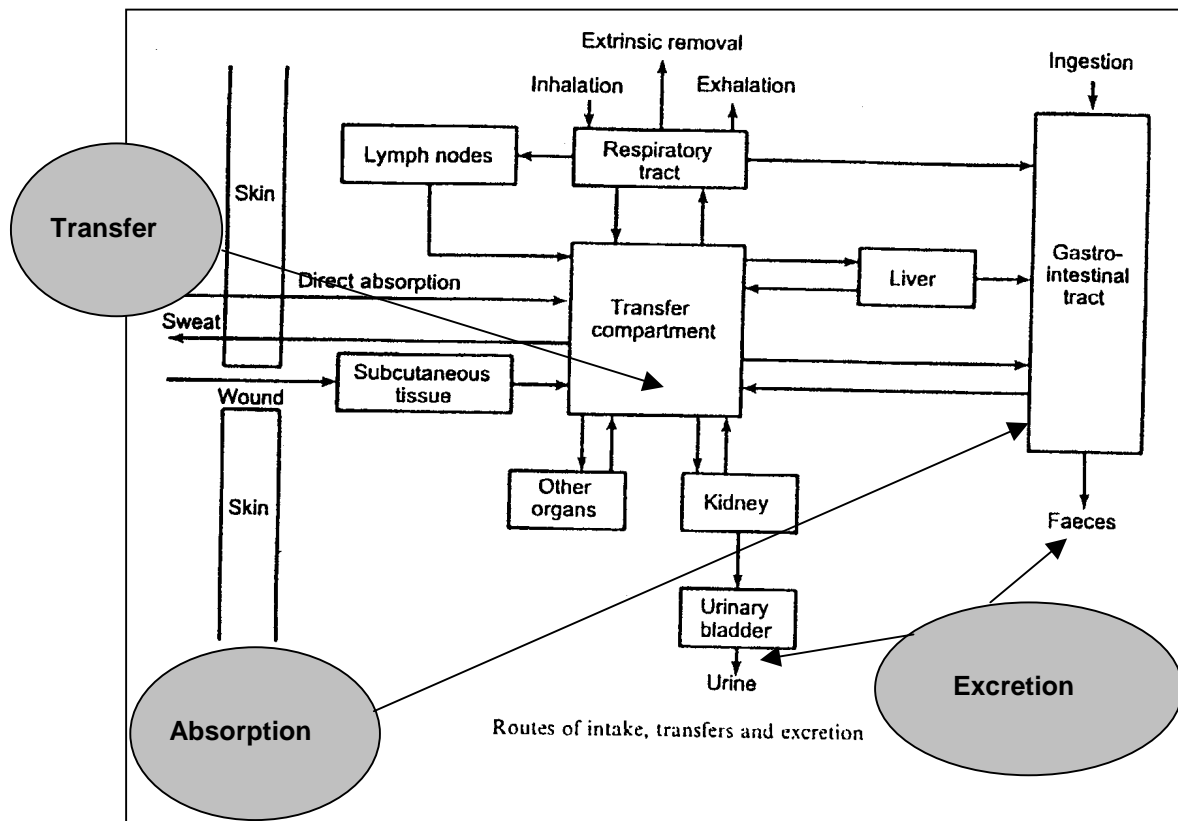


Figure 5. Routes of intake



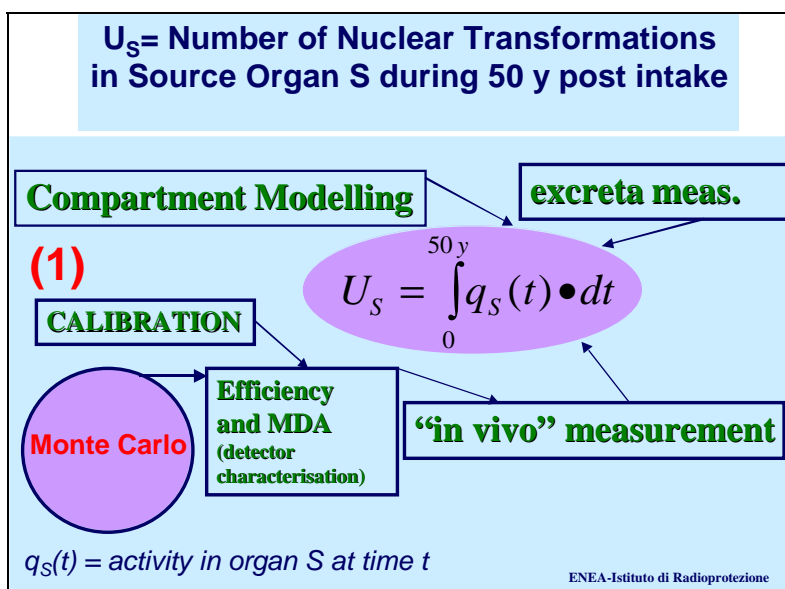
To perform accurate *in vivo* measurements it is necessary to rely on very accurate calibrations that imply the evaluation of the detection system efficiency and the minimum detectable activity (MDA):

$$MDA = \frac{3 + 4.65 \cdot S_B}{t \cdot \varepsilon}$$

where MDA is the *a priori* MDA (Bq), ε is the *in vivo* detection efficiency (cts $\cdot s^{-1} \cdot Bq^{-1}$), t is the measuring time (s) and S_B is the uncertainty of the counts in the region of interest for the blank measurement (subject related counts) (cts).

The efficiency evaluation is based on a suitable calibration phantom that should be as much as possible representative of the individual to be measured. In this framework Monte Carlo analyses can play a fundamental role for an accurate efficiency determination (and thereafter MDA assessment). Examples of applications in this field will be discussed later.

Figure 6. The role of Monte Carlo simulations in U_s determination



Finally, $E(50)$ is linked to the SEE and the SAFs (see Figure 7) that are calculated using Monte Carlo codes (and tabulated for a large range of photon energies) relying on the aforementioned anthropomorphic mathematical models.

The present paper will be focused on two main aspects in which Monte Carlo techniques can play a fundamental role: the calibration procedures of *in vivo* monitoring devices and the SAF evaluation. Finally a significant example of Monte Carlo aided design of a complex head calibration phantom for *in vivo* measurements of bone-seeker nuclides will be presented.

Anthropomorphic phantoms for calibrations

As it is well known the calibration conditions should be as close as possible to the routine measurement on the contaminated subject. Due to the large subject-specific variations concerning the measurement conditions the calibration situation can in principle differ from the reality to a great extent

Figure 7. Formulation of the SEE and Monte Carlo role in its determination

(2) SEE = SPECIFIC EFFECTIVE ENERGY [MeV/(g*nt)]

$$SEE(T \leftarrow S) = \sum_R E_R Y_R W_R SAF(T \leftarrow S)_R$$

E_R = Emitted energy from Radiation R
 Y_R = Yield of Radiation R
 W_R = Radiation R weighting factor

MONTE CARLO

SAF (specific absorbed fraction) = fraction of the radiating energy emitted by a source organ that is absorbed in a given target organ/target organ mass. (MIRD Pamphlet or ICRP-30 Supplements Tabulations)

ENEA-Istituto di Radioprotezione

This is the reason why a large variety of plastic calibration phantoms, to be filled with radioactive solutions or solid sources (spheres, rods, etc.), have been proposed to fulfil a series of reliability requirements. Some significant examples of such phantoms are the St. Petersburg phantom, which is composed by modular polyethylene boxes (Figure 8). Each box contains four rods with different radioactive sources: ^{57}Co (122-136 keV photons) which can reproduce a contamination from technetium, ^{60}Co (1.17-1.33 keV photons) and ^{137}Cs (662 keV), both typical of an accident in the nuclear industry and ^{40}K (1.46 MeV), representative of the natural content of potassium in the body soft tissue. The phantom has been employed in a European intercomparison. Another very popular calibration phantom for whole body contaminations is the BOMAB phantom (Figure 9), constituted by ten cylindrical (circular and elliptical basis) elements that can be filled with liquid or gel radioactive materials.

Figure 8. The St. Petersburg phantom

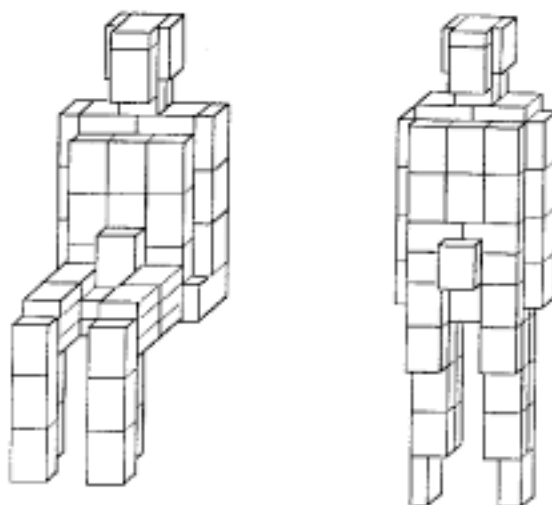
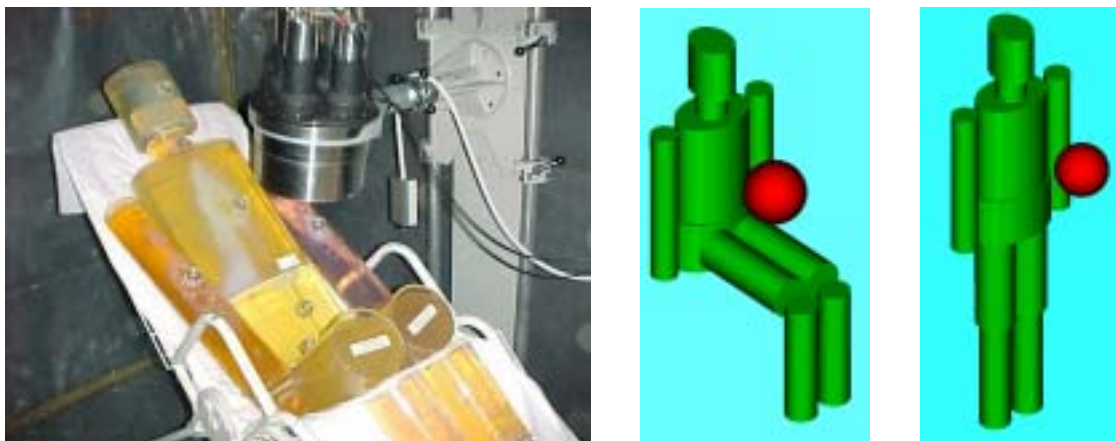


Figure 9. The BOMAB phantom



The BOMAB calibration configurations can easily be modelled by Monte Carlo, allowing calculating correction coefficients to the counting efficiency to take into account density and composition variations in the radioactive solution (see Figure 10).

Figure 10. BOMAB phantom calibration for whole body contamination (e.g. ^{137}Cs) and the MCNP model of a “standard chair” and “bed” measurement postures



Other phantoms that should be briefly mentioned are the Lawrence Livermore National Laboratory (LLNL) phantom for lung measurements (Figure 11), the Bottle phantom (Figure 12) which allows to simulate different body sizes, and the thyroid ANSI phantom (Figure 13). Of particular importance are the head phantoms that will be treated later on.

Figure 11. The LLNL phantom for lung measurements



Figure 12. Bottle whole body phantom to simulate different body sizes

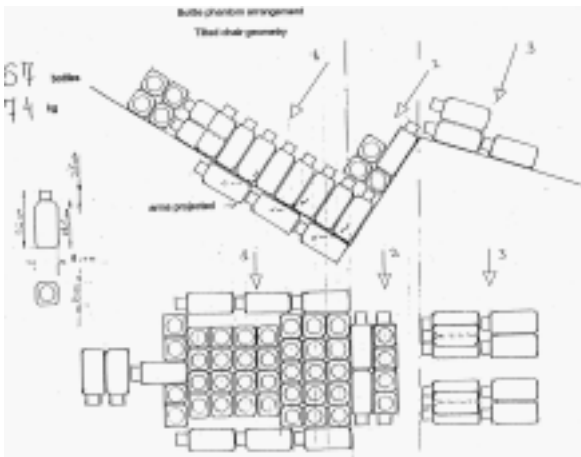


Figure 13. ANSI thyroid phantom

The neck is modelled with a PMMA cylinder with a cylindrical hole containing a point source



How accurate and suitable are the available calibration phantoms?

It should be pointed out that all the experimental phantoms employed in the calibration procedure are in any case simplified and it is not always easy to evaluate the degree of deviation from the *in vivo* real measurement introduced by the calibration itself. Furthermore the assumption of a homogeneous distribution of the contaminant in the target organ or in the whole body can constitute in many cases a very rough approximation.

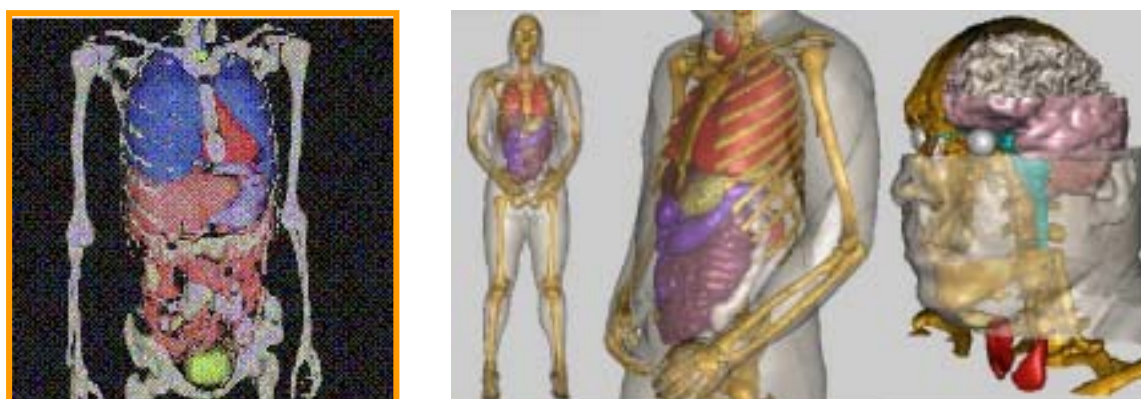
The use of more detailed experimental phantoms, and, where necessary, Monte Carlo evaluations based on very complex mathematical phantoms is necessary in the case of nuclides present in single organs of complex geometry, in presence of significant variations of dimensions and morphology of the investigated subjects, especially for low energy gamma emitters and when a very low minimum detectable activity (MDA) is required (the case of the *in vivo* measurement of actinides).

A very significant example in this field are the studies carried out by Kramer, *et al.* (Radiation Protection Bureau, Ontario, Canada) [7,8] on the influence of the lung deposition conditions on the counting efficiencies. An analytical MCNP model of the trunk was developed for the simulation of different source geometries. The uncertainty on the ^{239}Pu (17 keV) source geometric distribution can cause underestimations by a factor of 4, overestimation by a factor ~30 until the complete loss of the countings vs. an assumed homogeneous distribution of the nuclide in the lungs.

Kramer validated his model against the LLNL and JAERI experimental calibration phantoms. The validation suggested an improvement to the model, with the addition of a detailed representation of the sternum and the ribs.

To guarantee that the calibration factors of the detection system are as close as possible to the real measurement conditions, improved computer softwares have been developed. These models usually rely on sophisticated mathematical phantoms that have been being developed for some years in the major radiation protection and medical physics institutes around the world [9-17]. Two significant examples of these so-called “voxel models” directly taken from CT scans, NMRI scans or colour pictures of anatomical slices are reported in Figure 14.

Figure 14. The Golem male phantom (courtesy M. Zankl) from CT scans (left) and the VIP man (courtesy G. Xu) from photographic images of an executed man



The software “MC_in vivo” [18,19] developed by J. Hunt of the *Instituto de Radioprotecao e Dosimetria* (Rio de Janeiro, Brazil) was written in visual basic (VB5) and is operative under Windows 95. It is based, with some modifications, on the VOXEL phantom NORMAN developed by the National

Radiological Protection Board (NRPB, UK) and is able to model a large variety of subject-detector configurations and calculate the associated counting efficiencies (Figures 14 and 15). The software performances were compared with EGS4, whilst an experimental benchmarking was carried out on ^{241}Am -contaminated head phantoms (National Radiation Protection Institute phantom – Czech Republic, BfS phantom – Germany, and BPAM-001 that is included in the USA Transuranium and Uranium Registry Americium Bone Phantoms and consists of a cranium of a donor who was contaminated 25 years before death). This benchmarking put in evidence significant discrepancies due to the different models adopted (the experimental and the mathematical (NORMAN) phantoms) and to the actual contamination distribution in the experimental phantoms employed.

Figure 15. Sagittal section of the voxel phantom NORMAN, showing a homogeneous deposition of ^{235}U in the lung detected by an NaI detector

The circles represent interaction points of the 186 keV photons towards the detector and within the detector itself

Courtesy of John Hunt

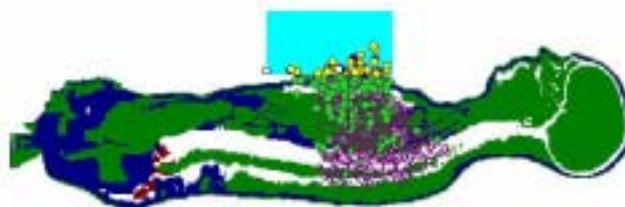


Figure 16. Axial section of the voxel phantom NORMAN, showing a point deposition of ^{241}Am in the rear part of the lung detected by an NaI crystal coupled with a Phoswich detector

The circles represent interactions of the 59.5 keV photons towards the detector and within the detector itself

Courtesy of John Hunt



A software characterised by similar features and based on the MCNP code has been developed jointly by the University of Texas, the Lawrence Livermore National Laboratory and the Los Alamos National Laboratory. The code MRIPP [20], available from the NEA Data Bank, includes a database of voxel anthropoid phantoms and is addressed to calculate correction factors to be applied to the efficiencies evaluated on the basis of very simplified calibration sources (spherical, cylindrical, etc.) to take into account the real measurement condition of the contaminated subject.

An example of Monte Carlo aided design of a head calibration phantom

It is of some interest to mention a research activity carried out at ENEA-Radiation Protection Institute addressed at developing a head calibration phantom for ^{241}Am measurements [21,22]. As it is well known the measurement of ^{241}Am (59.5 keV photon emission) in the bone is an easier way to determine the plutonium burden. In fact plutonium has an associated very low energy photon emission (17 keV) and an *in vivo* measurement of its content can be subject to enormous uncertainties,

especially related to the body size variations. Due to these reasons, for an effective and fast screening on internal contamination from actinides it is recommended to determine the activity of ^{241}Am in the bone (skull or knee).

The mean free paths at this photon energy are:

- 1.7 cm in cortical bone.
- 3.6 cm in trabecular bone.
- 4.5 cm in soft tissue.

The contamination distribution can be assumed homogeneous on the bone surfaces. As a function of time after intake one can also assume that the nuclide migrates inside the bone, therefore generating a homogeneous volumetric contamination (as a first approximation).

Due to the difficulties associated with such kinds of measurements it was decided to design a calibration phantom of the head with morphological characteristics as close as possible to the *in vivo* measurement condition.

Traditionally such phantoms are developed painting the internal and external bone surface by radioactive paints; this process, however, does not guarantee a homogeneous application of the paint.

It was therefore decided to put calibrated point sources in optimised position to approximate as much as possible a homogeneous distribution of the radionuclide and calculate a correction coefficient using Monte Carlo.

As far as the plastic phantom is concerned, it should be representative of the European Standard Man (Caucasian Standard Man).

The density and the composition of the constituent materials should follow the standard tissue equivalent materials suggested by the ICRU (International Commission on Radiation Units and Measurements).

A commercial AldersonTM developed for angiography studies was used, and was modified following the indications obtained from Monte Carlo simulations (see Figure 17).

Figure 17. A skull for anatomical studies and the AldersonTM plastic phantom adopted, with modifications, for the calibrations



The role of Monte Carlo modelling was:

- Evaluating the volumes of bone macro-regions (24) of the head in which centroids the calibrated sources should have been placed.
- Modelling the calibration condition and evaluating a correction coefficient to the calibration factor, (depending on the head-detector configuration) to take into account the difference between the *in vivo* measurement on the subject (assumed in this case homogeneous, though this is debatable) and the calibration measurement (with point distributed sources).

To summarise the design and construction procedure, CT scans of the plastic Alderson phantom were taken and a series of slices were modelled with MCNP in an analytical way (non-voxel approach) (Figures 18-19). A 3-D model of the head was built where the volume calculations of 24 nearly iso-volumetric macro-regions were performed. The plastic phantom was thereafter drilled (Figure 20) in the 24 positions suggested by the Monte Carlo simulations and the point sources were placed in each hole and closed with plastic caps. At the end the calibrations were performed and simulated by Monte Carlo (Figure 21). The two configurations treated by Monte Carlo were the homogeneous source distribution (*in vivo* measurement) and the heterogeneous source distribution (calibration condition).

Figure 18. A CT slice of the head (right) and its MCNP model (left)

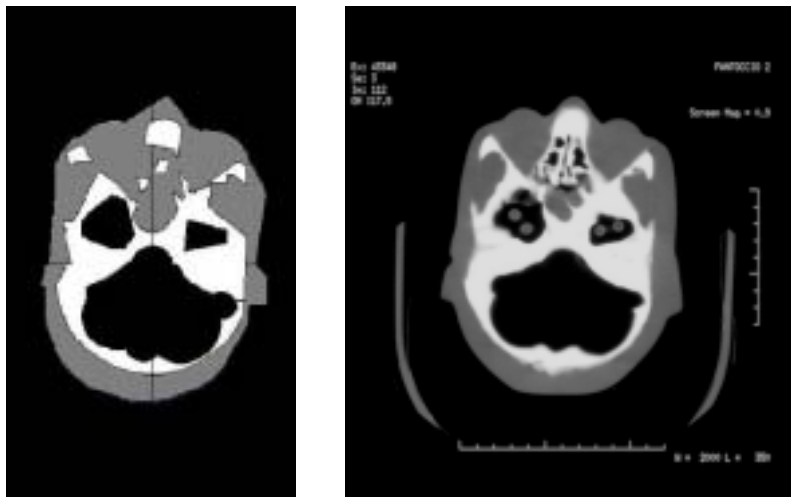


Figure 19. The 3-D final MCNP model

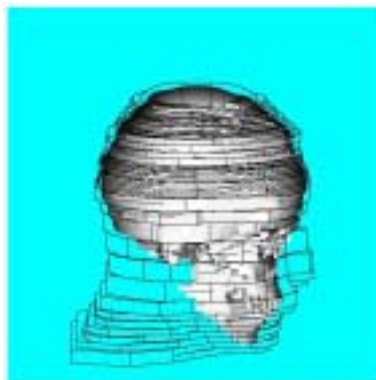
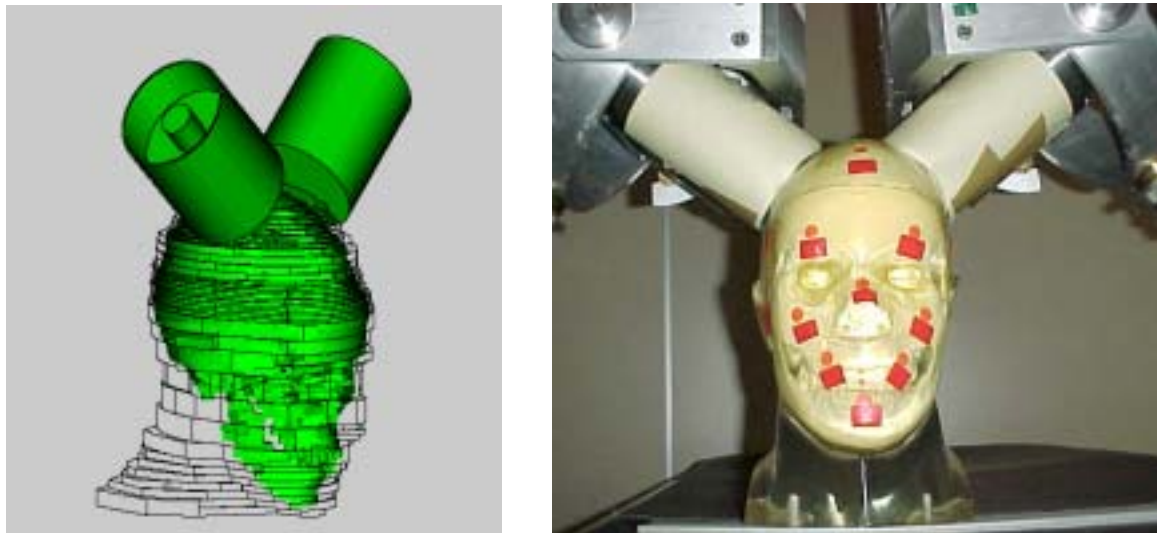


Figure 20. Drilling operations



Figure 21. A calibration measurement (right) and its MCNP model (left)



It should be pointed out that the closer the detector is to the head, the higher the discrepancy between the two conditions and the higher should be the correction coefficient to be applied. An important element to be taken into account is also the position of the single point sources with respect to the detector. If the calibration condition is chosen such that a point source is very close to the detector window centre, a further, much higher counting rate occurs, if compared to the *in vivo* condition. This is to explain that a careful calibration strategy should be adopted.

The “calibration/*in vivo* measurement” procedure adopted is as follows:

- 1) Calculate a calibration correction factor to take into account the source distribution difference (at about 20 cm head-detector distance (homogeneous-heterogeneous) (CH).
- 2) Calculate a correction factor due to the distance (from 20 cm to 1 cm) assuming a homogeneous source distribution in the bone (CD).

- 3) Perform the calibrations at 20 cm distance to minimise the effects of point source positioning on the measurements.
- 4) Perform the *in vivo* measurements at 1 cm distance to minimise the measurement time for a fast screening and apply the composition of the two correction coefficients to the counting (CH*CD).

Table 2 summarises the results of the experiments and simulations.

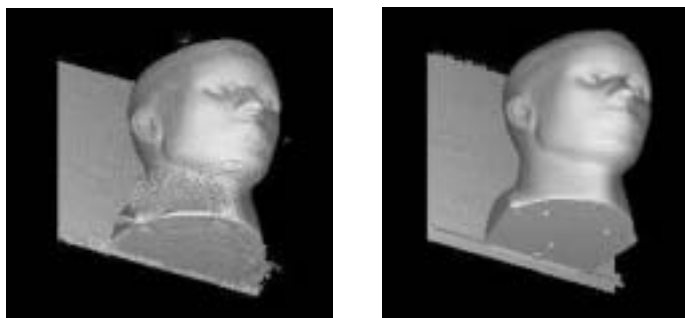
Table 2. Results of calibrations and numerical simulations

Head surface to detector distance (cm)	MCNP (homog.)/WBC measurement ratio	MCNP (etherog.)/WBC measurement ratio	MCNP (homog.)/etherog. correction factor
~ 1	0.77	0.87	0.89
~ 10	0.85	0.89	0.96
~ 15	0.98	0.99	0.99
~ 20	1.00	1.02	0.98

A very satisfactory agreement can be noted, though some criticisms can nevertheless be formulated against the design procedure and the optimisation of the 24 source positioning.

The main limit of the procedure consists in that it relies on a rather crude 3-D model of the head, consisting of rather thick layers the contours of which were drawn on the basis of a by-hand best fit of the region boundaries. The correction factors obtained in this way are based on the assumption that the Monte Carlo geometrical model is a good approximation of the reality; the optimisation of the 24-source positioning depends on the same assumption.

Figure 22. The 3-D reconstructed CT head image to be implemented in MCNP

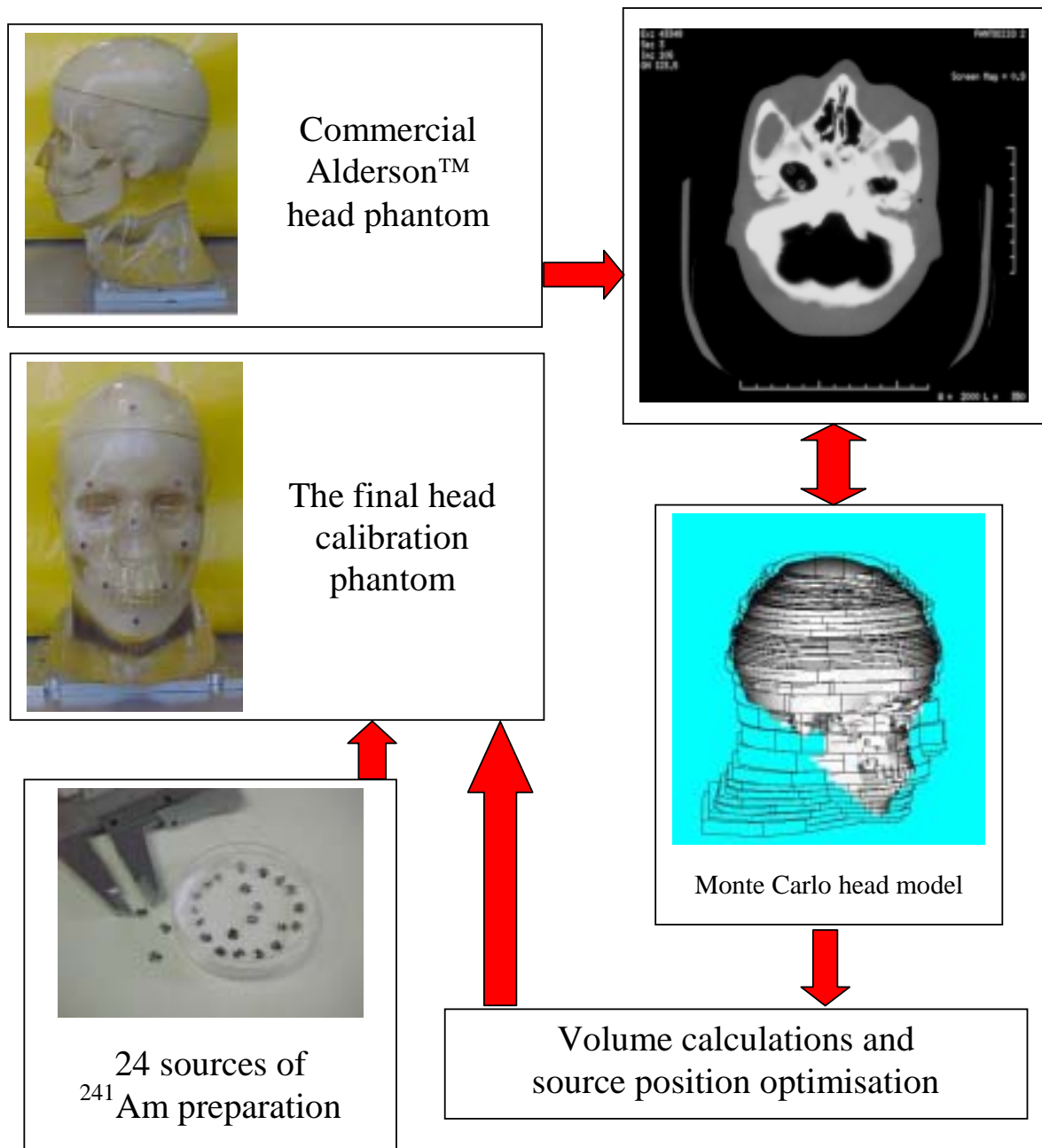


A new and exhaustive approach to the design of the head phantom should rely on a geometry fully based on the CT scan Hounsfield number, an accurate segmentation and a new optimisation of the 24 point sources with an improved voxel model of the head. This methodology should guarantee both a reliable source distribution (in the homogeneous distribution case) and a good simulation of the radiation transport within a model as close as possible to the *in vivo* and calibration conditions.

Apart from the intrinsic limitations of the procedure, its logic can indicate a satisfactory coupling between measurements and Monte Carlo modelling to obtain reliable calibrations.

The voxel head phantom being implemented in MCNP is shown in Figure 23.

Figure 23. Procedure adopted for the development of the calibration head phantom



Monte Carlo evaluation of specific absorbed fractions (SAF)

As explained in the introductory part of the paper, the absorbed fraction (AF) is one of the fundamental quantities employed for the calculation of doses from incorporated radionuclides. It is defined as the fraction of the emitted energy from a given source organ that is absorbed by a given target organ. The specific absorbed fraction (SAF) is obtained from AF divided by the target organ mass. This transfer quantity is therefore crucial for the evaluation of the committed equivalent dose and the committed effective dose and variations in the employed SAF values have an immediate

influence on the committed dose evaluation. For quite some time, the most widely used set of SAF values has been extracted from Monte Carlo (and sometimes “point kernel”) calculations based on the MIRD mathematical phantom, which is, as already explained, analytical [23]. It should be pointed out here that the MIRD model is affected by significant approximations and simplifications compared with the strong heterogeneity of a real subject.

Taking into account the strong dependence of the SAF values on the organ shape and relative position, in the last three years a series of studies have been undertaken at the international level addressed at producing new sets of SAF values based on realistic voxel phantoms and the Monte Carlo method.

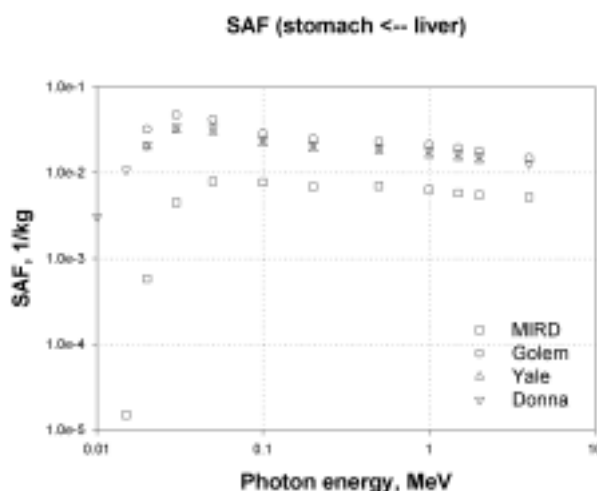
D.J. Jones (NRPB) performed his studies in 1998 using NORMAN [24], while Yoriatz, *et al.* employed a phantom developed by Zubal at Yale University to calculate new SAF values using MCNP [25,26].

A fruitful collaboration between NRPB and GSF allowed evaluating the SAF variations depending on the usage of MIRD models of various ages and the voxel phantoms Golem, CHILD and BABY. Of particular interest is an investigation on internal doses based on new SAF values for a large series of radionuclides employed in the medical field.

Some very recent evaluations by M. Zankl [27-29] demonstrate the influence of the mathematical anatomical model employed on the calculation of SAFs. In Figure 24 is reported the SAF behaviour as a function of energy in the case of “liver to stomach” irradiation. The satisfactory agreement among the different voxel models can be noted, whilst a high systematic discrepancy for the MIRD model is evident. The reason of such a disagreement is that stomach and liver are organs in strong contact with each other in a real subject, while the minimum distance between the two organs in the MIRD model is more than 2 cm. This is the reason why the low-energy photons emitted from the liver do not reach the stomach in the MIRD model, though they easily reach the stomach in the voxel models. In general there is a satisfactory agreement for a large number of organ couples, but the average organ-organ distances are smaller in the voxel models, thus leading to significant differences between the two sets of SAFs.

Figure 24. Comparison of SAF values obtained with different mathematical models of the man (MIRD and voxel approach)

Courtesy of M. Zankl



The influence of more or less realistic mathematical models employed in the dosimetric assessment should not be neglected and is more crucial in internal dosimetry than external dosimetry. The importance of correct SAF evaluations is also confirmed by the further uncertainty associated with the metabolic model of the investigated radionuclide. The contemporary usage of unreliable SAFs and unreliable metabolic models could lead to extremely inaccurate dose evaluations.

Conclusions

The validity of a Monte Carlo result is strongly linked to the correspondence of the model to the real irradiation experience to be simulated: the more complete and accurate the modelling, the more accurate the obtained results. Therefore, notwithstanding the fact that every model adopted for the simulation implies inherent simplifications to be accepted, there are details of the experiment to be modelled that cannot be neglected and should be represented very carefully due to their importance for the response to be determined by the simulation

The examples presented, also in the lecture on external dosimetry, demonstrate that a Monte Carlo result characterised by a low statistical error cannot be automatically judged as reliable. Of absolute importance is in fact the accuracy of the modelling. Every result should be, on the basis of these considerations, presented with its associated statistical uncertainty (precision) and an indication of the systematic deviations (accuracy) that can be due to several factors, including the cross-section files employed.

To conclude, the set-up of a Monte Carlo simulation is very similar to the preparation of an experiment, characterised by various degrees of complexity. The availability of advanced code packages that could be used in every laboratory dealing with radiation physics problems should suggest the need for non-extemporary use of these tools.

Training initiatives at the European level are therefore to be encouraged in the field of radiation protection dosimetry along with thematic workshops on specific computational dosimetry applications.

REFERENCES

- [1] International Commission on Radiological Protection (ICRP), *Recommendations of the International Commission on Radiological Protection*, Publication 60, Annals of ICRP 21(1-3), Pergamon Press, Oxford (1991).
- [2] International Commission on Radiation Units and Measurements (ICRU), *Conversion Coefficients for Use in Radiological Protection against External Radiation*, Report 57, Bethesda, MD, USA (1993).
- [3] ICRP, *Conversion Coefficients for Use in Radiological Protection against External Radiation*, Publication 74, Pergamon Press, Oxford (1995).

- [4] ICRU, *Conversion Coefficients for Use in Radiological Protection against External Radiation*, Report 57, Bethesda, MD, USA (1998).
- [5] ICRP, *Limits for Intake of Radionuclides by Workers*, Part I, Publication 30, Annals of ICRP, Pergamon Press, Oxford (1978).
- [6] ICRP, *Report of the Task Group on the Reference Man*, Publication 23, Pergamon Press, Oxford (1975).
- [7] Kramer, G.H., L.C. Burns and S. Yiu, "Lung Counting: Evaluation of Uncertainties in Lung Burden Estimation Arising from a Heterogeneous Lung Deposition Using Monte Carlo Code Simulations", *Radiat. Prot. Dosim.* 74(3), 173-182 (1997).
- [8] Kramer, G.H. and P. Crowley, "An Improved Virtual Torso Phantom", *Radiat. Prot. Dosim.*, 88(3), 233-237 (2000).
- [9] Zankl, M., R. Vedit, G. Williams, K. Schneider, H. Fendel, N. Petoussi, G. Drexler, "The Construction of Computer Tomographic Phantoms and their Application in Radiology and Radiation Protection", *Radiat. Environ. Biophys.*, 27, 153-164 (1988).
- [10] Veit, R., M. Zankl, N. Petoussi, E. Mannweiler, G. Williams, G. Drexler, *Tomographic Anthropomorphic Models, Part I: Construction Technique and Description of Models of an 8 Week Old Baby and a 7 Year Old Child*, GSF-Bericht No. 3/89, GSF – Forschungszentrum für Umwelt und Gesundheit, Neuherberg, Germany (1989).
- [11] Zankl, M., N. Petoussi-Henß, A. Wittman, "The GSF Voxel Phantoms and their Application in Radiology and Radiation Protection", *Proceedings of the Workshop on Voxel Phantom Development*, 6-7 July 1995, National Radiological Protection Board, Chilton, UK, 98-104 (1996).
- [12] Jones, D.G., "A Realistic Anthropomorphic Phantom for Calculating Organ Doses Arising from External Photon Irradiation", *Radiat. Prot. Dosim.*, 72(1) (1997).
- [13] Dimbylow, P.J., "The Development of Realistic Voxel Phantoms for Electromagnetic Field Dosimetry" *Proceedings of the Workshop on Voxel Phantom Development*, P.J. Dimbylow (ed.), NRPB, Chilton, UK (1995).
- [14] Zubal, I.G. and C.R. Harrell, "Voxel-based Monte Carlo Calculations of Nuclear Medicine Images and Applied Variance Reduction Techniques", *Image and Vision Computing*, 10(6) July/August (1992).
- [15] Zubal, I.G., *et al.*, "Computerized Three-dimensional Segmented Human Anatomy", *Med. Phys.*, 21 (2) (1994).
- [16] Zubal, I.G., *et al.*, "Two Dedicated Software, Voxel-based, Anthropomorphic (Torso and Head) Phantoms", *Proceedings of the Workshop on Voxel Phantom Development*, P.J. Dimbylow (ed.), NRPB, Chilton, UK (1995).
- [17] Xu, X.G., T.C. Chao, A. Bozkurt, "VIP-MAN: An Image-based Whole-body Adult Male Model Constructed from Color Photographs of the Visible Human Project for Multi-particle Monte Carlo Calculations", *Health Physics*, 78(5) (2000).

- [18] Hunt, J., “Método de Calibração de um Sistema de Medida in vivo através da simulação matemática da Fonte de Radiação e do Detector”, Doctorate Thesis in Biology (Nuclear Bioscience), University of Rio de Janeiro, Brazil (1998).
- [19] Hunt, J.G., I. Malàtovà and S. Foltànovà, “Calculation and Measurement of Calibration Factors for Bone Surface Seeking Low Energy Gamma Emitters and Determination of ^{241}Am Activity in Real Case of Internal Contamination”, *Radiat. Prot. Dosim.*, 82(3), 215-218 (1999).
- [20] RSICC Computer Code Collection, *MRIPP 1.0: Magnetic Resonance Image Phantom Code System to Calibrate In Vivo Measurement Systems*, NEA Data Bank, Reference MRIPP: CCC-0655/01 (1997).
- [21] Gualdrini, G., P. Battisti, R. Biagini, P. De Felice, A. Fazio, P. Ferrari, “Development and Characterisation of a Head Calibration Phantom for *In Vivo* Measurements of Actinides”, *Appl. Rad. Isot.*, 53, 387-393 (2000).
- [22] Gualdrini, G., P. Ferrari, P. Battisti, P. De Felice and L. Pierotti, “MCNP Analytical Models of a Calibration Head Phantom for Bone-seeker Nuclides *In Vivo* Measurements”, Monte Carlo 2000, Lisbon, October 2000, Springer-Verlag (ed.), to be published.
- [23] Snyder, W.S., M.R. Ford, G.G. Warner, *Estimates of Specific Absorbed Fractions for Photon Sources Uniformly Distributed in Various Organs of a Heterogeneous Phantom*, nm/mird Pamphlet No. 5, Health Physics Division, Oak Ridge National Laboratory (ORNL), Oak Ridge, TN (1978).
- [24] Jones, D.G., “A Realistic Anthropomorphic Phantom for Calculating Specific Absorbed Fractions of Energy Deposited from Internal Gamma Emitters”, *Radiat. Prot. Dosim.*, 79(1-4) (1998).
- [25] Yoriyaz, H., A. dos Santos, M.G. Stabin R. Cabezas, “Absorbed Fractions in a Voxel-based Phantom Calculated with the MCNP-4B Code”, *Med. Phys.*, 27(7), (2000).
- [26] Stabin, M.G. and H. Yoriyaz, “Photon Absorbed Fractions Calculated in the Trunk of an Adult Male Voxel-based Phantom”, *Health Phys.*, 82, No. 1, pp. 21-44 (2002).
- [27] Smith, T.J., A. Phipps, N. Petoussi-Henß and M. Zankl, “Impact on Internal Dose of Photon SAFs Derived with the GSF Adult Male Voxel Phantom”, *Health Phys.*, 80(5), 477-485 (2001).
- [28] Smith, T.J., N. Petoussi-Henß and M. Zankl, “Comparison of Internal Doses Estimated by MIRD and Voxel Techniques for a “Family” of Phantoms”, *European Journal of Nuclear Medicine*, Published online, 20 June 2000.
- [29] Zankl, M., Private Communication, August 2000.

PENELOPE: SPECIFIC FEATURES AND APPLICATIONS

**F. Salvat,^a J.M. Fernández-Varea,^a J. Sempau,^b J. Asenjo,^{a,c}
A. Sánchez-Reyes,^c X. Llovet^d and C. Campos^a**

^a Facultat de Física (ECM), Universitat de Barcelona
Diagonal 647, 08028 Barcelona, Spain

^b Institut de Tècniques Energètiques, Universitat Politècnica de Catalunya
Diagonal 647, 08028 Barcelona, Spain

^c Servicio de Oncología Radioterápica, Hospital Clínic Universitari de Barcelona
Villarroel 170, 08036 Barcelona, Spain

^d Serveis Científic-Tècnics, Universitat de Barcelona
Lluís Solé i Sabarís 1-3, 08028 Barcelona, Spain

Abstract

Specific features of the Monte Carlo code PENELOPE, which are either implemented in the current public version 2001 or have been recently developed to be introduced in future releases of the code, are briefly described. Results from simulations of various practical problems are also reviewed: dosimetry of beta sources for intravascular brachytherapy, X-ray generation by keV electron bombardment and dose distributions in water from MeV photon and electron beams.

Introduction

PENELOPE [1] (an acronym for PENetration and Energy LOss of Positrons and Electrons... and photons) is a general-purpose Monte Carlo code for the simulation of coupled electron-photon transport in arbitrary materials (elements and compounds with atomic numbers $Z \leq 92$). It covers the energy range from 1 GeV down to (nominally) 100 eV. PENELOPE is structured as a FORTRAN77 subroutine package; the user must provide the MAIN steering program, which controls the evaluation of the histories and performs the scoring of relevant quantities. The distribution package includes tools for transport simulation in complex (quadratic) geometries and variance reduction.

Since the first release of the code in 1996, a considerable effort has been devoted to improve the adopted physical models and the electron-positron transport mechanics. The current 2001 version has recently been run in an extensive series of benchmark comparisons with experiments from the literature [2]. For moderately high energies (say, above 10 keV or so), satisfactory agreement was found in all the considered cases, thus confirming the reliability of the whole simulation scheme.

Here, some peculiarities of the adopted interaction models and electron-positron transport mechanics are considered. Results of our current research work, involving the calculation of doses from beta sources, the emission of X-ray and bremsstrahlung from targets irradiated by keV electron beams and the dosimetry of photon and electron beams, are also presented.

Interaction models

In PENELOPE, most of the interactions of electrons and photons with matter are described in terms of semi-analytical differential cross-sections (DCS), with parameters determined from the most reliable data currently available. Details of the various interaction models can be found in Ref. [1]. Here we mention only the most relevant recent improvements in interaction physics.

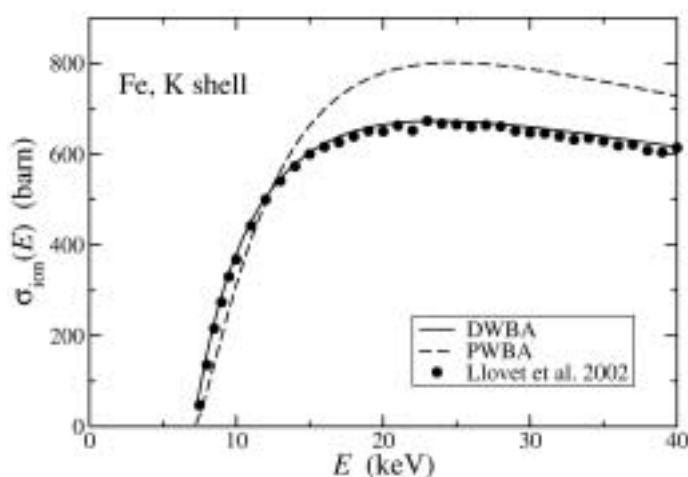
Ionisation of inner shells by electron and positron impact

To allow the simulation of characteristic X-ray emission from samples irradiated by electron beams, we have recently modified the description of inner-shell ionisation by electron impact. The default model for inelastic collisions is too schematic to describe X-ray emission with the required accuracy. Nevertheless, it does account correctly for the average stopping and energy straggling in the whole energy range. To avoid conflict with the inelastic scattering model, the ionisation of inner shells has been considered as an independent process in which the projectile produces vacancies in the inner (K and L) shells of the target atom, without losing energy or changing its direction of motion, i.e. the state of the projectile remains unaltered in ionising events. The produced ions then relax to the ground state by emission of characteristics X-rays and Auger electrons. To be consistent, the relaxation of ions after “true” inelastic collisions has been switched off. In this way, to simulate inner-shell ionisation only the total (integrated) cross-section for ionisation in each inner shell is required. These cross-sections have been calculated using an optical-data model in which the required information on the target is obtained from the partial photoelectric cross-section of the considered shell [3]. This model is essentially equivalent to the plane-wave (first) Born approximation and is also closely related to the Weizsäcker-Williams method of virtual quanta. Files with electron and positron ionisation cross-sections of the K- and L-shells for all the elements ($Z \leq 92$) have been included in the PENELOPE database.

It is worth mentioning that the plane-wave Born approximation is applicable only to projectiles with kinetic energies much higher than the ionisation energy of the active electron shell. Recently an elaborate code for calculating ionisation cross-sections using the distorted-wave Born approximation has been developed. This approach accounts for the distortion of the projectile wave functions by the field of the target and also allows a consistent description of electron exchange effects. These effects are important only when the projectile energy is comparable to the ionisation energy of the active electron shell. Figure 1 compares theoretical cross-sections for ionisation of the K-shell of iron atoms obtained from the plane-wave and distorted-wave Born approximations with results from absolute measurements by Llovet, *et al.* [4]. The distorted-wave cross-section is seen to be in excellent agreement with the experiment, while the cross-section obtained from the plane-wave Born approximation departs systematically (both in magnitude and “shape”) from the measured data. The simulations of X-ray spectra described below were performed by using ionisation cross-sections calculated by the distorted-wave method.

Figure 1. K-shell ionisation cross-sections for Fe by electron impact

The continuous and dashed curves represent results from calculations with the distorted-wave and the plane-wave Born approximations, respectively. The symbols are measured absolute ionisation cross-sections from Ref. [4].



Bremsstrahlung emission by electrons and positrons

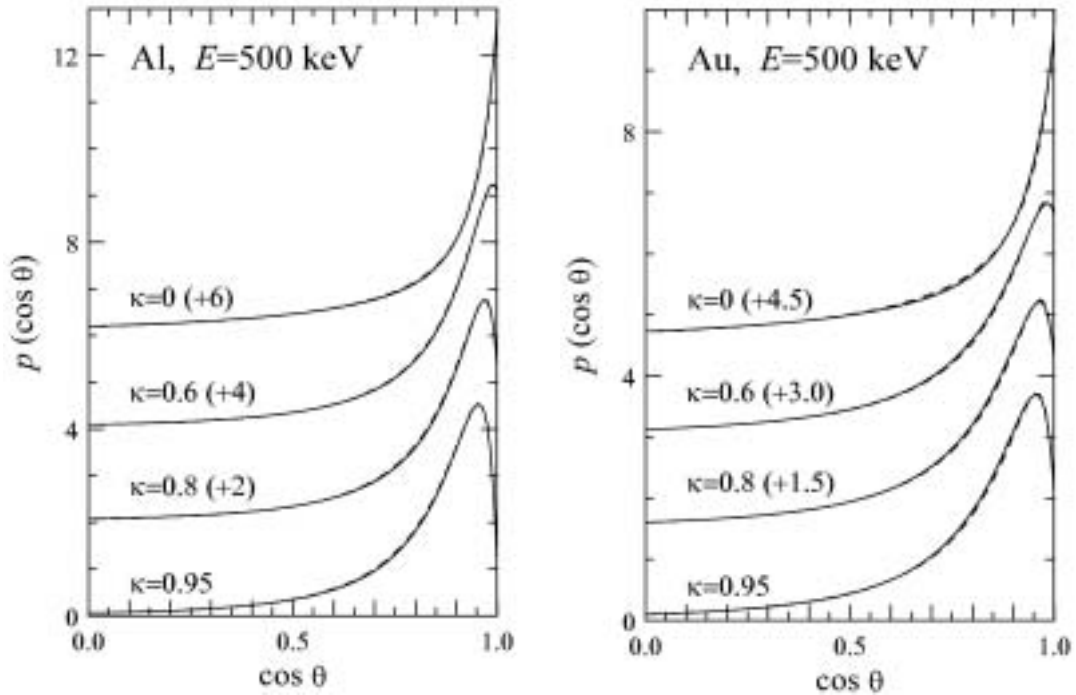
This energy-loss mechanism is described by means of the scaled (energy-loss) DCSs tabulated by Seltzer and Berger [5]. These DCSs are used both to obtain the total cross-section for bremsstrahlung emission and to sample the energy of the photons. For projectiles with energies below 500 keV, the angular distribution of emitted quanta is described by means of an analytical distribution [6] that closely reproduces the partial-wave shape functions calculated by Kissel, *et al.* [7] (see Figure 2). Thus, correlations between photon energy and direction of emission are fully accounted for. At higher energies, for which partial-wave shape functions are not available, the initial photon direction is generated from the boosted dipole distribution.

Incoherent scattering of photons

The simulation of photon Compton scattering is based on DCSs obtained from the impulse approximation [1]. These DCSs consistently account for the fact that target electrons are bound as well as for Doppler broadening (i.e. the broadening of the energy spectrum of photons scattered into a

Figure 2. Shape functions (angular distributions) for bremsstrahlung emission by 500 keV electrons in the fields of Al and Au atoms

Dashed curves are partial-wave shape functions of Kissel, et al. [7]. Continuous curves represent the analytical fits adopted in PENELOPE. For visual aid, curves have been shifted upwards in the amounts indicated in parentheses.



given direction that results from the motion of the target electrons). In Figure 3 we compare Compton DCSs, differential in the energy E' of the scattered photon, obtained from the impulse approximation and from the familiar Klein-Nishina formula, which assumes that the target electrons are free and at rest. The effect of binding causes a reduction of the DCS at large E' (the energy transfer must be larger than the ionisation energy of the target electron); due to Doppler broadening, the scattered photon may have energies substantially lower than the Klein-Nishina cut-off value. With the aid of a simple parameterisation of the Compton profiles of the different atomic electron shells, the random sampling of Compton events is performed analytically.

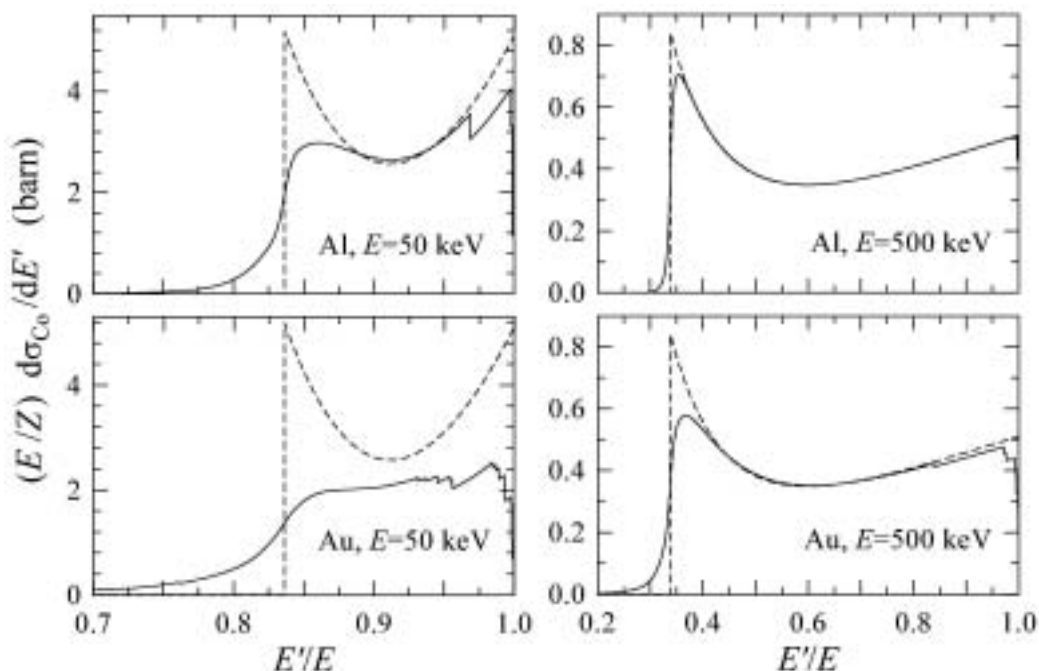
Electron transport mechanics

The most characteristic feature of PENELOPE is the use of mixed (Class II) simulation for electrons and positrons. Here, as well as in the more conventional Class I schemes, the key ingredient is the transport mechanics, i.e. the strategy followed to determine the global displacement and energy loss of an electron after a given path length s (measured along its trajectory). PENELOPE implements the so-called “random hinge” method, which is known to provide a faithful description of the combined effect of the multiple soft interactions that occur between a pair of consecutive hard interactions [1,8]. Since the latter are described individually from the corresponding DCSs, the influence of the transport mechanics on the simulation results is weaker than for Class I simulations.

The simulation is controlled by a few parameters which determine the cut-off angular deflection and energy loss that separate hard and soft interactions. In the case of elastic scattering, the cut-off deflection is defined dynamically as a function of the energy of the projectile. At low energies, the

Figure 3. Energy DCSs for Compton scattering of 50 and 500 keV photons by Al and Au atoms

The continuous curves represent the DCS obtained from the impulse approximation; the dashed curves are calculated from the Klein-Nishina formula



cut-off deflection tends to zero and the simulation of elastic events becomes purely detailed. This feature implies that PENELOPE benefits from the advantages of Class II simulation at high energies (where the cut-off value is relatively large and very few hard elastic collisions occur) and retains the accuracy of detailed simulation at low energies (where it is needed to describe the intense effect of elastic deflections).

Recently, refinements have been introduced aimed to account for the effect of the energy variation along a step on the transport parameters [1]. These energy-loss corrections lead to better accuracy and stability of the code and allow a certain relaxation of the simulation parameters. That is, the simulation can be made somewhat faster without sacrificing accuracy. It is worth mentioning here that to ensure the reliability of the results the number of steps (or soft events) along each electron history must be “statistically sufficient” (i.e. larger than ~ 10).

An important modification of the code logic has been introduced in version 2001 of PENELOPE to allow the user to limit the length of each step. The method consists in introducing “delta interactions” (i.e. virtual interactions that do not affect the state of the projectile), which occur whenever an electron exceeds the pre-selected maximum allowed step length. This gives direct control on the evolution of tracks and allows the user to perform more refined simulation in “thin” regions, where the use of large step lengths could impair the accuracy of the results.

Dosimetry of beta sources

Monte Carlo simulation has become a valuable tool for beta-source dosimetry, where measurements are difficult due to the short range of the beta particles and the associated large dose gradients. As an example, we consider the characterisation of two beta sources (^{90}Sr - ^{90}Y and ^{32}P) which are commonly

used in intravascular brachytherapy (IVBT) treatments. The conventional description of the dose distributions from linear brachytherapy sources is based on the so-called radial dose function $g(r)$, which is proportional to the radial dose multiplied by the square of the radial distance r and is normalised to unity at $r = 2$ mm. This function describes the effects of absorption and scatter along the transverse axis of the source, thus suppressing the influence of the inverse square law.

PENELOPE has been used to simulate dose distributions from a high-dose-rate ^{90}Sr - ^{90}Y source by Asenjo, *et al.* [9]. The source is a 30-mm-long train consisting of twelve seeds of 2.5 mm each. Figure 4 shows the radial dose function for a single ^{90}Sr - ^{90}Y seed in water calculated with different Monte Carlo codes: ITS3 [10], EGS4 [11] and also PENELOPE and MCNP4C [9]. The overall agreement between $g(r)$ functions obtained with the four codes is seen to be reasonable, although some differences show up at intermediate distances which are relevant to IVBT. In particular, the MCNP4C radial dose function is slightly higher than the one obtained using ITS3, and both curves are somewhat higher than the $g(r)$ function from PENELOPE. On the other hand, EGS4 yields the lowest $g(r)$ function. The differences between the simulated radial dose functions should be ascribed to the physical modelling implemented in the various Monte Carlo codes, as well as the different multiple scattering theories used.

Figure 4. Radial dose function $g(r)$ for a high-dose-rate ^{90}Sr - ^{90}Y seed in water [9]

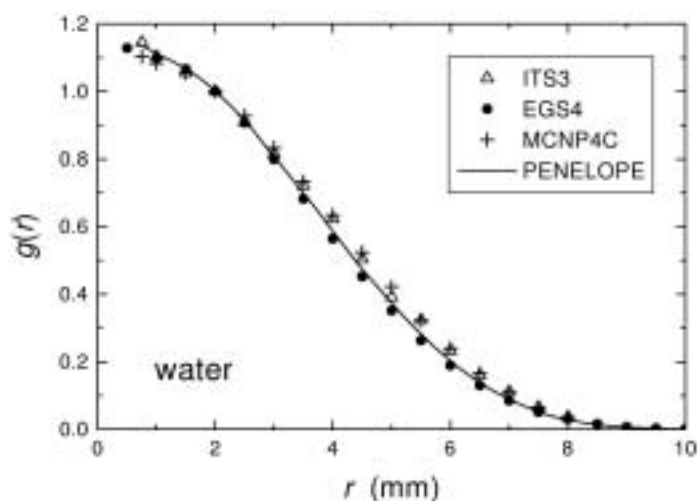


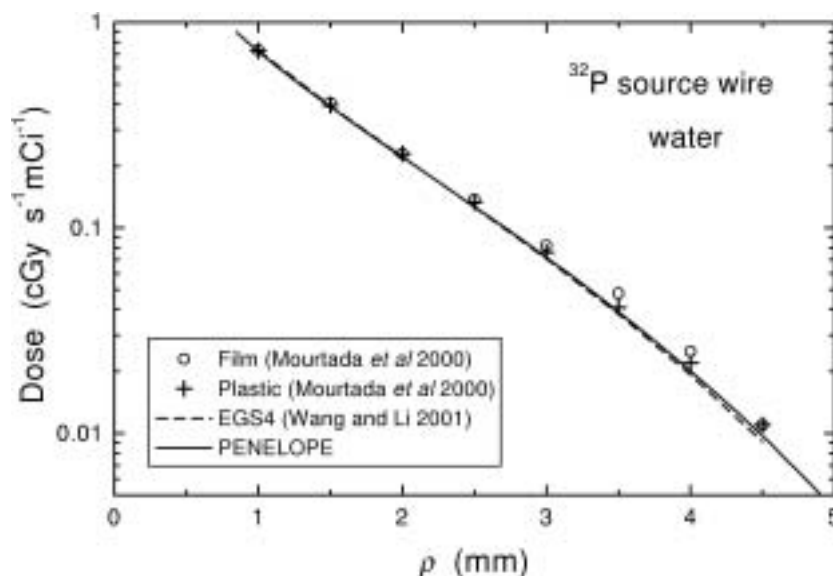
Figure 5 displays the radial dose from a 27-mm-long linear ^{32}P source at the “mid-plane” (i.e. the plane perpendicular to the source axis that crosses the source at half its height). Simulation results from PENELOPE and EGS4 [12] are compared with experimental data of Mourtada, *et al.* [13]. Both Monte Carlo curves are in reasonable agreement and reproduce quite well the experimental values obtained with plastic scintillators, whereas the radiochromic film data depart at intermediate and large depths. It is worth mentioning that the results from the scintillator are expected to be more accurate than those using film, since the latter were measured in an A-150 phantom and had to be re-scaled to yield the dose in water [13].

X-ray and bremsstrahlung emission

PENELOPE has been used intensively for the simulation of X-ray generation by keV electron beams. This kind of calculation is intrinsically very inefficient due to the fact that production events (i.e. inner-shell ionisation, bremsstrahlung emission) occur very seldom. To obtain results with low

Figure 5. Radial dose at the midplane of a 27-mm-long linear ^{32}P source wire in water

The continuous and dashed curves are simulation results using PENELOPE and EGS4 [12], respectively



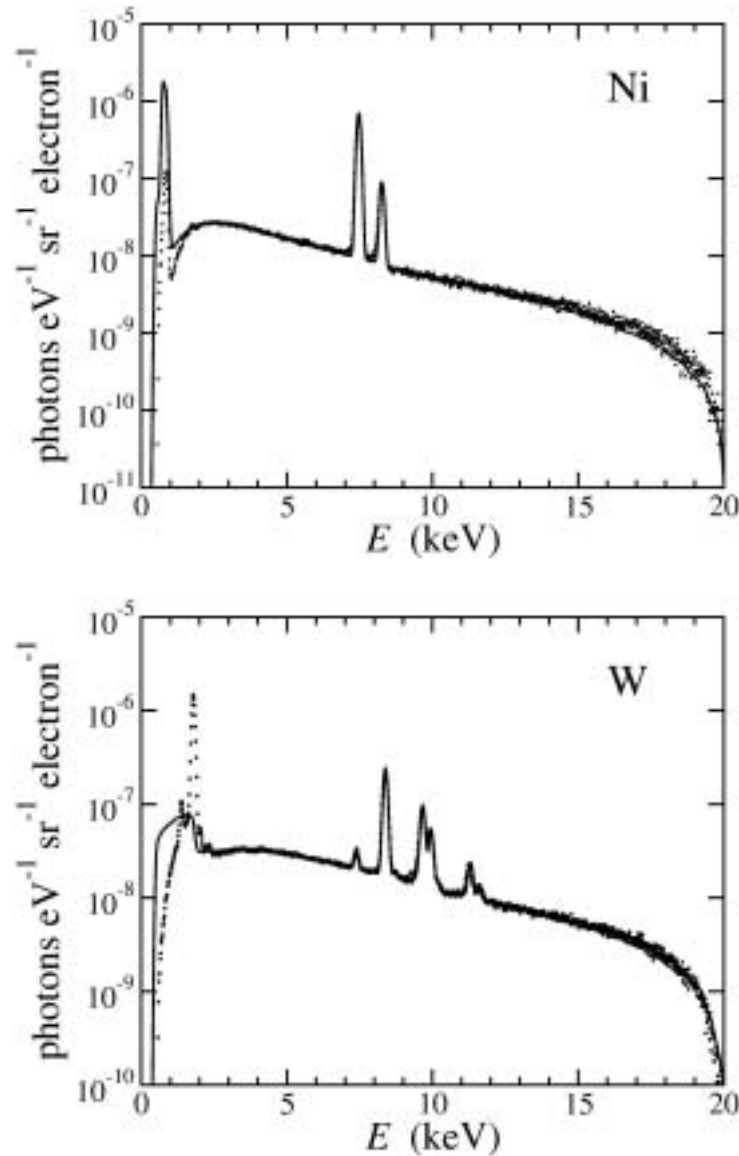
statistical uncertainties with reasonable computation times, variance-reduction techniques have to be applied. It suffices to apply interaction forcing [14], i.e. the probabilities of occurrence of the interesting processes are artificially increased and, to keep the simulation unbiased, radiations resulting from the forced interaction are assigned a weight less than unity. The result is a large gain in efficiency, i.e. a substantial reduction of the statistical uncertainty for a given calculation time.

In our studies we use X-ray spectra measured on a Cameca SX-50 electron microprobe, with a Si(Li) energy dispersive X-ray spectrometer. The electron beam impinges normally on the surface of the specimen and the detector covers a small solid angle about a direction corresponding to a take-off angle of 40 degrees. The recorded spectra are transformed into absolute units (i.e. probability of emission of a photon per unit energy, unit solid angle and incident electron) using the procedure described by Acosta, *et al.* [14]. The estimated overall uncertainties of the absolute spectra are about 4-8%.

Figure 6 compares results from PENELOPE simulations for 20 keV electron beams impinging normally on bulk samples of nickel and tungsten with absolute spectra measured under the same conditions. Results from the Monte Carlo simulations were convolved with a Gaussian distribution, with an empirical energy-dependent width, to account for the response of the detector. Notice that the simulated spectra are properly normalised (i.e. in absolute units). The experimental spectra were found to differ systematically from the simulations by a constant factor, slightly larger than unity and that increases with the atomic number of the material. The “measured” spectra plotted in Figure 6 for nickel and tungsten are the absolute spectra multiplied by 1.06 and 1.10, respectively. It should also be mentioned that PENELOPE does not simulate characteristic M lines, which are visible in the low-energy part of the measured spectrum of tungsten.

In the energy interval from ~ 3 keV to ~ 15 keV, where the intrinsic efficiency of the Si(Li) detector is nearly constant with energy, the results of the simulation are found to be in close agreement with measured absolute spectra. Outside this intermediate energy range simulation and experiment are seen to differ in a systematic way. At low energies, $E < 3$ keV, the observed discrepancies are mainly due to the loss of efficiency caused by absorption in the detector window and passive layers, which has not been accounted for.

Figure 6. Measured (dots) and simulated (solid lines) X-ray spectra from bulk samples of Ni and W generated by 20 keV electron beams at normal incidence



This kind of comparison is very useful to check the reliability of the physical models adopted in the simulation. Thus, the small differences found between the characteristic peak intensities of measured and simulated spectra indicate slight inconsistencies in the ionisation cross-sections and relaxation data adopted in the simulation. These differences could be minimised by empirically adjusting the transition rates.

Photon and electron beam dosimetry

Simulations of electron accelerators stimulated the development of several parts of PENELOPE. The first application of the code to this field was the work of Mazurier, *et al.* [15] on the dosimetry of photon beams from a Saturne 43 accelerator. They found almost perfect agreement between simulation results and their experimental data.

Dose distributions in water produced by electron beams from a Siemens Mevatron KDS linac, located at the Hospital Clínic de Barcelona, were measured and compared with simulation results [16]. The measurements were performed using an ion chamber and a silicon detector. The Monte Carlo simulations, on the other hand, were carried out by splitting the problem into two parts. First, the transport of radiation through the accelerator head was considered in detail and the state variables of all particles exiting the system were stored in the so-called phase space file (PSF). This first simulation step characterises the radiation “source”. In a second stage, these particle states were read from the PSF and the simulation was continued through air (and possible filtering materials) and a semi-infinite water phantom, thus modelling the complete experimental set-up. This two-step technique permits a substantial reduction in the calculation time because it allows re-using the PSF for different downstream geometries without having to recalculate the source characteristics.

Measurements and simulations were performed for electron beams with different nominal energies. In Figure 7, the energy deposited per unit depth in water by a 6 MeV electron beam is represented as a function of depth in water. Since the absolute value of the deposited energy per incident electron is usually not known experimentally, it is common to normalise depth doses to their maximum. In a second series of experiments, the accelerator beam was partially blocked up by a 3.1-mm-thick Cu slab, thus causing a strongly varying flux gradient across the radiation field. This obstruction produced interesting lateral dose profiles in the water phantom, as shown in Figure 8.

Besides simulation convenience, another advantage of splitting the simulation into two steps is that some relevant features of the beam can be readily obtained from the PSF. In Figure 9, the spectrum of contaminating photons, mainly produced by bremsstrahlung emission in the metallic bodies that limit the beam inside the accelerator head, is displayed. In this case, PENELOPE is compared with the well-known Monte Carlo code EGS4/PRESTA.

Figure 7. Measured (dots) and simulated (solid line) relative depth-dose of a 6 MeV electron beam from the Siemens Mevatron KDS linac in water

The dashed line corresponds to the difference between PENELOPE results and the experimental data

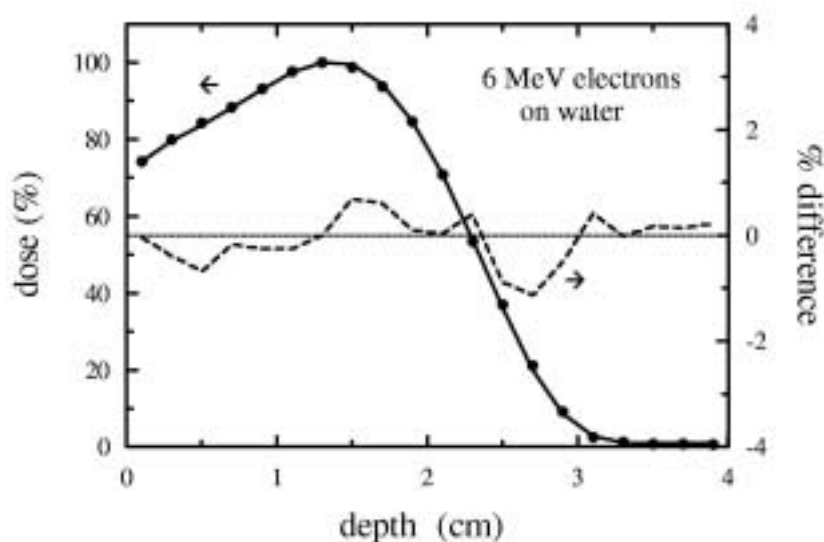


Figure 8. Measured (symbols) and simulated (solid lines) lateral dose profiles of a $10 \times 10 \text{ cm}^2$, 12 MeV electron beam from the Siemens Mevatron KDS linac at different depths in water. The right half of the beam was blocked up by a 3.1-mm-thick Cu slab.

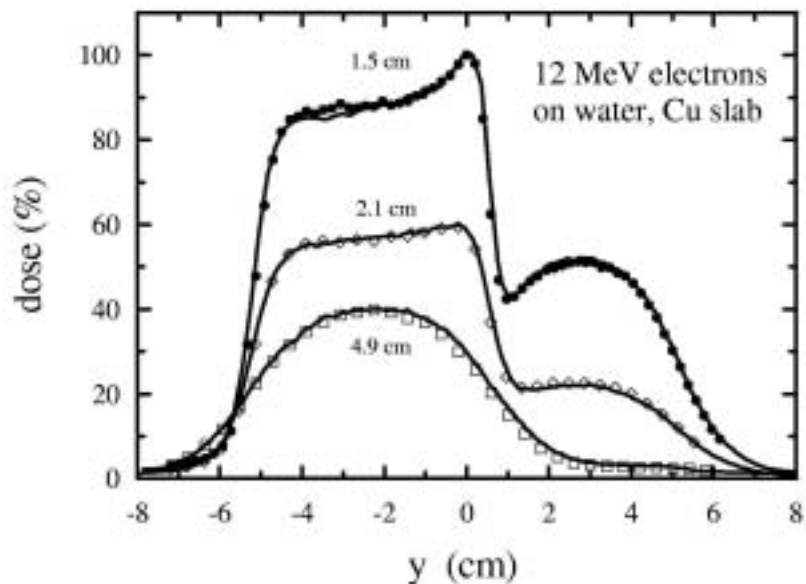
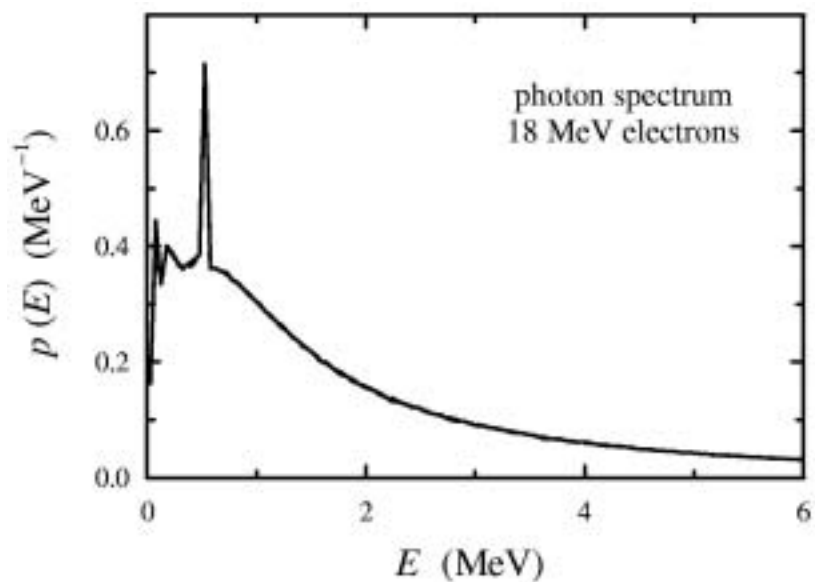


Figure 9. Spectrum of photons in the PSF of an 18 MeV electron beam

Solid and dashed curves are results from simulations with PENELOPE and EGS4/PRESTA, respectively. The two spectra were normalised to unity.



Acknowledgements

This work has been partially supported by the Spanish *Fondo de Investigación Sanitaria*, project nos. 00/1070 and 01/0093.

REFERENCES

- [1] Salvat, F., J.M. Fernández-Varea, E. Acosta and J. Sempau, *PENELOPE, A Code System for Monte Carlo Simulation of Electron and Photon Transport*, OECD/Nuclear Energy Agency, Issy-les-Moulineaux, France (2001). Also available in PDF format from <http://www.nea.fr>.
- [2] Sempau, J., J.M. Fernández-Varea, E. Acosta and F. Salvat, “Experimental Benchmarks of the Electron Transport Algorithms Implemented in PENELOPE”, *Nucl. Instrum. Meth. B*, in press.
- [3] Cullen, D.E., J.H. Hubbell and L. Kissel, *EPDL97: The Evaluated Photon Data Library, '97 Version*, Lawrence Livermore National Laboratory Report UCRL-50400, Vol. 6, Rev. 5 (1997).
- [4] Llovet, X., C. Merlet and F. Salvat, “Measurements of Absolute Cross-sections for K-shell Ionization of Fe and Mn by Electron Impact”, *J. Phys. B: At. Mol. Opt. Phys.*, 35, 973-982 (2002).
- [5] Seltzer, S.M. and M.J. Berger, “Bremsstrahlung Energy Spectra from Electrons with Kinetic Energy 1 keV-10 GeV Incident on Screened Nuclei and Orbital Electrons of Neutral Atoms with $Z = 1-100$ ”, *At. Data Nucl. Data Tables*, 35, 345-418 (1986).
- [6] Acosta, E., X. Llovet and F. Salvat, “Monte Carlo Simulation of Bremsstrahlung Emission by Electrons”, *Appl. Phys. Lett.*, 80, 3228-3230 (2002).
- [7] Kissel, L., C.A. Quarles and R.H. Pratt, “Shape Functions for Atomic-field Bremsstrahlung from Electrons of Kinetic Energy 1-500 keV on Selected Neutral Atoms $1 \leq Z \leq 92$ ”, *At. Data Nucl. Data Tables*, 28, 381-460 (1983).
- [8] Bielajew, A.F. and F. Salvat, “Improved Electron Transport Mechanics in the PENELOPE Monte Carlo Model”, *Nucl. Instrum. Meth. B*, 173, 332-343 (2001).
- [9] Asenjo, J., J.M. Fernández-Varea and A. Sánchez-Reyes, “Characterization of a High-dose-rate ^{90}Sr - ^{90}Y Source for Intravascular Brachytherapy by Using the Monte Carlo Code PENELOPE”, *Phys. Med. Biol.*, 47, 697-711 (2002); Asenjo, J., J.M. Fernández-Varea, A. Sánchez-Reyes and C-K. Wang, “Radial Dose Function of a ^{90}Sr - ^{90}Y Seed in Water and A150: Comment on “Calibration and Characterization of Beta-particle Sources for Intravascular Brachytherapy””, *Med. Phys.*, 25, 339-346 (1998), *Med. Phys.* (in press).
- [10] Soares, C.G., D.G. Halpern and C-K. Wang, “Calibration and Characterization of Beta-particle Sources for Intravascular Brachytherapy”, *Med. Phys.*, 25, 339-346 (1998).
- [11] Wang, R. and X.A. Li, “A Monte Carlo Calculation of Dosimetric Parameters of $^{90}\text{Sr}/^{90}\text{Y}$ and ^{192}Ir SS Sources for Intravascular Brachytherapy”, *Med. Phys.*, 27, 2528-2535 (2000).
- [12] Wang, R. and X.A. Li, “Monte Carlo Characterization of a ^{32}P for Intravascular Brachytherapy”, *Med. Phys.*, 28, 1776-1785 (2001).

- [13] Mourtada, F.A., C.G. Soares, S.M. Seltzer and S.H. Lott, "Dosimetry Characterization of ^{32}P Catheter-based Vascular Brachytherapy Source Wire", *Med. Phys.*, 27, 1770-1776 (2000).
- [14] Acosta, E., X. Llovet, E. Coleoni, J.A. Riveros and F. Salvat, "Monte Carlo Simulation of X-ray Emission by Kilovolt Electron Bombardment", *J. Appl. Phys.*, 83, 6038-6049 (1998).
- [15] Mazurier, J., F. Salvat, B. Chauvenet and J. Barthe, "Simulation of Photon Beams from a Saturne 43 Accelerator Using the Code PENELOPE", *Phys. Med.*, 15, 101-110 (1999).
- [16] Sempau, J., A. Sánchez-Reyes, F. Salvat, H. Oulad ben Tahar, S.B. Jiang, J.M. Fernández-Varea, "Monte Carlo Simulation of Electron Beams from an Accelerator Head Using PENELOPE", *Phys. Med. Biol.*, 46, 1163-1186 (2001).

SESSION III

Chair: A.E. Nahum

TRACK STRUCTURE SIMULATION: A BASIC TOOL FOR MOLECULAR RADIATION BIOLOGY AND NANODOSIMETRY

Bernd Grosswendt

Physikalisch-Technische Bundesanstalt, Germany

Abstract

As is well known from radiation chemistry, the kinetics of radiation-induced systems strongly depends on the distribution of atomic or molecular species produced by primary interactions of ionising radiation in matter or, and this is the same, on the particle track structure. Far-reaching consequences can also be expected, therefore, if biological systems are exposed to ionising radiation, the more so as the radiation-sensitive parts of such systems are located inside highly structured cells. In consequence, the knowledge of track structure is one of the prerequisites for a deeper understanding of radiation-induced effects in radiation chemistry and radiation biology.

After a short overview of basic physical aspects of the track structure of electrons, photons and light ions (protons, α -particles, carbon ions) in liquid water, a few consequences of their radiation interaction in nanometric volumes are discussed, which can be related to radiation damage within segments of the DNA molecule and to bio-effect cross-sections of mammalian cells for ionising particles. Here, special emphasis is laid on the stochastic nature of ionisation cluster-size formation in liquid water and on its potential application in nanodosimetric measurements.

Introduction

Inspecting the commonly applied procedures for simulating the penetration of electrons through matter (as, for instance, in MCNP or EGS4), it should be stated that none of them is suited for track structure calculations. This is because they are based, more or less exclusively, on condensed-history models (see the overview by Grosswendt [1]). These models treat the whole set of low-energy transfer interactions within the framework of the continuous-slowing-down approximation which assumes continuous energy losses along straight path segments and is not able to distinguish interaction points of low energy transfers. Since such models are focused simply on energy transfer, they are also not usable for treating the yield of different kinds of target species produced by electron interactions (ionised atoms or molecules, atoms or molecules at specified excitation states, dissociation products). In consequence, condensed-history models cannot be employed to solve problems which are sensitive, for instance, to the distance distribution of target species produced by a series of successive electron interactions representing the structure of an electron track segment. Examples of such problems are the damage to sub-cellular structures in radiation biology and the dynamics of chemical reaction chains in radiation chemistry, which strongly depend on the spatial distribution of radiation-induced target species. Here, it is commonly accepted that the track structure of ionising particles represents the starting point for the induction of many radio-biological or radio-chemical effects.

To support this hypothesis, let us first assume a narrow beam of monoenergetic 100 keV photons penetrating the front face of a water cylinder, 20 cm in diameter and height, along the cylinder's main axis. If one were able to follow by eye the path each photon takes within the phantom after having penetrated its front face, a picture like that shown in Figure 1 would be seen: the photons are scattered elastically by Rayleigh scattering or inelastically by Compton scattering, transferring part of their initial energy to secondary electrons, or they are absorbed by the photoelectric effect and leave the greater part of their energy to photoelectrons. In consequence, a great number of secondary electrons is set in motion during photon slow-down whose starting points, due to the large mean free interaction length of photons and due to their strong angular scattering ability, are distributed over the whole volume of the water cylinder. If one were also able to track the paths of secondary electrons through the phantom, a picture like that presented in Figure 2 would be seen: the electron paths appear only as more or less extended small spots, showing that the ranges of secondary electrons are generally much smaller than the mean free path lengths of photons. To demonstrate this fact quantitatively, Figure 3 shows the mean free interaction length $\lambda_{\text{tot}}(T)$ of photons and the continuous-slowing-down range

Figure 1. Movement of 100 keV photons in a water cylinder in the case of perpendicular incidence along the phantom's main axis

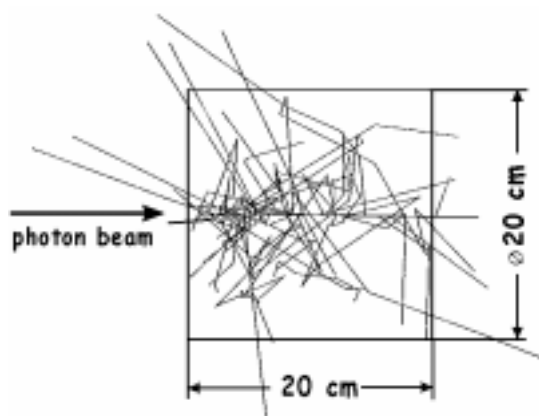


Figure 2. Tracks of secondary electrons liberated in water by the 100 keV photons of Figure 1

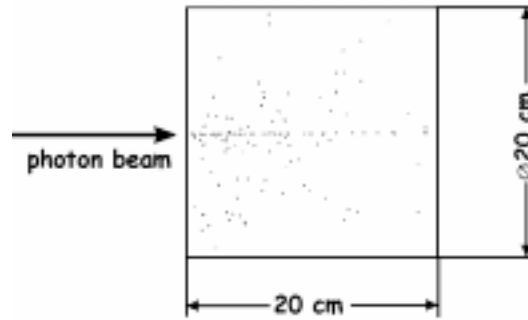
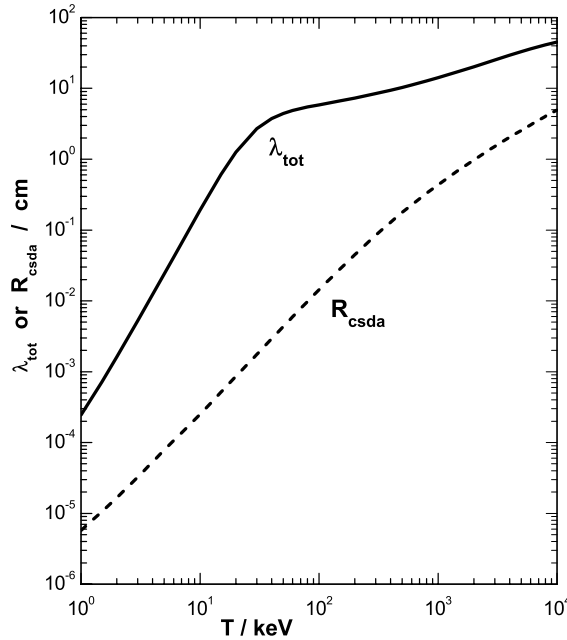


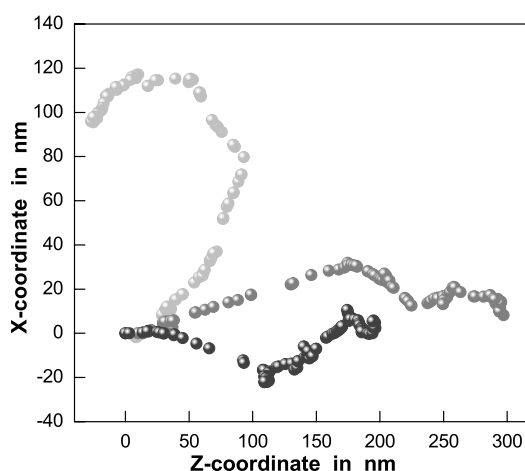
Figure 3. Mean free interaction length λ_{tot} of photons at energy T in water, in comparison with the continuous-slowing-down range R_{csda} of electrons at the same energy



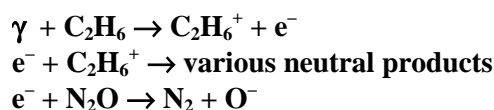
$R_{\text{csda}}(T)$ of electrons in liquid water, as a function of the primary particle energy T . The great difference between $R_{\text{csda}}(T)$ and $\lambda_{\text{tot}}(T)$ is obvious from the figure. At the same initial energy the mean free photon interaction length is greater than the electron range by a factor of up to 10^3 . Due to the large number of interactions an electron suffers upon its complete slow-down. An electron path, however, is highly structured. To give an example, Figure 4 shows the projection of the spatial distribution of ionisation events of three electrons at 2.72 keV in liquid water, on a nanometre scale. The entity of all ionisation events caused by each electron upon its complete degradation looks like a string of beads and is quite different from a homogeneous distribution which is implicitly assumed if radiation quality is defined on the basis of macroscopic-quantities-like absorbed dose.

Bearing these facts in mind, let us now repeat the radio-chemical experiment of Robinson and Freeman [2] who irradiated a dilute solution of nitrous oxide in liquid ethane with an absorbed dose of 765 Gy of ^{60}Co - γ -radiation and measured the yield of molecular nitrogen as a function of the nitrous oxide concentration. Due to photon interactions in the liquid, ionised ethane molecules are formed which are accompanied by secondary electrons. These electrons are degraded in ethane by excitation

Figure 4. Projection of the spatial distribution of ionisation events of three 2.72 keV electrons in liquid water

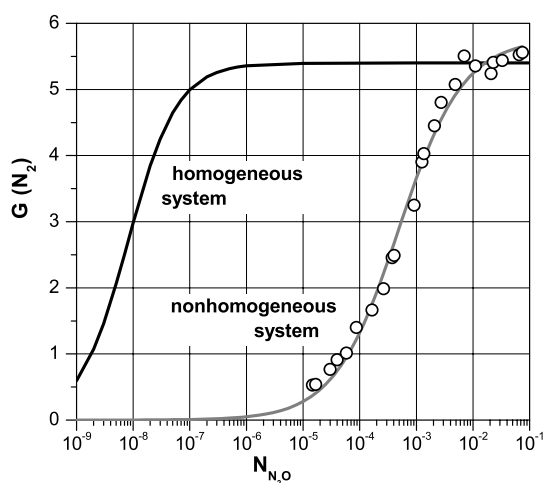


or ionisation processes forming additional pairs of ionised ethane molecules and electrons at lower energies. At thermal energies, the electrons interact with the ionised ethane molecules forming various neutral products or they interact with the nitrous oxide molecules to form molecular nitrogen. Molecular nitrogen is thus produced according to the following chemical reaction chain:



The result of the measurements is presented in Figure 5. It shows the mean number $G(\text{N}_2)$ of nitrogen molecules formed per 100 eV absorbed energy in the nitrous-oxide/ethane solution, as a function of the mole fraction $N_{\text{N}_2\text{O}}$ of nitrous oxide. Whereas the symbols represent the results of the measurement, the unbroken curve shows the yield of molecular nitrogen if one assumes that thermalised electrons, ethane ions and nitrous oxide molecules are homogeneously distributed over the irradiated sample [3]. Common to both data sets is that, with increasing nitrous oxide concentration, the yield of

Figure 5. Mean number $G(\text{N}_2)$ of N_2 molecules formed per 100 eV absorbed energy in a $\text{C}_2\text{H}_6\text{-N}_2\text{O}$ solution, as a function of the mole fraction of N_2O



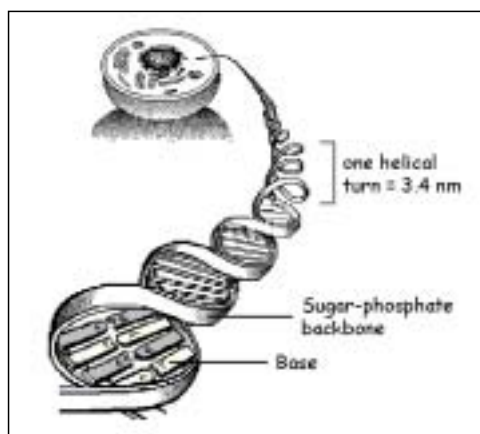
molecular nitrogen first increases and reaches a limiting value afterwards. The inset of the measured increase of the nitrogen yield as compared with that expected for a homogeneous distribution of reaction species is, however, markedly shifted to higher values of the nitrous oxide concentration. This can be explained by the fact that, in consequence of the track structure of electrons, the dilute solution of nitrous oxide in liquid ethane is transformed from a homogeneous system into a system with a non-homogeneous distribution of ethane ions and thermalised electrons. As compared with the homogeneous system, the number of ions in the neighbourhood of a thermalised electron is increased in the non-homogeneous system. Hence, the probability of electron-ion recombination in such a system is always greater than that of electron interactions with nitrous oxide molecules. To get the same nitrogen yield as in the homogeneous system, therefore, the nitrous oxide concentration must be markedly increased.

The role of track structure in radiation biology

The interpretation of the radio-chemical experiment of Robinson and Freeman can be generalised to any other irradiated system. By inelastic interactions of primary particles (photons, electrons, light ions) or by interactions of secondary electrons with the atoms or molecules of irradiated matter, a non-random distribution of ionised or excited species is produced and, in general, also a distribution of neutral, ionised or excited fragments. All of these irradiation products can interact with each other, with thermalised electrons or with neutral constituents in their neighbourhood with a probability which depends on the distance between the different potential reactants. In consequence, the development of the irradiated system with time strongly depends on the species occurring and on the spatial distributions of their number density produced by radiation interaction.

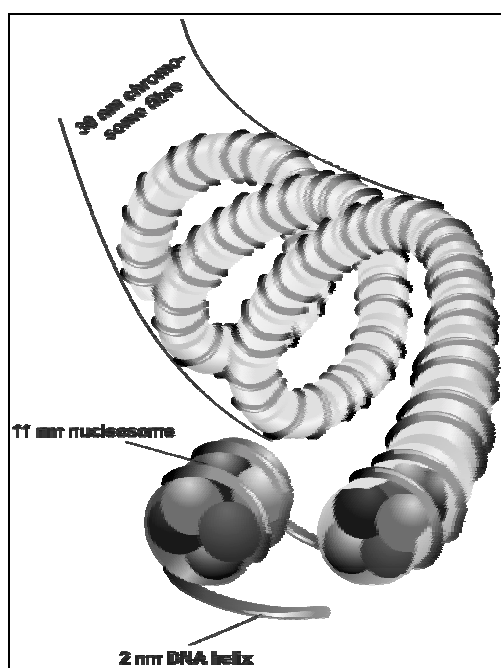
The importance of the spatial distribution of interaction events is even more obvious if one considers, instead of the irradiation of a homogeneous system, the irradiation of an initially non-homogeneous system consisting of micro-heterogeneities embedded in a homogenous medium. Examples of such systems are cell nuclei or the DNA molecule which can be assumed, in a living cell, to be surrounded by liquid water. Segments of the DNA are commonly accepted to represent the most important radiation-sensitive targets of biological systems, and the induction of double-strand breaks within the DNA to represent the most critical radiation damage. To give an impression of its microstructure, Figure 6 shows a schematic view of the double helix of DNA, consisting of a sugar-phosphate backbone and a long series of successive base pairs at a distance of 0.34 nm. The double helix has a diameter of about 2 nm, and one helical turn covers a distance of about 3.4 nm.

Figure 6. Schematic view of the double helix of DNA



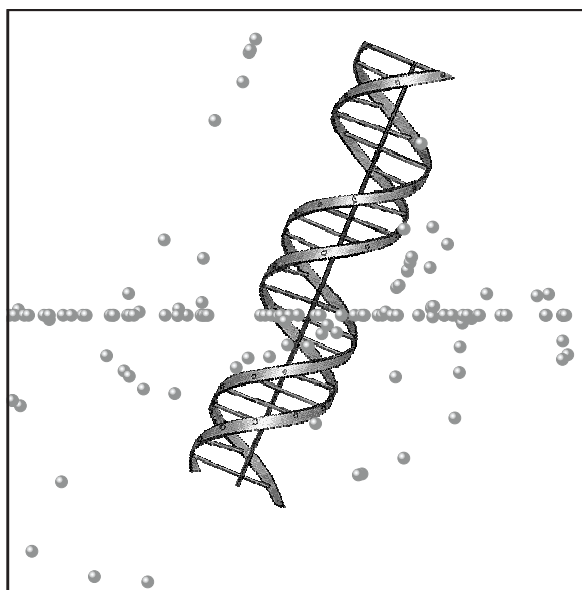
A rough sketch of the structure of a chromosome fibre is presented in Figure 7. Here, the DNA is wrapped around a nucleosome core (about 7 nm in diameter and composed of eight histone proteins) and forms a cylindrical structure, about 11 nm in diameter. The nucleosomes are packed together forming the chromosome fibre, which has a diameter of about 30 nm. For details on the geometrical structure of DNA and of higher order structures of chromosomes (nucleosome, chromosome fibre) see, for instance, the overview by Friedland, *et al.* [4]. If such complicated systems are irradiated by ionising radiation, irradiation products may occur by radiation interaction with the constituents of the micro-heterogeneities or by interaction of the latter with radiation-induced products of the surrounding water as, for instance, OH radicals. Since the probability of such interactions strongly increases with decreasing distance of the interacting species, radiation damage to the heterogeneities also depends strongly on the number density of the reactants. Hence, it appears, at least, questionable to base the effects of ionising radiation exclusively on the spatial distribution of absorbed dose, as is common practice in the fields of protection against ionising radiation and of dosimetry for therapy purposes. Because of its definition as the mean specific energy in a vanishing but still macroscopic volume of specified mass [5], the quantity absorbed dose applies without any restriction only to homogeneous systems and does not take into account microscopic geometrical structures or the track structure of ionising particles. It is therefore really doubtful, as pointed out by Paretzke [6], whether quantities exclusively based on absorbed dose actually provide a physical measure to correlate with actual or potential radiation-induced effects because their induction and time development may strongly depend on the track structure of ionising radiation. From the point of view of numerical radiation biology, therefore, a track-structure-simulation procedure is needed which also takes into account the micro-heterogenic structure of an irradiated medium.

Figure 7. Schematic view of the structure of the chromosome fibre



A reasonable approach for this purpose is the idea that the greater part of radiation damage to biological systems is induced by the overlay of the track structure of ionising radiation and of the geometrical structure of DNA. To give an impression of this procedure, Figure 8 shows an overlay of a segment of DNA and of a track segment of one 60 MeV carbon ion in liquid water. Here, the particle's track structure is represented by the ensemble of interaction points due to ionising interactions

Figure 8. Overlay of a 10 nm track segment of one 60 MeV carbon ion in liquid water and a segment of DNA

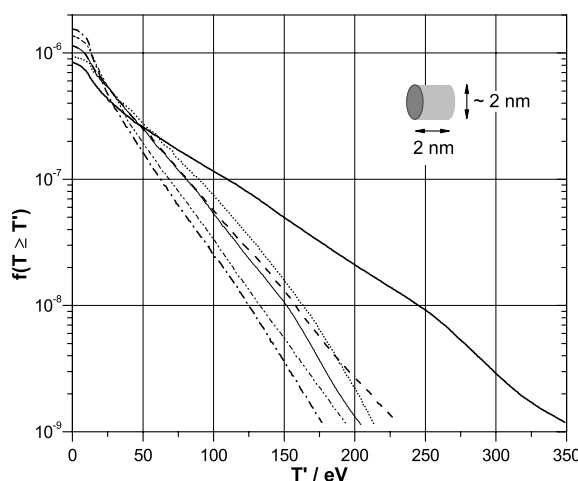


of the carbon ions along a travelling length of 10 nm or due to ionising interactions of the accompanying secondary electrons. Ionisation damage to the DNA can be studied by randomly positioning the DNA segment within a volume covering the particle's track segment and by counting the number of ionisations directly occurring within the DNA segment. For details of this procedure and of more sophisticated methods which also take into account the atomic structure of DNA, see the overviews on the computational modelling of radiation-induced DNA damage by Nikjoo, *et al.* [7,8] and for the time development of track structure, in particular, the publication by Pomplun and Terrissol [9].

The simplest model used in the past for the investigation of radiation damage to sub-cellular structures is their approximation by homogeneous cylinders. This model has been used, for instance, by Goodhead and Nikjoo [10] to determine the frequencies of energy deposition in DNA segments, nucleosomes, and segments of the chromosome fibre by low-energy X-rays, 100 keV electrons, 0.5 MeV protons and 3 MeV α -particles. Figure 9 shows their results for the frequency $f(T \geq T')$ of energy deposition T greater than or equal to T' in a single cylinder, 2 nm in diameter and height, randomly positioned in water, which is irradiated by six different radiation qualities at an absorbed dose of 1 Gy. Common to all radiation qualities, the frequency of energy deposition in the DNA-sized target strongly decreases with increasing T' . If one analyses, however, the gradient of the frequency curves, a dependence on radiation quality is obvious. The decrease of the frequency with increasing limit T' of energy deposition is greatest for the 100 keV electrons and smallest for the 3 MeV α -particles. In the case of an energy deposition T of greater than or equal to 100 eV, for instance, the deposition frequency is highest for the 3 MeV α -particles; in order of its amount, this frequency is followed by that for carbon X-rays, 0.5 MeV protons, aluminium X-rays, titanium X-rays and finally by that for the 100 keV electrons. As pointed out by Goodhead and Nikjoo [10], this order of energy deposition frequencies resembles the general sequence of the radio-biological effectiveness of the investigated radiation qualities in producing double-strand breaks, cell killing and other cellular effects. Here, the comparably high effectiveness of low-energy electrons (represented by the carbon X-rays) is of particular interest.

Figure 9. Frequency $f(T \geq T')$ of energy deposition T greater than or equal to T' in a single cylinder, 2 nm in diameter and height, randomly positioned in water

(—) 3 MeV α -particles, (•••) carbon X-rays, (- - -) 0.5 MeV protons,
 (—) aluminium X-rays, (- · · -) titanium X-rays, (-•-) 100 keV electrons

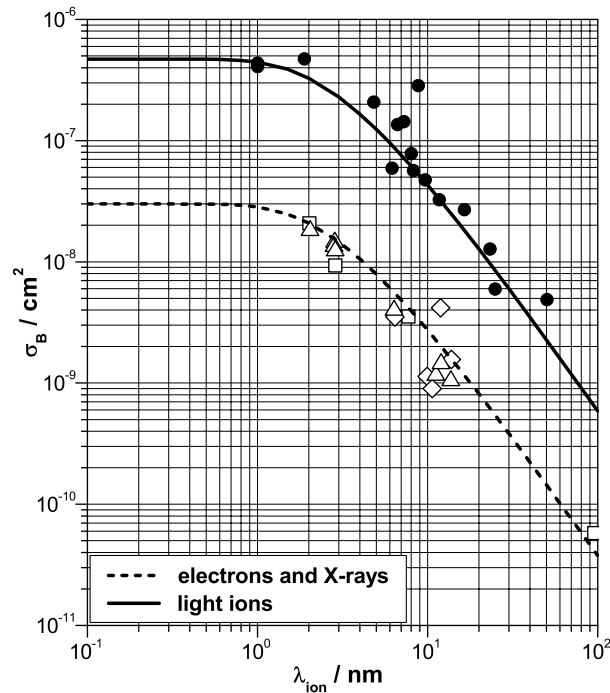


But, as regards radiation damage to biological systems, there is the still unanswered question of which type of interaction effect is the most important one and can be made responsible for the greater part of the effectiveness of ionising radiation. There are, however, some hints that impact ionisation is the most critical effect. As was shown, for instance, by Brenner and Ward [11], the yields of clusters of multiple ionisations produced by ionising radiation of different quality within sites 2-3 nm in size correlate well with observed yields of double-strand breaks. Through the analysis of ionisation clusters, it was concluded that two ionisations are required for the induction of one double-strand break of DNA. Similarly, by modelling DNA damage induced by Auger electrons of incorporated ^{125}I , Nikjoo, *et al.* [12] it was found that two ionisations are necessary to induce one single-strand break and four ionisations to induce one double-strand break. We can, therefore, assume that the ionisation process is the most important interaction effect as regards radiation damage to DNA. This assumption is also suggested by the dependence of bio-effect cross-sections σ_B on the mean free path length λ_{ion} of different radiation qualities with respect to primary ionisation in liquid water, as discussed in detail by Simmons and Watt [13]. They found out that the cross-sections of some types of mammalian cells (see Figure 10) scale much better with λ_{ion} than with linear-energy transfer, which is usually applied in microdosimetry. The saturation for $\lambda_{\text{ion}} < 2$ nm and the strong decrease of σ_B with increasing λ_{ion} implies that, to explain σ_B , at least two ionisations must be produced within a length of 2 nm, which nicely corresponds with the diameter of DNA.

The simulation of track structure of photons, electrons and light ions

As discussed, one indispensable prerequisite for a detailed understanding of radiation-induced effects in matter is the knowledge of the spatial distribution of target species, which are initially produced by single ionising particles during their penetration through matter. One of the most important tasks of applied radiation research is, therefore, the simulation of the track structure of ionising radiation. Here, the track is defined as the totality of interaction points of a particle in matter supplemented by the types of accompanying interactions or by the generated kinds of target species (ionised or excited molecules, dissociation products).

Figure 10. Bio-effect cross-section σ_B [13] of some types of mammalian cells as a function of the mean free ionisation path length λ_{ion} of ionising particles in liquid water



Photons

The track-structure simulation for photons is based, in a first step, on macroscopic interaction cross-sections (the so-called linear attenuation coefficients) and performed by following the path, which each photon actually travels through matter, from one interaction point to the other. In a second step, the energy transport by secondary particles is simulated. In this connection, the setting-in-motion of secondary particles and the scattering of photons at each interaction point are taken into account using theoretical models which more or less nicely agree with experimental data. It can, therefore, be assumed that the spatial distribution of photon interactions and the energies and directions of secondary particles liberated at each interaction point are reasonably well sampled when the usual procedures are followed. Due to the fact that the mean photon interaction length is generally much longer than the range of liberated secondary electrons (see Figure 3), a photon track can be assumed to be a collection of single electron tracks the starting points of which are distributed over comparably long distances. The key problem of photon-track-structure simulation is, therefore, the simulation of the structure of electron tracks.

Electrons

As stated in the introduction, condensed-history models which are commonly employed for simulating the penetration of electrons through matter are not suited for track-structure calculations because they treat the whole set of low-energy transfer interactions within the framework of the continuous-slowing-down approximation which assumes continuous energy losses along straight path segments and bundles together all energy transfers smaller than a predefined energy limit. This cut-off energy is, as a rule, at least of the order of a few keV and covers the major part of all electron

interactions occurring. It is, therefore, the contribution of low-energy electrons that prevents the use of the commonly applied Monte Carlo procedures to also calculate the track structure of electrons and photons. This contribution is, however, of particular importance since:

- Low-energy electrons are produced in an enormous number during the slow-down of any kind of ionising radiation.
- Their stopping power is comparable to that of heavy charged particles.
- Their range is of the same order or even markedly smaller than the sizes of sub-cellular structures.

As a result, any pair of succeeding interaction points of low-energy electrons is separated by small distances and may decisively influence the time development of radiation-induced non-homogeneous systems (see discussion above) and, in consequence, also potential chemical reaction yields or the creation of radiation damage.

To calculate the track structure of electrons, the electron degradation in matter must be simulated from one interaction point to the other, taking into account elastic electron scattering, impact excitation and impact ionisation. At each point of interaction, the electron's flight direction in the case of elastic scattering or its energy loss and flight direction in the case of inelastic scattering is to be calculated, including the kind of target species produced. These data must be supplemented by the energies and flight directions of secondary particles set in motion by the scattering process. The main steps necessary to follow the histories of electrons are, therefore:

- The determination of the distance to the subsequent point of interaction.
- The determination of the type of interaction the electron suffers at this point.
- The sampling of the energy loss and the new flight direction caused by the selected interaction process, possibly supplemented by the energies and flight directions of secondary particles.

If we suppose that the target molecules can be treated as independent points homogeneously distributed in space, the travelling length of an electron at energy T between two successive interaction points is governed by an exponential probability density characterised by the mean free path length concerning electron scattering. This mean free path length is given by the reciprocal macroscopic total scattering cross-section which is equal to the sum of the macroscopic cross-sections with respect to elastic scattering, of the significant excitation processes and of impact ionisation. If external electromagnetic fields are not taken into account, it can be assumed that the electrons travel along straight lines which connect successive interaction points.

The type of event an electron suffers at each interaction point is sampled from the discrete probabilities of interaction effects taken into account in the calculation. These probabilities are given by the ratios of cross-sections with respect to a specified interaction process to that of total electron scattering. In the case of elastic interaction, the polar angle of the electron's flight direction after scattering relative to its initial direction is determined on the basis of the differential elastic cross-section, assuming in addition that the azimuthal scattering angle is uniformly distributed between 0 and 2π . If excitation to a particular state has been selected, the initial electron energy must be reduced by the excitation energy required for the process, assuming, however, that the electron direction remains unchanged. In the case of impact ionisation (only single ionisation is commonly taken into account), a secondary electron is liberated which may be able to contribute to the energy

transport and which must, therefore, be treated in the same way as the primary electron. For this purpose, not only the energy loss and the direction of the initial electron after impact ionisation must be determined but also the energy and direction of the secondaries.

The complete history of a primary electron is simulated as long as its energy has been degraded to a value smaller than the lowest threshold energy of inelastic interaction processes which might be of importance for the problem studied. If, for instance, the ionisation process is assumed to be the decisive interaction effect, the cut-off energy is equal to the ionisation threshold. The degradation of secondary electrons is treated like that of the primaries if their initial energy is greater than the pre-defined energy threshold; otherwise it is assumed that they come to rest directly at their source point. This latter assumption is also made in the case of photons emitted after excitation events, apart from the excitation of Rydberg states which may lead to auto-ionisation. For details of the treatment of electron interactions see, for instance, the publications by Paretzke [6], Terrissol [14], Grosswendt and Waibel [15], Zaider, *et al.* [16], Lappa, *et al.* [17], Uehara, *et al.* [18], Pimblott, *et al.* [19] Nikjoo, *et al.* [20], Bigildeev and Michalik [21], Grosswendt and Pszona [22], and De Nardo, *et al.* [23].

Light ions (protons, α -particles, bare carbon ions)

Apart from special applications, the main interest in the track structure of protons, α -particles and carbon ions is that of projectiles at reduced energies of higher than 1 MeV/u. The range of these particles is greater than 25 μm and thus much longer than the diameter of cell nuclei. In view of such long ranges and of the fact that the diameter of a segment of DNA is about 2 nm, and the diameter of a nucleosome or of a chromosome-fibre segment about 11 nm or 30 nm, it is necessary to perform track-structure simulations only for track segments about 100 nm in length, at least, for the most part. In consequence of the projectiles' collision stopping power and of their detour factor [24], it can be assumed that along such short segments the influence of elastic scattering on the particles' energy and flight direction, and the change of the primary particles' energy due to impact ionisation or excitation can be neglected. In addition, it follows from the minor influence which charge changing processes of higher-energy protons exert on their W-value [25] that it is unnecessary to take them into account.

In view of these facts and if only the ionisation component of track structure is taken into account, the structure of α -particle track segments at an energy of a few MeV is almost exclusively based on their ionisation cross-section, on the spectral and angular distribution of secondary electrons produced by impact ionisation and on the properties of secondary electron degradation. The main steps of the simulation of their track segments are therefore:

- The determination of the distance to the successive point of ionisation impact interaction.
- The determination of the energy and direction of the secondary electron set in motion.
- The simulation of electron transport.

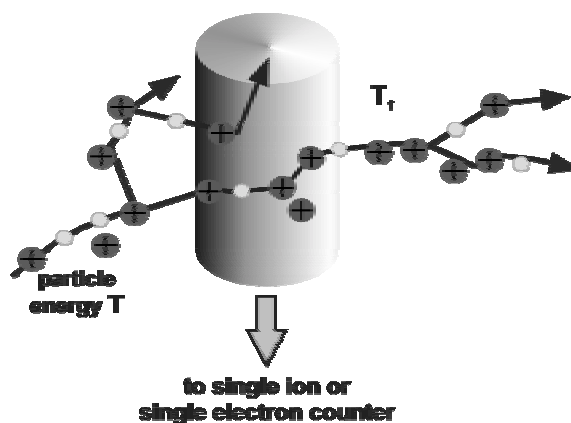
As in the case of electrons, the travelling distance between two successive interaction points of α -particles can be calculated in the conventional way using an exponential probability density. In the framework of the present model, this probability density is completely determined by the mean free path length concerning impact ionisation. The appropriate ionisation cross-sections of a variety of gases can be determined, for instance, from the semi-empirical model of Rudd, *et al.* [26] for protons, or they can be derived from the Hansen-Kochbach-Stolterfoht (HKS) model published by ICRU [27]. If the Rudd model is applied, the cross-sections for α -particles or bare carbon ions at energy T_{ION} can

be calculated from the proton data at energy $T_p = (m_p/m_{\text{ION}}) \times T_{\text{ION}}$ by multiplication with the square of the effective charge of the projectile (m_p or m_{ION} is the proton mass or the mass of an α -particle or a carbon ion). To simulate the secondary electron distribution produced by impact ionisation of the light ions, the semi-empirical model of Rudd, *et al.* [28] for protons can be applied, or again the HKS model which gives not only the single-differential but also the double-differential cross-section with respect to the energy and emission angle of secondary electrons. After determination of the secondary electron energy, the polar angle of the electron's flight direction relative to that of the primary light ion can be sampled using the latter double-differential cross-section of the HKS model. The azimuthal angle of the electron direction can be assumed to be uniformly distributed between 0 and 2π . For the details of the simulation of track structure of heavy ions see, for instance, the publications by Zaider, *et al.* [16], Grosswendt and Pszozna [22], De Nardo, *et al.* [23], Krämer and Kraft [29], and Wilson and Nikjoo [30].

The application of the simulation of track structure in nanodosimetry

As mentioned above, the simplest simulation procedure applied in the past for the investigation of radiation damage to sub-cellular structures (DNA, nucleosome, chromosome strand) is the approximation of their geometrical properties by homogeneous cylinders. The special appeal of this procedure is that it can be realised experimentally, at least in an approximate way (nanodosimetry), and used for studying the stochastic nature of radiation interaction in nanometre-sized volumes. To define a “nanometric” target in nanodosimetry, a gas-filled interaction chamber is employed, which is operated at low gas pressure and includes a well-specified cylindrical volume. The investigation of the stochastics of radiation interaction is performed with a measuring device which is able to count single ions or single low-energy electrons produced within the cylindrical volume by ionising radiation either due to primary particle interactions or due to interactions of secondary electrons. Figure 11 presents a schematic view of the measuring principle which is applicable for determining the probability distribution $P(v,T)$ of ionisation cluster-size formation by single ionising particles at energy T . Here, the ionisation cluster size is defined as exactly the number v of ionisations which are produced by single particles within a well-defined volume. This kind of measuring method was applied, for instance, by Garty, *et al.* [31] for studying the formation of ionisation clusters by protons, α -particles and carbon ions in nanometric volumes of propane at a density of $2.1 \mu\text{g}/\text{cm}^3$. To simulate a target of nanometre size, a counting volume was used which had a mean diameter of about 3.7 mm. At the applied propane density, the mass per area of this diameter was equal to $0.78 \mu\text{g}/\text{cm}^2$, which is

Figure 11. Schematic view of the measuring principle applied in nanodosimetry to investigate the stochastics of radiation interaction

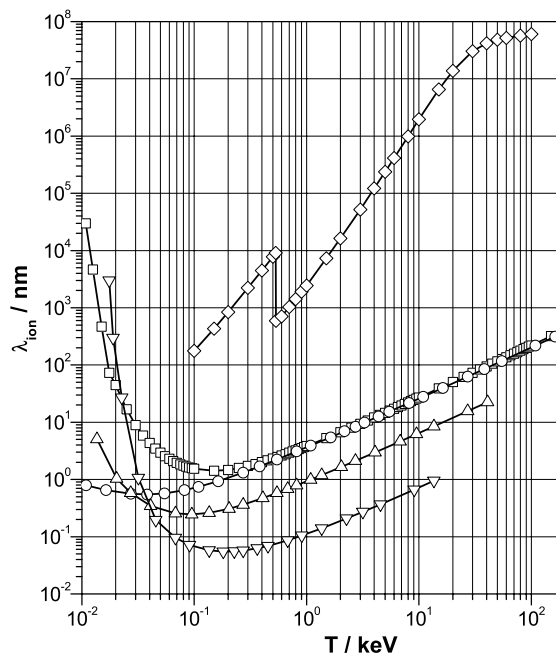


equivalent to about 8 nm if a density of 1.0 g/cm^3 is assumed. The latter procedure of simulating nanometric biological targets by specified volumes, a few mm in diameter, of a low-pressure gas was justified by Grosswendt [32] for propane-based tissue-equivalent gas, using liquid water as a substitute to biological material. For detailed descriptions of other nanodosimetric measuring devices which were applied to α -particles or electrons, see the publications by Grosswendt and Pszozna [22] and De Nardo, *et al.* [23].

To estimate what happens if an ionising particle traverses a cylindrical target at half its height along a diameter, let us assume that inelastic interactions of secondary electrons within the target volume can be neglected. In this case, the mean ionisation cluster size is equal to the ratio of the target diameter to the mean free path length λ_{ion} of primary particles as regards ionisation [32]. In view of this fact, it is natural for purposes of radiation protection or radiation therapy to compare the mean ionisation lengths λ_{ion} of different radiation qualities in liquid water. Such data are plotted in Figure 12 for photons, electrons, protons, α -particles and bare carbon ions on a nanometre scale, as a function of their initial energy. Here, the energy T_{ION} of light ions is expressed by the energy T of electrons at the same velocity: $T = (m/m_{\text{ION}}) \times T_{\text{ION}}$ (m represents the electron mass and m_{ION} the mass of an ion). For photons, the mean ionisation length λ_{ion} at energy T was set equal to the mean free interaction length λ_{tot} of photon scattering in water (see Figure 3). If we compare the photon data with those of electrons, completely different interaction properties in matter become obvious. The path lengths of photons are much longer than those of electrons, at least down to 100 eV, which proves again that photon tracks can be interpreted as a collection of single electron tracks. As far as the interaction properties of protons are concerned, it can be emphasised that at energies T greater than about 500 eV (corresponding to a proton energy of about 0.92 MeV) their ionisation path lengths are almost the same as those of electrons. As compared with the ionisation lengths of the other light ions at energies T greater than 500 eV (corresponding to an α -particle energy of about 3.7 MeV and to an energy of

Figure 12. Mean free path length λ_{ion} with respect to ionisation of photons, electrons and light ions in liquid water as a function of energy T

\diamond – photons, \square – electrons, \circ – protons, Δ – α -particles, ∇ – bare carbon ions



bare carbon ions of about 11 MeV), the values of λ_{ion} of electrons or protons are greater than those of the α -particles by almost a factor of four and greater than those of bare carbon ions by a factor of about 36. In consequence, the mean distance between successive ionisation events due to carbon ions should be smaller than that due to α -particles at the same velocity by a factor of about 9 and smaller than that due to protons or electrons by a factor of about 36. Nevertheless, the strong ionisation capability of low-energy electrons is obvious as their mean free ionisation path lengths at energies around 150 eV are comparable with those of α -particles at $T = 1.7$ keV (see Figure 12) which corresponds to an α -particle energy of about 12.5 MeV.

To give an impression of characteristic differences in the track structure of the four different kinds of primary particles at the same velocity, Figure 13 shows examples of the ionisation component of track segments, 100 nm in length at a density of 1.0 g/cm³, of a 2.72 keV electron, a 5 MeV proton, a 20 MeV α -particle, and a bare 60 MeV carbon ion in propane. The similarity of the track segments of electrons and protons is obvious, as is the increasing ionisation density within the track segments of the α -particle and of the bare carbon ion with increasing ion charge. The dependence of the mean ionisation cluster size in nanometric targets on radiation quality can be assumed to behave in a similar manner. Hence, at the same velocity, the probability of large clusters should be much higher in the case of an irradiation with bare carbon ions than with α -particles; and the probability of the formation of larger clusters in the case of an irradiation with α -particles higher than with electrons or protons. To demonstrate this fact, Figure 14 presents the probability distribution $P(v,T)$ of cluster size v in a cylindrical volume of propane, 2 nm in diameter and height at a density of 1.0 g/cm³, determined by Monte Carlo simulation of the track structure of the three different types of light ions in question (the results for 2.72 keV electrons are omitted because they are very similar to those of 5 MeV protons).

Figure 13. Track segment, 100 nm in length at a density of 1.0 g/cm³, of one 2.72 keV electron, one 5 MeV proton, one 20 MeV α -particle and one 60 MeV bare carbon ion in propane

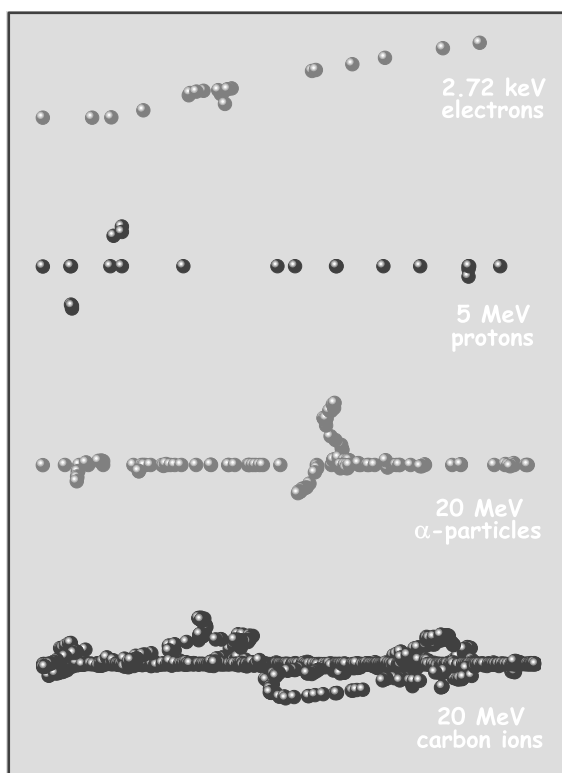
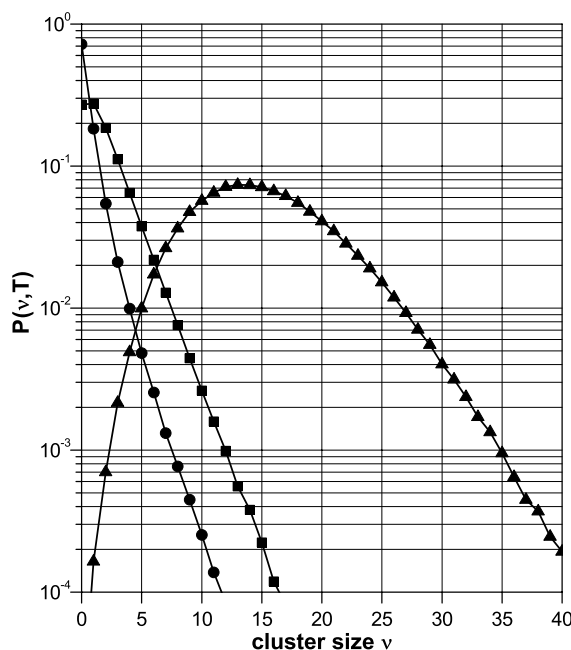


Figure 14. Probability distribution $P(v,T)$ of the formation of ionisation cluster size v by light ions in a propane cylinder, 2 nm in diameter and height at a density of 1.0 g/cm³

● – 5 MeV protons, ■ – 20 MeV α -particles, ▲ – 60 MeV bare carbon ions



The probability distribution concerning the cluster-size formation by 5 MeV protons shows a very high probability of zero cluster size followed by a very steep monotonous decrease of $P(v,T)$ with increasing cluster size v . As compared with protons, the probability distribution for 20 MeV α -particles looks quite similar apart from a reduced probability of zero events and a less pronounced gradient. For bare 60 MeV carbon ions, however, a completely different probability distribution is obvious, with a very low probability of cluster size zero and a marked maximum at cluster size 13. This very different behaviour of $P(v,T)$ for light ions at the same velocity can be easily explained by the strong decrease of the mean free ionisation path length of the particles with increasing ion charge.

Bearing in mind that the yields of clusters of multiple ionisation in sites, 2-3 nm in size, correlate well with observed yields of double strand breaks of DNA [11], the probability of the formation of ionisation clusters of size $v \geq 2$ in volumes, a few nm in diameter, should correlate with the cross-section of radiation-induced biological effects. To check this assumption, the cumulative distribution function $F_2(T) = \sum P(v,T)$ for $v \geq 2$ was calculated for electrons, and plotted as a function of their mean free path length λ_{ion} with respect to ionisation in liquid water. Figure 15 shows the results for primary electrons at energies between 20 eV and 100 keV in a cylinder, 2 nm in diameter and height [33]. The distribution function $F_2(T)$ versus λ_{ion} looks like an arrow showing its top at $\lambda_{ion} = 1.41$ nm which corresponds to an electron energy of 150 eV (see Figure 12). The right-hand side of the arrow represents the probability $F_2(T)$ of multiple ionisation as a function of λ_{ion} at energies between 150 eV and 100 keV, whereas the left-hand side represents $F_2(T)$ at lower energies. In order to correlate the probability of cluster-size formation with radio-biological effects, $F_2(T)$ was scaled at an electron energy of 200 eV to the bio-effect cross-sections σ_B of Simmons and Watt [13] for electrons or X-rays, which are presented by the lower curve of Figure 10, as a function of the mean free ionisation path length of electrons in liquid water. The scaled values of $F_2(T)$ are plotted in Figure 16 in comparison with the bio-effect cross-sections given by Simmons and Watt, as a function of energy T .

Figure 15. Cumulative distribution function $F_2(T)$ of electrons in a liquid water cylinder, 2 nm in diameter and height, as a function of their mean free path length λ_{ion} with respect to ionisation

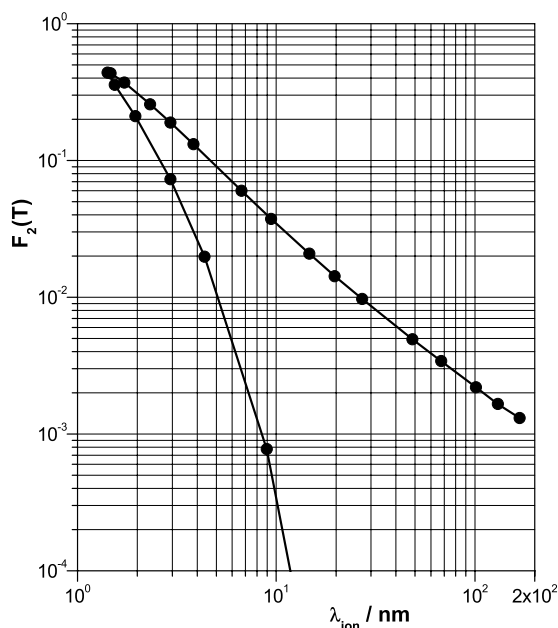
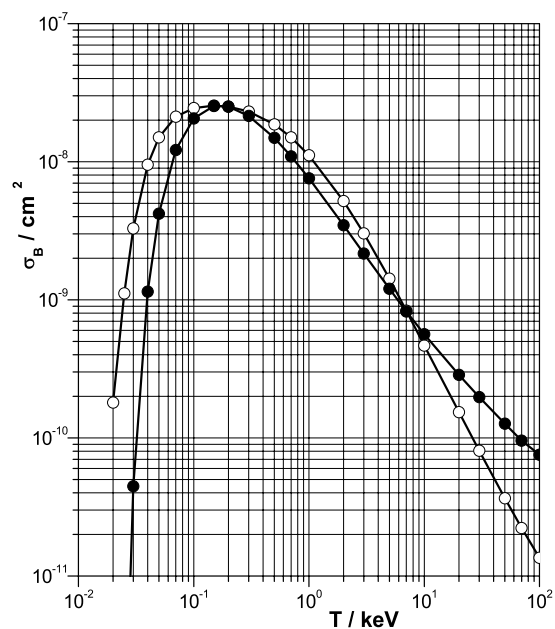


Figure 16. Bio-effect cross section σ_B of electrons as a function of energy T

○ – cross-section σ_B for electrons and X-rays according to Simmons and Watt [13], ● – scaled distribution function $F_2(T)$



At first glance, it can be seen that the energy dependence of the cross-section and of that of the scaled distribution function is quite similar. The quantity $F_2(T)$ for nanometric volumes could, therefore, be used as a physical measure which is strongly correlated to observed radio-biological effects. For further details and a few aspects of the scaled distribution function for α -particles and photons, see the publication by Grosswendt [33].

Conclusion

To come to an end of the present overview, it can be stated that the simulation of track structure of ionising particles is an indispensable tool for molecular radiation biology and nanodosimetry. It allows the calculation of the initial distribution of interaction products in matter or of the initial damage to sub-cellular structures which represent the starting points of the development of any radiation-induced radio-chemical or radio-biological effect. In addition, it can be applied in radiation metrology to study physical quantities which are measurable and directly correlate with the induction of radiation damage to DNA. Here, one of the most promising topics, at present, is the investigation of ionisation cluster-size formation in nanometric volumes which is based on the track structure of ionising radiation and might be used in the future for a redefinition of radiation quality in terms of bio-effect cross-sections.

REFERENCES

- [1] Grosswendt, B., *Physics of Electron and Photon Transport for Dosimetry Calculations*, these proceedings.
- [2] Robinson, M.G. and G.R. Freeman, *J. Chem. Phys.*, 55, 5644-5650 (1971).
- [3] Freeman, G.R., in *Kinetics of Nonhomogeneous Processes*, Freeman, G.R. (ed.), John Wiley & Sons, New York, pp. 1-18 (1987).
- [4] Friedland, W., P. Jacob, H.G. Paretzke and T. Stork, *Radiat. Res.* 150, 170-182 (1998).
- [5] International Commission on Radiation Units and Measurements (ICRU), *Fundamental Quantities and Units for Ionizing Radiation*, Report 60, Bethesda, MD, USA (1998).
- [6] Paretzke, H.G., in *Kinetics of Nonhomogeneous Processes*, G.R. Freeman (ed.), John Wiley & Sons, New York, pp. 89-170 (1987).
- [7] Nikjoo, H., P. O'Neill, D.T. Goodhead and M. Terrissol, *Int. J. Radiat. Biol.*, 71, 467-483 (1997).
- [8] Nikjoo, H., P. O'Neill, M. Terrissol and D.T. Goodhead, *Radiat. Environ. Biophys.*, 38, 31-38 (1999).
- [9] Pomplun, E. and M. Terrissol, *Radiat. Environ. Biophys.*, 33, 279-292 (1994).
- [10] Goodhead, D.T. and H. Nikjoo, *Int. J. Radiat. Biol.*, 55, 513-529 (1989).
- [11] Brenner, D.J. and J.F. Ward, *Int. J. Radiat. Biol.*, 61, 737-748 (1992).
- [12] Nikjoo, H., R.F. Martin, D.E. Charlton, M. Terrissol, S. Kandaiya and P. Lobachevsky, *Acta Oncol.*, 35, 849-856 (1996).

- [13] Simmons, J.A. and D.E. Watt, *Radiation Protection Dosimetry: A Radical Reappraisal*, Medical Physics Publishing, Madison, WI, USA (1999).
- [14] Terrissol, M. *Méthode de simulation du transport d'électrons d'énergies comprises entre 10 eV and 30 keV*, Doctoral Thesis n° 839, University Paul Sabatier, Toulouse, France (1978).
- [15] Grosswendt, B. and E. Waibel, *Nucl. Instrum. and Meth.*, 155, 145-156 (1978).
- [16] Zaider, M., D.J. Brenner and W.E. Wilson, *Radiat. Res.*, 95, 231-247 (1983).
- [17] Lappa, A.V., E.A. Bigildeev, D.S. Burmistrov and O.N. Vasilyev, *Radiat. Environ. Biophys.*, 32, 1-19 (1993).
- [18] Uehara, S., H. Nikjoo and D.T. Goodhead, *Phys. Med. Biol.*, 37, 1841-1858 (1992).
- [19] Pimblott, S.M., J.A. LaVerne and A. Mozumder, *J. Phys. Chem.*, 100, 8595-8606 (1996).
- [20] Nikjoo, H., S. Uehara and D.J. Brenner, in *Microdosimetry, an Interdisciplinary Approach*, D.T. Goodhead, P. O'Neill and H.G. Menzel (eds.), The Royal Society of Chemistry, Cambridge, UK, pp. 3-10 (1997).
- [21] Bigildeev, E.A. and V. Michalik, *Radiat. Phys. Chem.*, 47, 197-207 (1996).
- [22] Grosswendt, B. and S. Pszozna, *Radiat. Environ. Biophys.*, 41, 91-102 (2002).
- [23] De Nardo, L., P. Colautti, V. Conte, W.Y. Baek, B. Grosswendt and G. Tornielli, *Radiat. Environ. Biophys.*, 41, 235-256 (2002).
- [24] ICRU, *Stopping Powers and Ranges for Protons and Alpha Particles*, Report 49, Bethesda, MD, USA (1993).
- [25] Grosswendt, B. and W.Y. Baek, *Radiat. Prot. Dosim.*, 61, 267-274 (1995).
- [26] Rudd, M.E., Y-K. Kim, D.H. Madison and J.W. Gallagher, *Rev. Mod. Phys.*, 57, 965-994 (1985).
- [27] ICRU, *Secondary Electron Spectra from Charged Particle Interactions*, Report 55, Bethesda, MD, USA (1996).
- [28] Rudd, M.E., Y-K. Kim, D.H. Madison and T.J. Gay, *Rev. Mod. Phys.*, 64, 441-490 (1992).
- [29] Krämer, M. and G. Kraft, *Radiat. Environ. Biophys.*, 33, 91-109 (1994).
- [30] Wilson, W.E. and H. Nikjoo, *Radiat. Environ. Biophys.*, 38, 97-104 (1999).
- [31] Garty, G., S. Shchemelinin, A. Breskin, R. Chechik, G. Assaf, I. Orion, V. Bashkurov, R. Schulte and B. Grosswendt, *Nucl. Instrum. and Meth. Phys. Res.*, A 492, 212-235 (2002).
- [32] Grosswendt, B., *Radiat. Environ. Biophys.*, 41, 103-112 (2002).
- [33] Grosswendt, B., in *Advanced Monte Carlo for Radiation Physics, Particle Transport Simulation and Applications*, A. Kling, F. Barão, M. Nakagawa, L. Távora, P. Vaz (eds.), Springer-Verlag, Berlin, pp. 237-250 (2001).

INTERMEDIATE- AND HIGH-ENERGY NUCLEAR REACTIONS IN DOSIMETRY CALCULATIONS

Alfredo Ferrari^{1,*} and Paola R. Sala^{2,*}

¹ European Laboratory for Particle Physics (CERN), CH-1211 Geneva 23, Switzerland

² ETH Zürich, CH-8093 Zürich, Switzerland

* *On leave from INFN Milan, Via Celoria 16 20133 Milan, Italy*

Abstract

The physics foundations of hadronic interactions as implemented in most Monte Carlo codes are presented along with a few practical examples. The description of the relevant physics is schematically split into the major steps in order to stress the different approaches required for a full understanding of nuclear reactions at intermediate and high energies. Due to the complexity of the problem, only a few semi-qualitative arguments are developed in this paper. The description will be forcibly schematic and somewhat incomplete, but will hopefully be useful for a first introduction to this topic. Practical examples taken from the FLUKA code are used throughout the paper in order to supplement the theoretical description.

Introduction

A very first question concerning the modelling of nuclear interactions could be, why Monte Carlo and not different approaches? Actually, the Monte Carlo approach to nuclear reactions has several advantages when used in full transport radiation codes. While several successful non-Monte-Carlo models exist for low-medium energies (up to the pion production threshold), the description of nuclear interactions when particle production is open becomes more and more complex and difficult to accommodate within numerical models other than Monte Carlo.

Main steps of h-A interactions

The approach to hadronic interaction modelling presented here is the one adopted by most state-of-the-art codes. In this “microscopic” approach, each step has a sound physical basis. Performances are optimised comparing with particle production data at single interaction level. Absolutely no tuning on “integral” data, like calorimeter resolutions, thick target yields, etc., is performed. Therefore, final predictions are obtained with minimal free parameters, fixed for all energies and target/projectile combinations. Results in complex cases as well as scaling laws and properties come out naturally from the underlying physical models and the basic conservation laws are fulfilled *a priori*. All the examples/results presented in the following have been obtained with FLUKA [1,2,3] and should be typical of codes adopting similar approaches. High-energy hadron-nucleus (h-A) interactions can be schematically described as a sequence of the following steps:

- Glauber-Gribov cascade and high-energy collisions.
- (Generalised) IntraNuclear cascade.
- Pre-equilibrium emission.
- Evaporation/fragmentation/fission and final de-excitations.

Individual aspects of the interaction simulation can be of particular relevance for some applications rather than for others; for example, those critical for calorimetry applications are discussed in [4]. However the overall coherence of a successful model is based on its ability to describe very different problems within the same, self-consistent, physics approach. Before briefly discussing each individual step, a few words about the modelling of hadron-nucleon collisions are required in order to understand more complex hadron-nucleus or nucleus-nucleus collisions.

Hadron-nucleon interaction models

A comprehensive understanding of hadron-nucleon interactions over a large energy range is of course a basic ingredient for a sound description of hadron-nucleus interactions. Elastic, charge exchange and strangeness exchange reactions, are described as far as possible by phase-shift analysis and/or fits of experimental differential data. Standard eikonal approximations are often used at high energies.

At the low-energy end (below 100 MeV) the p-p and p-n cross-sections rapidly increase with decreasing energy. There is a factor three at the lowest energies between the n-p and the p-p cross-sections, as expected on the basis of symmetry and isospin considerations, while at high energies they tend to be equal.

The total cross-section for the two isospin components present in the nucleon-nucleon amplitude is given by:

$$\begin{aligned}\sigma_T^1 &= \sigma_{pp} \\ \sigma_T^0 &= 2\sigma_T^{np} - \sigma_T^{pp}\end{aligned}$$

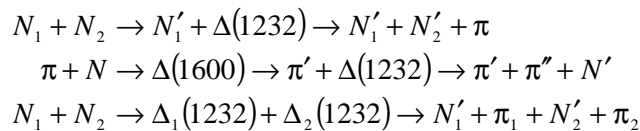
The same decomposition can be shown to apply for the elastic and reaction cross-sections as well.

The cross-section for pion-nucleon scattering is dominated by the existence of several direct resonances, the most prominent one being the $\Delta(1232)$. Given the pion isotopic spin ($T = 1$), the three π charge states correspond to the three values of T_z . Thus, in the pion-nucleon system two values of T are allowed: $T = \frac{1}{2}$ and $T = \frac{3}{2}$, and two independent scattering amplitudes, $A_{\frac{1}{2}}$ and $A_{\frac{3}{2}}$, enter in the cross-sections. Using Clebsh-Gordan coefficients all differential cross-sections can be derived from the three measured ones: $\sigma(\pi^+p \rightarrow \pi^+p)$, $\sigma(\pi^-p \rightarrow \pi^-p)$, $\sigma(\pi^-p \rightarrow \pi^0n)$.

As soon as particle production (inelastic hadron-nucleon interactions) are concerned, the description becomes immediately more complex. Two families of models are adopted, depending on the projectile energy, those based on individual resonance production and decays, which cover the energy range up to 3-5 GeV, and those based on quark/parton string models, which can provide reliable results up to several tens of TeV.

h-N interactions at intermediate energies

The lowest threshold inelastic channel, single pion production, opens already around 290 MeV in nucleon-nucleon interactions, and becomes important above 700 MeV. In pion-nucleon interactions the production threshold is as low as 170 MeV. Both reactions are normally described in the framework of the isobar model: all reactions proceed through an intermediate state containing at least one resonance. There are two main classes of reactions, those which form a resonant intermediate state (possible in π -nucleon reactions) and those which contain two particles in the intermediate state. The former exhibit bumps in the cross-sections corresponding to the energy of the formed resonance. Examples are reported below:



Partial cross-sections can be obtained from one-boson exchange theories and/or folding of Breit-Wigner with matrix elements fixed by N-N scattering or experimental data. Resonance energies, widths, cross-sections, branching ratios are extracted from data and conservation laws, whenever possible, making explicit use of spin and isospin relations. They can also be inferred from inclusive cross-sections when needed.

For a discussion of resonance production, see for example [5,6,7].

Inelastic h-N interactions at high energies (DPM, QGSM, ...)

As soon as the projectile energy exceeds a few GeVs, the description in terms of resonance production and decay becomes more and more difficult. The number of resonances which should be

considered grows exponentially and their properties are often poorly known. Furthermore, the assumption of one or two resonance creation is unable to reproduce the experimental finding that most of the particle production at high energies occurs neither in the projectile nor the target fragmentation region, but rather in the central region, for small values of Feynmann X variable. Different models, based directly on quark degrees of freedom, must be introduced.

The features of “soft” interactions (low p_T interactions) cannot be derived from the QCD Lagrangian, because the large value taken by the running coupling constant prevents the use of perturbation theory. Models based on interacting strings emerged as a powerful tool in understanding QCD at the soft hadronic scale, that is in the non-perturbative regime. An interacting string theory naturally leads to a topological expansion. In QCD, gluons are coloured, thus strongly self-interacting. Suppose quarks are held together by colour lines of force, the gluon-gluon interaction will pull them together into the form of a tube or a string. Since quarks are confined, the energy required to “stretch” such a string is increasingly large until it suffices to materialise a quark/anti-quark couple from the vacuum and the string breaks into two shorter ones, with still quarks at both ends. Hence because of quark confinement, theories based on interacting strings are powerful tools in understanding QCD at the soft hadronic scale, that is in the non-perturbative regime. An interacting string theory naturally leads to a topological expansion. At high energies, such an expansion had already been developed before the establishment of QCD: the Reggeon-Pomeron calculus in the framework of perturbative Reggeon Field Theory. The Dual Parton Model [8] is one of these models (another very similar example is the Quark-Gluon-String-Model [9,10]) and it is built introducing partonic ideas into a topological expansion which explicitly incorporates the constraints of duality and unitarity, typical of Regge’s theory. In DPM hadrons are considered as open strings with quarks, anti-quarks or di-quarks sitting at the ends; mesons (colourless combination of a quark and an anti-quark $q\bar{q}$) are strings with their valence quark and anti-quark at the ends. At sufficiently high energies the leading term in the interactions corresponds to a Pomeron (IP) exchange (a closed string exchange), which has a cylinder topology. When an unitarity cut is applied to the cylindrical Pomeron two hadronic chains are left as the sources of particle production. While the partons out of which chains are stretched carry a net colour, the chains themselves are built in such a way as to carry no net colour, or to be more exact to constitute colour singlets like all naturally occurring hadrons. As a consequence of colour exchange in the interaction, each colliding hadron splits into two coloured systems, one carrying colour charge c and the other \bar{c} . The system with colour charge c (\bar{c}) of one hadron combines with the system of complementary colour of the other hadron, to form two colour-neutral chains. These chains appear as two back-to-back jets in their own centre-of-mass systems.

The exact way of building up these chains depends on the nature of the projectile-target combination (baryon-baryon, meson-baryon, anti-baryon-baryon, meson-meson); examples are shown in Figures 1 and 2, and further details can be found in the original DPM references [8,3].

The chains produced in an interaction are then hadronised. DPM gives no prescriptions on this stage of the reaction. All the available chain hadronisation models, however, rely on the same basic assumptions, the most important one being chain universality; that is, chain hadronisation does not depend on the particular process which originated the chain, and that until the chain energy is much larger than the mass of the hadrons to be produced, the fragmentation functions (which describe the momentum fraction carried by each hadron) are the same. As a consequence, fragmentation functions can in principle be derived from hard processes and e^+e^- data and the same functions and (few) parameters should be valid for all reactions and energies; actually mass and threshold effects are non-negligible at the typical chain energies involved in hadron-nucleus reactions. Transverse momentum is usually added according to uncertainty considerations. The examples in Figures 3 and 4 show the ability of the FLUKA, DPM-based model to reproduce the features of particle production; further examples can be found in [1,3].

Figure 1. Leading two-chain diagram in DPM for p - p scattering. The colour (r – red, b – blue, g – green, \bar{r} – anti-red, \bar{b} – anti-blue and \bar{g} – anti-green) and quark combination shown in the figure is just one of the allowed possibilities.

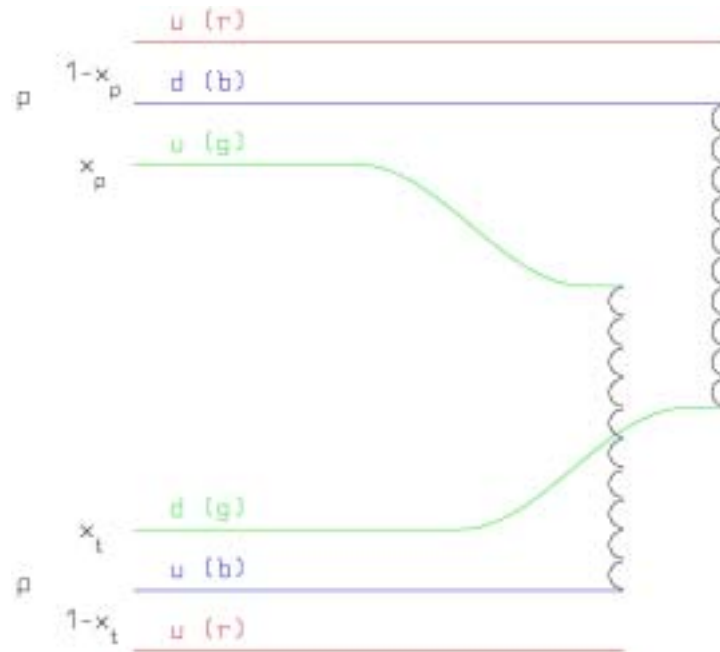


Figure 2. One of leading two-chain diagrams in DPM for π^+p scattering. The colour and quark combination shown in each figure is just one of the allowed possibilities.

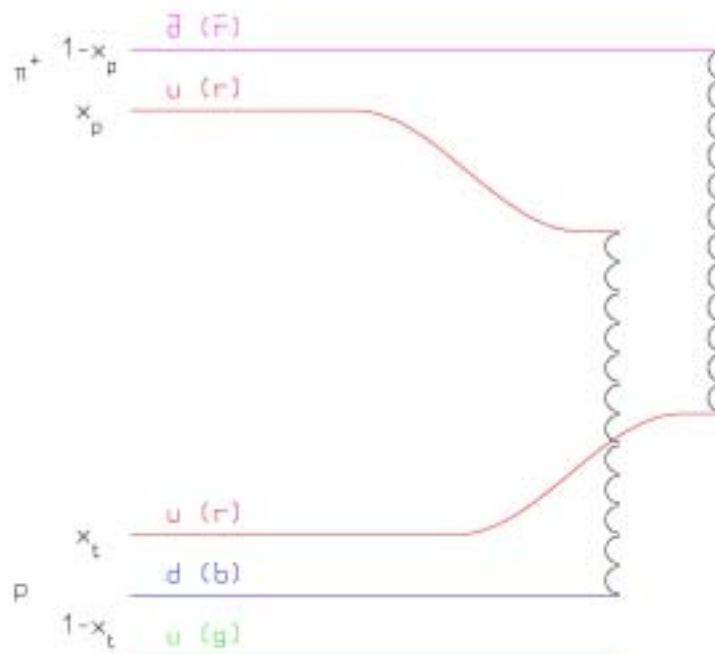


Figure 3. Feynman x_F^* spectra of positive and negative particles from (π^+, p) at 250 GeV/c

Exp. data (symbols) from [11].

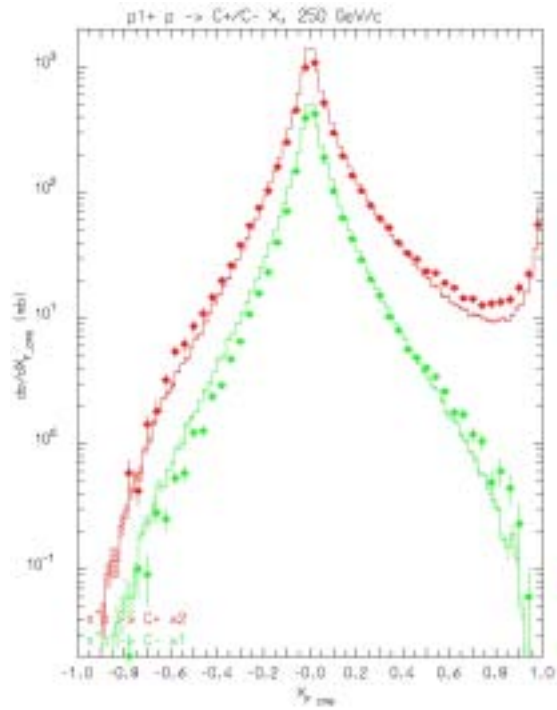
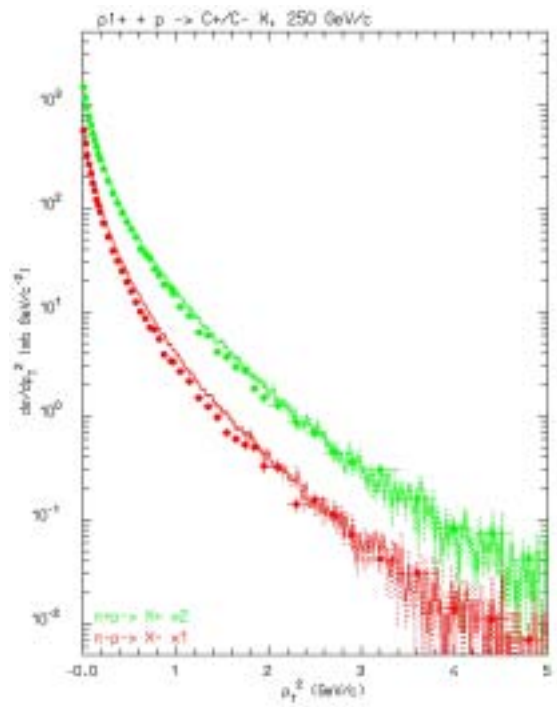


Figure 4. Transverse momentum (p_T) spectra of positive and negative particles from (π^+, p) at 250 GeV/c

Exp. data (symbols) from [11].



(Generalised) IntraNuclear Cascade basic assumptions

At energies high enough to consider coherent effects as corrections, a hadron-nucleus (h-A) reaction can be described as a cascade of two-body interactions, concerning the projectile and the reaction products. This is the mechanism called IntraNuclear Cascade (INC). INC models were developed at the infancy of the computer era with great success in describing the basic features of nuclear interactions in the 0.2-2 GeV range. Modern INC models had to incorporate many more ideas and effects in order to describe in reasonable way reactions at higher and lower energies. Despite particle trajectories being described classically, many quantistic effects have to be incorporated in these (Generalised)INC models, such as Pauli blocking, formation time, coherence length, nucleon anti-symmetrisation and hard core nucleon correlations. A thorough description of the (G)INC model used in FLUKA can be found in [1,3]. The basic assumptions are:

- Primary and secondary particles moving in the nuclear medium.
- Interaction probability from $\sigma_{free} + \text{Fermi motion} \times \rho(r) + \text{exceptions (ex. } \pi)$.
- Glauber cascade at high energies.
- Classical trajectories (+) nuclear mean potential (resonant for π s!!).
- Curvature from nuclear potential \rightarrow refraction and reflection.
- Interactions are incoherent and uncorrelated.
- Interactions in projectile-target nucleon CMS \rightarrow Lorentz boosts.
- Multi-body absorption for π, μ^-, K^- .
- Quantum effects (Pauli, formation zone, correlations...).
- Exact conservation of energy, momenta and all additive quantum numbers, including nuclear recoil.

h-A at high energies: the Glauber-Gribov cascade

The Glauber [12,13] formalism provides a powerful and elegant method to derive elastic, quasi-elastic and absorption h-A cross-sections from the free hadron-nucleon cross-section and the nuclear ground state only. Inelastic interactions are equivalent to multiple interactions of the projectile with ν target nucleons. The number of such “primary” interactions follows a binomial distribution (at a given impact parameter, b):

$$P_{r,\nu}(b) \equiv \binom{A}{\nu} P_r^\nu(b) [1 - P_r(b)]^{A-\nu}$$

where $P_r(b) \equiv \sigma_{hN}^{-1} T_r(b)$, and $T_r(b)$ is the profile function (folding of nuclear density and scattering profiles along the path). On average:

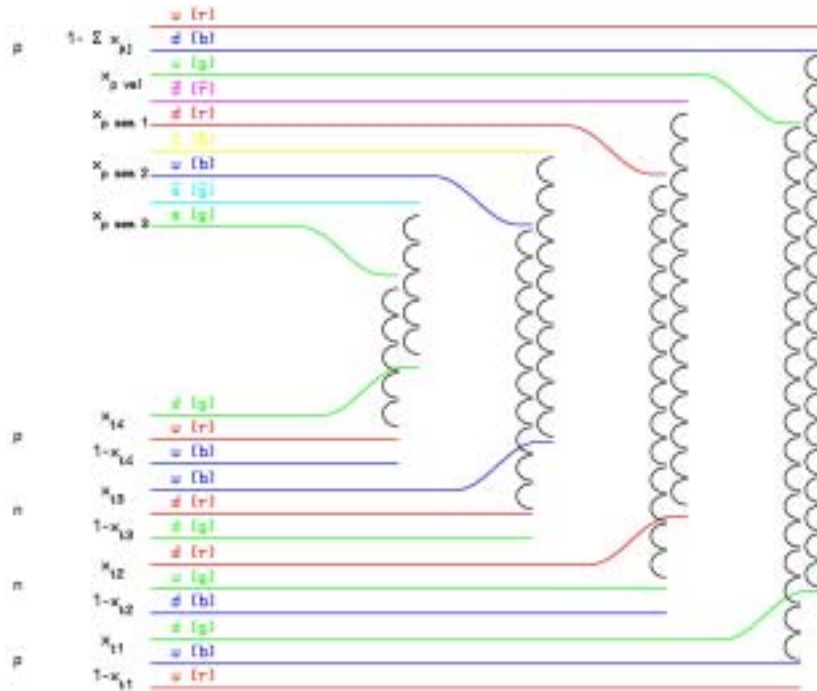
$$\langle \nu \rangle = \frac{Z\sigma_{hp,r} + N\sigma_{hm,r}}{\sigma_{hA,abs}}$$

$$\sigma_{hA,abs}(s) = \int d^2\vec{b} \left[1 - \left(1 - \sigma_{hN,r}(s) T_r(b) \right)^A \right]$$

The Glauber-Gribov [14-16] model represents the diagram interpretation of the Glauber cascade. The ν interactions of the projectile originate 2ν chains, out of which two chains (valence-valence chains) struck between the projectile and target valence (di)quarks, $2(\nu - 1)$ chains (sea-valence chains) between projectile sea $q - \bar{q}$ and target valence (di)quarks.

A pictorial example of the chain building process is depicted in Figure 5 for p -A: similar diagrams apply to π -A and \bar{p} -A respectively.

Figure 5. Leading two-chain diagrams in DPM for p -A Glauber scattering with four collisions. The colour and quark combinations shown in the figure are just one of the allowed possibilities.



The distribution of the projectile energy among many chains naturally softens the energy distributions of reaction products and boosts the multiplicity with respect to hadron-hadron interactions (see Figure 6). The building up of the multiplicity distribution from the multiple collisions can be appreciated from Figure 7, where the multiplicity distribution for Al and Au targets at 250 GeV/c are presented together. In this way, the model accounts for the major A-dependent features without any degree of freedom, except in the treatment of mass effects at low energies.

The Fermi motion of the target nucleons must be included to obtain the correct kinematics, in particular the smearing of p_T distributions. All nuclear effects on the secondaries are accounted for by the subsequent (G)INC.

Figure 6. Rapidity distribution of charged particles produced in 200 GeV proton collisions on hydrogen, argon and xenon target, data from [17]

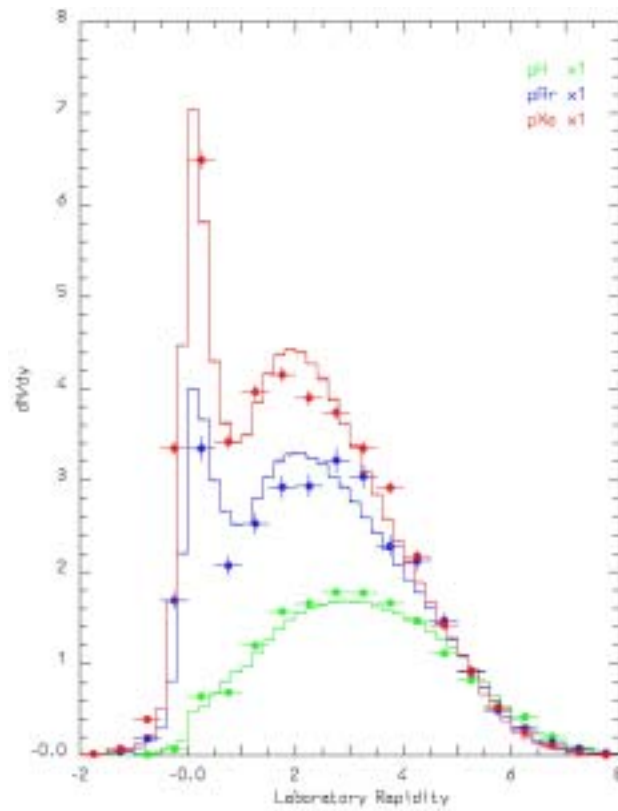
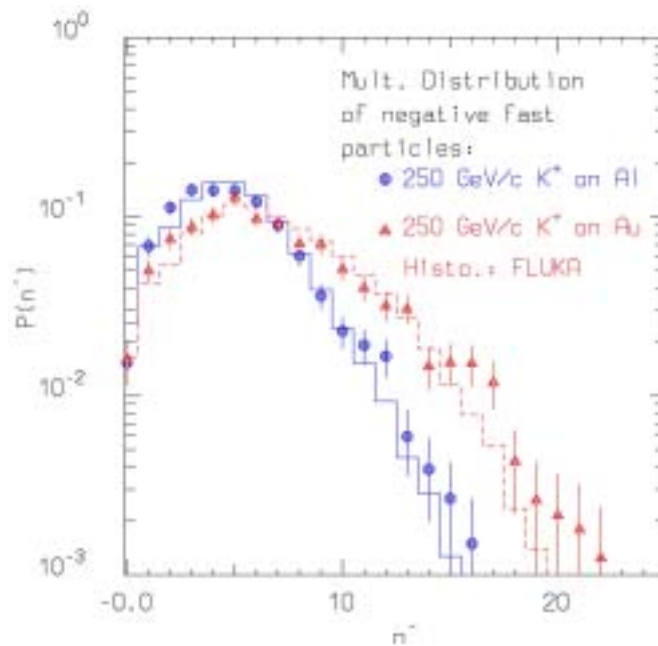


Figure 7. Multiplicity distribution of negative shower particles for 250 GeV/c K^+ on aluminium and gold targets (right), data from [18]



Formation Zone

The Formation Zone concept is essential to understand the observed reduction of the re-interaction probability with respect of the naive free cross-section assumption. It can be understood as a “materialisation” time. A qualitative estimate can be given as follows: in the frame where $p_{\parallel} = 0$, the time necessary for materialisation \bar{t} is:

$$\bar{t} = \Delta t \approx \frac{\hbar}{E_T} = \frac{\hbar}{\sqrt{p_T^2 + M^2}}$$

Going to lab system:

$$t_{lab} = \frac{E_{lab}}{E_T} \bar{t} = \frac{\hbar E_{lab}}{p_T^2 + M^2}$$

The condition for possible re-interaction inside a nucleus is:

$$\mathbf{v} \cdot t_{lab} \leq R_A \approx r_0 A^{\frac{1}{3}}$$

At high energies, the “fast” (from the emulsion language) particles produced in the Glauber cascade have a high probability to materialise already outside the nucleus without triggering a secondary cascade. Only a small fraction of the projectile energy is thus left available for the INC and the evaporation (see Figure 9 and the section entitled *h-A at high energies: The invariance of the target fragmentation region*).

Coherence length

Another critical issue is the “coherence” length after elastic, or quasi-elastic reactions. In analogy with the formation zone concept, such interactions cannot be localised better than the position uncertainty connected with the four-momentum transfer of the collision. Re-interactions occurring at distances shorter than the coherence length would undergo interference and cannot be treated as independent interactions on other nucleons. The coherence length concept has been applied to the secondaries in elastic, quasi-elastic or more generally quasi-two-body interactions, with the following recipe: given a two-body interaction with four-momentum transfer $q = p_{1i} - p_{1f}$, between a particle $1i$ and a nucleon $2i$ with final particles (which could be resonances) $1f$ and $2f$ the energy transfer seen in a frame where the particle 2 is at rest is given by:

$$\Delta E_2 = \mathbf{v}_2 \cdot \mathbf{q} = \frac{q \cdot p_{2i}}{m_2} \quad (1)$$

From the uncertainty principle this ΔE corresponds to an indetermination in proper time given by $\Delta \tau \cdot \Delta E_2 = \hbar$, that boosted to the lab frame gives a coherence length:

$$\Delta x_{lab} = \frac{p_{2lab}}{m_2} \cdot \Delta \tau = \frac{p_{2lab}}{m_2} \frac{\hbar}{\mathbf{v}_2} \quad (2)$$

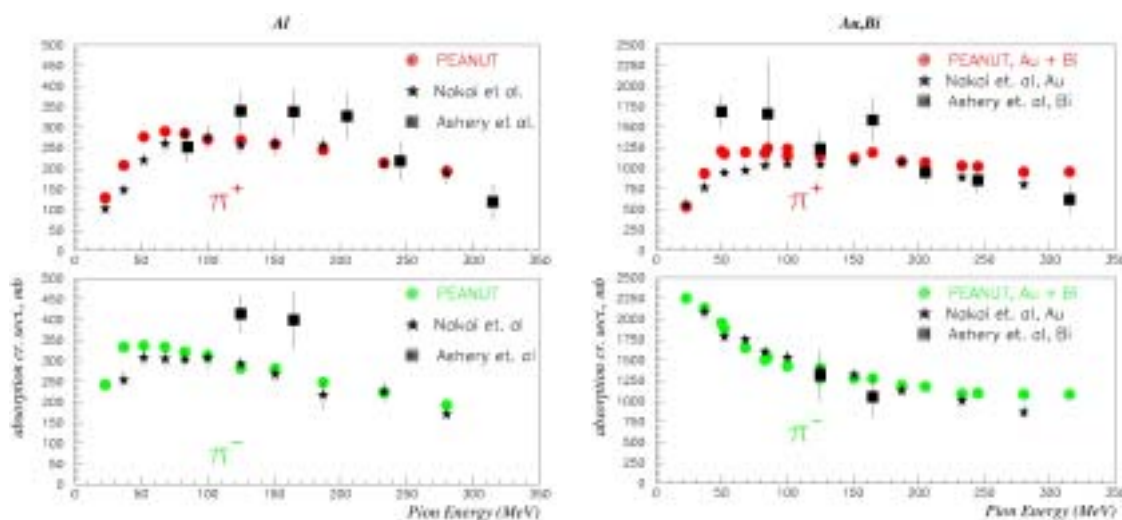
Intermediate energy pions in nuclei

An accurate description of pion production and interactions is essential in many problems involving hadronic showers, for instance in the evaluation of doses, radiation damage and single-event upset rates in mixed field generated by high energy beams, both at accelerators and at aircraft altitudes and in open space due to galactic cosmic rays and solar particle events. A proper description of pion interactions on nuclei in the sub-GeV energy range should take into account:

- The resonant nature of the π - N interaction, mostly dominated by the $\Delta(1232)$.
- The effect of the nuclear medium on the π - N interaction.
- The possibility of absorption (both s-wave and p-wave) on two or more nucleons.
- The resonant nature of the pion-nucleus potential, which varies rapidly with the pion energy.

In particular, the importance of multi-nucleon pion absorption can be easily estimated from the values in Figure 8, where available experimental data are compared with FLUKA predictions. Further details are outside the scope of the present paper; a more detailed description can be found in Refs. [3,19].

Figure 8. Computed and experimental [20,21] pion absorption cross-section on aluminium (left) and on gold or bismuth (right) as a function of energy



Pre-equilibrium

At energies lower than the π production threshold a variety of pre-equilibrium models have been developed [22] following two leading approaches: the quantum-mechanical multi-step model and the exciton model. The former has very good theoretical background but is quite complex, while the latter relies on statistical assumptions, and it is simple and fast. Exciton-based models are often used in Monte Carlo codes to join the INC stage of the reaction to the equilibrium one.

As an example the main lines of the FLUKA implementation are outlined in the following. The INC step goes on until all nucleons are below a smooth threshold around 50 MeV, and all particles but nucleons (typically pions) have been emitted or absorbed. At the end of the INC stage a few particles

may have been emitted and the input configuration for the pre-equilibrium stage is characterised by the total number of protons and neutrons, by the number of particle-like excitons (nucleons excited above the Fermi level), and of hole-like excitons (holes created in the Fermi sea by the INC interactions), by the “compound” nucleus excitation energy (actually the nucleus is not yet at all in an equilibrated state and the term “compound” is somewhat incorrect), and by the “compound” nucleus momentum. All the above quantities can be derived by proper counting of what occurred during the INC stage. The exciton formalism of FLUKA follows that of M. Blann and co-workers [23-26], with some modifications:

- Inverse cross-sections from systematics.
- Correlation/formation zone/hardcore effects on re-interactions: the escape probability for an exciton in the continuum is calculated as sum of the probabilities in three zones. The first is the largest between the hardcore and the formation ones, the second extends up to the correlation radius (here re-interactions are allowed only on the non-correlated nucleon specie), the third is the remaining nuclear volume.
- Constrained exciton state densities for the configurations 1p-1h, 2p-1h, 1p-2h, 2p-2h, 3p-1h and 3p-2h.
- Energy-dependent form for the single particle density g_x [27].
- Position dependent parameters = point-like values:
 - First step – n_h holes generated in the INC step at positions \vec{x}_i :

$$\rho_{n_h}^{loc} = \frac{\sum_{i=1}^{n_h} \rho(\vec{x}_i)}{n_h} ; E_{F n_h}^{loc} = \frac{\sum_{i=1}^{n_h} E_F(\vec{x}_i)}{n_h} \quad (3)$$

- When looking at re-interaction – consider neighbourhood:

$$\rho_{n_h}^{nei} = \frac{n_h \rho_{n_h}^{loc} + \rho^{ave}}{n_h + 1} ; E_{F n_h}^{nei} = \frac{n_h E_{F n_h}^{loc} + E_F^{ave}}{n_h + 1} \quad (4)$$

- Subsequent steps – go towards average quantities:

$$\rho_{n_h+1}^{loc} = \rho_{n_h}^{nei} ; E_{F n_h+1}^{loc} = E_{F n_h}^{nei} \quad (5)$$

- Angular distributions of emitted particles in the fast particle approximation.

For further details see Ref. [3].

Evaporation, fission and nuclear break-up

At the end of the reaction chain, the nucleus is a thermally equilibrated system, characterised by its excitation energy. This system can “evaporate” nucleons, or fragments, or γ rays, or even fission, to dissipate the residual excitation. The evaporation and fission probability for a particle of type j , mass m_j , spin $S_j \cdot \hbar$ and kinetic energy E are given by [28]:

$$P_j = \frac{(2S_j + 1)m_j}{\pi^2 \hbar^3} \int_{U_j}^{U_i - Q_j - \Delta_j} \sigma_{\text{inv}} \frac{\rho_f(U_f)}{\rho_i(U_i)} E dE$$

$$P_F = \frac{1}{2\pi\hbar} \frac{1}{\rho_i(U_i)} \int_0^{(U - B_F)} \rho_F(U - B_F - E) dE$$

where ρ is the nuclear level density, U_i and U_f are the excitation energy of the initial and final nuclei, B_F is the fission barrier, Q_j the reaction Q for emitting a particle of type j , and σ_{inv} is the cross-section for the inverse process, which takes into account a possible Coulomb barrier. Under standard approximations, the evaporation spectrum has a Maxwellian shape:

$$P_j(E) dE \approx K E e^{-\frac{E}{T}} dE$$

where T ($T \approx \sqrt{U - \Delta/a}$) is the nuclear temperature, usually in the MeV range (a is level density parameter $\approx A/8 \text{ MeV}^{-1}$, and Δ is the pairing energy).

Neutron emission is favoured over charged particle emission, due to the Coulomb barrier, especially for medium-heavy nuclei. Moreover, the excitation energy is higher in heavier nuclei due to the larger cascading chances and larger number of primary collision in the Glauber cascade at high energies, and a is smaller, thus the average neutron energy is smaller. Therefore, the neutron multiplicity is higher for heavy nuclei than for light ones. For light residual nuclei, where the excitation energy may overwhelm the total binding energy, a statistical fragmentation (Fermi Break-up) model is more appropriate (see [1,3,29] for the FLUKA implementation).

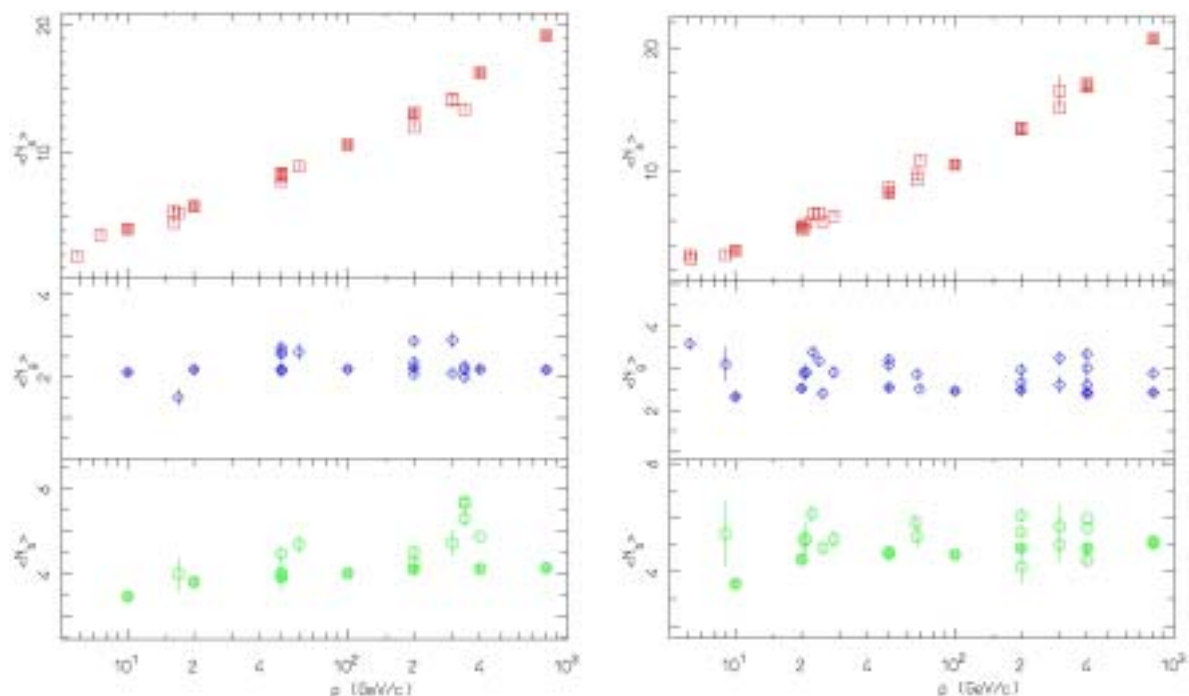
The evaporation/fission/break-up processes represent the last stage of a nuclear interaction and are responsible for the exact nature of the residuals left after the interactions. However, for a coherent self-consistent model, the mass spectrum of residuals is highly constrained by the excitation energy distribution found in the slow stages, which in turn is directly related to the amount of primary collisions and following cascading which took place in the fast stages.

h-A at high energies: The invariance of the target fragmentation region

The description of nuclear interactions as a sequence of well-defined physics processes, each one governed by its own laws, is very useful in understanding the complex dynamics of these collisions, and leads also to a natural Monte Carlo implementation, in which each stage begins at the final state of the previous one. The power of this approach will be demonstrated in the following, where the most basic properties of hadron-nuclear collisions in the multi-GeV range are explained by means of the concepts introduced in the previous sections.

The Glauber cascade and the formation zone act together in reaching a regime where the “slow” part of the interaction is almost independent of the particle energy. This can easily be verified looking at charged particle average multiplicities and multiplicity distributions as a function of energy (Figure 9). “Fast” (or “shower”) tracks (charged particles with $\beta = \frac{v}{c} > 0.7$), coming from the projectile primary interactions, show the typical \approx logarithmic increase observed for h-N interactions. As previously shown in Figures 6 and 7, the average multiplicity and its variance are directly related to the distribution of primary collisions as predicted by the Glauber approach. Due to the very slow variation of hadron-nucleon cross-section from a few GeV up to a few TeVs, the Glauber cascade is almost energy independent and the rise in the multiplicity of “fast” particles is related only to the increased multiplicity of the elementary h-N interactions.

Figure 9. Shower, grey and black tracks multiplicities for π^- (left) and protons (right) on emulsion, as a function of the projectile momentum. Open symbols are experimental data from various sources, full symbols are FLUKA results.

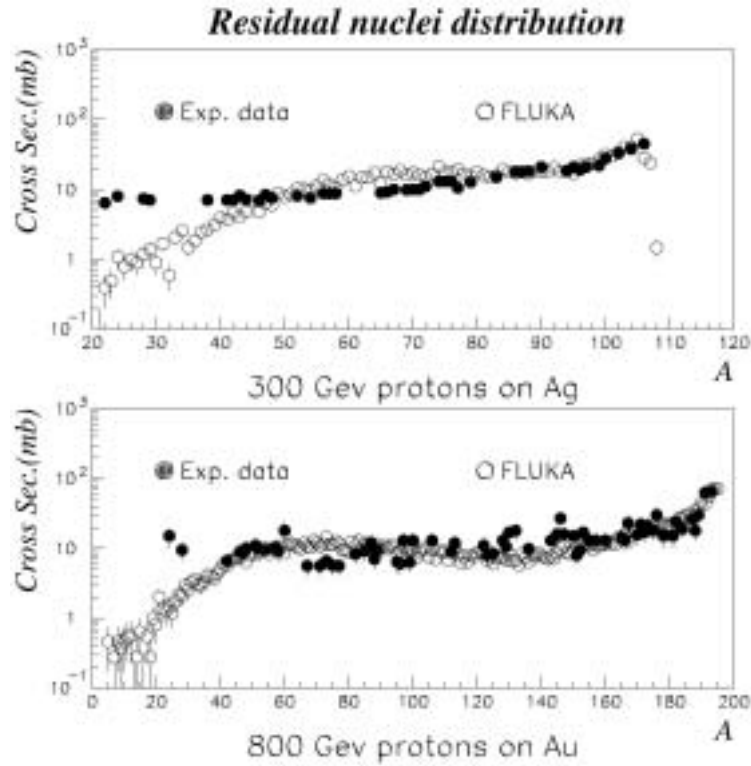


Due to the onset of formation zone effects, most of the hadrons produced in the primary collisions escape the nucleus without further re-interactions. Further cascading only involves the slow fragments produced in the target fragmentation region of each primary interaction, and therefore it tends to quickly saturate with energy as the Glauber cascade reaches its asymptotic regime. This trend is well reflected in the average multiplicity (and multiplicity distribution) of “grey” tracks (charged particles with $0.3 < \beta < 0.7$), which are mostly protons produced in secondary collisions during the intranuclear cascade and pre-equilibrium phases.

At the end of the cascading process, the residual excitation energy is directly related to the number of primary and secondary collisions that took place. Each collision indeed leaves a “hole” in the Fermi sea which carries an excitation energy related to its depth in the Fermi sea. According to the considerations outlined previously, evaporation products as well as residual excitation functions should reach an almost constant condition as soon as the Glauber mechanism and the formation zone are fully developed. This can be verified looking at the production of “black” tracks (charged particles with $\beta < 0.3$), which are mostly evaporation products. The data reported in Figure 9 demonstrate how they saturate as well, and how this property is nicely reproduced by models based on the assumptions outlined in this paper.

The ultimate nature of the residual left after an interaction also depends on complicated details of nuclear structure which are often difficult to include in a Monte Carlo approach. In particular, spin- and parity-dependent calculations are unmanageable due to their complexity, and in any case would be fairly useless due to the impossibility of accounting for these quantum numbers during the fast stages of the reactions. Nevertheless the general features of isotope production are reasonably reproduced; Figure 10 shows the computed and measured mass distributions of residuals after 300 GeV proton

Figure 10. Residual nuclei mass distribution.
 Experimental data are from [30] for silver and [31] for gold.



interactions on silver and 800 GeV protons on gold. The agreement is fairly good in the spallation region close to the target mass, and still reasonable down to very light masses where the observed discrepancy is due more to the lack of a fragmentation model in the calculation than to deficiencies in the physics of the fast stages.

Recent examples of successful applications to complex problems of models like those described in this paper can be found in [32-34].

Examples of (G)INC calculations

In the previous sections, a brief description of the processes occurring during hadronic inelastic interactions in the energy range of interest was given. In the present section, a few representative comparisons between model results and experimental data on particle production in the energy range of interest are discussed. All the presented results were obtained using the FLUKA code, and most of them rely on the model used for the intermediate energy range, known as PEANUT (PreEquilibrium Approach to NUClear Thermalization). This model combines both an INC part and a pre-equilibrium part. Nuclear potential effects (refraction and reflection) are modelled into the code, as well as quantistic effects, like Pauli blocking, nucleon-nucleon correlations, fermion anti-symmetrisation, coherence length and formation zone. For pion-induced interactions, the approach of PEANUT is very different from all other available (G)INC codes, none of which includes a complex optical potential or absorption effects computed according to modern approaches.

From plain INC to more complex models

Weaknesses of traditional INC codes have been described in the literature for quite some time. Some examples are given here in an attempt to illustrate the sources of such deficiencies. In order to demonstrate the effect of the various ingredients, the same projectile-target combination, 80.5 MeV protons on ^{90}Zr , has been computed under different assumptions and the results compared with experimental data [35,36]. Four different trials were performed, always using PEANUT with all or only a few of the ingredients at work. The results of the exercise are presented in Figures 11-14 for (p,xn) and in Figures 15-18 for (p,xp). In all these figures as well as in following ones, experimental data are plotted as full symbols joined by a line, while model results are given either by symbols with error bars or by histograms with shaded areas representing the statistical error.

Figure 11. $^{90}\text{Zr}(\text{p},\text{xn})$ at 80.5 MeV, plain INC (see text) calculation

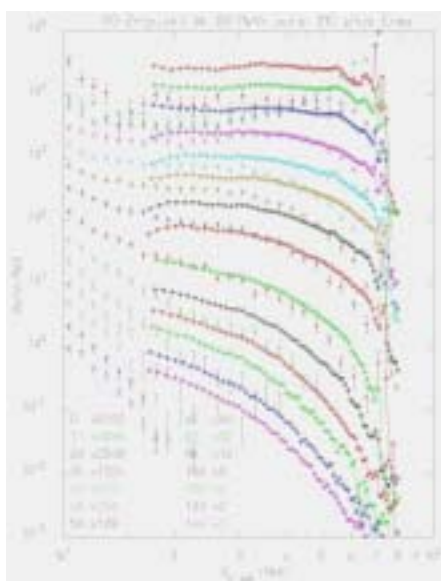


Figure 12. $^{90}\text{Zr}(\text{p},\text{xn})$ at 80.5 MeV, plain INC plus pre-equilibrium (see text) calculation

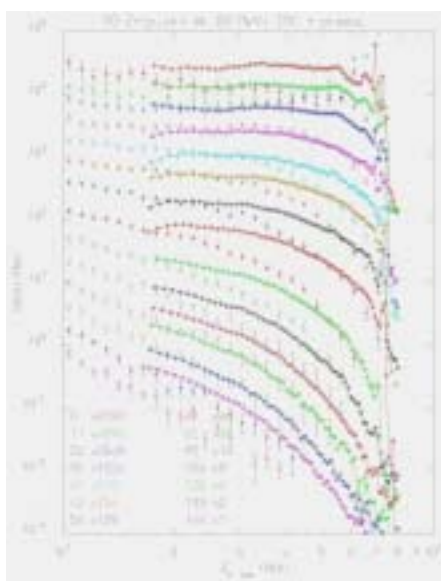


Figure 13. $^{90}\text{Zr}(p,xn)$ at 80.5 MeV, PEANUT (see text) calculation with no quantum effect, but Pauli blocking

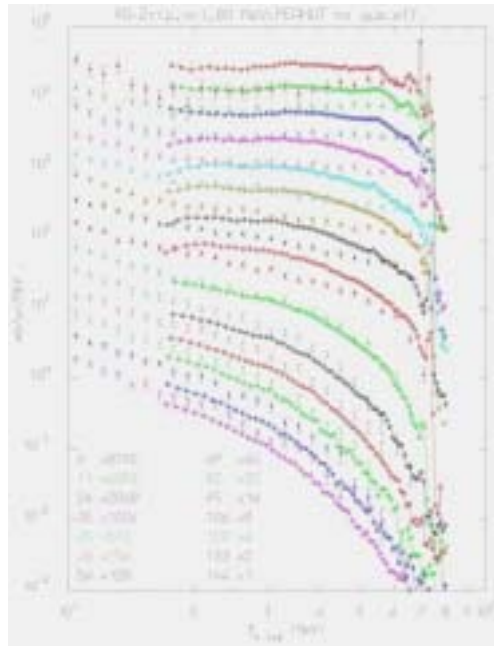


Figure 14. $^{90}\text{Zr}(p,xn)$ at 80.5 MeV, full PEANUT (see text) calculation

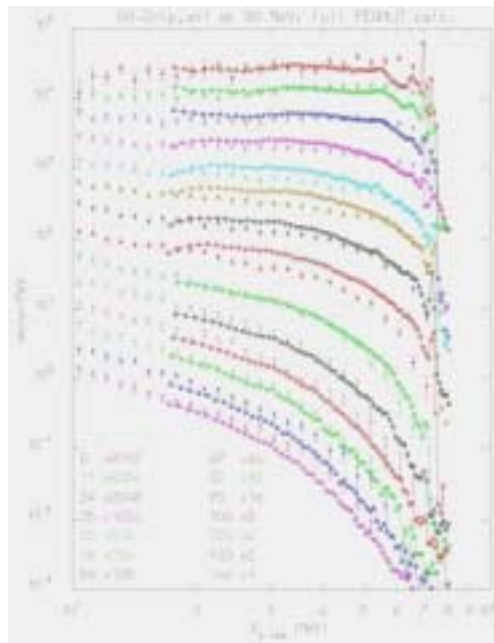


Figure 15. $^{90}\text{Zr}(p,xp)$ at 80.5 MeV, plain INC (see text) calculation

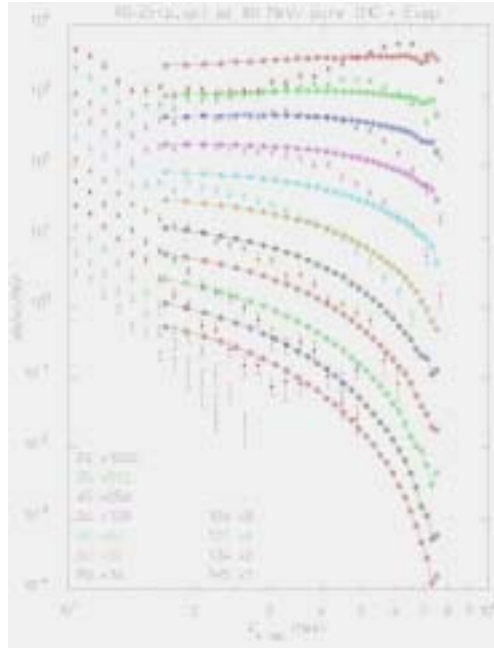


Figure 16. $^{90}\text{Zr}(p,xp)$ at 80.5 MeV, plain INC plus pre-equilibrium (see text) calculation

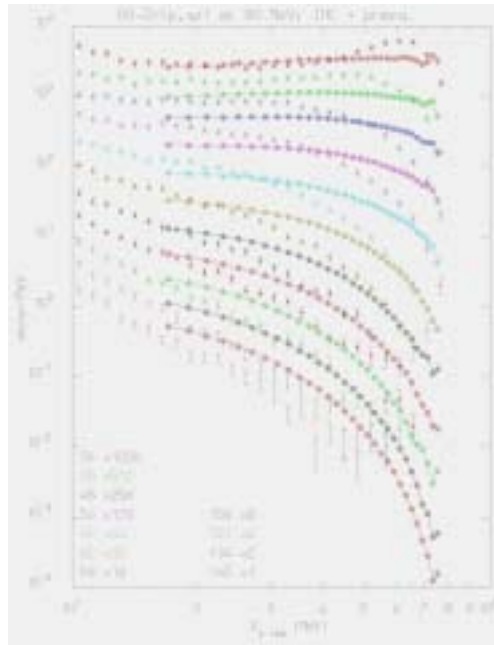


Figure 17. $^{90}\text{Zr}(p,xp)$ at 80.5 MeV, PEANUT (see text) calculation with no quantum effect, but Pauli blocking

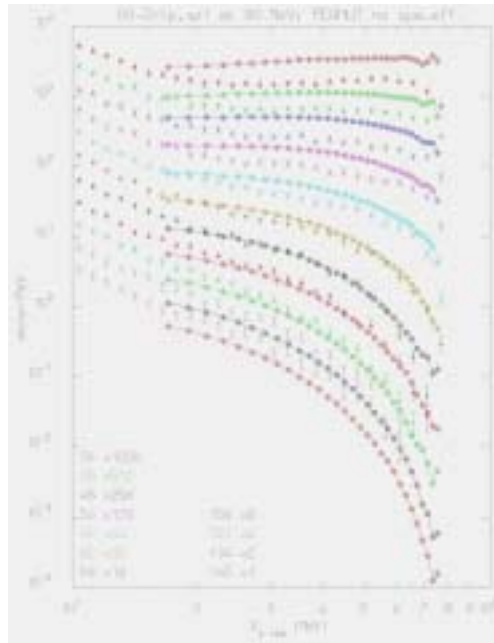
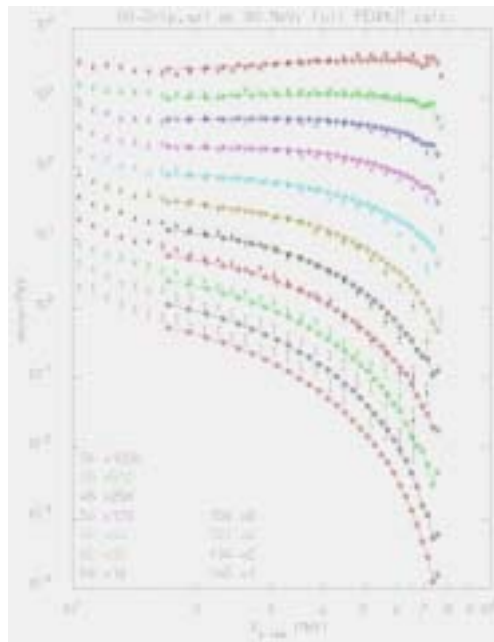


Figure 18. $^{90}\text{Zr}(p,xp)$ at 80.5 MeV, full PEANUT (see text) calculation



The first attempt (Figures 11,15) was performed using a plain INC approach with no pre-equilibrium stage, no refraction and reflection and only Pauli blocking activated among the quantistic effects. The transport threshold for secondary nucleons was set equal to the average binding energy. As can be easily seen, results are very poor, with an overestimation of the forward peak and a strong underestimation of backward angle emission. These results were obtained with assumptions which are quite consistent with those used by the “classical” INC models but, as usual in PEANUT, the binding energy has been correctly set at each emission stage to match the actual reaction Q-value.

The second trial does not yet use refraction and reflection but the pre-equilibrium stage is there. There is a clear improvement in the results, particularly at backward angles, but large discrepancies still exist.

The third trial was performed switching on all the refraction and reflection machinery, but still limiting the quantistic effects to Pauli blocking alone. There is a great improvement, with a reasonable description of backward angles, though discrepancies still exist at the forward ones. The reason for these last deficiencies is related to the effect of particle curvature in the nucleus which both increases the particle track length and hence the re-interaction probability, and at the same time “pushes” particles towards the nucleus centre, again increasing the interaction probability.

The fourth and last trial was performed with all quantistic effects on, that is with coherence length, nucleon correlation and fermion anti-symmetrisation effects on. Clearly they are effective in increasing particle mean free paths in the nuclear medium resulting in a quite reasonable description of the whole spectrum at all angles.

The effect of particle curvature on interaction rates is typical of INC codes which include refraction and reflection [37,38]. The reason for the good results, at least for angle-integrated spectra, of INC models based on straight trajectories (like the old Bertini INC) probably lies in the compensating effect of the lack both of mechanisms able to lengthen particle mean free paths, and of the curvature effect which operates in the opposite direction. The price is a poor description of angular distributions, at least for energies not much larger than typical potential energies.

Two examples of charged pion production (and possibly re-interaction) along the lines described earlier (see *h-N interactions at intermediate energies* and *Intermediate energy pions in nuclei*) at intermediate energies can be found in Figure 19, compared with available experimental data. Many more examples can be found in Refs. [1-3].

Coalescence

Composite particles, ranging from deuterons to alphas and even larger fragments, can obviously be emitted during the interaction “slow” stages (evaporation, fission, fragmentation, see *Evaporation, fission and nuclear break-up*). However, higher-energy, lower-intensity composite fragments can also be emitted through non-equilibrium processes. In particular mechanisms based on coalescence of energetic individual nucleons or light fragments into larger fragments when close in phase space were proposed many years ago as a natural explanation of high-energy composite particle production [40]. These ions, even though relatively rare, can have a substantial dosimetric impact and should not be neglected. An example of triton production by means of the coalescence model embedded into FLUKA is shown in Figure 20 compared with available experimental data [41].

Figure 19. Double-differential distributions of charged pions produced by neutrons of $\langle E_n \rangle = 383$ (left) and 542 MeV (right)

Experimental data from [39]

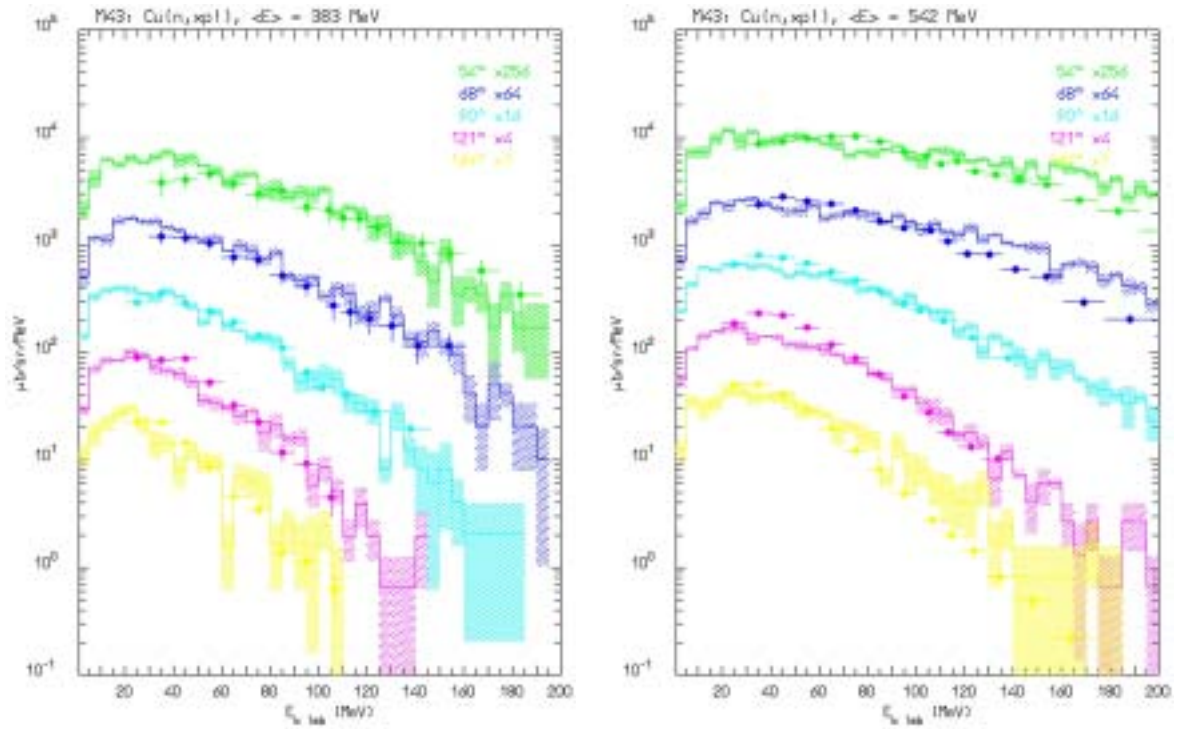
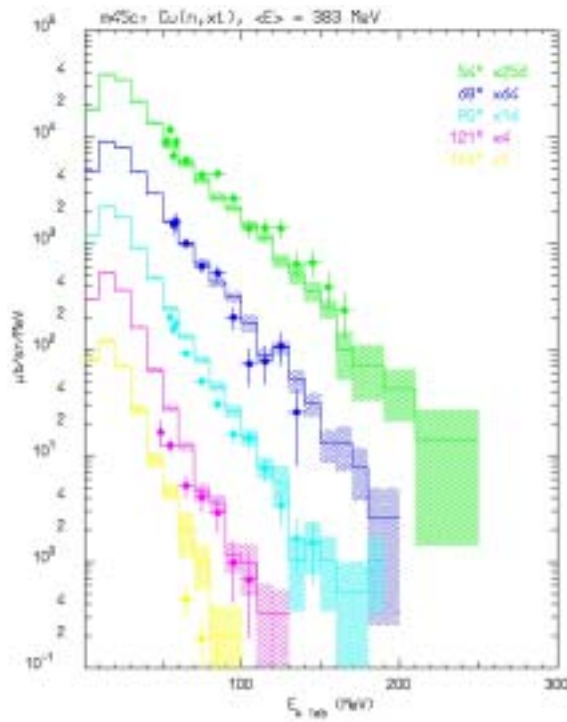


Figure 20. Double-differential distributions of tritons produced by neutrons of $\langle E_n \rangle = 38$

Experimental data from [41]



Nucleus-nucleus collisions

The topic of ion-ion nuclear interactions is very wide and cannot be treated in an exhaustive way in an introductory paper like the present one.

Only a few hints will be given in the following for a proper generalisation of intranuclear cascade approach to nucleus-nucleus collisions.

The approach to nucleus-nucleus cascading

In the intermediate-energy range (≈ 100 MeV/n to few GeV/n), as well for the cascade part of high-energy reactions, three main classes of microscopic models are suitable for Monte Carlo applications. These are all microscopic kinetic models including the propagation and mutual interactions of pion and nucleon resonances. Similar two-body collision terms, mostly based on free scattering, are used for individual hadron-hadron collisions in strict analogy with the hadron-nucleus case. The three approaches differ mostly in their treatment of the nuclear field and the corresponding propagation of particles in the nuclear medium.

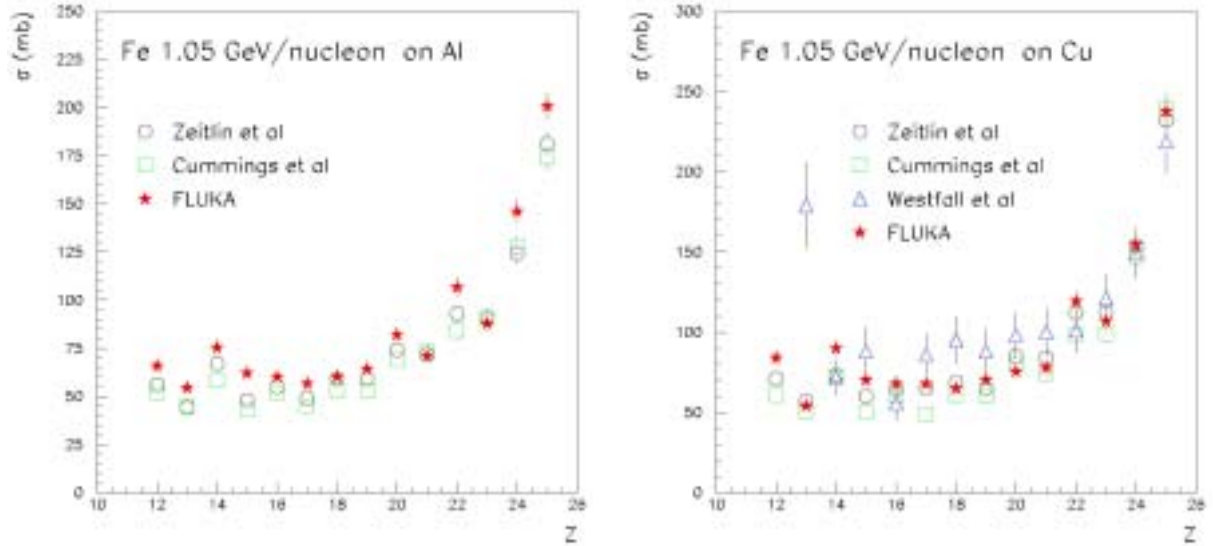
- (Generalised) IntraNuclear Cascade models:
 - Nucleon mean field.
 - Semi-classical trajectories.
- Quantum Molecular Dynamics models [45,46]:
 - Gaussian packet wave functions for nucleons.
 - Nucleon mean field as the sum of two-body potentials.
- BUU (Boltzmann-Uehling-Uhlenbeck) equation-based models [47-50]:
 - Time evolution equation of the nucleon (pions...) one-body phase-space distribution.
 - Test particle method (semi-classical trajectories in a self-consistent mean field).

(G)INC and QMD models have been successfully implemented into Monte Carlo generators and sometimes extended up to very high energies (see for example [46,51-57]) and to the treatment of all hadrons by means of the Glauber approach extended to AA collisions and of string models (like DPM).

FLUKA has been successfully extended [58] to cover nucleus-nucleus collisions, using the DPMJET [51-54] code at high (> 5 GeV/n) energies, and an extensively modified version of the RQMD-2.4 code[55-57]. Examples of the performances of FLUKA when running with the modified RQMD-2.4 model are presented in Figure 21 compared with experimental data for fragment production at 1.05 GeV/n.

Figure 21. Fragment charge cross-sections for 1.05 GeV/n Fe ions on Al (left) and Cu (right)

♣ – FLUKA, ○ – Zeitlin, et al. [60], □ – (1.5 GeV/n) Cummings, et al. [62], Δ – (1.88 GeV/n) Westfall, et al. [61]



The Glauber formulation for A-A collisions

The extension of the Glauber approach to nucleus-nucleus collisions is a classical approach and the details can be easily found in the literature (i.e. [42-44]).

When extended to nucleus-nucleus collisions, the Glauber quantum mechanical approach leads to (B and A nucleons for the projectile/target respectively):

$$\begin{aligned}
 \sigma_{BA \text{ abs}}(s) &= \sigma_{BA \text{ T}}(s) - \sigma_{BA \text{ el}}(s) - \sigma_{BA \text{ qe}}(s) = \\
 &= \sigma_{BA \text{ r}}(s) - \sigma_{BA \text{ qe}}(s) \equiv \int d^2 \vec{b} \mu_{BA \text{ abs}}(\vec{b}, s) \\
 &= \int d^2 \vec{b} \int d^3 \vec{w} |\Psi_{iB}(\vec{w})|^2 \int d^3 \vec{u} |\Psi_{iA}(\vec{u})|^2 \\
 &\quad \cdot \left\{ 1 - \prod_{k=1}^B \prod_{j=1}^A \left\{ 1 - \left[1 - |S_{hN}(\vec{b} - \vec{r}_{j\perp} + \vec{d}_{k\perp}, s)|^2 \right] \right\} \right\}
 \end{aligned}$$

where, as usual, $\sigma_{BA \text{ abs}}(s)$ is the absorption (particle production) cross-section as a function of the centre of mass energy, $\sigma_{BA \text{ T}}(s)$ is the total one, $\sigma_{BA \text{ el}}(s)$ the (coherent) elastic one and $\sigma_{BA \text{ qe}}(s)$ the quasi-elastic (incoherent elastic) cross-section. All of them can be computed out of the Glauber formalism.

The string interpretation for the Glauber cascade in nucleus-nucleus collision is similar to the one of hadron-nucleus reactions. In addition to valence-valence and sea-valence chains, sea-sea chains are also possible when both the projectile and target nucleon of a specific term in the Glauber expansion suffer more than one primary collision.

Once the primary collision configuration is selected according to this formalism, the description proceeds pretty much in the same way as in the hadron-nucleus case. Chains are stretched and

hadronised, the formation zone is taken into account and possible cascading in both the projectile and target nucleus is performed. At the end of the fast stages, spectator nucleons and nucleons which have not escaped the system are grouped into projectile- and target-like residuals each one with the excitation energy resulting from the previous events. Evaporation/fission/fragmentation is then performed for both the projectile and target residuals. An example of an implementation along these ideas can be found in [59].

Conclusions

Hadron interaction modelling is advanced enough to provide reliable estimates of particle production and propagation under most circumstances. Most of the basic features of nuclear interactions can be understood in terms of a general scheme where the fast, cascade, pre-equilibrium and equilibrium (“slow”) stages can be naturally concatenated, each one explaining for some of the experimental observables, and linked together in a coherent and self-consistent picture. This approach can be naturally exploited in Monte Carlo models which become very powerful tools in predicting interaction properties over a wide energy range and for a variety of applications, ranging from basic research to applied physics.

These features make them ideal tools for dosimetry calculations, where all particle species must be correctly described over a wide energy range, which spans from sub-MeV heavy recoils up to several tens or hundreds of GeV (or GeV/n) for commercial and space mission dosimetry.

REFERENCES

- [1] Fassò, A., A. Ferrari, J. Ranft and P.R. Sala, “New Developments in FLUKA Modelling of Hadronic and EM Interactions”, *Proceedings of SARE-3*, KEK-Tsukuba, H. Hirayama (ed.), 7-9 May 1997, KEK report Proceedings 97-5, 32 (1997).
- [2] Fassò, A., A. Ferrari, J. Ranft and P.R. Sala, “FLUKA: Status and Prospective for Hadronic Applications”, *Proceedings of the MonteCarlo 2000 Conference*, Lisbon, 23-26 October 2000, A. Kling, F. Barão, M. Nakagawa, L. Távora, P. Vaz (eds.), Springer-Verlag Berlin, 955 (2001).
- [3] Ferrari, A. and P.R. Sala, “The Physics of High Energy Reactions”, *Proceedings of Workshop on Nuclear Reaction Data and Nuclear Reactors Physics, Design and Safety*, A. Gandini, G. Reffo (eds.), Trieste, Italy, April 1996, 2, 424 (1998).
- [4] Ferrari, A. and P.R. Sala, “Physics Processes in Hadronic Showers”, *Proceedings of the IX International Conference on Calorimetry in High Energy Physics*, Annecy, 9-14 October 2000, B. Aubert, J. Colas, P. Nédelec, L. Poggioli (eds.), Frascati Physics Series, 31 (2001).
- [5] Huber, S. and J. Aichelin, “Production of Δ and N^* Resonances in the One-boson Exchange Model”, *Nucl. Phys.*, A573, 587 (1994).

- [6] Engel, A., W. Cassing, U. Mosel, M. Schäfer, Gy. Wolf, “Pion-nucleus Reactions in a Microscopic Transport Model”, *Nucl. Phys.*, A572, 657 (1994).
- [7] Teis, S., W. Cassing, M. Effenberger, A. Hombach, U. Mosel, Gy. Wolf, “Pion-production in Heavy-ion Collisions at SIS Energies”, *Z. Phys.*, A 357, 451 (1997).
- [8] Capella, A., U. Sukhatme, C-I. Tan and J. Tran Thanh Van, “Dual Parton Model”, *Phys. Rep.*, 236, 225 (1994).
- [9] Kaidalov, A., “The Quark-gluon Structure of the Pomeron and the Rise of Inclusive Spectra at High Energies”, *Phys. Lett.*, B116, 459 (1982).
- [10] Kaidalov, A. and K.A. Ter-Martirosyan, “Pomeron as Quark-gluon Strings and Multiple Hadron Production at SPS-collider Energies”, *Phys. Lett.*, B117, 247 (1982).
- [11] Adamus, M., *et al.*, “Charged Particle Production in K^+p , π^+p and pp Interactions at 250 GeV/c”, *Z. Phys.*, C39, 311 (1988).
- [12] Glauber, R.J. and G. Matthiae, “High-energy Scattering of Protons by Nuclei”, *Nucl. Phys.*, B21, 135 (1970).
- [13] Glauber, R.J., “High-energy Collision Theory”, in *Lectures in Theoretical Physics*, A.O. Barut and W.E. Brittin (eds.), Interscience, NewYork (1959).
- [14] Gribov, V.N., “Glauber Corrections and the Interaction between High-energy Hadrons and Nuclei”, *Sov. Phys. JETP*, 29, 483 (1969).
- [15] Gribov, V.N., “Interaction of Gamma Quanta and Electrons with Nuclei at High Energies”, *Sov. Phys. JETP*, 30, 709 (1970).
- [16] Bertocchi, L., “Graphs and Glauber”, *Nuovo Cimento*, 11A, 45 (1972).
- [17] De Marzo, C., *et al.*, “Multi-particle Production on Hydrogen, Argon and Xenon Targets in a Streamer Chamber by 200-GeV/c Proton and Antiproton Beams”, *Phys. Rev.*, D26, 1019 (1982).
- [18] Ajinenko, I.V., *et al.*, “Multiplicity Distribution in K^+Al and K^+Au Collisions at 250 GeV/c and a Test of the Multiple Collision Model”, *Z. Phys.*, C42, 377 (1989).
- [19] Fassò, A., A. Ferrari, J. Ranft and P. R. Sala, “FLUKA: Performances and Applications in the Intermediate Energy Range”, *Proceedings of the Specialists Meeting on Shielding Aspects of Accelerators, Targets & Irradiation Facilities*, Arlington, 28-29 April 1994, OECD/NEA, 287 (1995).
- [20] Ashery, D., I. Navon, G. Azuelos, *et al.*, “True Absorption and Scattering of Pions on Nuclei”, *Phys. Rev.*, C23, 2173 (1981).
- [21] Nakai, K., T. Kobayashi, T. Numao, T.A. Shibata, J. Chiba and K. Masutani, “Measurements of Cross-sections for Pion Absorption by Nuclei”, *Phys. Rev. Lett.*, 44, 1446 (1979).
- [22] Gadioli, E. and P.E. Hodgson, *Pre-equilibrium Nuclear Reactions*, Clarendon Press, Oxford, (1992).

- [23] Blann, M., “Hybrid Model for Pre-equilibrium Decay in Nuclear Reactions”, *Phys. Rev. Lett.*, 27, 337 (1971).
- [24] Blann, M., “Importance of the Nuclear Density Distribution on Pre-equilibrium Decay”, *Phys. Rev. Lett.*, 28, 757 (1972).
- [25] Blann, M. and H.K. Vonach, “Global Test of Modified Pre-compound Decay Models”, *Phys. Rev.*, C28, 1475 (1983).
- [26] Blann, M., “Pre-compound Analyses of Spectra and Yields Following Nuclear Capture of Stopped π^- ”, *Phys. Rev.*, C28, 1648 (1983).
- [27] Shlomo, S., “Energy Level Density of Nuclei”, *Nucl. Phys.*, A539, 17 (1992).
- [28] Weisskopf, V.F., “Statistics and Nuclear Reactions”, *Phys. Rev.*, 52, 295 (1937).
- [29] Ferrari, A., P.R. Sala, J. Ranft and S. Roesler, “Cascade Particles, Nuclear Evaporation, and Residual Nuclei in High-energy Hadron-nucleus Interactions”, *Z. Phys.*, C70, 413 (1996).
- [30] Porile, N.Y.T., G.T. Cole and C. Rudy, “Nuclear Reactions of Silver with 25.2 GeV ^{12}C Ions and 300 GeV Protons”, *Phys. Rev.*, C19, 2288 (1979).
- [31] Sihver, L., K. Aleklett, W. Loveland, P.L. McGaughey, D.H.E. Gross and H.R. Jaqaman, “Gold Target Fragmentation by 800 GeV Protons”, *Nucl. Phys.*, A543, 703 (1992).
- [32] Gschwendtner, E., C.W. Fabjan, N. Hessey, T. Otto and H. Vincke, “Measuring the Photon Background in the LHC Experimental Experiment”, *Nucl. Instr. Meth.*, A476, 222 (2002).
- [33] Arnould, H., *et al.*, “Experimental Verification of Neutron Phenomenology in Lead and Transmutation by Adiabatic Resonance Crossing in Accelerator-driven Systems”, *Phys. Lett.*, B458, 167 (1999).
- [34] Battistoni, G., A. Ferrari, T. Montaruli and P.R. Sala, “Comparison of the FLUKA Calculations with CAPRICE94 Data on Muons in Atmosphere”, *Astropar. Phys.*, 17, 477 (2002).
- [35] Trabandt, M., W. Scobel, M. Blann, *et al.*, “Pre-equilibrium Neutron Emission in the Reactions ^{90}Zr , ^{208}Pb (p, xn) with 80 MeV Projectiles”, *Phys. Rev.*, C39, 452 (1989).
- [36] Cowley, A.A., A. van Kent, J.J. Lawrie, *et al.*, “Pre-equilibrium Proton Emission Induced by 80 and 120 MeV Protons Incident on ^{90}Zr ”, *Phys. Rev.*, C43, 678 (1991).
- [37] Chen, K., Z. Fraenkel, G. Friedlander, “VEGAS: A Monte Carlo Simulation of Intranuclear Cascades”, *Phys. Rev.*, 166, 949 (1968).
- [38] Chen, K., G. Friedlander and J.M. Miller, “Effects of Using a Velocity-dependent Potential in a Monte Carlo Simulation of Intranuclear Cascades”, *Phys. Rev.*, 176, 1208 (1968).
- [39] Bchle, R., J. Franz, P. Koncz, *et al.*, Neutron-induced Pion Production on Carbon, Copper and Bismuth at Intermediate Energies”, *Nucl. Phys.*, A515, 541 (1990).

- [40] Butler, S.T. and C.A. Pearson, “Deuterons from High-energy Proton Bombardment of Matter”, *Phys. Lett.*, 1, 77 (1962).
- [41] Franz, J., P. Koncz, E. Rssle, “Neutron-induced Production of Protons, Deuterons and Tritons on Copper and Bismuth”, *Nucl. Phys.*, A510, 774 (1990).
- [42] Engel, J., T.K. Gaisser, P. Lipari and T. Stanev, “Nucleus-nucleus Collisions and Interpretation of Cosmic-ray Cascades”, *Phys. Rev.*, D46, 5013 (1992).
- [43] Charagi, S.K. and S.K. Gupta, “Coulomb-modified Glauber Model Description of Heavy-ion Reaction Cross-sections”, *Phys. Rev.*, C41, 1610 (1990).
- [44] Bialas, A., M. Bleszynski and W. Czyz, “Multiplicity Distributions in Nucleus-nucleus Collisions at High Energies”, *Nucl. Phys.*, B111, 461 (1976).
- [45] Aichelin, J., ““Quantum” Molecular Dynamics – A Dynamical Microscopic n-body Approach to Investigate Fragment Formation and the Nuclear Equation of State in Heavy-ion Collisions”, *Phys. Rep.*, 202, 233 (1991) and references therein.
- [46] Niita, K., S. Chiba, T. Maruyama, T. Maruyama, H. Takada, T. Fukahori, Y. Nakahara and A. Iwamoto, “Analysis of the (N,xN') Reactions by Quantum Molecular Dynamics Plus Statistical Decay Model”, *Phys. Rev.*, C52, 2620 (1995).
- [47] Bertsch, G.F. and S. Das Gupta, “A Guide to Microscopic Models for Intermediate-energy Heavy-ion Collisions”, *Phys. Rep.*, 160, 189 (1988).
- [48] Wolf, Gy., G. Batko, W. Cassing, U. Mosel, K. Niita and M. Schaefer, “Dilepton Production in Heavy-ion Collisions”, *Nucl. Phys.*, A517, 615 (1990).
- [49] Wolf, Gy., W. Cassing and U. Mosel, “Eta and Dilepton Production in Heavy-ion Reaction”, *Nucl. Phys.*, A545, 139c (1992).
- [50] Li, B.A. and W. Bauer, “Pion Spectra in a Hadronic Transport Model for Relativistic Heavy-ion Collisions”, *Phys. Rev.*, C44, 450 (1991).
- [51] Ranft, J., “Dual Parton Model at Cosmic-ray Energies”, *Phys. Rev.*, D51, 64 (1995).
- [52] Ranft, J., *DPMJET Version II.5*, code manual, hep-ph/9911232 (1999).
- [53] Ranft, J., *New Features in DPMJET Version II.5*, hep-ph/9911213 (1999).
- [54] Ranft, J., *Baryon Stopping in High-energy Collisions and the Extrapolation of Hadron Production Models to Cosmic Ray Energies*, hep-ph/0002137 (2000).
- [55] Sorge, H., H. Stöcker and W. Greiner, “Relativistic Quantum Molecular Dynamics Approach to Nuclear Collisions at Ultrarelativistic Energies”, *Nucl. Phys.*, A498, 567c (1989).
- [56] Sorge, H., H. Stöcker and W. Greiner, “Poincaré Invariant Hamiltonian Dynamics: Modelling Multi-hadronic Interactions in a Phase Space Approach”, *Ann. Phys. (N.Y.)*, 192, 266 (1989).

- [57] Sorge, H., “Flavor Production in Pb (160A GeV) on Pb Collisions: Effect of Color Ropes and Hadronic Rescattering”, *Phys. Rev.*, C52, 3291 (1995).
- [58] Andersen, V., F. Ballarini, G. Battistoni, *et al.*, *The FLUKA Code for Space Applications: Recent Developments*, solicited talk at the World Space Congress 2002, 34th Scientific Assembly of the Committee on Space Radiation (COSPAR), 10-19 October, Houston, Texas, to be published in *Adv. Space Res.*
- [59] Ferrari, A., P.R. Sala, J. Ranft and S. Roesler, “The Production of Residual Nuclei in Peripheral High-energy Nucleus-nucleus Interactions”, *Z. Phys.*, C71, 75 (1996).
- [60] Zeitlin, C., L. Heilbronn, J. Miller, *et al.*, “Heavy Fragment Production Cross-sections from 1.05 GeV/nucleon ⁵⁶Fe in C, Al, Cu, Pb and CH₂ Targets”, *Phys. Rev.*, C56, 388 (1997).
- [61] Westfall, G.D., L.W. Wilson, P.J. Lindstrom, *et al.*, “Fragmentation of Relativistic ⁵⁶Fe”, *Phys. Rev.*, C19, 1309 (1979).
- [62] Cummings, J.R., W.R. Binns, T.L. Garrard, *et al.*, “Determination of the Cross-sections for the Production of Fragments from Relativistic Nucleus-nucleus Interactions. I. Measurements”, *Phys. Rev.*, C42, 2508 (1990).

MODELLING CHARGED-PARTICLE ENERGY-LOSS STRAGGLING

H. Grady Hughes and Richard E. Prael

Los Alamos National Laboratory

Group X-5, MS F663

Los Alamos NM 87545 USA

Abstract

We present the current forms of the algorithms used to model collisional energy-loss straggling for electrons and for heavy charged particles in MCNP5 and MCNPX. We also describe a recent improvement in the logic for applying the straggling models for heavy charged particles, and show illustrative results for the improved logic.

Introduction

Monte Carlo simulation of charged-particle transport is a difficult matter. In contrast to neutral particles, whose transport can be regarded as a series of free flights between isolated, localised interactions, charged particles in matter experience very large numbers of small, long-range Coulomb interactions with atomic electrons and with the screened charges of nuclei. This circumstance makes the cost of a direct Monte Carlo simulation of charged-particle transport prohibitive for most situations of practical interest, even with present-day computers. In order to achieve a manageable Monte Carlo capability, it has been necessary to rely on a variety of analytic and semi-analytic multiple scattering theories which attempt to use the fundamental cross-sections and the statistical nature of the transport process to predict probability distributions for significant quantities, such as energy loss and angular deflection. These theories are limited by a variety of approximations and constraints; in particular they are generally invalid unless the energy loss of the charged particle is small compared to its starting energy. Therefore multiple scattering theories must be applied for sufficiently short paths along the charged particle's trajectory. The technique of dividing the charged particle's trajectory into segments that are large compared to the microscopic mean free path, but small enough for the application of multiple scattering theories is called the "condensed history" method. This approach to Monte Carlo for charged particles was essentially invented by Martin J. Berger, whose 1963 paper [1] described the techniques that have guided Monte Carlo code development ever since. Based on the methods of that work, Berger and Stephen M. Seltzer developed the ETRAN series of electron/photon transport codes [2]. These codes have been maintained and enhanced for many years at the National Institute of Standards and Technology, and are the basis for the Integrated TIGER Series (ITS) [3,4], a system of general-purpose, application-oriented electron/photon transport codes developed by John A. Halbleib, Ronald P. Kensek, and others at Sandia National Laboratories. The electron transport physics of the MCNP code [5] is largely based on that of the Integrated TIGER Series. In this paper we will concentrate on two of the multiple scattering theories important to MCNP and to its high-energy version MCNPX [6]. These are the Landau [7] theory for energy-loss straggling of electrons and the Vavilov [8] theory applicable to heavy charged particles. We will also discuss a recent improvement in the detailed logic of heavy charged particle transport relevant to the application of the Vavilov model.

Landau theory for electron energy-loss straggling

For the mean collisional energy loss of electrons, MCNP uses an analytic representation given by Berger [1] based on a combination of the Bethe-Bloch stopping power [9-11] and the Møller [12] cross-section for electron-electron scattering. Because an electron step represents the cumulative effect of many individual random collisions, fluctuations in the energy loss rate will occur. Thus the energy loss will not simply be the mean collisional energy loss $\bar{\Delta}$; rather there will be a probability distribution $f(s,\Delta)d\Delta$ from which the energy loss Δ for the step of length s can be sampled. Landau [7] studied this situation under the simplifying assumptions that the mean energy loss for a step is small compared with the electron's energy, that the energy parameter ξ defined below is large compared with the mean excitation energy of the medium, that the distribution of energy losses ϵ from individual collisions can be adequately represented (above some minimum related to the mean ionisation energy) by:

$$w(\epsilon) = \frac{\xi}{s\epsilon^2} \quad (1)$$

based on the Rutherford [13] cross-section, and that the formal upper limit of the individual energy losses ϵ can be extended to infinity. With these simplifications, Landau found that the energy loss distribution can be expressed as:

$$f(s, \Delta) d\Delta = \phi(\lambda) d\lambda$$

in terms of $f\phi(\lambda)$, a universal function of a single scaled variable:

$$\lambda = \frac{\Delta}{\xi} - \log \left[\frac{2\xi m v^2}{(1-\beta^2) I^2} \right] + \delta + \beta^2 - 1 + C \quad (2)$$

Here m and v are the mass and speed of the electron, δ is the density effect correction, β is v/c , I is the mean excitation energy of the medium, and C is Euler's constant ($C = 0.5772157\dots$). The parameter ξ is defined by:

$$\xi = \frac{2\pi e^4 N Z z^2}{m v^2} s$$

where e is the charge of the electron, NZ is the number density of atomic electrons, and z is the charge of the projectile ($z = -1$ for electrons). The universal function is:

$$\phi\lambda = \frac{1}{2\pi i} \int_{x-i\infty}^{x+i\infty} e^{\mu \log \mu + \lambda \mu} d\mu \quad (3)$$

where x is a positive real number specifying the line of integration.

For purposes of sampling, $\phi(\lambda)$ is negligible for $\lambda < -4$, so this range is ignored. Börsch-Supan [14] originally tabulated $\phi(\lambda)$ in the range $-4 \leq \lambda \leq 100$, and derived for the range $\lambda > 100$ the asymptotic form:

$$\phi(\lambda) \approx \frac{1}{w^2 + \pi^2} \quad (4)$$

in terms of the auxiliary variable w , where $\lambda = w + \log w + C - 3/2$. The developers of the ITS code have extended Börsch-Supan's tabulation, keeping the same range, but increasing the resolution. Sampling from this tabular distribution accounts for approximately 98.96% of the cumulative probability for $\phi(\lambda)$. For the remaining large- λ tail of the distribution, ITS uses the approximate form $\phi(\lambda) \approx w^{-2}$, which is easier to sample than Eq. (4), but is still quite accurate for $\lambda > 100$. Currently, MCNP follows the same procedures as ITS for the sampling of straggling.

Blunck and Leisegang [15] have extended Landau's result to include the second moment of the expansion of the cross-section. Their result can be expressed as a convolution of Landau's distribution with a Gaussian distribution:

$$f^*(s, \Delta) = \frac{1}{\sqrt{2\pi\sigma}} \int_{-\infty}^{\infty} f(s, \Delta') \exp \left[-\frac{(\Delta - \Delta')^2}{2\sigma^2} \right] d\Delta'$$

Blunck and Westphal [16] provided a simple form for the variance of this Gaussian:

$$\sigma_{\text{BW}}^2 = 10 \text{ eV} \cdot Z^{4/3} \bar{\Delta}$$

Subsequently, Chechin and Ermilova [17] investigated the Landau/Blunck-Leisegang theory, and derived an estimate for the relative error:

$$\epsilon_{\text{CE}} \approx \left[\frac{10\xi}{I} \left(1 + \frac{\xi}{10I} \right)^3 \right]^{-1/2}$$

due to the neglect of higher-order moments. Based on this work, Seltzer [18] describes and recommends a correction to the Blunck-Westphal variance:

$$\sigma = \frac{\sigma_{\text{BW}}}{1 + 3\epsilon_{\text{CE}}}$$

This completes the purely theoretical description of the Landau straggling model as it is used in ITS and essentially identically in MCNP and MCNPX. However, examination of Eq. (2) and Eq. (4) shows that unrestricted sampling of λ will not result in a finite mean energy loss. Therefore, a final *ad hoc* adjustment to the sampling algorithm must be made. In the initialisation phase of the codes, a material- and energy-dependent cut-off λ_c is computed subject to the condition that the integral of the energy-loss distribution up to λ_c gives the correct mean energy loss. During the transport phase, this cut-off is imposed as an upper limit on the sampled value of λ . In this way, the correct mean energy loss is preserved.

Vavilov theory for heavy charged-particle straggling

For heavier charged particles losing energy through collisions with atomic electrons, a more realistic theory is needed. In particular the assumption of unlimited energy losses from individual collisions is no longer valid, and a maximum possible individual energy loss ϵ_{max} must be introduced. For an unrestricted theory (typical of Class I condensed history models in the sense of Berger), this maximum is known from relativistic kinematics:

$$\epsilon_{\text{max}} = \frac{2mc^2\beta^2\gamma^2}{1 + 2\gamma(m/M) + (m/M)^2}$$

where $\beta = v/c$ and $\gamma = (1 - \beta^2)^{-1/2}$ are the usual relativistic parameters for the projectile, and M and m are the rest masses of the projectile and the electron, respectively. In terms of ϵ_{max} the single-collision energy-loss cross-section of Eq. (1) now becomes [19]:

$$w(\epsilon) = \frac{\xi}{s\epsilon^2} \left(1 - \frac{\epsilon\beta^2}{\epsilon_{\text{max}}} \right), \quad \epsilon \leq \epsilon_{\text{max}}; \quad w(\epsilon) = 0, \quad \epsilon > \epsilon_{\text{max}}$$

Working from these assumptions, Vavilov [8] developed a more general theory of energy straggling. In terms of previously defined quantities and the new dimensionless parameter:

$$\kappa = \frac{\xi}{\epsilon_{\text{max}}}$$

Vavilov defines a new form for the scaled energy-loss variable:

$$\lambda_v = \frac{\Delta - \bar{\Delta}}{\varepsilon_{\max}} - \kappa(1 + \beta^2 - C)$$

Now the probability distribution for energy loss becomes:

$$f(s, \Delta)d\Delta = \frac{1}{\xi} \phi_v(\lambda_v, \kappa, \beta^2) d\lambda_v$$

where the new function to be sampled for the energy-loss variable is:

$$\phi_v(\lambda_v, \kappa, \beta^2) = \frac{\kappa}{\pi} e^{\kappa(1+\beta^2 C)} \int_0^\infty e^{\kappa f_1(y)} \cos(y\lambda_v + \kappa f_2(y)) dy \quad (5)$$

written in terms of two auxiliary functions:

$$f_1(y) = \beta^2 \{\log y + \text{Ci}(y)\} - \cos y - y \text{Si}(y)$$

$$f_2(y) = y \{\log y + \text{Ci}(y)\} + \sin y + \beta^2 \text{Si}(y)$$

which are themselves written in terms of auxiliary special functions, the sine integral $\text{Si}(y)$, and the cosine integral $\text{Ci}(y)$.

This analytic representation is obviously a difficult one, consisting of combinations and integrals of quite complicated functions. However, from a theoretical point of view, its real difficulty lies in the fact that the distribution to be sampled, Eq. (5), depends explicitly on the projectile energy (through the factor β^2) and on the energy- and material-dependent parameter κ . By contrast the distribution function in Eq. (3) can be sampled without regard to the energy of the projectile or the characteristics of the medium; those quantities appear only in the translation from the scaled variable λ to the actual energy loss Δ by Eq. (2). The additional complexity of Eq. (5) makes the practical application of the Vavilov theory in Monte Carlo a challenging problem. This situation has been addressed by a variety of investigators (see Refs. [20-25] for an introductory sample). In MCNP5 and MCNPX, we currently use a version of an algorithm described by Rotondi and Montagna [26], and we are evaluating several other methods as well. This topic is an active area of investigation in recent new MCNP development.

An improvement in condensed-history logic

Guided by earlier success in the simulation of electrons by the modified Class I algorithms of the Integrated Tiger Series, the initial versions of MCNPX exploited a similar distinction between “energy steps” and smaller “angular substeps”, and relied on similar logic for associating the sampling of energy-loss straggling with the energy steps. For heavy charged particles, this system often works well, but has been found wanting in some cases, especially in the calculation of straggled energy spectra when thin regions are important. In this section we will briefly describe the old and new versions of the condensed-history transport logic for heavy charged particles, and show some computational tests to illustrate improvements from the new logic.

In earlier versions of MCNPX, the transport logic was essentially as shown in the following somewhat simplified pseudocode:

```

For charged particle with energy E, find initial energy interval J, with  $E_J > E \geq E^{J+1}$ .
Begin CELL LOOP.
  Get N = preset number of substeps per energy step ( $N > 1$ ).
  Begin ENERGY LOOP.
    Sample straggled energy deviation  $\Delta$  for step size  $p = (E_J - E_{J+1})/q_J$ , where  $q_J$  is
      the mean stopping power in energy interval J.
    (*) Define an effective stopping power  $Q_J = q_J + \Delta/p$  for substeps within interval J.
      Set default substep size =  $p/N$ .
      Begin SUBSTEP LOOP n = 1, N.
    (*) Find distances to time and energy cutoffs
      Find distances to possible interaction, and to surface crossing.
      Select d = the minimum of all of these and the default substep.
      Advance the particle by d and scatter the direction based on d and E.
    (*) Set  $E = E - Q_J d$  (adjust J if necessary).
      Select appropriate case:
        Process energy or time cutoff (terminate track).
        Process inelastic interaction (make secondaries and terminate track).
        Process elastic interaction (decrease E and adjust J if necessary).
        Process surface crossing. Cycle CELL LOOP.
        Process uneventful end of substep.
      If (energy group has changed) cycle ENERGY LOOP.
    End SUBSTEP LOOP.
  End ENERGY LOOP.
End CELL LOOP.

```

The three steps marked with an asterisk (*) above involve unnecessary approximation. The second of these (concerning cut-offs) is not particularly damaging, since it affects only the very end of the particle track. However, the first and last represent a more severe approximation. The problem is that the sampling of the straggling is done for a step (p) that is always longer than the actual step to be taken by the particle. Since the straggling theory is not linear in step size, this interpolated sampling is generally not accurate. The situation is exacerbated when there are many small zones or thin foils in the problem.

Furthermore, the straggling sample is always related to the energy interval containing the beginning of the step, even if the particle falls into a lower energy interval by the end of the step. This produces a small, but systematic error. Finally, this logic is unnecessarily complex, since the SUBSTEP loop can be ended either by its normal count, or by the energy group having changed. This is the well-known MCNP vs. ITS step-counting issue, which has been studied and discussed [27] in the context of electron transport.

In recent versions of MCNPX and in the developmental version of MCNP5, we have replaced this transport logic with a more straightforward approach that largely avoids these approximations. The new logic is essentially represented by the following pseudocode:

For charged particle with energy E , find initial energy interval J , with $E_J > E \geq E_{J+1}$.

Begin CELL LOOP.

Get N = preset number of substeps per energy step ($N > 1$).

Begin ENERGY LOOP.

Set default substep size = p/N , as before.

Begin SUBSTEP LOOP.

Find distances to possible interaction, and to surface crossing.

Select d = the minimum of these and the default substep.

Sample straggled energy change δE_d for actual substep size d .

Set $E = E - \delta E_d$ (adjust J if necessary).

Check for energy cutoff (adjust endpoint and terminate track).

Check for time cutoff (adjust endpoint and terminate track).

Select appropriate case:

Process inelastic interaction (make secondaries and terminate track).

Process elastic interaction (decrease E and adjust J if necessary).

Process surface crossing. Cycle CELL LOOP.

Process uneventful end of substep.

If (energy group has changed) cycle ENERGY LOOP.

End SUBSTEP LOOP.

End ENERGY LOOP.

End CELL LOOP.

These seemingly minor changes in logic can make a significant difference for situations in which the shortcomings of the previous approach were important. The principal improvement with the new logic is that the sampling of straggling is now almost always done based on the step size that is actually traversed by the particle. The only exception is the last sub-step of a track that is terminated (and adjusted after the straggling sample) by time or energy cut-off. This generally represents a negligible fraction of the total sub-steps in the problem, and is not certain to occur at all. A secondary benefit is that the treatment of the energy and time cut-offs is handled more naturally and more accurately.

In order to illustrate the considerable difference that the new logic can make, we have compared the two algorithms for the case of a mono-energetic, mono-directional beam of 157.2 MeV protons on a uniform water target. (This problem is based on a user's application whose strange results motivated us to re-examine the straggling logic [28].) The average energy deposition as a function of depth and the energy spectrum of the proton flux at a specific depth (15 cm) were calculated using the old and the new condensed-history algorithm. The problem was simulated twice. In the first case, the target was divided into slabs 1 mm thick, so that a large number of interruptions of the natural sub-step were encountered. In the second case, only the region deeper than 15 cm was divided into 1 mm slabs; the first 15 cm were divided into three 5 cm thick slabs. This allowed us to test the sensitivity of the two algorithms to differences in the geometry specification. Figure 1 shows details of the energy-deposition peak for both simulations. Results from the simulation with uniform 1 mm slabs are marked as "1 mm regions" in this figure, while those from the mixed 5 cm/1 mm simulation are marked as "5 cm regions". The old algorithm exhibits an un-physical sensitivity to the details of the geometry specification, as well as a noticeable artefact at the peak for the coarsely-resolved 5 cm case. In contrast, the new method produces a smoother profile for the peak, and shows essentially no sensitivity to the details of the representation of the geometry. Figure 2 shows the energy spectrum of the proton flux at

a depth of 15 cm in the water target, calculated with the old and new algorithms and for the same two physically equivalent representations of the geometry. With the old logic, the severe sensitivity to the geometry model and the presence of strange artefacts are even more apparent in these results. The new logic again shows a more realistic profile and a satisfactory insensitivity to the geometric representation. Although we do not show the results here, we have also compared the new calculations with LAHET results and have found good agreement. We conclude that the new transport logic for heavy charged particles is an unambiguous improvement, and we have implemented this treatment as the default model in recent versions of MCNPX and in the new developmental version of MCNP5.

Figure 1. Energy deposition as a function of depth for 157.2 MeV protons normally incident on water

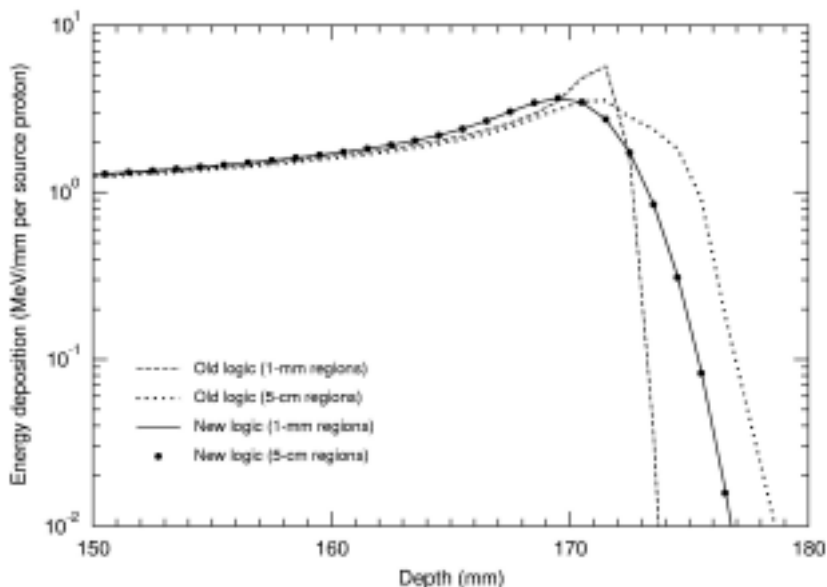
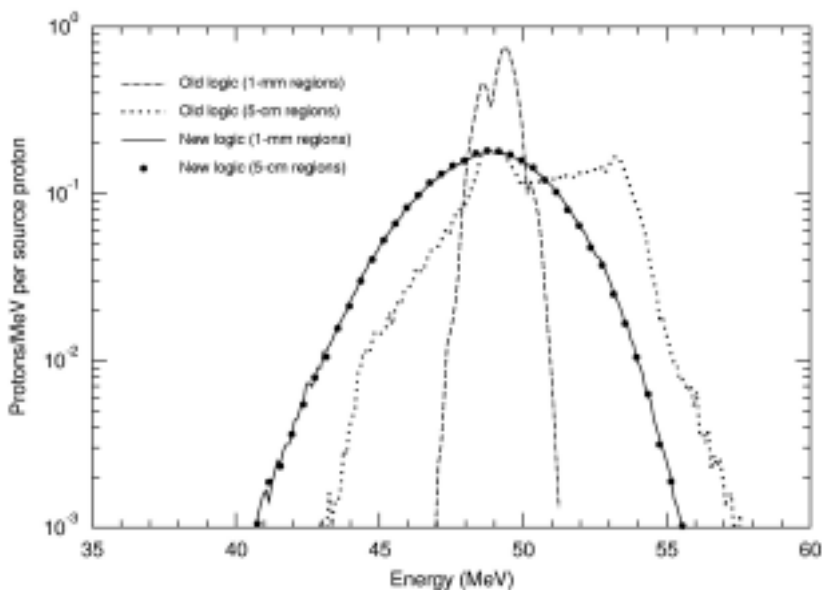


Figure 2. Proton energy spectrum at 15 cm depth for 157.2 MeV protons normally incident on water



REFERENCES

- [1] Berger, M.J. “Monte Carlo Calculation of the Penetration and Diffusion of Fast Charged Particles”, in *Methods in Computational Physics*, Vol. 1, B. Alder, S. Fernbach and M. Rotenberg (eds.), Academic Press, New York (1963), 135.
- [2] Seltzer, Stephen M., “An Overview of ETRAN Monte Carlo Methods”, in *Monte Carlo Transport of Electrons and Photons*, Theodore M. Jenkins, Walter R. Nelson and Alessandro Rindi (eds.), Plenum Press, New York (1988), 153.
- [3] Halbleib, J.A., “Structure and Operation of the ITS Code System”, in *Monte Carlo Transport of Electrons and Photons*, Theodore M. Jenkins, Walter R. Nelson and Alessandro Rindi (eds.), Plenum Press, New York (1988), 249.
- [4] Halbleib, J.A., R.P. Kensek, T.A. Mehlhorn, G.D. Valdez, S.M. Seltzer and M.J. Berger, *ITS Version 3.0: The Integrated TIGER Series of Coupled Electron/Photon Monte Carlo Transport Codes*, Sandia National Laboratories report SAND91-1634 (March 1992).
- [5] X-5 Monte Carlo Team, *MCNP – A General Monte Carlo N-particle Transport Code, Version 5, Volume I: Overview and Theory*, Los Alamos Report LA-UR-03-1987, 24 April 2003.
- [6] Hughes, H.G., M.B. Chadwick, R.K. Corzine, H.W. Egdorf, F.X. Gallmeier, R.C. Little, R.E. MacFarlane, S.G. Mashnik, E.J. Pitcher, R.E. Prael, A.J. Sierk, E.C. Snow, L.S. Waters, M.C. White and P.G. Young, “Status of the MCNPX Transport Code”, in *Advanced Monte Carlo for Radiation Physics, Particle Transport Simulation and Applications*, Proceedings of Monte Carlo 2000 Conference, Lisbon, 23-26 October 2000, Springer, ISBN 3-540-41795-8.
- [7] Landau, L., *On the Energy Loss of Fast Particles by Ionization*, *J. Phys. USSR*, 8, 201 (1944).
- [8] Vavilov, P.V., “Ionization Losses of High-energy Heavy Particles”, *Soviet Physics JETP*, Vol. 5 No. 4, 749 (1957).
- [9] Bethe, H.A., “Zur Theorie des Durchgangs schneller Korpuskularstrahlen durch Materie”, *Ann. Phys.*, 5, 325 (1930).
- [10] Bethe, H.A., “Scattering of Electrons”, *Z. Physik*, 76, 293 (1932).
- [11] Bloch, F., “Stopping Power of Atoms with Several Electrons”, *Z. Physik*, 81, 363 (1933).
- [12] Møller, C., “Zur Theorie des Durchgang schneller Elektronen durch Materie”, *Ann. Physik.*, 14, 568 (1932).
- [13] Rutherford, E., “The Scattering of α and β Particles by Matter and the Structure of the Atom”, *Philos. Mag.*, 21, 669 (1911).

- [14] Börsch-Supan, W., “On the Evaluation of the Function $\phi(\lambda) = \frac{1}{2\pi i} \int_{x-i}^{x+i\infty} e^{\mu \log \mu + \lambda \mu} d\mu$ for Real Values of λ ”, *J. Res. National Bureau of Standards*, 65B, 245 (1961).
- [15] Blunck, O. and S. Leisegang, “Zum Energieverlust schneller Elektronen in dünnen Schichten”, *Z. Physik*, 128, 500 (1950).
- [16] Blunck, O. and K. Westphal, “Zum Energieverlust energiereicher Elektronen in dünnen Schichten”, *Z. Physik*, 130, 641 (1951).
- [17] Chechin, V.A. and V.C. Ermilova, “The Ionisation-loss Distribution at Very Small Absorber Thickness”, *Nucl. Instr. Meth.*, 136, 551 (1976).
- [18] Seltzer, Stephen M., “Electron-photon Monte Carlo Calculations: The ETRAN Code”, *Appl. Radiat. Isot.*, Vol. 42, No. 10, 917 (1991).
- [19] Rossi, Bruno, *High-energy Particles*, Prentice-Hall, Incorporated, New York (1952).
- [20] Seltzer, Stephen M. and Martin J. Berger, “Energy-loss Straggling of Protons and Mesons: Tabulation of the Vavilov Distribution”, in *Studies in Penetration of Charged Particles in Matter*, Nuclear Science Series, Report Number 39, Committee on Nuclear Science. Publication 1133, National Academy of Sciences – National Research Council, Washington, D.C. (1964).
- [21] Schorr, B., “Programs for the Landau and the Vavilov Distributions and the Corresponding Random Numbers”, *Computer Phys. Comm.*, 7, 215 (1974).
- [22] Sigmund, P. and K.B. Winterbon, “Energy Loss Spectrum of Swift Charged Particles Penetrating a Layer of Material”, *Nuclear Instruments and Methods in Physics Research*, B12, 1 (1985).
- [23] Bukin, A.D. and N.A. Grozina, “Monte Carlo Simulation of Fluctuations of the Ionization Losses of Heavy Charged Particles”, *Computer Phys. Comm.*, 78, 287 (1994).
- [24] Van Ginneken, A., “Fluctuations of Muon Energy Loss and Simulation of Ionization Cooling”, *Nuclear Instruments and Methods in Physics Research*, A 362, 213 (1995).
- [25] Chibani, Omar, “New Algorithms for the Vavilov Distribution Calculation and the Corresponding Energy Loss Sampling”, *IEEE Transactions on Nuclear Science*, Vol. 45 No. 5, 2288 (1998).
- [26] Rotondi, A. and Paolo Montagna, “Fast Calculation of Vavilov Distribution”, *Nuclear Instruments and Methods in Physics Research*, B47, 215 (1990).
- [27] Schaart, Dennis R., Jan Th.M. Jansen, Johannes Zoetelief and Piet F.A. de Leege, “A Comparison of MCNP4C Electron Transport with ITS 3.0 and Experiment at Incident Energies between 100 keV and 20 MeV: Influence of Voxel Size, Substeps and Energy Indexing Algorithm”, *Phys. Med. Biol.*, 47, 1459 (2002).
- [28] Prael, R.E., *Proposed Modification to the Charged Hadron Tracking Algorithm in MCNPX*, Los Alamos National Laboratory Research Note X-5-RN(U)00-30, 23 August 2000, LA-UR-00-4027.

NEUTRON AND GAMMA-RAY DOSIMETRY OF THE TOKAI-MURA AND SAROV CRITICALITY ACCIDENTS USING A DETERMINISTIC TRANSPORT METHODOLOGY

C.R.E. de Oliveira, C.C. Pain, M.D. Eaton, A.K. Ziver, A.J.H. Goddard

Computational Physics and Geophysics Group
Department of Earth Sciences and Engineering
Imperial College of Science Technology and Medicine
Exhibition Road, London 2AZ, UK
E-mail: r.transport@imperial.ac.uk

Abstract

A deterministic transport methodology has been used to analyse two criticality accidents – JCO fuel processing in Tokai-mura, Japan and the Sarov experiment in Russia – in an effort to calculate both the neutron and gamma-ray exposure rates, and neutron-induced activities received by the personnel. The methodology, implemented in the coupled radiation-hydrodynamics code FETCH, is based on the finite element-spherical harmonics solution of the neutron and gamma-ray transport equation. The exposure rates at the workers' positions were obtained using a ray-tracing technique followed by neutron-induced activation calculations based on the code FISPACT (European Activation Code System), which is linked to the neutron spectra and fluences calculated by FETCH. Results from our calculations are presented and compared against other published work incorporating measurements and calculations using other transport methods. This enables us to highlight similarities and differences in the framework of dosimetry data and methods used.

Introduction

Encouraging consistency between worker dosimetry and doses inferred from FETCH modelling [1] in association with ICRU fluence-to-dose data [2] has been obtained for the Tokai-mura criticality accident. The purpose of the present paper is to compare and extend our previous findings to those obtained after examination of the Sarov accident [3]. Both neutron and gamma-ray dosimetry were calculated for the two criticality accidents together with neutron-induced post-accident activations. The latter was performed using the FISPACT [4] code and the neutron spectra obtained from FETCH representing various parts of the body.

The JCO criticality accident occurred in 1999 in Tokai-mura, Japan, and the Sarov incident in Russia in 1997. Both of these accidents were due to violations of safety precautions by workers. The latter incident took place in a fuel processing plant; the former at an experimental facility. These particular criticality accidents were selected because they represent critical configurations of completely different neutron spectra:

- The JCO accident, representing a situation in which criticality was achieved in a well-moderated (thermalised) system [5-7].
- The Sarov accident, representing a situation in which criticality occurs in a fast system where high-energy neutrons dominate the neutron spectrum [3].

Both accidents were modelled with the finite element transient transport theory code FETCH and calculations were carried out to determine both neutron and gamma-ray doses when accidents took place. In addition, post-accident dosimetry calculations were performed using the FISPACT code to determine activations inside the workers' bodies due to neutron-induced reactions. The calculated activations are ^{24}Na in blood and ^{32}P in urine. Gold and indium activations arising from (n,γ) reactions were also calculated. The results were compared to those measured, and were calculated using other methods.

Two particular “measures” are proposed for investigation, namely the neutron/gamma-ray ratio in any resulting radiation field (and the relevance of this to, say, dose thresholds), and the impact of such a ratio on post-accident dosimetry (in particular the sensitivity of the ^{24}Na whole-body average activation to the neutron/gamma ratio – with corresponding yields from criticality accidents). These measures have been investigated with the aid of the two criticality accidents, which can be used as benchmarks.

Fluence and dose calculation methods

The following steps outline the work performed to determine the doses to various organs as a result of criticality accidents:

- Determine neutron fluxes by solving time-dependent transport equation for the two over-critical systems representing the criticality accidents over a time interval.
- Determine gamma-ray fluxes arising from prompt gamma rays (fission gammas) and the secondary gamma rays by performing gamma-ray transport calculations using a fixed source in the system. The latter (secondary gamma rays) is due to (n,γ) reactions occurring in the system.

- Use ray-tracing technique to determine neutron and gamma ray fluxes at the pixels representing the various organs in the body.
- Convert the energy-integrated fluxes to neutron and gamma-ray doses at these points using the appropriate flux-to-dose conversion factors.

Theoretical background

The numerical methods used to model the criticality accidents are based on the EVENT [8] module of the FETCH code, which solves the coupled neutron and gamma-ray radiation transport problem using finite-element formulation. An introduction to the methodology implemented is presented in this section.

Calculation of neutron fluxes

The time-dependent Boltzmann transport equation for neutron angular flux $\phi(\mathbf{r}, \Omega, E, t)$ is determined from the following equation:

$$\frac{1}{v} \frac{\partial \phi(\mathbf{r}, \Omega, E, t)}{\partial t} + \Omega \cdot \nabla \phi(\mathbf{r}, \Omega, E, t) + \mathbf{H} \phi(\mathbf{r}, \Omega, E, t) = S(\mathbf{r}, \Omega, E, t) \quad (1)$$

where v is the particle speed, $S(\mathbf{r}, \Omega, E, t)$ a distributed source, the form of which depends on the type of problem that is being solved (constant source or eigenvalue – K_{eff}), and \mathbf{H} is the collision operator defined in terms of the total cross-section and differential cross-section by:

$$\mathbf{H} \phi(\mathbf{r}, \Omega, E, t) \equiv \sigma_t(\mathbf{r}, E, t) \phi(\mathbf{r}, \Omega, E, t) - \int_{4\pi} d\Omega' \sigma_s(\mathbf{r}; \Omega', E' \rightarrow \Omega, E, t) \phi(\mathbf{r}, \Omega', E', t) \quad (2)$$

In calculating doses at the time of the criticality event, steady-state neutron sources are used in the coupled formulation, which can be defined when K_{eff} is equal to unity and the neutron flux is time-independent as given by the following equation:

$$S(\mathbf{r}, \Omega, E, t) = \frac{\chi(E)}{4\pi K_{\text{eff}}} \int dE' \int_{4\pi} d\Omega' \psi(\mathbf{r}, \Omega', E', t) v(E') \sigma_f(\mathbf{r}, E', t) \quad (3)$$

where $S(\mathbf{r}, \Omega, E, t) = s(\mathbf{r}, \Omega, E)$, K_{eff} is equal to unity, the number of neutrons emitted per fission is given by $v(E)$ and $\chi(E)$ is the neutron fission spectrum. In the case of gamma rays the $\chi(E)$ is replaced by the empirical formula presented below.

Solution of the transport equation is achieved via a multi-group variational finite-element spherical-harmonics procedure [8]. This procedure provides a fast and geometrically flexible methodology for radiation transport and dosimetry modelling.

Calculation of gamma-ray fluxes

The BUGLE-96 [9] multi-group cross-section library has been used to model the neutron and gamma-ray interactions. The library contains 47 neutron and 20 gamma-ray energy groups for a range of nuclides, and was originally developed for LWR (mainly PWRs) and related applications.

Gamma-ray fluxes are calculated using the same formulation presented above but replacing neutron interactions with those of gamma rays. The sources used are due to prompt gamma rays and secondary gamma rays. The former are those which are emitted simultaneously during the fission process and have been extensively studied for uranium systems. For the purposes of this study, an empirical formula for the spectrum of the prompt gamma rays has been taken from [10]. The midpoint of the energy bounds for the gamma-ray cross-sections (taken from the BUGLE-96 library) was used to calculate the prompt gamma spectrum. The energy-dependent empirical formula is given by:

6.6 gammas/fission-MeV	0.1 < E < 0.6 MeV
2.0exp(-1.78E)	0.6 < E < 1.5 MeV
7.2exp(-1.09E)	1.5 < E < 10.5 MeV

Contributions from secondary gamma rays are included by introducing an additional source term to take into account sources arising from (n,γ) reactions. With this source term, gamma-ray transport equations for each energy group form a coupled system of equations, which are solved using the FETCH code to determine fluxes at each finite element mesh point.

Dose calculations using the ray-tracing method

The neutron and gamma-ray fluences (time-integrated fluxes) were calculated from an eigenvalue calculation representing an over-critical system, followed by a fixed-source gamma-ray calculation. In the fixed-source calculation, contributions from the secondary gamma rays are included, which provide the framework for the coupled neutron/gamma-ray calculations. A \$2 excess reactivity is used to model the criticality accidents.

To calculate doses around the models (at workers positions), a ray-tracing method [11] was used. It is applied from the dose points to the surface of the models by making appropriate changes to fluxes along the rays. In the figures, we show the position of dose points, which represent the position of various organs in relation to models. The points were placed using the information regarding the height of workers, and from sketches showing their positions at the time of accidents [12-13]. The six points shown are hands, head, upper body, lower body, upper legs and lower legs.

The scalar flux values throughout the finite-element mesh were calculated; the ray-tracing technique was then applied in the void surrounding the assemblies to determine the mean group flux values at each of the dose points. The flux values were divided by the total fission rate at each position. This provided calibration of the results to match the fission rate $F(t)$ of the accident. Thus scalar fluxes at position \mathbf{r} and at a given time t into the transient are given by:

$$\phi(\mathbf{r}, t) = F(t) \frac{\phi'(\mathbf{r})}{F'(t)} \quad (4)$$

where:

$$F' = \int_E dE \int_V dV \sigma_f \phi'(\mathbf{r}) = \int_V dV \sum_{g=1}^G \sigma_{fg}(\mathbf{r}) \phi_g(\mathbf{r}) \quad (5)$$

In this way, the time variation of neutron fluxes at each dose position during the incident can be calculated. The flux values are finally integrated over time to calculate the fluence (total number of neutrons or gamma rays per unit area) at each during the complete transient. The fluence at the start of accident up to time T is thus calculated from:

$$\phi(\mathbf{r}) = \int_0^T \phi(\mathbf{r}, t) dt \quad (6)$$

This method of calibrating the time-dependent fluxes is widely used as described in Hetrick [14].

Conversion factors C_F were then used to calculate the physical dose D in grays (= J/kg) to various organs in the region of the pixels from the fluence at these points, using:

$$D = \int_E C_F \phi dE$$

The above equation is used to calculate doses for gammas and neutrons using the appropriate flux-to-dose conversion factors as shown in Figure 8, which are based on ICRU 57 [2].

Results

In this section we present the important results obtained from performing transient criticality calculations to show the neutron and gamma-ray doses determined, which are followed by the activation calculations obtained for neutron-induced reactions. First, we present the calculated spectra at two locations (hands and lower torso) to show the physics differences in the models, which significantly affect doses and activations.

It is important to point out that dose predictions were made using a burst of 4.0×10^{16} fissions for Tokai-mura and 2.0×10^{16} fissions for Sarov, which lasted 2 seconds.

The neutron and gamma-ray spectra

The spectra at the two pixel positions are presented in Figures 3 and 4 for neutrons and gamma rays, respectively, for the two accidents. The neutron spectra for the Tokai-mura accident are thermalised (a “soft spectrum”) in contrast to the Sarov, which is dominated by fast neutrons (a “hard spectrum”). This property of the neutron spectra is very important, as it significantly affects the doses and activations arising from the two accidents.

The gamma-ray spectra presented in Figure 4 show some differences between the two incidents. Tokai-mura gives more high-energy photons compared to Sarov.

In the Tokai-mura incident neutrons are moderated due to the presence of the water in the jacket of the tank and in the uranyl nitrate solution itself. It can be seen from Figure 2 that neutrons seen in the lower torso are of lower energies than those seen in the hands. This is due to the presence of the water jacket. This neutron spectrum is similar to that listed in [12,13], which was calculated on the tank’s perimeter. The spectrum for gamma rays is also similar to our results shown in Figure 4.

It can be clearly seen (Figure 3) that the neutrons are highly energetic in the Sarov incident, which shows a typical “hard” neutron spectrum generated in metal uranium systems.

Neutron and gamma-ray dose predictions

The dose predictions were performed for the six pixels; namely, hands, head, upper body, lower body, upper legs and lower legs. Tables 1 and 2 give neutron and gamma-ray doses, in grays calculated at various positions representing the organs in the body. Table 1 gives results for Tokai-mura and Table 2 for Sarov. In the case of Tokai-mura neutron doses are an order of magnitude smaller than those calculated for Sarov. This is due to spectral differences presented previously. In Tokai-mura less biological damage can be observed because of the thermal-dominated spectrum. The Sarov incident has caused more biological damage, as the neutron spectrum is dominated by fast neutrons. The fact that hands are nearer to the uranium sphere for the Sarov accident explains why the neutron fluence is larger for all but the lower-energy groups compared to the lower torso.

The presence of the water in the tank and the water jacket of the Tokai-mura incident results in the release of gamma-rays from neutron capture, increasing the ratio of gamma-to-neutron doses. The doses listed in Tables 1 and 2 are those for incident neutrons and gamma rays. Neutrons incident in the body will result in the production inside the body of secondary gamma rays from neutron capture. Thus a large percentage of doses for incident neutrons are actually from the gamma rays produced in the body. The larger the part of the body the greater the production of gamma rays, as each neutron is more likely to be scattered and have its energy reduced so that it reaches thermal energies from which it is more likely to be captured and produce secondary gamma rays.

For the Tokai-mura incident the overall worker “A” dose in terms of Gy Eq (Gray equivalent in gamma-rays) was estimated as being 16 and 20 Gy Eq. The dose in grays can be converted to Gy Eq by multiplying the relative biological effectiveness (RBE) factor, which has been estimated to be a factor of 1.7. The RBE depends on the tissue, the neutron spectrum and is therefore case-dependent. The overall dose estimate of 16-20 Gy Eq is consistent with the neutron doses presented in Table 2.

Estimation of doses requires a convolution of the conversion coefficients for each tissue type representing the biological target with the energy-dependence fluence. The conversion coefficients were obtained by interpolating in energy the factors listed in RBF57 [2]. Figures 5 and 6 present skin doses for neutrons and gamma rays respectively for both incidents, which are shown at various positions relative to the centre position of the workers. The neutron and gamma-ray dose profiles for the Sarov incident are expected to peak nearest the uranium sphere at the upper torso and decay (decrease) roughly with the square of the distance from the sphere centre (as the fissile region is relatively small). However, doses from Tokai-mura incident show they are highest in the head region, as this position is not shielded from the high-energy neutrons by the water jacket.

In Figure 7, fluence-to-dose conversion factors used to calculate doses are presented for neutrons and gamma rays, which are taken from ICRU 57 [2].

We have generated flux contours from FETCH calculations and presented them in Figures 8 and 9 for neutrons and gamma rays respectively. Figure 8 shows relative group fluxes for the fast, intermediate and thermal energy groups, corresponding to Group 1, (17.3-14.2 MeV), Group 24 (368.8-297.2 keV) and Group 47 (0.1-0.00001 eV).

Figure 9 shows the gamma-ray contours for Group 1 (16-14 MeV), Group 10 (1.5-1.0 MeV) and Group 20 (20.0-10.0 keV). All were normalised to total fission rate of $4.0E+16$.

Activation calculations

Neutron-induced activations are accurate methods of determining doses to organs, which can only be carried after the accident, once irradiation has taken place. In order to calculate activations arising in a body, sophisticated computer codes should be used. One such code is FISPACT [4], which is available from the UKAEA Culham as part of their fusion research programme. FISPACT can be used to determine activities in materials (in this case various organs in the body) that are subject to neutron irradiation over a period of time. The decay of radioactive isotopes over a “decay time” can be calculated following this irradiation period. The decay data is based on the ENDF/B-V and VI internationally accepted nuclear data libraries and are included in FISPACT to allow activity calculations over specified activation and decay periods. The code uses a software called EASY (European Activation System), which incorporates all the data libraries to be used in a user-friendly format. The code has access to a number of up-to-date cross-section libraries (WIMS, VITAMIN-J, GAM-II, XMAS and TRIPOLI), which cover a wide range of application areas ranging from fission to fusion reactors.

FISPACT calculations were performed to calculate neutron-induced activities such as the ^{24}Na activity in blood and the ^{32}P activity in urine. These activities are being used to estimate the neutron exposure levels to which the workers were subject during the accident [16]. Table 3 gives Bq/Gy for $^{23}\text{Na}(n,\gamma)^{24}\text{Na}$ reaction. The mass of tissue which was assumed to be irradiated was 1 kg in Table 3.

^{32}P is generated by the thermal neutron activation of ^{31}P in the $^{31}\text{P}(n,\gamma)^{32}\text{P}$ reaction and also by fast neutron activation of ^{32}S in the $^{32}\text{S}(n,p)^{32}\text{P}$ reaction in urine. An attempt has been made to calculate ^{32}P by irradiating P only using FISPACT. Results from these calculations together with $^{197}\text{Au}(n,\gamma)^{198}\text{Au}$ and $^{115}\text{In}(n,\gamma)^{116}\text{In}$ reaction rates are represented in Table 4. The half-life of ^{32}P , ^{198}Au and ^{116}In are 14.3 days, 2.7 days and 14.2 seconds respectively. It should be noted that ^{116}In has the shortest half life of all the thermal neutron-induced reactions considered.

Comparisons against measurements and uncertainties

In this section, an attempt is made to identify major uncertainties associated in our calculations with the prediction of exposure rates. It is not intended to assess the full set of uncertainties in calculations or measurements; therefore we compare our results against those available in published works.

The dominating uncertainties are due to the exact positions of the workers (bodies) with respect to the critical assemblies and the total fissions (the initial burst) that occurred during accidents (or source terms). It is important to point out that there are uncertainties in the measured values which will not be discussed here as they are beyond the scope of this report. The calculated exposure rates predicted are very sensitive to these two effects. This is seen in the case of the Sarov accident, for which the hand neutron dose rates are well below the measured value (calculated 40 GyEq and measured 1 700 GyEq), indicating that the positioning of hands should be closer to the experiment than what has been modelled. The average neutron dose to the upper part of the body for Sarov was calculated as 30 GyEq, which compares well with the measured value of 40 GyWEq. The gamma-ray dose, however, does not compare in that accuracy, 2.5 GyEq was measured and 0.45 GyEq was calculated. This discrepancy may arise from gamma-ray source term uncertainties (total source strength and spectrum). It should be noted that we have modelled the prompt gamma-ray spectrum and not included the fission product gamma rays.

For the Tokai-mura accident the measured dose for the worker “A” is 5.7 GyEq for neutrons and 8.9 GyEq for gamma rays. FETCH predictions are in the range of 1-9 GyEq depending on the part of the body for neutrons and 1-2 GyEq for gamma rays. Again, a large discrepancy in the gamma-ray doses are observed as was seen in the Sarov case.

Conclusions

In this paper, we have developed and applied a deterministic method, embraced in the transient criticality finite element code FETCH, to recent criticality incidents, namely Tokai-mura in Japan and Sarov in Russia. The interested reader can refer to Ref. [17] to obtain information about other criticality accidents that have occurred up to the present date.

To estimate exposures to workers arising from neutrons and gamma rays we have developed a numerical technique based on a “ray-tracing method”. By applying this method, we were able to estimate doses to various organs of the workers, which are presented in this report. It has been found that due to contrast of the spectral characteristics of neutrons in the two accidents the ratio of neutron to gamma-ray doses differs significantly, and hence the amount of biological damage that the workers have experienced.

In order to estimate activation levels inside the body as a result of neutron and gamma-ray irradiation, we obtained and mounted the FISPACT code and performed a number of activation calculations to determine ^{24}Na levels in blood and ^{32}P in urine.

Initial results from these calculations are presented.

As a result of this study we have demonstrated that the FETCH methodology could provide an independent method to assess doses and activations received by workers in cases such as criticality accidents.

Acknowledgements

We would like to thank Alan Edwards and David Lloyd of the National Radiological Protection Board, Chilton, UK, for providing invaluable advice during this work and the HSE for funding this work.

REFERENCES

- [1] Pain, C.C., C.R.E. de Oliveira, A.J.H. Goddard, M.D. Eaton, S. Gundry and A.P. Umpleby, "Transient Analysis and Dosimetry of the Tokai-mura Criticality Incident", accepted for publication in *Nuclear Science and Engineering* (2003).
- [2] Snyder, W.S., M.J. Cook, E.S. Nasset, L.R. Karhausen, G.P. Howells and I.H. Tipton, *Report of the Task Group on Reference Manual*, ICRU Report 57, Pergamon Press (1998).
- [3] International Atomic Energy Agency, *The Criticality Accident in SAROV*, IAEA, Vienna, Feb. (2001).
- [4] Forrest, R.A., *FISPACT-2001: User Manual*, UKAEA FUS 450 (2001).
- [5] Sumita, K., *Overview of Tokai-mura Accident*, International Symposium on the Criticality Accident in Tokai-mura – Medical Aspects of Radiation Emergency, Chiba, Japan (2000).
- [6] Saito, S., *Outline of the Criticality Accident in the JCO Fuel Conversion Test Facility*, International Symposium on the Criticality Accident in Tokai-mura – Medical Aspects of Radiation Emergency, Chiba, Japan (2000).
- [7] Konchalovsky, M.V. A.E. Baranov, A.V. Kolganov, A.V. Barabanova and S.V. Filin, *Sarov Criticality Accident in 1997*, International Symposium on The Criticality Accident in Tokai-mura – Medical Aspects of Radiation Emergency, Chiba, Japan (2000).
- [8] de Oliveira, C.R.E., "An Arbitrary Geometry Finite Element Method for Multi-group Neutron Transport Equation", *Prog. Nucl. Energy*, 18, 227 (1986).
- [9] White, J.E., D.T. Ingersoll, C.O. Slater and R.W. Roussin, "BUGLE-96: A Revised Multi-group Cross-section Library for LWR Applications Based on ENDF/B-VI Release 3", RISC Data Library Collection, Oak Ridge National Laboratory (1996).
- [10] Profio, A.E., *Radiation Shielding and Dosimetry*, John Wiley (1978).
- [11] de Oliveira, C.R.E., M.D. Eaton, A.P. Umpleby and C.C. Pain, "Finite-element Spherical Harmonics Solutions of the 3-D Kobayashi Benchmarks with Ray-tracing Void Treatment", *Prog. Nucl. Energy*, 39, 243 (2001).
- [12] Momose, T., N. Tsujimura, T. Takasaki, K. Kanai, O. Kurihara, N. Hayashi and K. Shinohara, "Dose Evaluation Based on ^{24}Na Activity in the Human Body at the JCO Criticality Accident in Tokai-mura", *J. Radiat. Res.*, 42, S95-S105 (2001).

- [13] Muramatsu, Y., Y. Noda, H. Yonehara, N. Ishigure, S. Yoshida, M. Yukawa, K. Tagami, T. Ban-nai, S. Uchida, T. Hiram, M. Akashi and Y. Nakamura, “Determination of Radionuclides Produced by Neutrons in Heavily Exposed Workers of the JCO Criticality Accident in Tokai-mura for Estimating an Individual’s Neutron Fluence”, *J. Radiat. Res.*, 42, S117-S128 (2001).
- [14] Hetrick, D.L., *Dynamics of Nuclear Reactors*, La Grange Park, Illinois USA, American Nuclear Society (1993).
- [15] Ishigure, N., A. Endo, Y. Yamaguchi and K. Kawachi, *Dose Reconstruction for Heavily Exposed Patients of the Criticality Accident in Tokai-mura*, International Symposium on the Criticality Accident in Tokai-mura – Medical Aspects of Radiation Emergency, Chiba, Japan (2000).
- [16] Nishimura, Y., H. Takada, K. Miyamoto, Y. Watanabe, F. Kouno, N. Kurada, H.S. Kim and M. Yikawa, “Determination of ^{32}P in Urine for Early Estimation of the Neutron Exposure Level for Three Victims of the JCO Criticality Incident”, *J. Radiol. Prot.*, 22, 25-29 (2002).
- [17] McLaughlin, T.P., S.P. Monahan, N.L. Pruvost, V.V. Frlov, B.G. Ryazanov and V.I. Sviridov, *A Review of Criticality Accidents*, LA-13638 (2000).

Table 1. Neutron and gamma-ray calculated doses (Eq) using FETCH for the Tokai-mura criticality accident giving doses to various organs

Pixel	Organ represented	Neutron dose (Gy)	Gamma dose (Gy)	Dose ratio
Hands	Skin	7.49	2.11	3.5
Head	Skin	9.07	2.52	4.0
Upper body	Skin	5.91	1.70	3.5
Upper body	Lungs	4.91	1.78	2.7
Lower body	Stomach	6.47	2.02	3.2
Lower body	Colon	4.51	1.84	2.7
Lower body	Liver	5.28	1.83	2.9
Lower body	Skin	5.23	1.69	3.1
Upper legs	Skin	3.09	0.95	3.2
Lower legs	skin	0.73	0.24	3.2

Table 2. Neutron and gamma-ray doses (Eq) for the Sarov criticality accident giving doses to various organs

Pixel	Organ represented	Neutron dose (Gy)	Gamma dose (Gy)	Dose ratio
Hands	Skin	40.2	0.6	67
Head	Skin	16.7	0.3	56
Upper body	Skin	30.9	0.5	62
Upper body	Lungs	23.4	0.5	47
Lower body	Stomach	22.4	0.4	56
Lower body	Colon	14.5	0.3	48
Lower body	Liver	18.0	0.3	60
Lower body	Skin	21.6	0.3	72
Upper legs	Skin	14.7	0.2	74
Lower legs	Skin	3.6	0.1	36

Table 3. Ration of induced activity of ^{24}Na to lung dose (grays in tissue). The activity in Bq is the number of ^{24}Na disintegrations per second just after the workers irradiated.

Activity	(Bq/Gy)	SAROV	JCO
^{24}Na in blood	Neutron + gamma rays	8.2E+5	1.6E+7
^{24}Na in blood	Neutron	1.7E+5	1.6E+7

Table 4. A comparison of measured (from Refs. [16,17]) and calculated (present work using the FETCH/FISPACT route) ^{24}Na activities in blood and ^{32}P activity in urine for the Tokai-mura incident. Note that calculated ^{32}P activity is from $^{31}\text{P}(n,\gamma)^{32}\text{P}$ reaction at the time of the incident.

Case study	Measurements [Bq ^{24}Na /g ^{23}Na]	Calculations [Bq ^{24}Na /g ^{23}Na]	Measurements ^{32}P in urine (Bq/ml)	Calculations ^{32}P in urine (Bq/ml)
Worker A	8.24E+04	1.62E+04	20.2	4.2
Worker B	4.34E+04	–	12.2	–
Worker C	1.23E+04	–	3.3	–

Table 5. Thermal neutron-induced activities calculated using FISPACT immediately after the accidents

Neutron-induced reactions	Sarov (Bq/kg)	JCO (Bq/kg)
$^{31}\text{P}(n,\gamma)^{32}\text{P}$	1.1E+05	1.2E+06
$^{197}\text{Al}(n,\gamma)^{198}\text{Au}$	9.0E+06	3.3E+09
$^{115}\text{In}(n,\gamma)^{116}\text{In}$	1.3E+10	8.7E+12

Figure 1. Schematic of the Sarov (FKBN-2M) experimental assembly and corresponding RZ geometry finite element (FETCH) model shown on the right

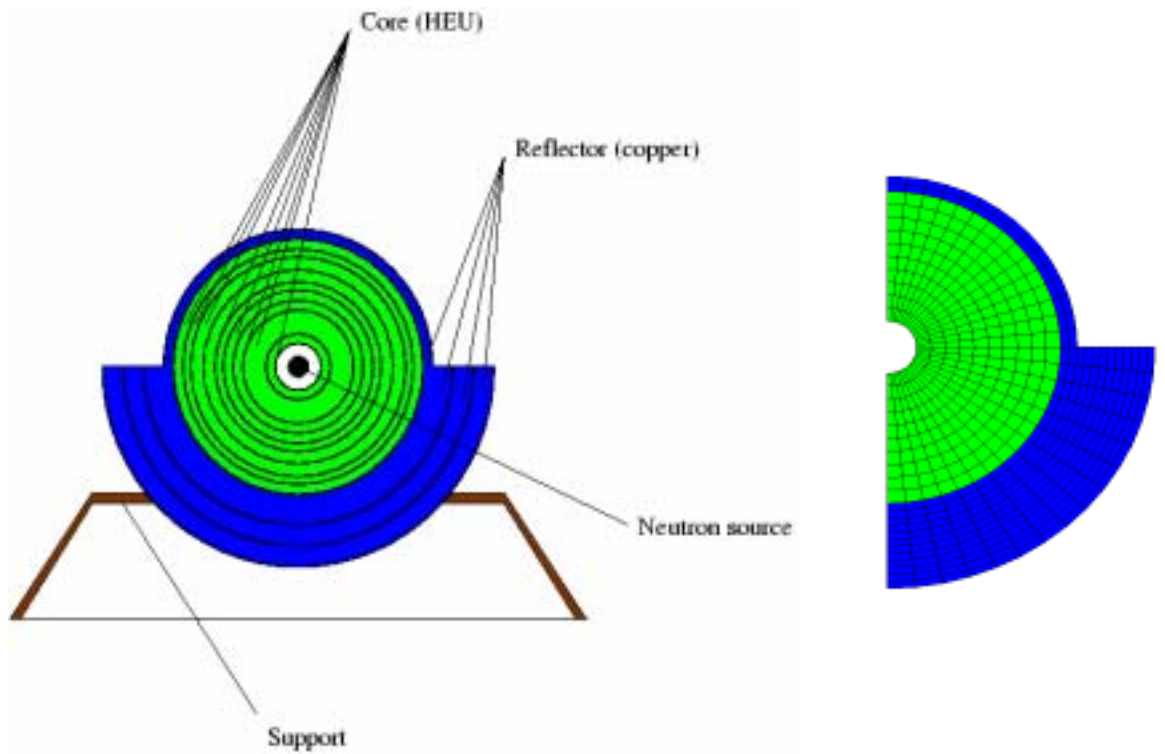


Figure 2. Schematic of the JCO precipitation vessel and corresponding RZ geometry model. The central axis of the tank is on the left.

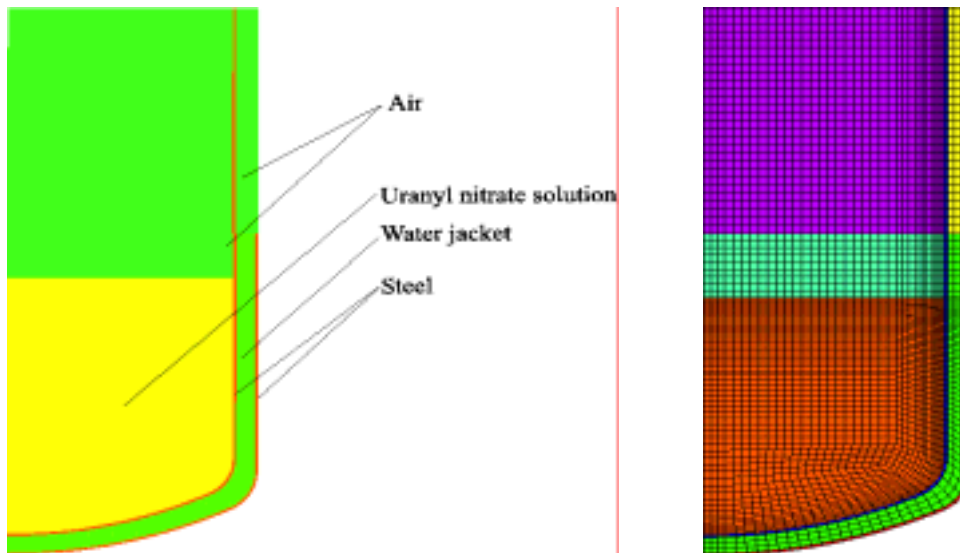


Figure 3. The neutron spectra for the Tokai-mura (left) and Sarov (right) at the “hands” and “lower torso”

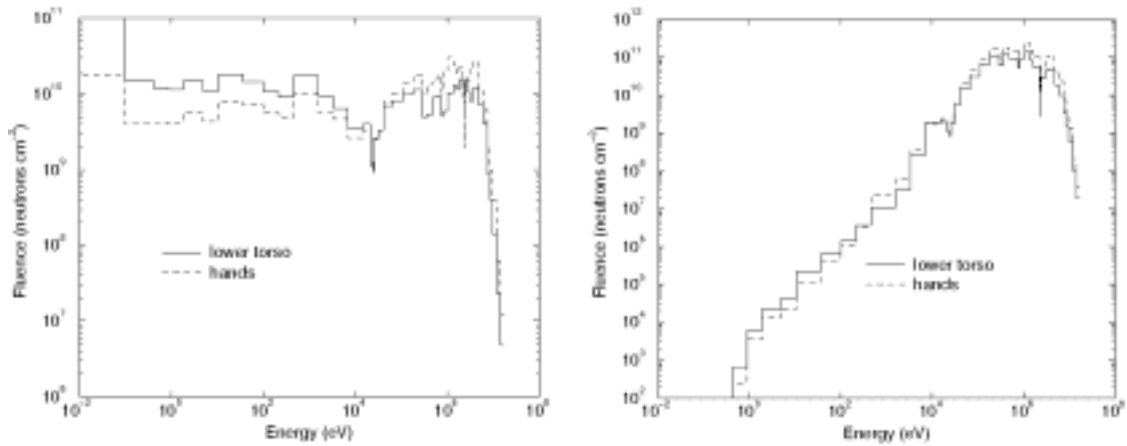


Figure 4. The gamma-ray spectra for the Tokai-mura (left) and Sarov (right) at the “hands” and “lower torso”

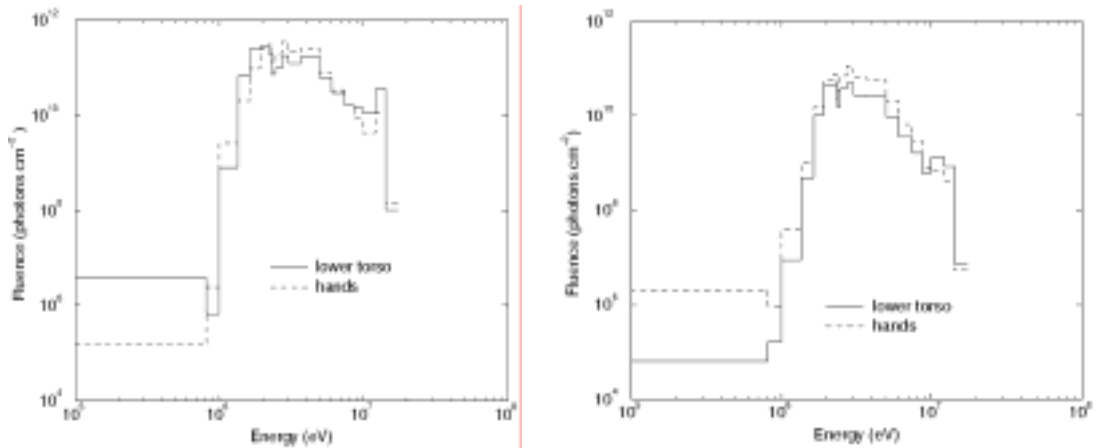


Figure 5. A comparison of the neutron skin doses for the criticality incidents using $4.0E+16$ fissions for Tokai-mura and $2.0E+16$ fissions for Sarov for the initial burst

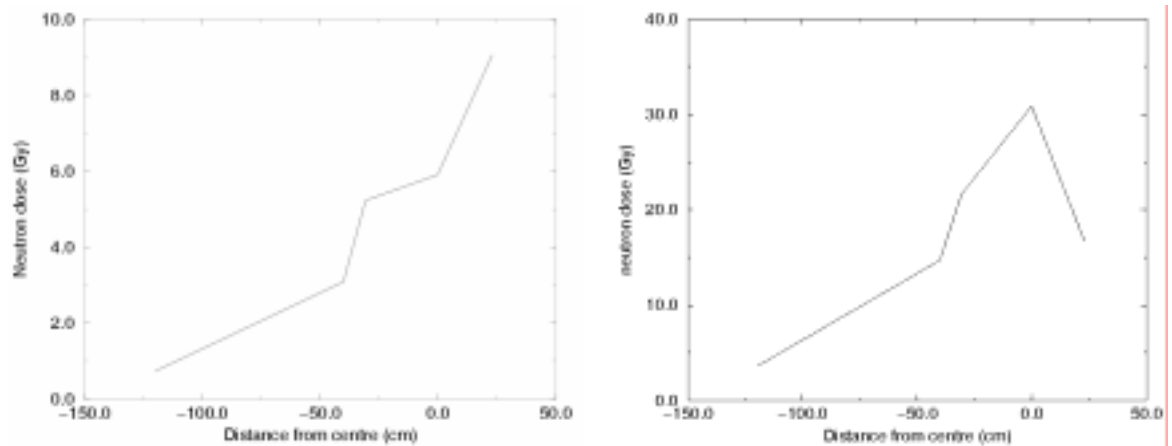


Figure 6. A comparison of the gamma skin doses for the criticality incidents using $4.0E+16$ fissions for Tokai-mura and $2.0E+16$ fissions for Sarov for the initial burst

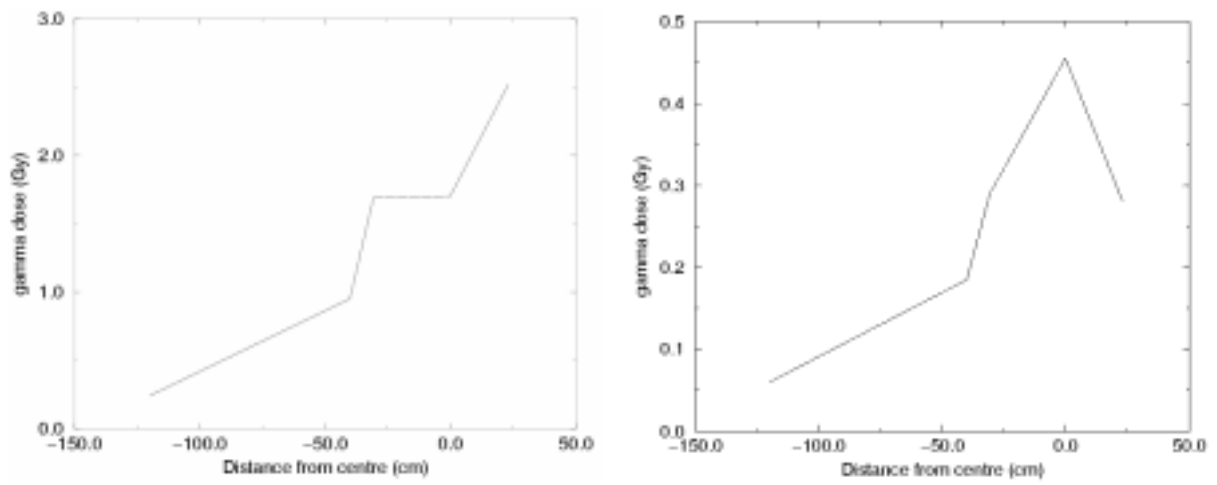


Figure 7. Conversion factors for skin obtained from ICRU 57 used in the calculations for neutrons and gamma-rays

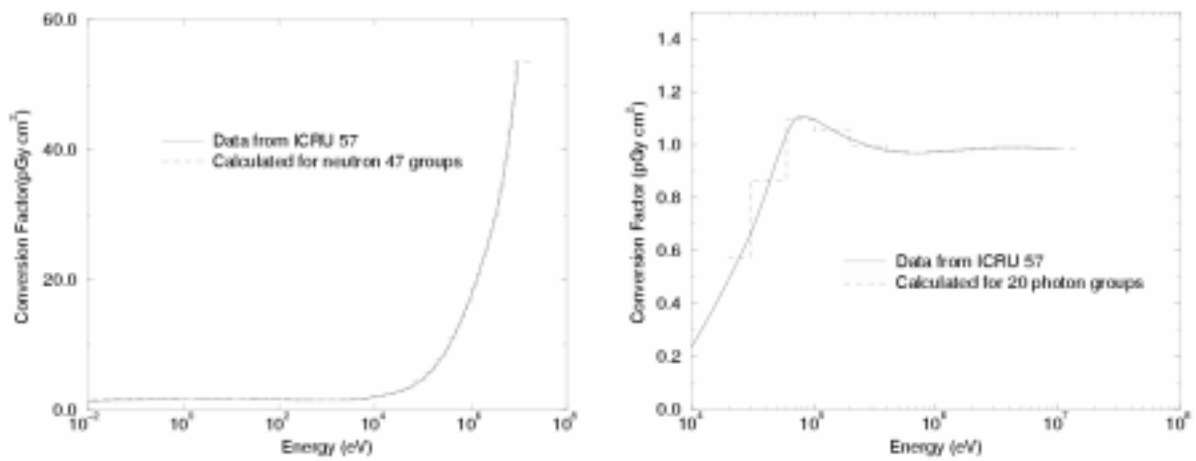


Figure 8. Neutron flux contours normalised to total source strength (Groups 1, 24 and 47)

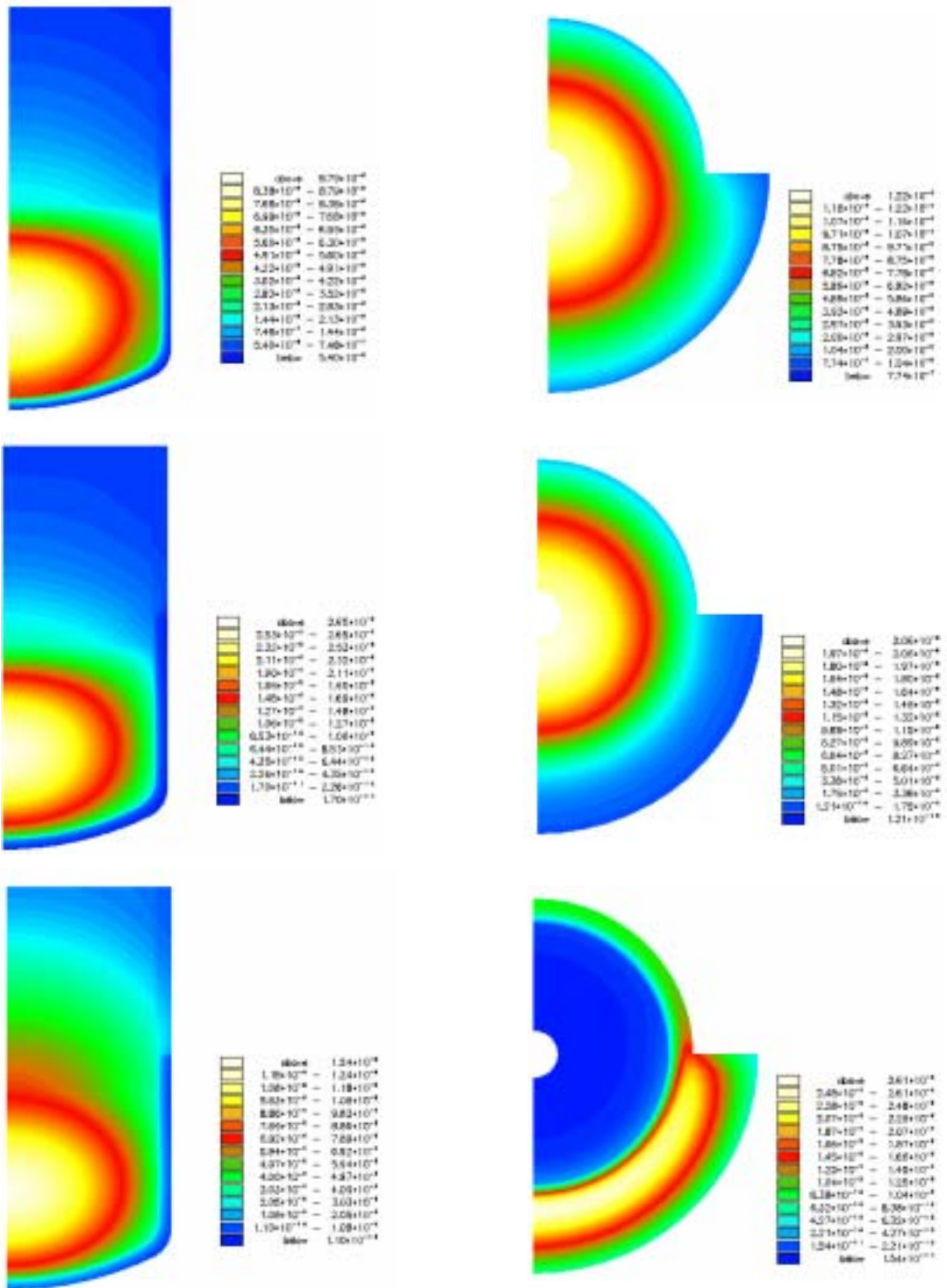


Figure 9. Gamma-ray flux contours normalised to total source strength (Groups 1, 10, 20)

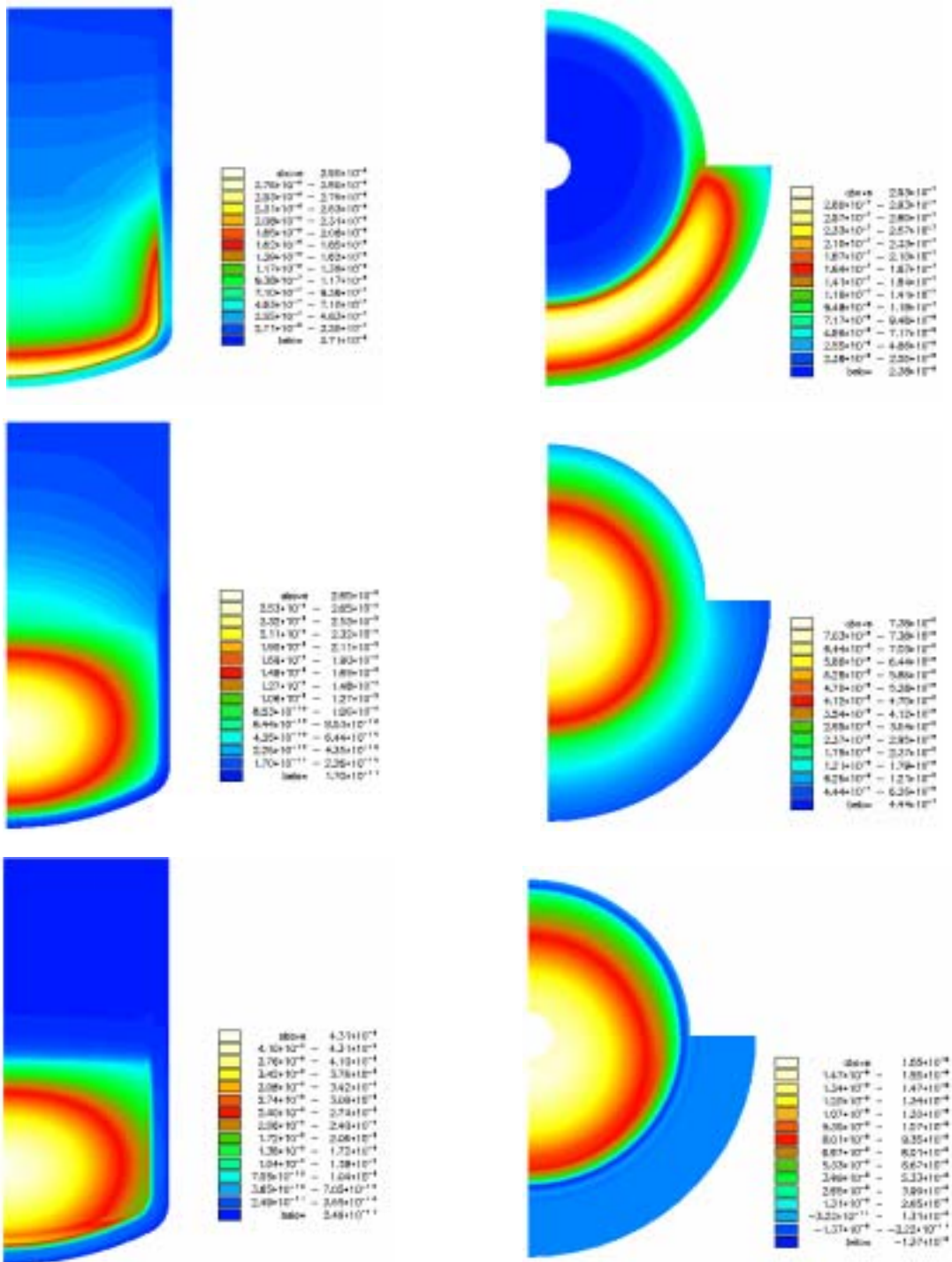
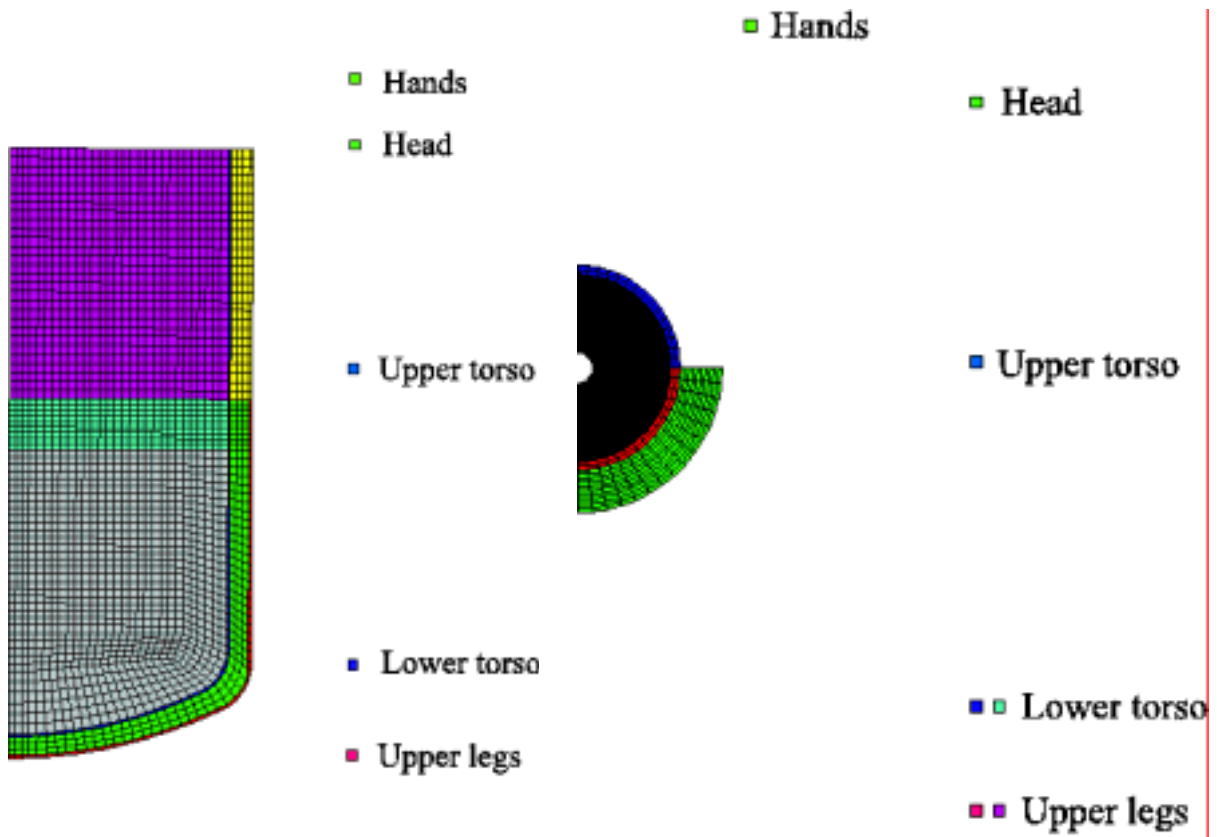


Figure 10. Dose points relative to the geometrical models of the Tokai-mura (left) and Sarov (right) assemblies



USING MCNPX FOR SPACE APPLICATIONS

G.W. McKinney, J.S. Hendricks, L.S. Waters
LANL, Nuclear Systems Design and Analysis Group
P.O. Box 1663 MS K575
Los Alamos, NM 87545 USA

T.H. Prettyman
LANL, Space and Atmospheric Sciences Group
P.O. Box 1663 MS D466
Los Alamos, NM 87545 USA

Abstract

The Los Alamos National Laboratory Monte Carlo N-Particle, eXtended-energy radiation transport code MCNPX [1] is rapidly becoming an international standard for a wide spectrum of high-energy radiation transport applications. One such application includes the study of gamma rays produced by cosmic-ray interactions within a planetary surface. Such studies can be used to determine surface elemental composition. This paper presents various MCNPX enhancements that make these gamma ray spectroscopy (GRS) simulations possible, gives elemental spectra results for a specific lunar material, provides a comparison between various high-energy physics models and shows results of an elemental least squares analysis using Lunar Prospector measurements.

Background

Gamma rays are produced in planetary surfaces by cosmic-ray interactions and by the decay of radioisotopes. For planetary bodies with thin atmospheres, such as the Earth's moon, the gamma-ray spectrum measured from orbit contains information on the abundance of major elements, including O, Si, Ti, Al, Fe, Mg and Ca, and radioactive elements, including Th, U and K. The Lunar Prospector mission acquired gamma-ray and neutron spectra at two altitudes (30 and 100 km) over the entire moon. We have binned these spectra on equal area squares to produce data sets from which maps of elemental abundance can be determined.

Lunar gamma-ray pulse-height spectra can be decomposed into components corresponding to gamma rays produced by radioactive decay, non-elastic reactions with energetic particles and thermal neutron capture. The shape of the spectral components can be assumed to be independent of composition. Their magnitude varies in proportion to the weight fraction of the element or radionuclide. For gamma rays produced by nuclear reactions, the magnitude of spectral components also varies in proportion to the number density of particles that induce reactions. The number density of thermal neutrons can be determined from thermal and epithermal neutron count rates measured by Lunar Prospector [2]. We assume that the number density of energetic particles (fast neutrons and energetic protons) is proportional to the effective atomic mass $\langle A \rangle$ of the surface material, which can be determined from fast neutron measurements. Maps of $\langle A \rangle$ have been developed by Gasnault [3].

The elemental components of the gamma-ray spectrum can be determined by simulating the galactic cosmic-ray shower, the transport of gamma rays produced by the shower through the surface to the spacecraft and their detection by the gamma-ray spectrometer. Simulations of the cosmic-ray shower were carried out using the general-purpose Monte Carlo radiation transport code MCNPX, which has been adapted with special tally features for planetary science applications. MCNPX extends the transport code MCNP [4] to include tracking of all particles at nearly all energies. As discussed below (see sub-section entitled *GRS analysis*), the elemental spectra calculated by MCNPX are fed into a detector transport code to generate elemental responses.

The Lunar Prospector gamma-ray spectrometer consisted of a BGO scintillation detector with a plastic-scintillator anti-coincidence shield. The pulse-height resolution of the spectrometer was ~13% full-width-at-half-maximum at 662 keV. At this resolution, most spectral features included contributions from multiple elements. Maps of Th have been made using the well-resolved 2.61 MeV gamma ray [5]. Maps of Fe have been made by analysing net count rates in the region above 7.5 MeV [2]. Contributions from Al to this region were ignored, which may influence the accuracy of Fe abundance in regions with low Fe. Maps of Fe and Ti have been made by deconvolution of the spectrum above 5.5 MeV [6]. We have extended the deconvolution method to 700 keV, using an elemental least-squares technique to determine the abundance of all major- and radioactive-elements [7].

Approach

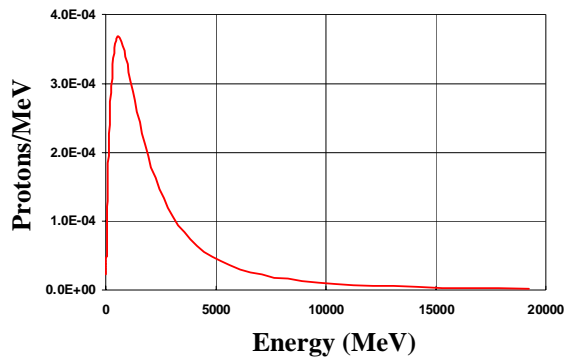
MCNPX offers a variety of capabilities to aid a scientist in performing analyses of particle transport applications. Examples include mesh tallies for viewing source and secondary particle production, multiple physics packages for validation comparisons, and code hooks to facilitate user-supplied enhancements.

Details of the MCNPX input used in this lunar GRS analysis, including source, geometry, physics and tally options, are provided in the following four sub-sections. In the last sub-section, details of the GRS elemental least-squares analysis are provided.

Cosmic-ray source

The cosmic-ray source was modelled as an energy-dependent proton source. While a more realistic cosmic-ray source includes a somewhat significant fraction of alpha particles (~4%) and a less significant fraction of heavy ions, normalisation on a per nucleon (i.e. proton) basis provides an adequate representation (and most high-energy codes do not provide heavy ion transport). Figure 1 shows the isotropic proton spectrum used as a source in MCNPX. This distribution has an average energy of about 1 GeV with a peak value at about .5 GeV.

Figure 1. Proton spectrum used in MCNPX



Lunar material

Lunar material varies significantly over the surface of the moon. For example, Th is concentrated on the near side of the Moon in and around Procellarum basin. The presence of radioactive materials may have played a significant role in the formation of the basaltic plains (or mare) that are visible from Earth. The lunar composition used in this analysis is the average composition of soil samples collected by Apollo 11 (see Table 1), which landed in south-western Tranquillitatis and sampled Ti-rich lunar maria [8]. For simplicity, the moon was modelled in MCNPX as an infinite slab. The density of the soil was arbitrarily selected to be 1 g/cm³.

Physics options

The following paragraphs provide an overview of the physics options exercised in MCNPX to perform the planetary GRS analysis. Physics details implemented within MCNPX for the various particles and energy regimes can be found in the MCNPX manual [1] and its associated references.

A high-energy source (> 1 GeV protons) producing a low-energy secondary particle tally (0-10 MeV gammas) requires the use of very accurate physics models and data. To this end, nine particle types were included on the MCNPX MODE card: protons, neutrons, photons, neutral pions, charged pions, deuterons, tritons, ³He and alphas. Neutral pions are important because they contribute to the gamma background. Charged pions can cause nuclear interactions similar to protons and neutrons, and the light ion transport can generate a significant bremsstrahlung background.

MCNPX provides one model for very high energies (FLUKA [9]), three models for intermediate energies (Bertini [10], ISABEL [11], CEM [12]), and tables or libraries for low-energy transport. Particles above 5 GeV are handled by the FLUKA interaction physics. Below this, one of the

Table 1. Lunar material ($\rho = 1.0$ g/cc)

Element	Isotope	Wt. fraction
Oxygen	8016	0.42520
Magnesium	Elemental	0.04782
Aluminium	13027	0.06658
Silicon	Elemental	0.19630
Calcium	Elemental	0.08391
Titanium	Elemental	0.04759
Iron	26054	0.00772
	26056	0.11676
	26057	0.00265
	26058	0.00034
Gadolinium	64154	9.863E-07
	64155	6.653E-06
	64156	9.143E-06
	64157	6.945E-06
	64158	1.095E-05
	64160	9.519E-06

intranuclear cascade (INC) models is invoked. Differences between the INC models include the nucleon density profile, nucleon cross-sections and energy cut-offs between stages. Default values were taken for these high-energy physics options, unless stated otherwise. For neutrons below 20 MeV, library transport was used.

Due to the fact that some of the nuclei of interest (Mg, Ti, Gd) are not included in the 150 MeV MCNPX libraries (LA150 [13]), this analysis was performed with the 20 MeV ENDF/B-VI neutron library (ENDF60 [14]). Use of the ENDF60 library means that below 20 MeV no protons or light ions were generated from neutron interactions. This also means that above 20 MeV models were used to sample the interactions. For the same reason, the LA150 proton library was not used. In this case, the physics models are used to sample the interactions and, although low-energy protons will produce light ions within these models, use of the models below 100 MeV is questionable. Photon cross-sections were taken from the MCPLIB02 library for all energies.

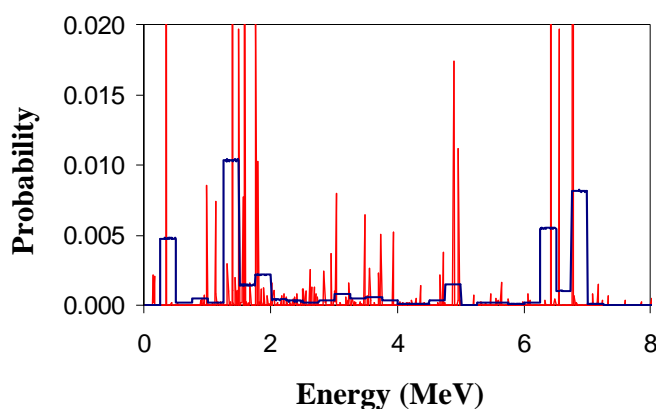
Gamma production enhancements

The simulation of neutron-induced gammas has always suffered from a lack of adequate precision in the gamma spectral data contained within the neutron cross-section library [15]. Some of these deficiencies have been addressed in the recent release of ENDF/B-VI libraries; however serious problems still exist. For example, Figure 2 presents the (n,γ) spectrum currently available in the ENDF/B-VI library for natural Ti (blue line). In contrast, Figure 1 also shows the gamma lines from a more complete compilation [6] (red line). Clearly the former spectrum is useless for a GRS analysis.

A new physics option was added to MCNPX to alleviate this problem. When this option is set, gamma production data for any nuclide and any reaction can be read from an auxiliary file. This data is properly normalised and used in place of the library data when gammas are produced from a neutron collision. For the results given in this paper, all capture gamma spectra were represented in this manner using data compiled by Reedy [16].

Figure 2. Gamma lines for Ti

Blue line is ENDF60 data and red is Reedy data.



Tally enhancements

Planetary GRS is always complicated by the fact that gamma production can result from numerous mechanisms, including intranuclear reactions, residual nuclei de-excitation, neutron inelastic reactions, bremsstrahlung, radioactive decay, etc. To deconvolve measured spectra into material composition requires the ability to separate simulated spectra into its various components, based on collisions (i.e. collided versus un-collided), source nuclei, reaction, etc. As mentioned earlier, MCNPX provides a convenient way to alter tallies in this manner. A special tally feature was developed that subdivides a tally into user-supplied bins, which enables the separation of spectra into various components based on the gamma-creation mechanism. Collided gammas can retain their creation information or be placed in a separate bin.

GRS analysis

A Monte Carlo detector gamma-ray transport code (McOGX) was used to convert MCNPX surface gamma-ray energy-angle distributions (for Apollo 11 soil) to elemental response functions. McOGX models the coincidence response of the Lunar Prospector gamma-ray spectrometer, which consists of a BGO scintillation detector surrounded by a plastic anti-coincidence shield. To produce a library of response functions, the components of the accepted spectrum were divided by weight fraction, the average atomic number in the case of high-energy reactions and the thermal neutron number density in the case of thermal neutron capture. A separate simulation was carried out to generate spectral components for the radioactive elements.

The abundance of all major and radioactive elements was determined by fitting the gamma-ray spectrum in the 700 keV to 9 000 keV region using library least-squares. The major element abundances were constrained to sum to one and Al was determined by correlation to Fe. The spectrum acquired during cruise (i.e. space flight) was used to represent the background from galactic gamma rays and activation of the BGO. Analysis of residuals for highland materials was used to adjust the cruise spectrum for additional build-up of radioactivity. Highland residuals were also used to modify the oxygen component to account for minor inconsistencies between the model and data at high energy, which may be due to errors in gamma-ray production data.

Results

MCNPX has the ability to output a plethora of simulation results. Its mesh tallies, general tallies, and history tape (HTAPE) capabilities have proven invaluable to understanding the underlying physics of many applications. Due to space limitations, only a subset of this output is presented in the following sub-sections.

Neutron and gamma production

The spatial production of secondary particles can be analysed most readily by using a mesh tally. In MCNPX this is accomplished by adding a few lines that describe the mesh in the input file. Rectangular, cylindrical or spherical meshes are available for a variety of output quantities, including track-based data (e.g. number of tracks, flux, dose, etc.), source data, energy deposition (i.e. ionisation, nuclear, recoil, etc.) and detector/DXTRAN tracks. For this application a 2 m cube, just below the incident proton source, was subdivided into 1 cm zones in two dimensions. A utility called GRIDCONV is provided with MCNPX to read the mesh data and convert it for viewing in various plotting packages. Figures 3 and 4 give the spatial dependence of the neutron and photon production within the lunar surface. The de-excitation gammas and bremsstrahlung photons generated along the path of an incident proton are quite evident in Figure 4.

Gamma spectra

With the tally enhancements discussed earlier, it is possible to tally gammas emerging from the lunar surface based on the interaction nuclei. Figures 5 and 6 give the un-collided capture gamma spectrum for Ti and Fe. Use of the Reedy (n, γ) production data is evident, especially for Ti.

It is also possible to obtain a separate tally bin for de-excitation gammas produced by spallation residual nuclei. Figure 7 shows the gamma spectra resulting from the Bertini break-up of oxygen into C and N (gammas from Li, Be and B also occur but are omitted for clarity). Figure 8 gives the collided and total photon spectra from all interactions.

Figure 3. Neutron production within a 2 m cube

Red arrow indicates proton source. Legend units are neutrons per incident proton.

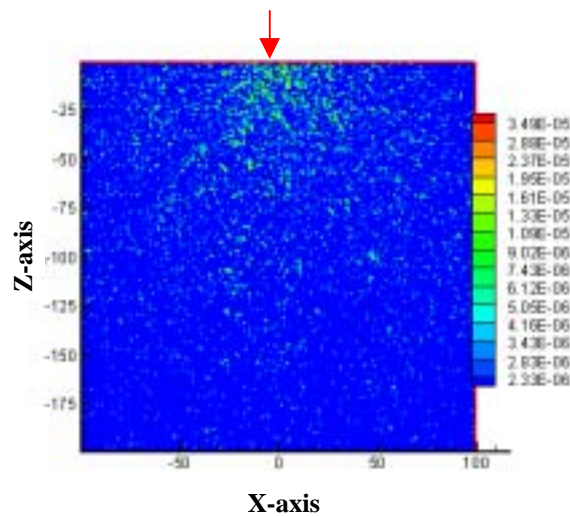


Figure 4. Photon/gamma production within a 2 m cube

Red arrow indicates proton source. Legend units are photons per incident proton.

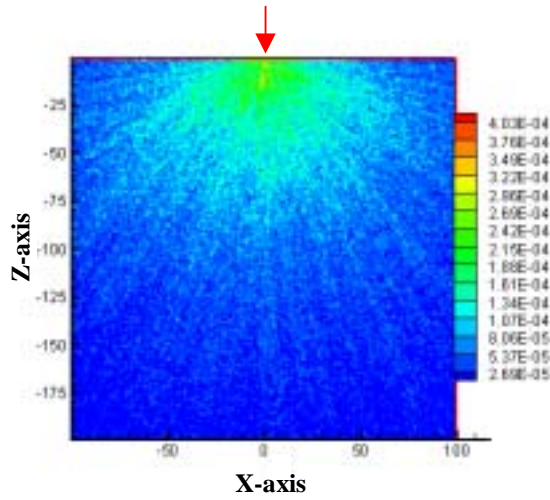


Figure 5. Un-collided (n, γ) spectrum for Ti

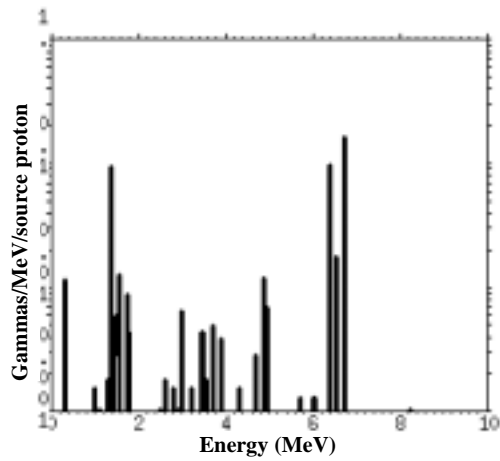


Figure 6. Un-collided (n, γ) spectrum for Fe

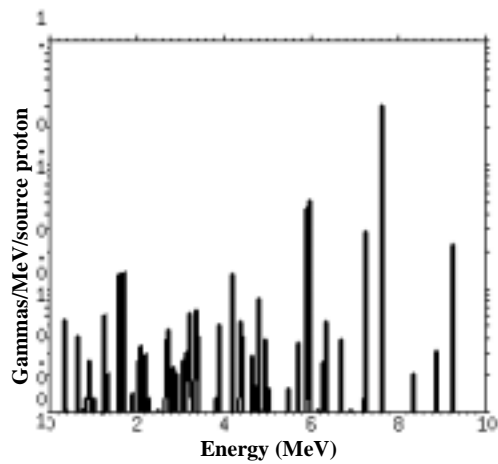


Figure 7. De-excitation gamma spectra from the break-up of oxygen into ^{12}C (black), ^{13}C (blue), ^{14}N (red) and ^{15}N (green)

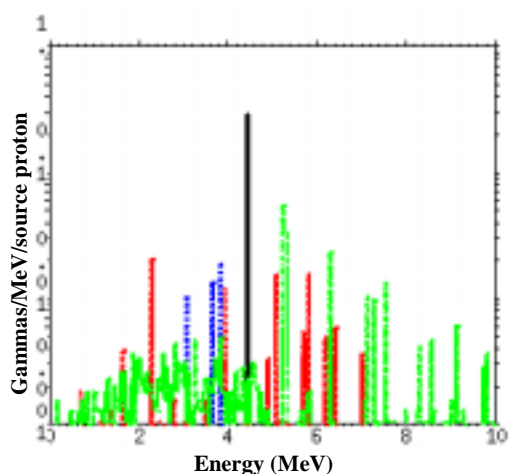
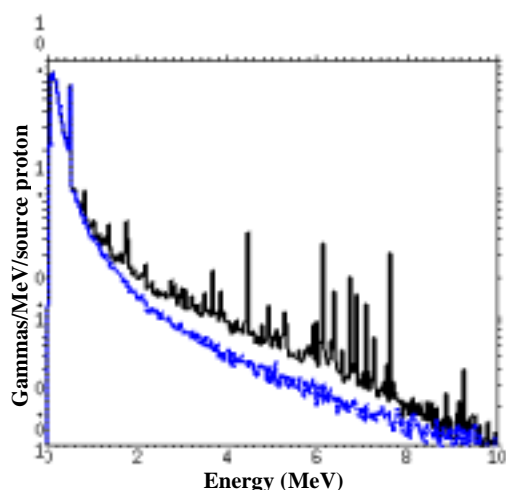


Figure 8. Total (black) and collided (blue) photon spectra



Impact of physics models

Spectral differences resulting from the Bertini and CEM INC models are clearly visible in Figure 9. The Bertini and ISABEL models gave nearly identical gamma spectra and resulted in the best comparison to lunar GRS measurements, while the CEM model had obvious discrepancies.

Lunar prospector analysis

The GRS detector response for the MCNPX gamma spectrum from the Apollo 11 material is compared to Lunar Prospector GRS measurements in Figure 10. The pulse height spectrum measured during the cruise phase of the mission was added to the modelled spectrum to account for background sources unrelated to lunar surface emissions. Note that the modelled spectrum does not include gamma rays from radioactive elements.

Figure 9. Total gamma spectra for the Bertini (black) and CEM (blue) INC models

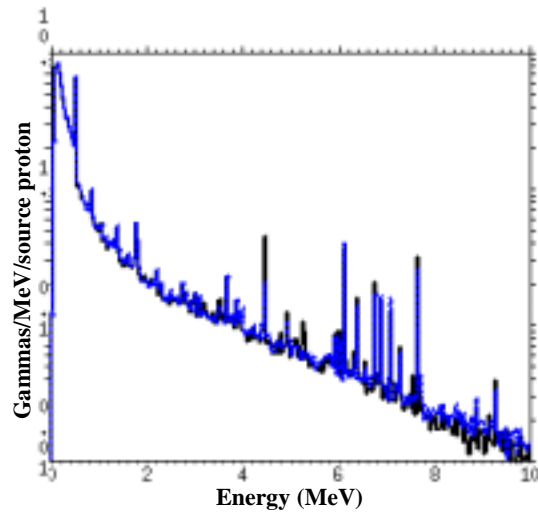
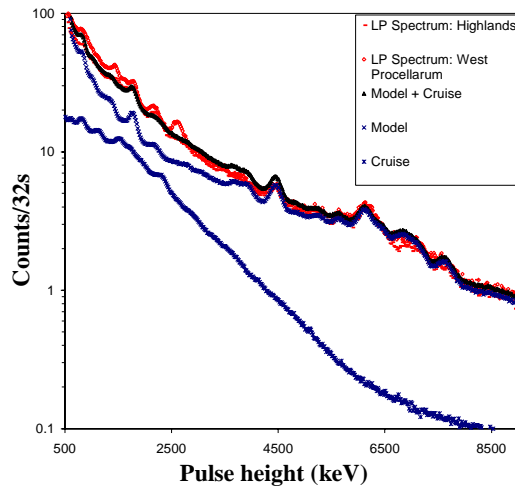


Figure 10. Comparison between MCNPX/MCOGX model of the Lunar Prospector gamma-ray spectrometer with lunar spectra measured over western Procellarum and the highlands



Least-squares fits to measured spectra acquired at high altitude and binned on 5° squares are shown in Figures 11-13 for the highlands, western Procellarum and Tranquillitatis. Major element abundances along with the thermal neutron number density (n_T) and average atomic number $\langle A \rangle$ used to modify the spectral components are given in the figure captions. Note that some spectral components, including the background spectrum measured during the cruise phase of the mission, were adjusted based on an analysis of residuals to account for activation of detector materials and prompt gamma-ray production in the detector by neutrons emitted from the surface.

Maps of all major elements have been constructed. SiO_2 and Al_2O_3 have maximum abundance in the highlands. TiO_2 and FeO maps are consistent with those previously published. The abundance of MgO is lowest in the highlands and highest in western Procellarum. Relatively high concentrations of MgO can be found in the South Pole Aitken basin.

Figure 11. Highlands: 0° latitude, -96.75° east longitude, $\langle A \rangle = 21.8$, $n_T = 2.02 \times 10^{-9} \text{ cm}^{-2}$. Major element composition: SiO₂ 44.5%, TiO₂ 0.3%, Al₂O₃ 30.2%, FeO 2.3%, MgO 0.0%, CaO 22.8%.

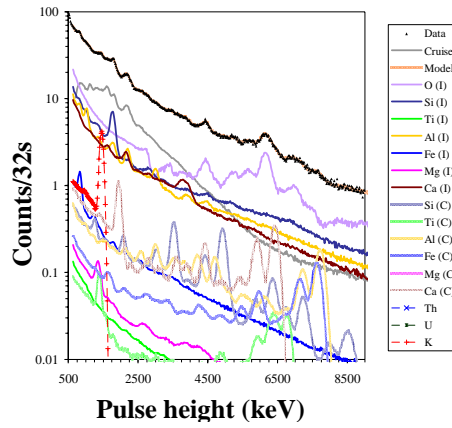


Figure 12. Western Procellarum: 0° latitude, -42.75° east longitude, $\langle A \rangle = 23.6$, $n_T = 7.85 \times 10^{-9} \text{ cm}^{-2}$. Major element composition: SiO₂ 50%, TiO₂ 8.1%, Al₂O₃ 3.4%, FeO 22%, MgO 10%, CaO 6.3%.

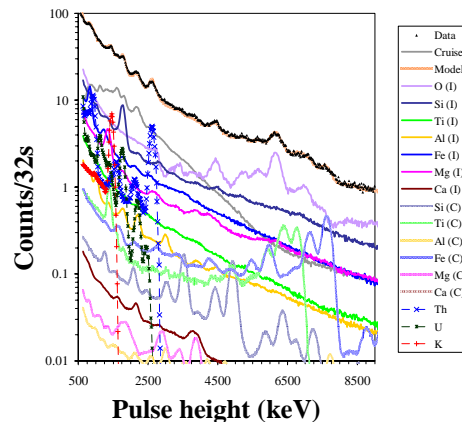
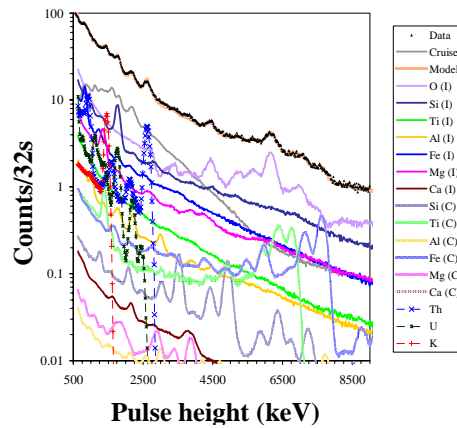


Figure 13. Tranquillitatis: 10° latitude, 22.5° east longitude, $\langle A \rangle = 23.6$, $n_T = 8.25 \times 10^{-9} \text{ cm}^{-2}$. Major element composition: SiO₂ 44.5%, TiO₂ 8.6%, Al₂O₃ 16%, FeO 12.8%, MgO 16%, CaO 1.2%.



Future work

The lunar GRS analysis will continue for other regions of the moon, yielding perhaps a finer resolution of composition maps, an analysis of errors and an improvement in the accuracy of nuclide components and detector background signals. A similar analysis is planned for Mars GRS measurements currently underway. Furthermore, additional MCNPX features are under development to enhance its usefulness for performing such analyses:

- *Coincidence tally enhancement.* This special tally feature will enable MCNPX to model the response of spectrometers with anti-coincidence shields, such as the Lunar Prospector gamma-ray spectrometer. Implementation of a coincidence tally in MCNPX will enable detailed characterisation of background sources (e.g. energetic electrons and protons) that interfere with measurements of gamma rays from the planetary surface. The tally will also aid in the design of future planetary spectroscopy systems, which may produce a correlated signal from a large number of detector elements.
- *Non-analogue pulse-height tallies.* This tally enhancement will allow the use of variance reduction techniques with pulse-height tallies. The current implementation requires analogue transport, which greatly increases the computational time required for detector simulations.
- *New INC CEM physics module.* Numerous speed and physics improvements have been made to the new INC CEM 2000 module which will be integrated into MCNPX in the near future.
- *Multi-processing.* Work is underway to extend the low-energy parallel processing capabilities within MCNPX to the high-energy physics modules. Preliminary implementations will include distributed-memory multi-processing with PVM.

Conclusions

The analysis documented here demonstrates the usefulness of MCNPX in planetary gamma-ray spectroscopy. Furthermore, new MCNPX features developed over the course of this analysis will prove extremely useful for other applications as well. Comparisons of MCNPX results to lunar GRS measurements are better than expected and have led to the identification of spectral features previously unknown. Through a library least-squares analysis, these simulation spectra have resulted in detailed maps of lunar composition.

REFERENCES

- [1] *MCNPX User's Manual*, L.S. Waters, ed., LANL Report TPO-E83-G-UG-X-0001 (1999).
- [2] Lawrence, D.J., *Lunar and Planetary Science XXXII*, 1830 (2001).
- [3] Gasnault, O., *et al.*, *GRL* 28 #19, 3797-3800 (2001).
- [4] *MCNP – A General Monte Carlo N-particle Transport Code*, J.F. Briesmeister, ed., LANL Report LA-13709-M, (2000).
- [5] Lawrence, D.J., *et al.*, *JGR* 105 #E8, 20307-20331 (2000).
- [6] Prettyman, T.H., *et al.*, *Lunar and Planetary Science XXXII*, 2122 (2001).
- [7] Prettyman, T.H., *et al.*, *Lunar and Planetary Science XXXIII*, 2012 (2001).
- [8] *Lunar Sourcebook*, G.H. Heiken, D.T. Vaniman and B.M. French, eds., Cambridge University Press (1991).
- [9] Aarnio, P.A., *et al.*, *FLUKA89*, Conseil Européenne, Organisation pour la Recherche Nucléaire, informal report (1990).
- [10] Bertini, H.W., *Phys. Rev.*, 188, 1711 (1969).
- [11] Yariv, Y., Z. Fraenkel, *Phys. Rev.*, C 24, 488 (1981).
- [12] Mashnik, S.G., A.J. Sierk, O. Bersillon, T.A. Gabriel, “Cascade-exciton Model Detailed Analysis of Proton Spallation at Energies from 10 MeV to 5 GeV”, *Nucl. Instr. Meth.*, A414, 68 (1998).
- [13] Chadwick, M.B., *et al.*, *LA150 Documentation of Cross-sections, Heating and Damage: Part A (Incident Neutrons) and Part B (Incident Protons)*, LANL Report LA-UR-99-1222 (1999).
- [14] Little, R.C., *et al.*, *Modern Nuclear Data for Monte Carlo Codes*, LANL Report LA-UR-00-4979 (2000).
- [15] Frankle, S.C., *Photon Production Assessment for the MCNP Data Libraries*, LANL Report LA-13092-MS (1996).
- [16] Reedy, R.C., S.C. Frankle, “Prompt Gamma Rays from Radiative Capture of Thermal Neutrons by Elements from Hydrogen through Zinc”, *Atomic Data Nucl. Data Tables*, in press (2002).

LIST OF PARTICIPANTS

AUSTRIA

ROLLET, Sofia
ARCS
Systems Development Radiation Safety
Health Physics Division
ARC Seibersdorf Research GmbH
2444 Seibersdorf

Tel: +43 50550 2482
Fax: +43 50550 2502
Eml: sofia.rollet@arcs.ac.at

BULGARIA

BELOUSOV, Sergey
INRNE-BAS
Boul. Tsarigradsko shose, 72
1784 Sofia

Tel: +359 2 7144 506
Fax: +359 2 9743 955
Eml: belousov@inrne.bas.bg

FRANCE

ANTONI, Rodolphe
CEA Saclay
SPR/SERD
F-91191 Gif-sur-Yvette Cedex

Tel: +33 (0) 1 69 08 73 26
Fax: +33 (0) 1 69 08 75 33
Eml: antoni@aquilon.cea.fr

BORNE, Francois
CEA DAM Ile-de-France
DASE/SPR
BP 8
F-91680 Bruyères-le-Châtel

Tel: +33 (1) 69 26 47 95
Fax: +33 (1) 69 26 70 61
Eml: francois.borne@cea.fr

COMTE, Nicolas
CEA Saclay
SPR-SERD
F-91191 Gif-sur-Yvette Cedex

Tel: +33 (0)1 69 08 53 25
Fax: +33 (0) 1 69 08 75 33
Eml: comte@aquilon.cea.fr

DORE, Frederic
MGP Instruments
BP-1
F-13113 Lamanon

Tel: +33 4 9059 6033
Fax: +33 4 9059 6089
Eml: fdore@mgpi.com.fr

LAMARCHE, Anne
CEA Cadarache
DED/SCCD/LDMN Bât. 225
F-13108 St. Paul-lez-Durance Cedex

Tel: +33 (0) 4 42 25 43 44
Fax: +33 (0) 4 42 25 23 67
Eml: anne.lamarche@cea.fr

MENARD, Stéphanie
IRSN/DPHD/SDOS/LRDE
BP 17
F-92262 Fontenay-aux-Roses Cedex

Tel: +33 (0)1 58 35 97 09
Fax: +33 (0)1 47 46 97 77
Eml: stephanie.menard@irsn.fr

GERMANY

BORCHERT, Hansjorg
University of Erlangen
Institute of Medical Physics
Krankenhausstr. 12
D-91054 Erlangen

Tel: +49 9131 8522828
Fax: +49 9131 8522824
Eml: hans@imp.uni-erlangen.de

SCHMIDT, Roman
TUV Sueddeutschland Bau und
Betrieb GmbH
Energie und Technologie
Abt.: EKS 3
Westendstrasse 199
D-80686 München

Tel: +49 89 5791 1567/9
Fax: +49 89 5791 1142
Eml: Roman.Schmidt@et.tuevsued.de

VOLMERT, Ben
WTI GmbH
Karl-Heinz-Beckurts-Str. 8
D-52428 Jülich

Tel: +49 2461 933 153
Fax: +49 2461 933 400
Eml: kuehl@wti.wse.de

ITALY

ROSETTI, Maurizio
ENEA
FIS-MET
Via Don Fiammelli, 2
I-40129 Bologna

Tel: +39 (051) 609 8313
Fax: +39 (051) 609 8062
Eml: rosetti@bologna.enea.it

THE NETHERLANDS

SMILJANIC, Ivan
Technische Universiteit Delft
Mekelweg 15
2629 JB Delft

Tel: +31 527 83 650
Fax: +31 527 89 011
Eml: i.smiljanic@iri.tudelft.nl

PORTUGAL

ALVES, Carla
Centro Regional de Oncologia de
Coimbra do IPOFG
Av. Bissaya Barreto
P-3000-075 Coimbra

Tel: +351 239 400200
Fax: +351 239 484317
Eml: calves@croc.min-saude.pt

CHAVES, Aderito Centro Regional de Oncologia de Coimbra do IPOFG Av. Bissaya Barreto P-3000-075 Coimbra	Tel: +351 239 400200 Fax: +351 239 484317 Eml: achaves@croc.min-saude.pt
DA SILVA CARDOSO, João Vitor Instituto Tecnológico e Nuclear (ITN) Departamento de Protecção Radiológica e Segurança Nuclear P-2686-953 Sacavém	Tel: +351 219946336 Fax: +351 219941995 Eml: lmri@itn.pt
DIAS DE OLIVEIRA, Augusto Manuel Instituto Tecnológico e Nuclear (ITN) DPRSN Estrada Nacional 10, Apartado 21 P-2686-953 Sacavém	Tel: +351 21 994 6297 Fax: +351 21 994 1995 Eml: adoliv@itn.pt
GIEB, Martin Instituto Tecnológico e Nuclear (ITN) Estrada Nacional 10 P-2686-953 Sacavém	Tel: +351 21 944 6019 Fax: +351 21 955 0117 Eml: Martin.Gieb@itn.pt
GONCALVES, Isabel F. Instituto Tecnológico e Nuclear (ITN) Física Estrada Nacional 10 P-2686-953 Sacavém	Tel: +351 21 994 6054 Fax: +351 21 994 1525 Eml: ifg@itn.pt
JACOB DA CRUZ, Katia Instituto Tecnológico e Nuclear (ITN) Estrada Nacional 10, Apartado 21 P-2686-953 Sacavém	Tel: +351 21 994 6000 Fax: +351 21 994 1995 Eml: katiadj@itn.pt
MARUJO MARQUES, Fernanda Instituto Tecnológico e Nuclear (ITN) Química Estrada Nacional 10, Apartado 21 P-2686-953 Sacavém	Tel: +351 21 9946225 Fax: +351 21 9941455 Eml: fmarujo@itn.pt
NEVES, Maria Instituto Tecnológico e Nuclear (ITN) DPRSN Estrada Nacional 10, Apartado 21 P-2686-953 Sacavém	Tel: +351 219946238 Fax: +351 219941995 Eml: mneves@itn.pt
OLIVEIRA, Carlos Instituto Tecnológico e Nuclear (ITN) Estrada Nacional 10 P-2685-953 Sacavém	Tel: +351 219946062 Fax: +351 219941995 Eml: coli@itn.pt

ORTIGAO, Catarina
LIP
Avieda Elias Garcia 14-10
P-1000-149 Lisboa

Tel: +351 217 973880
Fax: +351 217 937631
Eml: ortigao@lip.pt

PERALTA, Luis
LIP Investigator
University of Lisbon
Avieda Elias Garcia, 14-10
P-1000-149 Lisboa

Tel: +351 21 797 3880
Fax: +351 21 793 4631
Eml: luis@lip.pt

PIRES, Carla M.S.
Instituto Tecnológico e Nuclear (ITN)
Estrada Nacional 10, Apartado 21
P-2496-953 Sacavém

Tel: +351 21 994 6000
Fax: +351 21 994 1995
Eml: carlamsp@itn.pt

RODRIGUES, Pedro
Laboratorio de Instrumentacao e
Fisica Experimenta
LIP
Avieda Elias Garcia, 14-10
P-1000-149 Lisboa

Tel: +351 21 797 3880
Fax: +351 21 793 9631
Eml: psilva@lip.pt

TEIXEIRA, Nuno
Fac. Cien Medicas – UNL
Service Fisica Dep. Radioterapia Centro de
Lisboa do IPOFG
Av. D. Joao II, lote 4.69.01
P-1990-096 Lisboa

Tel: +351 964144880
Fax: +351 218980460
Eml: teixeira.nuno@mail.telepac.pt

TRINDADE, Andreia
Laboratorio de Instrumentacao e
Fisica Experimenta
LIP
Avenida Elias Garcia 14-10
P-1000-149 Lisboa

Tel: +351 21 797 3880
Fax: +351 21 793 4631
Eml: andreia@lip.pt

RUMANIA

AIOANEI, LAURENTIU COSTEL
Institute for Nuclear Research
P.O.Box 78
0300 Pitesti

Tel: ++40 48 213400
Fax: ++40 48 262449
Eml: avi@easynet.ro

SOUTH AFRICA

MATEVA, Tsvetana
De Beers Consolidated Mines
PO Box 82851
Southdale 2135

Tel: +27 11 374 6669
Fax: +27 11 374 6640
Eml: tsvetana.mateva@debeersgroup.com

SPAIN

EMBED SEGURA, Miguel
CIEMAT
Nuclear Fission Department
Avda. Complutense, 22
E-28040 Madrid

Tel: +34 913466731
Fax: +34 913466576
Eml: miguel.embed@ciemat.es

GOMEZ-ROS, Jose M.
CIEMAT
Dept. of Radiation Dosimetry
Avda. Complutense, 22 (Edif. 36)
E-28040 Madrid

Tel: +34 91 346 6322
Fax: +34 91 346 6393
Eml: jm.gomezros@ciemat.es

MORALEDA, Montserrat
CIEMAT
Avd. Complutense, 22
E-28040 Madrid

Tel: +34 913466237
Fax: +34 913466121
Eml: montse.moraleda@ciemat.es

SWITZERLAND

VAN GEEMERT, Rene
Paul Scherrer Institute
CH-5232 Villigen PSI

Tel: +41 56 3102883
Fax: +41 56 3104527
Eml: rene.vangeemert@psi.ch

UNITED KINGDOM

LOUGHLIN, Michael
UK Atomic Energy Authority
Room 2.60, Building D3
Culham Science Centre
Abingdon
Oxfordshire OX14 3BD

Tel: +44 (1235) 463328
Fax: +44 (1235) 463647
Eml: michael.loughlin@ukaea.org.uk

MA, Andy
Physics Department
University of Surrey
Guilford GU2 7XH

Tel: +44 1483 689 423
Fax: +44 1483 686 781
Eml: a.ma@surrey.ac.uk

UNITED STATES OF AMERICA

SHANNON, Michael P.
Georgia Institute of Technology
George Woodruff School of Mechanical Eng.
Neely Nuclear Research Center
900 Atlantic Drive
Atlanta, GA 30332-0405

Tel: +1 404 894 9954
Fax: +1 404 894 9325
Eml: gtg749d@prism.gatech.edu

INTERNATIONAL ORGANISATIONS

BERTHOU, Veronique
Institute for Transuranium Elements
Joint Research Centre
Postfach 2340
D-76125 Karlsruhe

Tel: +49 724 79 51 506
Fax: +49 724 795199 506
Eml: berthou@itu.fzk.de

MUELLER, Mario J.
CERN-TIS/RP-865-R-C11
CH-1211 Geneva 23

Tel: +41 22 76 74782
Fax: +41 33 76 79360
Eml: mario.mueller@cern.ch

LIST OF ORGANISERS, SPONSORS, TEACHERS

FRANCE

PIHET, Pascal
IRSN/DPHD
Commissariat à l'Énergie Atomique
BP N° 17
F-92265 Fontenay-aux-Roses Cedex

Tel: +33 1 46 54 91 21
Fax: +33 1 47 46 97 77
Eml: pascal.pihet@irsn.fr

GERMANY

GROSSWENDT, Bernd
Physikalisch-Technische Bundesanstalt
Bundesallee 100
D-38116 Braunschweig

Tel: +49 (531) 592 6002
Fax: +49 (531) 592 6015
Eml: Bernd.Grosswendt@ptb.de

KRAEMER, Michael
GSI
Planckstr. 1
D-64291 Darmstadt

Tel: +49 6159 712157
Fax: +49 6159 712106
Eml: m.kraemer@gsi.de

ITALY

GUALDRINI, Gianfranco
ENEA/ION/IRP
Via dei Colli 16
I-40136 Bologna

Tel: +39 (051) 609 8350
Fax: +39 (051) 609 8003
Eml: guald@bologna.enea.it

PELLICIONI, Maurizio
INFN
Laboratori Nazionali di Frascati
Casella Postale 56
I-00044 Frascati

Tel: +39 (06) 940 32246
Fax: +39 (06) 940 32364
Eml: maurizio.pellicioni@Inf.infn.it

PORTUGAL

BAPTISTA, Filomena
Instituto Tecnológico e Nuclear (ITN)
Estrada Nacional 10
P-2686-953 Sacavém Codex

Tel: +351 21 994 6088
Fax:
Eml: filobapt@itn.pt

CARVALHO SOARES, José
Président
Instituto Tecnológico e Nuclear (ITN)
Estrada Nacional 10
P-2686-953 Sacavém Codex

Tel: +351 (21) 994 6010
Fax: +351 (21) 955 0117
Eml: soaresjc@itn.pt

EIRO, Ana
Centro de Física Nuclear da
Universidade de Lisboa
Av. Prof. Gama Pinto, 2
P-1649-003 Lisboa Codex

Tel: +351 217950790 (Ext. 4224)
Fax: +351 21 7954288
Eml: ana.eiro@cc.fc.ul.pt

OLIVEIRA, Luisa
Instituto Tecnológico e Nuclear (ITN)
Estrada Nacional 10
P-2686-953 Sacavém

Tel: +351 21 994 6070
Fax:
Eml: luisaoliveira@itn.pt

VAZ, Pedro
Instituto Tecnológico e Nuclear (ITN)
Estrada Nacional 10
P-2686-953 Sacavém

Tel: +351 21 994 62 30
Fax: +351 21 994 10 39
Eml: pedrovaz@itn.pt

SPAIN

Salvat, Francesc
Facultat de Física (ECM)
Universitat de Barcelona
Diagonal 647
E-08028 Barcelona

Tel: +34 93 402 11 86
Fax: +34 93 402 11 74
Eml: cesc@ecm.ub.es

UNITED STATES OF AMERICA

HERTEL, Nolan E.
George Woodruff School of Mechanical Eng.
Georgia Institute of Technology
900 Atlantic Dr.
Atlanta, GA 30332-0405

Tel: +1 (404) 894 3601
Fax: +1 (404) 894 9325
Eml: nolan.hertel@me.gatech.edu

HUGHES, Grady
Los Alamos National Laboratory
Group CSS-4, MS D409
Los Alamos, NM 87545

Tel: +1 (505) 667 5957
Fax: +1 (505) 665 5538
Eml: hgh@lanl.gov

MCKINNEY, Gregg W.
Nuclear Systems Design and Analysis (D-10)
Los Alamos National Laboratory
PO Box 1663 MS K575
Los Alamos, NM 87545

Tel: +1 (505) 665 8367
Fax: +1 (505) 665 2897
Eml: gwm@lanl.gov

NAHUM, Alan E.
Radiation Oncology
Fox Chase Cancer Center
Philadelphia, PA 19111

Tel: +1 215 728 7128
Fax: +1 215 728 4789
Eml: a-nahum@fccc.edu

WATERS, Laurie S.
Los Alamos National Laboratory
MS K575
Los Alamos, NM 87544

Tel: +1 (505) 665 4127
Fax: +1 (505) 665 2897
Eml: lsw@lanl.gov

INTERNATIONAL ORGANISATIONS

FERRARI, Alfredo
CERN – SL Division
Bât. 864-2-D05
Mail Box Z03000
CH-1211 Genève 23

Tel: +41(0)22 76 76119
Fax: +41(0)22 76 77555
Eml: alfredo.ferrari@cern.ch

SARTORI, Enrico
OECD/NEA Data Bank
Le Seine-Saint Germain
12, boulevard des Iles
F-92130 Issy-les-Moulineaux

Tel: +33 1 45 24 10 72/78
Fax: +33 1 45 24 11 10/28
Eml: sartori@nea.fr

Fifty-eight (58) participants from 13 countries and 3 international organisations.

Questionnaire on the quality of OECD publications

We would like to ensure that our publications meet your requirements in terms of presentation and editorial content. We would welcome your feedback and any comments you may have for improvement. Please take a few minutes to complete the following questionnaire. Answers should be given on a scale of 1 to 5 (1 = poor, 5 = excellent).

Fax or post your answer before 31 December 2004, and you will automatically be entered into the prize draw to win a year's subscription to *OECD's Observer magazine*.*

A. Presentation and layout

1. What do you think about the presentation and layout in terms of the following:

	Poor	Adequate		Excellent	
Readability (font, typeface)	1	2	3	4	5
Organisation of the book	1	2	3	4	5
Statistical tables	1	2	3	4	5
Graphs	1	2	3	4	5

B. Printing and binding

2. What do you think about the quality of the printed edition in terms of the following:

Quality of the printing	1	2	3	4	5
Quality of the paper	1	2	3	4	5
Type of binding	1	2	3	4	5
Not relevant, I am using the e-book	<input type="checkbox"/>				

3. Which delivery format do you prefer for publications in general?

Print CD E-book (PDF) via Internet Combination of formats

C. Content

4. How accurate and up to date do you consider the content of this publication to be?

1 2 3 4 5

5. Are the chapter titles, headings and subheadings...

Clear Yes No
Meaningful Yes No

6. How do you rate the written style of the publication (e.g. language, syntax, grammar)?

1 2 3 4 5

D. General

7. Do you have any additional comments you would like to add about the publication?

.....
.....
.....

Tell us who you are:

Name: E-mail:

Fax:

Which of the following describes you?

IGO NGO Self-employed Student
Academic Government official Politician Private sector

Thank you for completing the questionnaire. Please fax your answers to:

(33-1) 49 10 42 81 or mail it to the following address:

Questionnaire qualité PAC/PROD, Division des publications de l'OCDE
23, rue du Dôme – 92100 Boulogne Billancourt – France.

Title: Computing Radiation Dosimetry - CRD

ISBN: 92-64-01671-6

OECD Code (printed version): 66 2004 11 1 P

* Please note: This offer is not open to OECD staff.

OECD PUBLICATIONS, 2, rue André-Pascal, 75775 PARIS CEDEX 16

PRINTED IN FRANCE

(66 2004 111 P) No. 53637 2004

© OECD, 1999.

© Software: 1987-1996, Acrobat is a trademark of ADOBE.

All rights reserved. OECD grants you the right to use one copy of this Program for your personal use only. Unauthorised reproduction, lending, hiring, transmission or distribution of any data or software is prohibited. You must treat the Program and associated materials and any elements thereof like any other copyrighted material.

All requests should be made to:

Head of Publications Service,
OECD Publications Service,
2, rue André-Pascal, 75775 Paris
Cedex 16, France.

© OCDE, 1999

© Logiciel, 1987-1996, Acrobat, marque déposée d'ADOBE.

Tous droits du producteur et du propriétaire de ce produit sont réservés. L'OCDE autorise la reproduction d'un seul exemplaire de ce programme pour usage personnel et non commercial uniquement. Sauf autorisation, la duplication, la location, le prêt, l'utilisation de ce produit pour exécution publique sont interdits. Ce programme, les données y afférentes et d'autres éléments doivent donc être traités comme toute autre documentation sur laquelle s'exerce la protection par le droit d'auteur.

Les demandes sont à adresser au :

Chef du Service des Publications,
Service des Publications de l'OCDE,
2, rue André-Pascal,
75775 Paris Cedex 16, France.